JOHANNES BERNHARD

# EXCLUSIVE VECTOR MESON PRODUCTION IN PP COLLISIONS AT THE COMPASS EXPERIMENT

# EXCLUSIVE VECTOR MESON PRODUCTION IN PP COLLISIONS AT THE COMPASS EXPERIMENT

JGU

JOHANNES GUTENBERG UNIVERSITÄT MAINZ

Dissertation
zur Erlangung des Grades
"Doktor
der Naturwissenschaften"

am Fachbereich 08 – Physik, Mathematik und Informatik

der Johannes-Gutenberg-Universität
in Mainz

JOHANNES BERNHARD
geb. in Limburg an der Lahn

Mainz, den 16.01.2014

TAG DER MÜNDLICHEN PRÜFUNG: 04.07.2014

Johannes Bernhard,
*Exclusive vector meson production in pp collisions at the COMPASS experiment,*
Dissertation zur Erlangung des Grades "Doktor der Naturwissenschaften"am Fachbereich 08 – Physik, Mathematik und Informatik der Johannes-Gutenberg-Universität Mainz **D77**

*For those who stay up late at night.*

*Buy the ticket. Take the ride.*

— Hunter S. Thompson

## ABSTRACT

Mechanisms for particle production in proton-proton collisions at intermediate energies are studied within the COMPASS collaboration using the COMPASS spectrometer at the M2 beam line of the SPS at CERN. The possible production mechanisms are investigated using the production of the vector mesons $\omega$ and $\phi$ and include resonant diffractive excitation of the beam proton with a subsequent decay of the resonance, central production and the related "shake-off" mechanism.
The data which were used for this thesis were collected in the years 2008 and 2009 with a 190 GeV/$c$ proton beam impinging on a liquid hydrogen target that was surrounded by a recoil proton detector (RPD). The RPD is an integral part of the newly developed hadron trigger system for which in addition several new detectors have been build. The performances of both RPD and hadron trigger system are scrutinised and efficiency parameters are extracted. A method for reconstruction of recoil protons and for calibration is developed and described.
The production of $\omega$ mesons is studied with the reaction $pp \to p\omega p$, $\omega \to \pi^+\pi^-\pi^0$ and the production of $\phi$ mesons with the reaction $pp \to p\phi p$, $\phi \to K^+K^-$ for momentum transfers squared between 0.1 $(\mathrm{GeV}/c)^2$ and 1 $(\mathrm{GeV}/c)^2$. The production ratio $\sigma(pp \to p\phi p)/\sigma(pp \to p\omega p)$ is determined as a function of the longitudinal momentum fraction $x_\mathrm{F}$ and compared to the OZI rule prediction. A significant violation of the OZI rule dependent on $x_\mathrm{F}$ is found and discussed with respect to resonant structures in the $p\omega$ mass spectrum. Removing the low $p\omega/p\phi$ mass region which includes these structures eliminates the $x_\mathrm{F}$ dependence. In addition, the spin density matrix element $\rho_{00}$, *i.e.* the spin alignment, for both $\omega$ and $\phi$ mesons is studied. One study is performed in the helicity frame that allows to discriminate resonant diffractive excitation. In a second study, a reference frame with respect to the direction of the momentum transfer is chosen which allows to single out central mechanisms like central production or shake-off. Dependences of the spin alignment on the invariant mass of the proton-vector meson system and $x_\mathrm{F}$ are found. These dependences can be related to resonant contributions to the $\omega$ meson production. The discussion of all results with respect to the expected production mechanisms concludes the thesis.

# ZUSAMMENFASSUNG

Produktionsmechanismen für Teilchenproduktion im mittleren Energiebereich wurden in Proton-Proton Kollisionen innerhalb der COMPASS-Kollaboration mit Hilfe des COMPASS-Spektrometers am SPS Beschleuniger am CERN untersucht. Die verschiedenen Produktionsmechanismen werden mittels Produktion der Vektormesonen $\omega$ und $\phi$ studiert und können die diffraktive Anregung des Strahlteilchens mit anschliessendem Zerfall der Resonanz, zentrale Produktion und den damit verwandten "Shake-off" Mechanismus enthalten.
Die für diese Arbeit verwendeten Daten wurden in den Jahren 2008 und 2009 mit 190 GeV/$c$-Protonen aufgenommen, die auf ein Flüssigwasserstofftarget trafen. Das Target war von einem Rückstoßprotonendetektor umgeben, der ein integraler Bestandteil des neuentwickelten Hadrontriggersystems ist. Für dieses System wurden außerdem einige neue Detektoren gebaut. Die Leistungsfähigkeit des Rückstoßprotonendetektors und des Triggersystems wird untersucht und Effizienzen extrahiert. Außerdem wird sowohl eine Methode zur Rekonstruktion von Rückstoßprotonen als auch eine Methode zur Kalibration des Rückstoßprotonendetektors entwickelt und beschrieben.
Die Produktion von $\omega$-Mesonen wurde in der Reaktion $pp \to p\omega p$, $\omega \to \pi^+\pi^-\pi^0$ und die Produktion von $\phi$-Mesonen in der Reaktion $pp \to p\phi p$, $\phi \to K^+K^-$ bei einem Impulsübertrag zwischen $0.1\,(\mathrm{GeV}/c)^2$ und $1\,(\mathrm{GeV}/c)^2$ gemessen. Das Produktionsverhältnis $\sigma(pp \to p\phi p)/\sigma(pp \to p\omega p)$ wird als Funktion des longitudinalen Impulsanteils $x_\mathrm{F}$ bestimmt und mit der Vorhersage durch die Zweigregel verglichen. Es ergibt sich eine signifikante Verletzung der Zweigregel, die abhängig von $x_\mathrm{F}$ ist. Die Verletzung wird in Verbindung zu resonanten Strukturen im $p\omega$-Massenspektrum diskutiert. Die $x_\mathrm{F}$-Abhängigkeit verschwindet, wenn man die Region niedriger $p\omega$- und $p\phi$-Masse entfernt, die solche resonanten Strukturen aufweist. Zusätzlich wird die Spinausrichtung bzw. das Spindichtematrixelement $\rho_{00}$ für $\omega$- und $\phi$-Mesonen untersucht. Die Spinausrichtung wird im Helizitätssystem analysiert, welches für eine Abgrenzung von resonanten, diffraktiven Anregungen geeignet ist. Außerdem wird die Spinausrichtung in einem Referenzsystem mit Bezug auf die Richtung des Impulsübertrags untersucht, mit dessen Hilfe zentrale Prozesse wie zentrale Produktion oder "shake-off" abgegrenzt werden. Auch hier wird eine Abhängigkeit von $x_\mathrm{F}$ und der invarianten Masse des $p\omega$-Systems beobachtet. Diese Abhängigkeit kann wieder auf die resonanten Strukturen in der Produktion von $\omega$-Mesonen zurückgeführt werden. Die Ergebnisse werden abschließend im Hinblick auf die verschiedenen Produktionsmechanismen diskutiert.

# CONTENTS

# 1 INTRODUCTION

The basic, point-like elementary particles are on the one hand *leptons*, such as the electron, and on the other hand *quarks*, which combine and form more complex objects like protons and neutrons. There are six types of leptons and six types of quarks plus their respective anti-particles which can interact through four fundamental forces: gravity, electro-magnetism, weak interaction and strong interaction. While gravity still lacks a description on the quantum level, the other three forces could successfully be described within one theoretical framework, the so-called *Standard Model* [73, 115, 127]. Being a relativistic quantum field theory, it combines three fundamental concepts: forces are mediated by *fields*, these fields are *quantised*, and they respect the *relativity* principle. The representatives of the force fields are called bosons. $W^{\pm}$ and $Z$ bosons carry the weak force, the photon carries the electro-magnetic force and the gluon mediates the strong interaction. There are several reviews and introductions to the Standard Model available, *e.g.* [87, 112].
The most complex of the three forces leading to a large variety of observed phenomena is the strong interaction. It is mediated by mass-less spin 1 particles, the gluons, which can couple either to quarks or to other gluons. Quarks are constituents of strongly interacting particles which are called hadrons. The quarks themselves are particles with spin $1/2$ and occur as six different types, called *flavours*: up, down, strange, charm, bottom, and top. Up to now, no excitation of any quark was found and their size is constrained to be smaller than $10^{-16}$ cm. Currently it is assumed that they are point-like particles. The quark masses span several orders of magnitude, starting from the lightest quarks at a few $\mathrm{MeV}/c^2$ to the heaviest known elementary particle, the top quark, with a mass of $172\,\mathrm{GeV}/c^2$. The quarks have electric charges $Q$ of either $\pm 1/3$ or $\pm 2/3$. A peculiarity of quarks is that they are not observed as single particles, but only in pairs or larger agglomerations because of the so-called confinement. Particles made of two quarks are called mesons, particles with three quarks are called baryons. Besides the already mentioned spin and electric charge, quarks have other important properties which are briefly summarised in context of this thesis in Table 1. There are quantum numbers to distinguish the different flavours, which are not conserved in electro-weak interactions. The *strangeness* $\mathcal{S}$ is $-1$ for a strange quark. Analogue quantum numbers exist for $c$ (*charm*, $+1$), $b$ (*bottom*, $-1$), and $t$ quarks (*top*, $+1$). Due to the similar masses of up and down quarks, an SU(2) symmetry occurs, the *isospin* $I$, which is only broken at the percent level. In analogy to the spin, the projection $I_3$ along the quantisation axis is $-1/2$ for down quarks and $+1/2$ for up quarks. It was introduced in an attempt by Heisenberg and (later) Wigner to explain the similar behaviour of neutron and proton for strong interactions.

| property | $d$ | $u$ | $s$ | $c$ | $b$ | $t$ |
|---|---|---|---|---|---|---|
| $Q$ el. charge | $-\frac{1}{3}$ | $+\frac{2}{3}$ | $-\frac{1}{3}$ | $+\frac{1}{3}$ | $-\frac{2}{3}$ | $+\frac{1}{3}$ |
| $I_3$ isospin | $-\frac{1}{2}$ | $+\frac{1}{2}$ | 0 | 0 | 0 | 0 |
| $\mathcal{S}$ strangeness | 0 | 0 | $-1$ | 0 | 0 | 0 |
| Mass (MeV/$c^2$) | $4.8^{+0.5}_{-0.3}$ | $2.3^{+0.7}_{-0.5}$ | $95 \pm 5$ | $1275 \pm 25$ | $4180 \pm 30$ | $173\,070$ $\pm 52 \pm 72$ |

Table 1: Quark properties [29].

The quantised field theory which describes the strong interaction is called Quantum ChromoDynamics, or short QCD[1]. It describes the strong interaction analogue to quantum electrodynamics. The charge equivalent in the strong interaction is the colour charge. Quarks (respectively anti-quarks) have one of the three existing colours $r$, $g$, and $b$ (respectively anti-colours $\bar{r}$, $\bar{g}$, and $\bar{b}$). No free quarks have been observed, but only hadrons. Thus, only colour-neutral objects (colour singlets) seem to be allowed by nature. This phenomenon is called *confinement*. Moreover, strong interactions do not depend on specific colours, they are invariant under colour transformations. Mathematically, this is expressed as a $\mathrm{SU(3)_c}$ symmetry where the index c stands for colour. Colour singlets are combinations of either all three colours (baryons) or a combination of a colour and the respective anti-colour (mesons). Theoretically, more complex combinations of four, five, etc. quarks are allowed, but are not found experimentally.
Gluons exchange colour between quarks. As the colour needs to be conserved at a gluon–quark vertex, gluons must carry one colour and one anti-colour. The possible colour combinations are found exploiting $\mathrm{SU(3)_c}$ symmetry. Denoting the three colours by 3 and the three anti-colours by $\bar{3}$, the combination yields $3 \otimes \bar{3} = 8 \oplus 1$. The result is an octet with eight anti-symmetric combinations and a symmetric singlet. The singlet itself is colour-neutral and therefore would not couple to other gluons and quarks. Hence, only the eight antisymmetric gluons are responsible for the strong interaction. Single gluons are confined like quarks, however combinations of two or more gluons could form free particles which are called glueballs.
Another important feature of strong interactions is the so-called asymptotic freedom. The strong coupling gets weaker as the energy increases and the distance decreases. Asymptotic freedom allows perturbative QCD calculations at large momentum transfers. In the non-perturbative range, a complete description is attempted using lattice QCD [129] which introduce a discrete Euclidean space-time lattice. However, many calculations are either not yet available or not yet precise enough. Thus, phenomenological models have to be used to describe strong interaction at the low energy scale, which are introduced in the following chapter.
This thesis concentrates on specific aspects of the strong interaction with the goal to contribute to the comprehension of particle production at energies of about 200 GeV. In the next section, a brief overview on the strong interaction is given. The pro-

1 An introduction is beyond the scope of this thesis and can be found within the review of Bethge *et. al.* [29], whereas an extensive listing of resources on QCD can be found in [95].

duction mechanisms are investigated at a momentum transfer squared between $0.1\,(\mathrm{GeV}/c)^2$ and $1\,(\mathrm{GeV}/c)^2$. At this scale, gluon exchanges are not dominant and the strong interaction can be described by exchanges of colour singlets (*e.g.* mesons) in effective theories. In the quark model, a hadron constitutes of a combination of quarks and/or anti–quarks which specifies the quantum numbers of the hadron. The production of the well-known mesons $\omega(782)$ and $\phi(1020)$ is used as a "standard candle" or "chemical tracer" to investigate the mechanisms with respect to the nature of the exchanged object. Due to the particular quark content of $\omega$ and $\phi$ it becomes possible to trace the exchange of strangeness and isospin in the reaction. In the quark model, such exchanges are illustrated by a simplified Feynman diagram which depicts the path of the constituent quarks for the process ("quark lines"). The phenomenological Okubo-Zweig-Iizuka rule states that only processes with connected quark lines are allowed. The rule predicts the yields of $\phi$ meson production compared to the yield of $\omega$ meson production. By studying possible violations of this rule, also with respect to kinematical dependencies, it is possible to investigate the importance of meson-exchanges. Furthermore, the spin of the $\omega$ and $\phi$ mesons allows to search for dependences on angular momentum. The spin alignment of the mesons is expected to be influenced by the production mechanism which allows for a study on the separation of different mechanisms.
The theoretical background for the outlined studies is summarised in Chapter 2. The production is investigated by the reaction $p_{\mathrm{beam}}\, p_{\mathrm{target}} \rightarrow p_{\mathrm{fast}}\, V\, p_{\mathrm{recoil}}$, $V = \omega, \phi$, which is measured at a beam momentum of $190\,\mathrm{GeV}/c$ in $pp$ collisions. The $\omega$ mesons are detected *via* the decay $\omega \rightarrow \pi^+\pi^-\pi^0$ and the $\phi$ mesons *via* the decay $\phi \rightarrow K^+K^-$. The measurement was performed in the years 2008 and 2009 with the COMPASS spectrometer, which is presented in Chapter 3. There, details on the relevant detectors for this thesis are given. In Chapter 4, the COMPASS recoil proton detector (RPD) is explained in detail. The reconstruction and calibration methods are described and the detector performance and efficiency is evaluated. The RPD is a key detector in the trigger system, which is described in Chapter 5. Both chapters include a description of the construction, the commissioning, and the operation of RPD, trigger system, and its components. Furthermore, the performance of the trigger system is discussed. The data selection and determination of the spectrometer acceptance is described in Chapter 6. In addition, the extraction of the $\omega$ and $\phi$ signals by a fit and a sideband subtraction method is shown. The physics analysis and discussion of results follows in Chapter 7. After the presentation of the kinematical properties of the data, the production ratio of $\phi$ to $\omega$ as a function of the Feynman variable $x_{\mathrm{F}}$ is shown. Then, the spin alignment of the vector mesons and its dependence on the discussed kinematical properties are studied within two different reference frames. The combined information of all results is then discussed with respect to the production mechanism. The thesis concludes with a summary of the results.

# 2

# THEORETICAL FRAMEWORK

In this chapter, an overview on the theoretical background for the analysis in the following chapters is given. The subject of this thesis is the production of the vector mesons $\omega$ and $\phi$ in proton–proton collisions.
First the quark model for mesons is explained and characteristics of $\omega$ and $\phi$ mesons are reviewed. A simple rule is found that allows for a prediction of the $\phi$ to $\omega$ production ratio. After the introduction of the kinematic properties of the production, the cross section and its spin dependence is discussed, which is connected to the spin-density matrix. The spin density matrix relates the spin alignment of the produced vector mesons to the production mechanism. The chapter concludes with a discussion of several production mechanisms.

## 2.1 QUARKS AND MESONS

The naïve quark model describes the characteristics of hadrons only by combinations of their constituent quarks.They are characterised by the quantum numbers of the bound system of quarks and antiquarks and the quantum numbers of the constituents. These numbers are conserved in the strong interaction and are discussed for quark-antiquark systems in the following.
The isospin $I$ has already been introduced in the previous chapter. The possible eigenvalues $I_3$ in the projection along the quantisation axis are $+1/2$ for each up/anti-down quark and $-1/2$ for each down/anti-up quark in a meson. The strangeness $\mathcal{S}$ is given as $-1$ for each strange quark and $+1$ for each anti-strange quark in a meson. The total spin of a hadron is composed of the two quark spins of $1/2$ each $\vec{S} = \vec{S}_1 + \vec{S}_2$, thus it is integer. Additionally, angular momentum $L$ between the quarks can be involved, which combines with the individual quark spins to the total meson spin $\vec{J} = \vec{L} + \vec{S}$. Angular momentum leads to mesons with higher spins above $J = 1$. Parity describes the behaviour under a change of sign of all space coordinates $\widehat{P}\,\Psi(\vec{r}) = \Psi(-\vec{r})$. Elementary particles have intrinsic parity which is opposite for quarks and anti-quarks, thus the parity is not only given by the angular momentum and receives an extra sign: $P = (-1)^{L+1}$. The charge conjugation $\widehat{C}$, also known as $C$-parity, describes the behaviour of the transformation of a particle to its anti-particle. The corresponding quantum number for mesons is $C = (-1)^{L+S}$. The charge conjugation is only defined for neutral systems. The strong interaction does not discriminate between charge states, therefore a generalised quantum number was introduced, the $G$-parity. It is a combination of a rotation of the isospin around the second axis and charge conjugation, $\widehat{G} = \widehat{C}\exp(i\pi I_2)$. The possible eigenvalues are $G = (-1)^I C = (-1)^{I+L+S}$.
A meson can be identified uniquely by its quantum numbers $I^G\,J^{PC}$, its mass and the quark content. Mesons can also be classified with the help of the quantum number $n$, which is introduced for radial excitations. The radial number $\nu = n + L - 1$

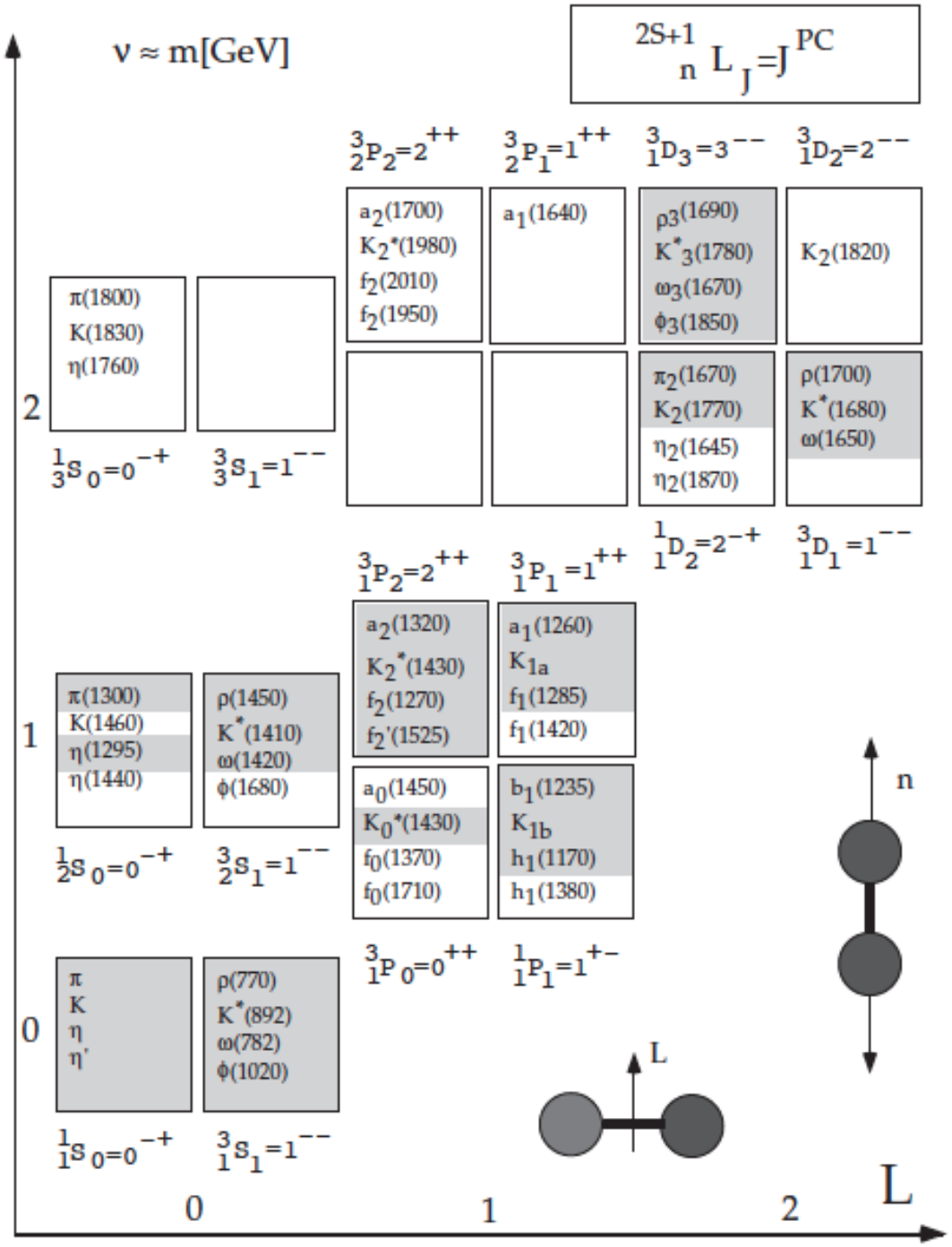


Figure 1: Meson spectrum taken from [17]: The mesons are classified in the standard notation $J^{PC}$ plus radial excitation number n and their mass in case of excitations. The vertical axis shows the radial number $\nu = n + L - 1$ which is correlated to the mass. The spectrum is horizontally ordered by the orbital excitation L.

combines orbital excitation (angular momentum) and radial excitation and is related to the meson mass. Figure 1 shows schematically the mass spectrum with respect to $\nu$ and $L$ for mesons made of the lightest quarks $u$, $d$ and $s$ and the common nomenclature. Larger meson masses are correlated to larger values of $\nu$ and $L$. For the lightest-ground state mesons, the explicit mass assignment is usually dropped. The grey-shaded mesons are firmly established, which means that they were found by experiments and there was agreement on the determined quantum numbers.

In contrast to the combination restrictions of quantum numbers in the naïve quark model, QCD allows for further states. Such states with quantum numbers which cannot be obtained by a combination of a quark and an anti-quark are called exotic mesons. Predictions include exotic mesons with more than two quarks (*tetra-quarks*, *mesonic molecules*) and states which include a gluonic excitation (*hybrids*), see [103] for a review. In addition, states with only bound gluons and no quarks (*glueballs*) are predicted. For a review on the experimental status, see [52]. An overview over theoretical models is given in [102]. The COMPASS collaboration *e.g.* has found evidence for the existence of an exotic meson, the $\pi_1(1600)$ with $J^{PC} = 1^{-+}$[14].

An approach to describe the light meson spectrum within group theory has been found using $\mathrm{SU}(3)_{\mathrm{flavour}}$, in which mesons are regarded as combinations of the flavours $u, d$ and $s$. The quark flavour states are eigenstates of the weak interaction, while the observed mesons with a fixed mass are eigenstates of the strong interaction and are not necessarily equal to the flavour eigenstates but rather a mix. It is found that light mesons with up and down flavours fit $\mathrm{SU}(2)_{\mathrm{flavour}}$ symmetry quite well because of the similar quark masses ($m_u \simeq m_d$). It was tried to include strangeness in the model despite the larger difference of up and down mass to the strange quark mass. In the $\mathrm{SU}(3)_{\mathrm{flavour}}$ model, a light $q\bar{q}$ system can be formed in nine different ways, analogously to $\mathrm{SU}(3)_{\mathrm{c}}$ as explained in Chapter 1, but now with flavours instead of colours. Figure 2 shows the meson nonets for spin 0 (*pseudoscalar*) and spin 1 (*vector*) mesons, ordered by charge and strangeness. As expected, $\mathrm{SU}(3)_{\mathrm{flavour}}$ symmetry is broken, which is seen by comparing the masses listed in Table 2. If $\mathrm{SU}(3)_{\mathrm{flavour}}$ symmetry was not broken, all masses would be expected to be the same. The $\phi$ meson has a mass which is about $240\,\mathrm{MeV}/c^2$ higher than the $\omega$ mass, mostly due to the different masses of strange and up-/down quarks. The $\rho$ and $\omega$ masses differ by about $7\,\mathrm{MeV}/c^2$, which means that already $\mathrm{SU}(2)_{\mathrm{flavour}}$ is broken. Gell-Mann interpreted [70] the small deviations from the expected average mass as mass splittings. He divided the strong interaction in a strong part with unbroken $\mathrm{SU}(3)_{\mathrm{flavour}}$ symmetry and a weaker part with broken symmetry, which is responsible for the small mass splittings. Note that the quark content of $\eta/\eta'$ and $\omega/\phi$ differs, which is explained within the next section.

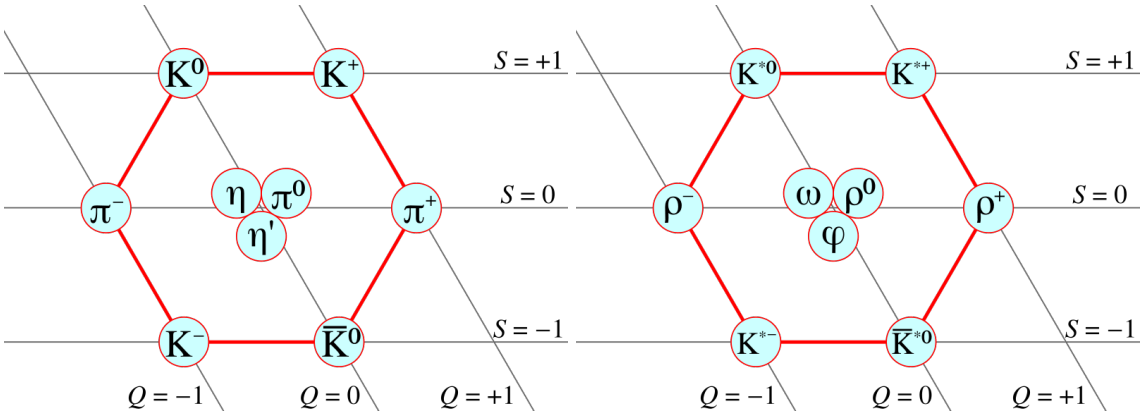


Figure 2: Meson nonets for spin 0 (left panel) and spin 1 (right panel) particles, taken from [59].

### 2.1.1 *Vector mesons*

The production mechanism is investigated with the help of the vector mesons $\omega$ and $\phi$. Their quark content is understood within $SU(3)_{\text{flavour}}$, where a possible combination of quarks for the non-strange, neutral vector mesons yields

$$\omega_1 = \frac{1}{\sqrt{3}}(u\bar{u} + d\bar{d} + s\bar{s}) \qquad \omega_8 = \frac{1}{\sqrt{6}}(u\bar{u} + d\bar{d} - 2s\bar{s}) \tag{1}$$

for the singlet and octet states, respectively. As already mentioned in the last section, the $\omega_1$ and $\omega_8$ states are flavour eigenstates while the strong eigenstates in general are a mixture, which can be parameterised as

$$\begin{pmatrix} \phi \\ \omega \end{pmatrix} = \begin{pmatrix} \cos(\vartheta) & -\sin(\vartheta) \\ \sin(\vartheta) & \cos(\vartheta) \end{pmatrix} \begin{pmatrix} \omega_1 \\ \omega_8 \end{pmatrix} \tag{2}$$

As an example, the $\phi$ meson is described as

$$\phi = \left(\frac{1}{\sqrt{6}}\cos(\vartheta) - \frac{1}{\sqrt{3}}\sin(\vartheta)\right)(u\bar{u} + d\bar{d}) + \left(-\frac{1}{\sqrt{3}}\sin(\vartheta) - \frac{2}{\sqrt{6}}\cos(\vartheta)\right)(s\bar{s}) \tag{3}$$

It is found on the one hand that the $\phi$ meson predominantly decays into kaons, which are particles containing strangeness ($\phi \to KK$). Table 3 shows that the observed branching to $KK$ is about five times higher than that of mesons with $u$ and $d$ quarks, such as $\pi^+$, $\pi^-$ or $\pi^0$. Hence, the $\phi$ meson seems to contain mostly strange quarks. On the other hand, the $\omega$ meson decays mostly into $\pi^+\pi^-\pi^0$, and thus seems to contain mostly up and down quarks.
If the $\phi$ is purely strange (*ideal mixing*), this requires $\cos(\vartheta_{id}) = \sqrt{2/3}$, *i.e.* $\vartheta_{id} = 35.3°$. Consequently, the quark content of the ideal $\omega$ is $\frac{1}{\sqrt{2}}(u\bar{u} + d\bar{d})$.
Equation 3 can be rewritten using $\cos(\vartheta_{id})$ and takes the simpler form

$$\phi = -\sin(\vartheta - \vartheta_{id})(u\bar{u} + d\bar{d}) - \cos(\vartheta - \vartheta_{id})(s\bar{s}) \tag{4}$$

The corresponding description for $\omega$ reads

$$\omega = \cos(\vartheta - \vartheta_{id})(u\bar{u} + d\bar{d}) - \sin(\vartheta - \vartheta_{id})(s\bar{s}) \tag{5}$$

| Meson | $I^G$ | Mass [MeV/$c^2$] | Quark content |
|---|---|---|---|
| *pseudoscalars* | | | |
| $\pi^0$ | $1^-$ | 134.98 | $1/\sqrt{2}(u\bar{u} - d\bar{d})$ |
| $\pi^\pm$ | $1^-$ | 139.57 | $u\bar{d}/\bar{u}d$ |
| $K^0$ | $1/2$ | 497.61 | $d\bar{s}$ |
| $K^\pm$ | $1/2$ | 493.68 | $u\bar{s}/\bar{u}s$ |
| $\eta$ | $0^+$ | 547.85 | $1/\sqrt{6}(u\bar{u} + d\bar{d} - 2s\bar{s})$ |
| $\eta'$ | $0^+$ | 957.78 | $1/\sqrt{3}(u\bar{u} + d\bar{d} + s\bar{s})$ |
| *vectors* | | | |
| $\rho^0$ | $1^+$ | 775.49 | $1/\sqrt{2}(u\bar{u} - d\bar{d})$ |
| $\rho^\pm$ | $1^+$ | 775.11 | $u\bar{d}/\bar{u}d$ |
| $K^{*0}$ | $1/2$ | 895.94 | $d\bar{s}$ |
| $K^{*\pm}$ | $1/2$ | 891.66 | $u\bar{s}/\bar{u}s$ |
| $\omega$ | $0^-$ | 782.65 | $1/\sqrt{2}(u\bar{u} + d\bar{d})$ |
| $\phi$ | $0^-$ | 1019.45 | $s\bar{s}$ |

Table 2: Properties of the strong eigenstates of pseudoscalar ($J^{PC} = 0^{-+}$) and vector mesons ($J^{PC} = 1^{--}$) [29]. The index $\pm$ at the meson name indicates charged mesons while 0 or no index indicate neutral mesons. Note, that the $G$-parity is not well-defined for mesons with strangeness and hence not listed for these mesons in the table. The quark content for charged particles is first listed for the positive meson, then for the negative meson in the form $+/-$.

The real, physical mixing angle can be determined by eliminating $\omega_1$ in Equation 2, leaving

$$\tan^2(\vartheta) = (m_\phi - m_{\omega 8})/(m_{\omega 8} - m_\omega). \tag{6}$$

However, $\omega_8$ is not a physical state and only represents the universal mass of the multiplet in case of exact $\mathrm{SU}(3)_{\mathrm{flavour}}$ symmetry. The $\omega_8$ mass can be determined as shown by Okubo and Gell-Mann by mass differences of other known mesons [70, 107, 108]. With the help of the afore-mentioned ansatz by Gell-Mann, a phenomenological parameterisation for the meson masses is found with the form

$$M = m_0 + m_1 S + m_2 \left( I\,(I+1) - \frac{1}{4} S^2 \right) \tag{7}$$

where $m_0$ is the mass due to the strong part of the interaction, and $m_1$, and $m_2$ are the masses due to the weak part. With this ansatz one finds $M_\rho = m_0 + 2\,m_2$, $M_{K*0} = m_0 + m_1 + 1/2\,m_2$, $M_{\overline{K*0}} = m_0 - m_1 + 1/2\,m_2$ and $M_{\omega 8} = m_0$. Eliminating $m_1$ and $m_2$ leads to the relation $1/2\,M_{K*0} + 1/2\,M_{\overline{K*0}} = 1/4\,M_\rho + 3/4\,M_{\omega 8}$. The

masses of $K^{*0}$ and $\overline{K^{*0}}$ are the same, hence the Okubo–Gell-Mann mass formula[1] follows as

$$M_{\omega 8} = \frac{4M_{K*0} - M_\rho}{3} = 0.936\,\mathrm{GeV}/c^2 \tag{8}$$

Applications of such mass predictions turn out to be precise at the percent level in the baryon sector, where $\mathrm{SU}(3)_{\mathrm{flavour}}$ applies in the same way and the same mass relations can be found. However, comparing the physical masses of different mesons, a better mass relation can be found when the squares of masses are used. This method results in $M_{\omega 8} = 0.929\,\mathrm{GeV}/c^2$.
Inserting $M_{\omega 8}$ and the meson masses from Table 2 in Equation 6, the physical mixing angle is determined to be $\vartheta = 39^\circ$ with a difference to ideal mixing of $\delta\vartheta = \vartheta - \vartheta_{id} = 3.7^\circ$. This means that $\omega$ and $\phi$ are close to pure states, but not entirely, and decays into mesons containing other than the dominant flavours of the vector meson are allowed and observed, *e.g.* $\phi \to \pi^+\pi^-\pi^0$ in 15.3% of all decays.

| Meson | Mass [MeV/$c^2$] | Width [MeV/$c^2$] | Branching |
|---|---|---|---|
| $\omega$ | $782.65 \pm 0.12$ | $8.49 \pm 0.08$ | $\omega \to \pi^+\pi^-\pi^0$ : 89.9% |
| | | | $\omega \to \gamma\pi^0$ : 8.3% |
| $\phi$ | $1019.45 \pm 0.02$ | $4.26 \pm 0.04$ | $\phi \to K^+K^-$ : 49.9% |
| | | | $\phi \to K^0_S K^0_L$ : 34.2% |
| | | | $\phi \to \pi^+\pi^-\pi^0/\rho\pi$ : 15.3% |

Table 3: Properties of the vector mesons $\omega$ and $\phi$ [29] including branchings to the most relevant channels. The short and long living $K^0$ eigenstates of the weak interaction are denoted $K^0_S$ and $K^0_L$.

### 2.1.2 *The Okubo-Zweig-IIzuka rule*

The successful description of the observed mesons by $\mathrm{SU}(3)_{\mathrm{flavour}}$ and the observation that meson decays conserve the original flavours of the constituents lead to the conclusion, that the initial flavour is transferred to the final state in a decay. This flavour flow can be imagined as quark lines from the vector meson to its decay products. Okubo [109], Zweig [134, 135] and Iizuka [86] formulated independently the phenomenological rule that all processes with disconnected quark lines are forbidden, which is today known as the OZI rule. This rule does not only hold for decay processes, but also for production mechanisms. Formulated in terms of production, there is no probability to produce strangeness from non-strange initial states. Iizuka wrote this condition as the ratio of production amplitudes

$$Z = \frac{\sqrt{2}\,\mathcal{A}(AB \to C + s\bar{s})}{\mathcal{A}(AB \to C + u\bar{u}) + \mathcal{A}(AB \to C + d\bar{d})} \stackrel{!}{=} 0 \tag{9}$$

1 It was later shown that no explicit parameterisation is necessary to derive the mass relation. For the derivation with symmetric constraints, see [71].

with $A$ and $B$ the initial, non strange particles and $C$ and $D$ the reaction products. The production amplitudes $\mathcal{A}$ [99] of the physical $\phi$ and $\omega$ mesons are compared in the next step. For this, Equations 4 and 5 are rewritten as a matrix equation:

$$\begin{pmatrix} \phi \\ \omega \end{pmatrix} = \begin{pmatrix} -\sin(\Delta\vartheta) & -\cos(\Delta\vartheta) \\ \cos(\Delta\vartheta) & -\sin(\Delta\vartheta) \end{pmatrix} \begin{pmatrix} u\bar{u} + d\bar{d} \\ s\bar{s} \end{pmatrix} \tag{10}$$

and inverted

$$\begin{pmatrix} u\bar{u} + d\bar{d} \\ s\bar{s} \end{pmatrix} = \begin{pmatrix} -\sin(\Delta\vartheta) & \cos(\Delta\vartheta) \\ -\cos(\Delta\vartheta) & -\sin(\Delta\vartheta) \end{pmatrix} \begin{pmatrix} \phi \\ \omega \end{pmatrix}. \tag{11}$$

With this and the notation $\mathcal{A}(AB \to C + (u\bar{u} + d\bar{d})) = 1/\sqrt{2}(\mathcal{A}(AB \to C + u\bar{u}) + \mathcal{A}(AB \to C + d\bar{d}))$, Equation 9 can be written as a ratio of $\phi$ and $\omega$ production amplitudes

$$\begin{aligned} Z &= \frac{\mathcal{A}(AB \to C + s\bar{s})}{\mathcal{A}\left(AB \to C + (u\bar{u} + d\bar{d})\right)} \\ &= \frac{-\cos(\vartheta - \vartheta_{id})\mathcal{A}(AB \to C + \phi) - \sin(\vartheta - \vartheta_{id})\mathcal{A}(AB \to C + \omega)}{-\sin(\vartheta - \vartheta_{id})\mathcal{A}(AB \to C + \phi) + \cos(\vartheta - \vartheta_{id})\mathcal{A}(AB \to C + \omega)} \\ &= \frac{-\mathcal{A}(AB \to C + \phi) - \tan(\vartheta - \vartheta_{id})\mathcal{A}(AB \to C + \omega)}{-\tan(\vartheta - \vartheta_{id})\mathcal{A}(AB \to C + \phi) + \mathcal{A}(AB \to C + \omega)} \end{aligned} \tag{12}$$

which is solved for the ratio of $\phi$ to $\omega$ production

$$\frac{\mathcal{A}(AB \to C + \phi)}{\mathcal{A}(AB \to C + \omega)} = -\frac{Z + \tan(\vartheta - \vartheta_{id})}{1 - Z\ \tan(\vartheta - \vartheta_{id})}. \tag{13}$$

The OZI rule states that $Z \stackrel{!}{=} 0$. Thus, Equation 13 simplifies to

$$\frac{\mathcal{A}(AB \to C + \phi)}{\mathcal{A}(AB \to C + \omega)} = -\tan(\vartheta - \vartheta_{id}). \tag{14}$$

The production cross section $\sigma$ is given [66] by the square of the absolute value of the production amplitude $\mathcal{A}$ and a phase space factor $f = \tau_{C\phi}/\tau_{C\omega}$

$$\sigma = \frac{4\pi}{\hbar} f |\mathcal{A}|^2. \tag{15}$$

The term $\tau_{CX}$ represents the phase space density of the final state $CX$. Inserting the deviation from ideal mixing $\vartheta - \vartheta_{id} = 3.7^\circ$ which was derived in the last section, the production cross section ratio $R$ of $\phi$ to $\omega$ mesons is predicted:

$$R = \sigma(AB \to C + \phi)/\sigma(AB \to C + \omega) = f\ \tan^2(\vartheta - \vartheta_{id}) = 4.2 \cdot 10^{-3}\ f. \tag{16}$$

The OZI rule is found to be well fulfilled in many experiments at different energies. An overview of measurements and implications of a possible violation will be discussed in Chapter 7.

## 2.2 SCATTERING PROCESSES

The vector mesons analysed in this thesis are produced in a scattering process, where a beam proton collides with a target proton. In this section, first general kinematic aspects for exclusive measurements are discussed, followed by the parameterisation of cross sections with the *S*-Matrix approach. In the next step, the spin of the involved particles is included in the approach, which leads to the spin-density matrix formalism. The spin-density matrix relates the spin alignment to the production process.

### 2.2.1 *Kinematics and cross section*

The total cross section $\sigma_{\text{tot}}$ includes elastic scattering and production of particles by inelastic scattering, $\sigma_{\text{tot}} = \sigma_{\text{el}} + \sigma_{\text{inel}}$. Absorption effects are not considered. The cross section of a given process is connected to the square of the scattering amplitude *via* Equation 15. The optical theorem relates the forward amplitude $f(0)$ for elastic scattering, *i.e.* the amplitude for scattering at zero degrees, to the total cross section [111]:

$$\sigma_{\text{tot}} = \frac{4\pi}{p} \text{Im}\, f(0) \tag{17}$$

where $p$ is the momentum of the scattered particle in the overall centre-of-mass frame. This means that the resulting cross section for elastic scattering can be connected to the cross section for the production of particles. Two particles scatter from initial states $|1\rangle$ and $|2\rangle$ to final states $\langle 3|$ and $\langle 4|$ with corresponding four-momenta $p_1, p_2, p_3, p_4$. A set of Lorentz-invariant variables is chosen to describe the kinematics of the process:

$$s = (p_1 + p_2)^2 = (p_3 + p_4)^2 \tag{18}$$
$$t = (p_1 - p_3)^2 = (p_2 - p_4)^2 \tag{19}$$
$$u = (p_1 - p_4)^2 = (p_2 - p_3)^2 \tag{20}$$

with $s + t + u = \sum_i m_i^2$ and the invariant masses $m_i^2 = p_i^2$. The variables $s, t$, and $u$ are called *Mandelstam* variables. The centre-of-mass energy of the system is given by $\sqrt{s}$, which is in the case of a fixed target experiment

$$\sqrt{s} = \sqrt{2E_1 m_2 + m_1^2 + m_2^2} \tag{21}$$

with beam particle $|1\rangle$ and target particle $|2\rangle$.
The scattering of particles involves the transfer of an intermediate exchange particle. With the help of the Mandelstam variables, three cases of the intermediate particle exchange are distinguished, depicted in Figure 3, where the horizontal direction represents the time while the vertical direction represents the momentum coordinate. The squared four-momentum of the exchange particle then equals either $s, t$, or $u$ and denotes the name of the process, as *e.g.* the $s$-channel process shown in the left panel. The physical region of a process is given by the available phase space

for the reaction. For instance in the $s$-channel, the relation $s \geq (m_1 + m_2)^2$ must be fulfilled.
In our case, the $t$ channel process is the most important. Mathematically, it is convenient to calculate the parameters first in $s$-channel processes and afterwards transcribe the results to the $t$-channel with a crossing relation as will be explained later on.

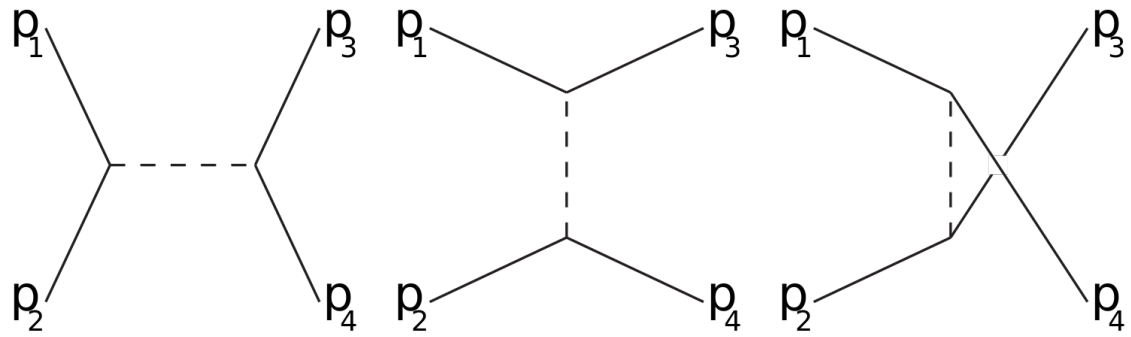


Figure 3: Fundamental two particle scattering processes. Left panel: s-channel, middle panel: t-channel, right: u-channel. The horizontal direction represents the time while the vertical direction represents the momentum coordinate.

The scattering matrix (*S-Matrix*) relates the initial state and the final state in a scattering process [57, 61]. The probability of the scattering to happen is given by the square of S-Matrix element $\langle 34|S|12\rangle$:

$$P_{12\to 34} = |\langle 34|S|12\rangle|^2 = \langle 12|S^\dagger|34\rangle\langle 34|S|12\rangle \tag{22}$$

The S-matrix has to respect unitarity for a interpretation as a probability for the process: $SS^\dagger = 1$. Processes with the same initial and final state are usually separated from the S-matrix, leaving the *T-matrix* that is governing transitions $i \to f$ for $i \neq f$:

$$\langle f|S|i\rangle = \delta_{fi} + i(2\pi)^4\delta^4\left(P_f - P_i\right)\langle f|T|i\rangle \tag{23}$$

with $P_i$ being the sum of all initial state momenta and $P_f$ the sum of all final state momenta. The probability is connected with the scattering cross section *via* Equation 15 and yields

$$\sigma_{12\to 34} = (2\pi)^4\delta^4\left(P_{34} - P_{12}\right)|\langle 34|T|12\rangle|^2 f \tag{24}$$

with $f = 1/(4|p_1|\sqrt{s})$ being the available phase space [111]. The crossing relation [124] states that the amplitude for the $s$-channel process $12 \to 34$ can be analytically continued to the amplitude for the $t$-channel[2] process $1\bar{3} \to \bar{2}4$

$$\mathcal{A}_{12\to 34}(s,t) = \mathcal{A}_{1\bar{3}\to\bar{2}4}(t,s) \tag{25}$$

which is done simply by replacing one incoming particle with an outgoing antiparticle with opposite momentum and *vice versa*. Thus, the relations obtained above for the $s$-channel case hold for the $t$-channel, as well. The cross section has a de-

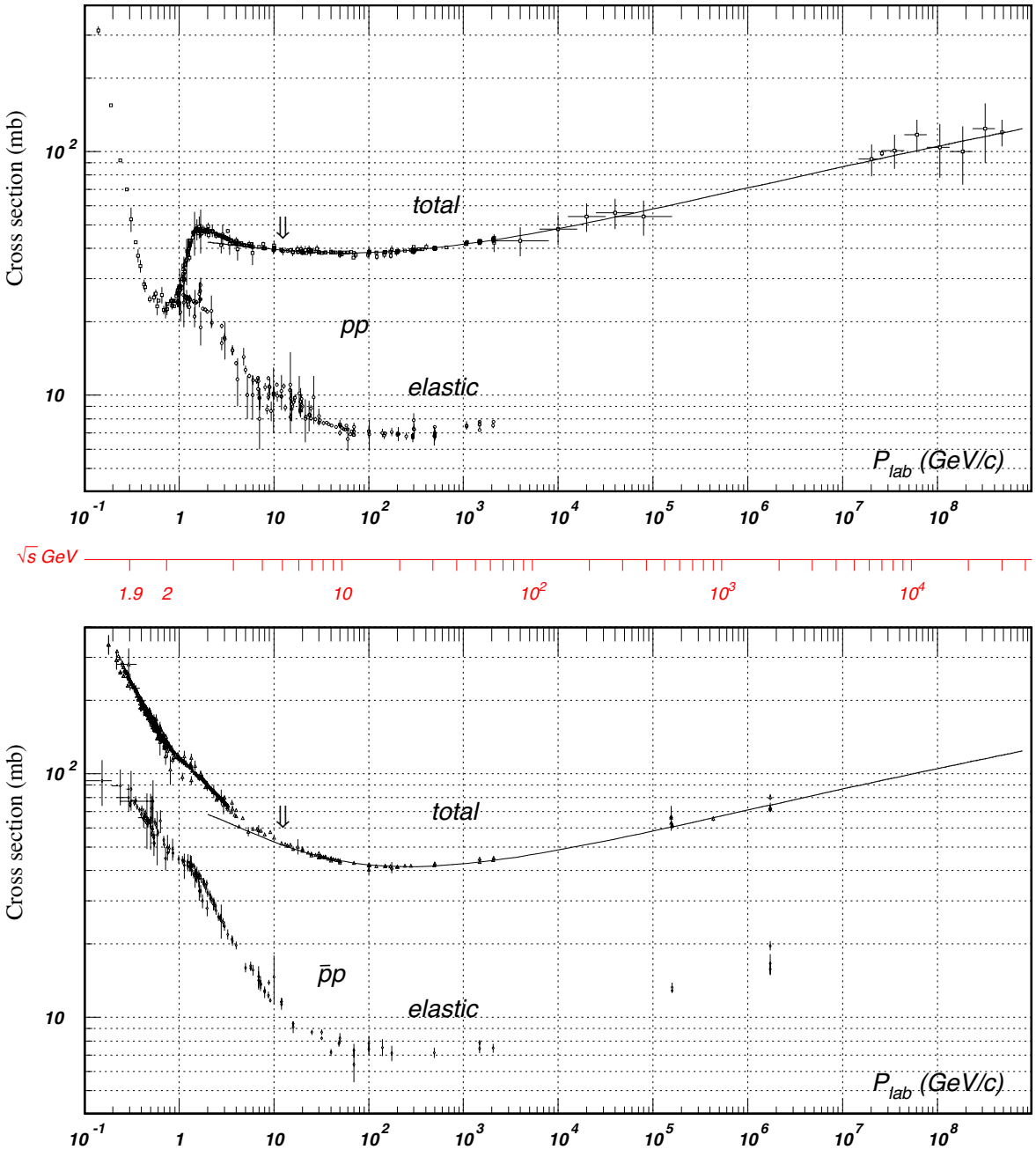


Figure 4: Total and elastic cross sections as a function of $\sqrt{s}$ and $p_{\text{lab}}$ for $pp$ collisions (upper panel) and $p\overline{p}$ scattering (lower panel). Taken from [29], for reference to the data origin see *ibid*.

pendence on the energy $\sqrt{s}$ and the momentum transfer $t$. The energy dependence has been measured over a wide range. In Figure 4 taken from [29], the total and elastic cross section for $pp$ scattering and $p\overline{p}$ scattering are plotted as a function of $\sqrt{s}$ and $p_{\text{lab}}$ for $pp$ collisions (upper panel) and $p\overline{p}$ scattering (lower panel). Three general observations can be made, starting first with the total cross section being either constant or changing very slowly as the energy increases. Second, the cross section of $p\overline{p}$ and $pp$ collisions show the same behaviour at higher energies and

2 This can be also done for the transition amplitude of the $u$-channel.

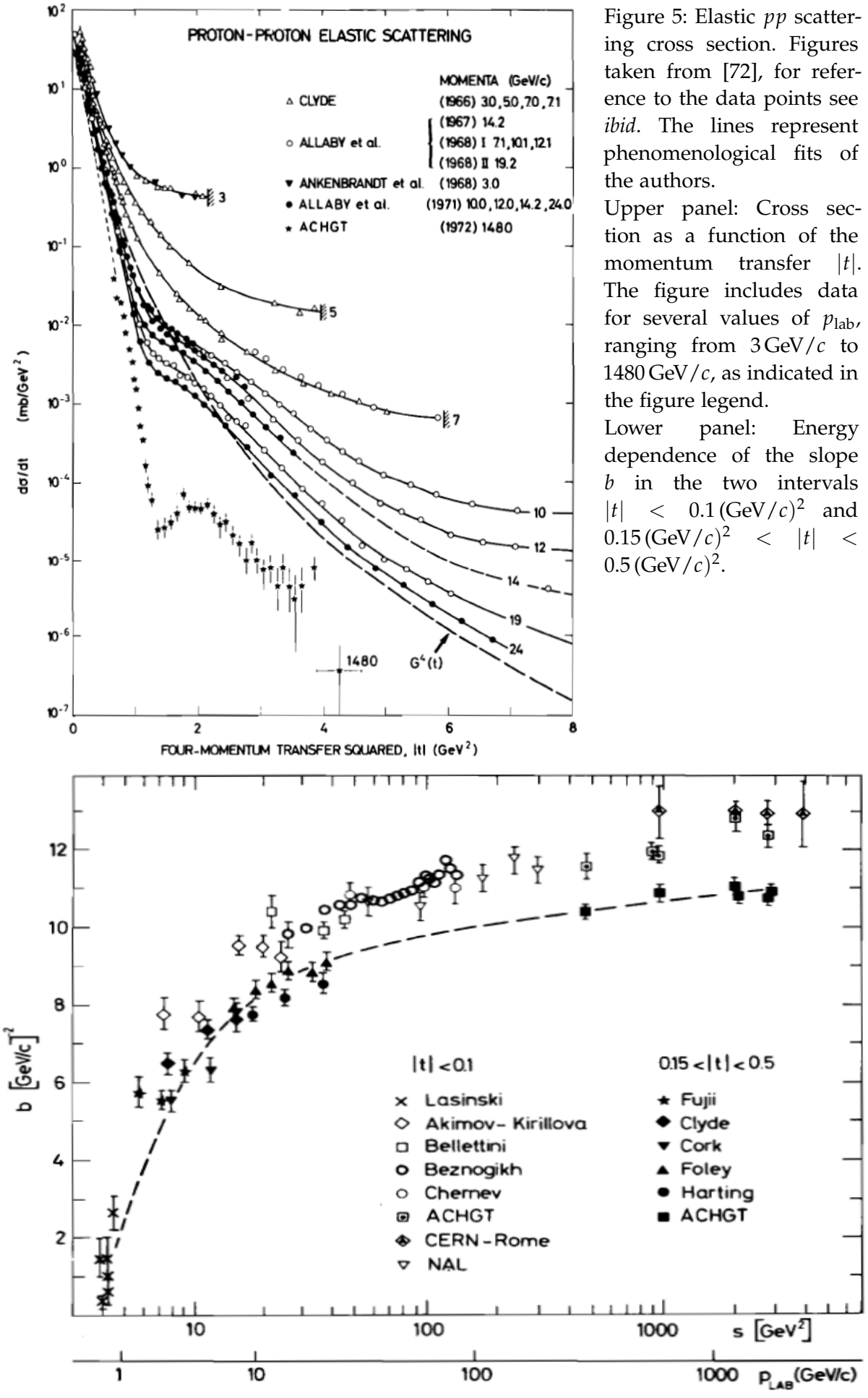


Figure 5: Elastic $pp$ scattering cross section. Figures taken from [72], for reference to the data points see *ibid*. The lines represent phenomenological fits of the authors.
Upper panel: Cross section as a function of the momentum transfer $|t|$. The figure includes data for several values of $p_{\text{lab}}$, ranging from $3\,\text{GeV}/c$ to $1480\,\text{GeV}/c$, as indicated in the figure legend.
Lower panel: Energy dependence of the slope $b$ in the two intervals $|t| < 0.1\,(\text{GeV}/c)^2$ and $0.15\,(\text{GeV}/c)^2 < |t| < 0.5\,(\text{GeV}/c)^2$.

converge at the same values. Third, the cross section varies smoothly with increasing energy and shows no structures. The dependence on the momentum transfer is related to the spatial structure of the scattered particles. The cross section as a function of the momentum transfer $|t|$ exhibits different structures as can be seen in the upper panel of Figure 5, taken from [72]. The data is shown for several values of $p_{\text{lab}}$, ranging from 3 GeV/$c$ to 1480 GeV/$c$, as indicated in the figure legend. At low $t < 0.5\,(\text{GeV}/c)^2$, the cross section exhibits a steep slope which is then followed by a diffractive pattern. This observation reminds of the diffraction phenomenon of light scattering off a black disc. In analogy to this, in the *diffractive model* or *optical model* the slope of the $t$-dependence is interpreted as the spatial dimension of the resolved structure when the elastic cross section is parameterised as $\mathrm{d}\sigma/\mathrm{d}t = A\,\exp(-b|t|)$. With this parameterisation, the radius of the resolved object is approximated by $R = 0.3\sqrt{b}\,\text{fm}$ when inserting the slope $b$ in units of $(\text{GeV}/c)^{-2}$ [111]. The lower panel of Figure 5 shows the slope $b$ as a function of $p_{\text{lab}}$. Typical values are found to be between 5 and 13 $(\text{GeV}/c)^{-2}$. This exponential parameterisation results also in a more simplified parameterisation of the total cross section. The relation $\mathrm{d}\sigma_{\text{el}}/\mathrm{d}t = (\pi/p^2)\,(\mathrm{d}\sigma_{\text{el}}/\mathrm{d}\Omega)$, where $\mathrm{d}\Omega$ denotes the solid angle in the centre-of-mass frame, and the insertion of the squared forward amplitude $|f(0)|^2 = (\mathrm{d}\sigma_{\text{el}}/\mathrm{d}\Omega)_{\theta=0}$ in Equation 17 lead to

$$\left(\frac{\mathrm{d}\sigma_{\text{el}}}{\mathrm{d}t}\right)_{\text{t=0}} = \frac{\sigma_{\text{tot}}^2}{16\pi}. \tag{26}$$

Comparison of the coefficients in Equation 26 and the exponential parameterisation leads to the elastic cross section

$$\frac{\mathrm{d}\sigma_{\text{el}}}{\mathrm{d}t}(s,t) = \frac{\sigma_{\text{tot}}^2}{16\pi}\,\exp(-b(s)|t|). \tag{27}$$

The integration of this formula over $t$ yields then the relation

$$\sigma_{\text{el}}(s) = \frac{\sigma_{\text{tot}}^2}{16\pi b(s)}. \tag{28}$$

It should be noted that deviations of this behaviour are usually treated with a different ansatz. The exponential parameterisation is usually generalised to the form $\mathrm{d}\sigma_{\text{el}}/\mathrm{d}t = A\,\exp\left(-\sum_{n=1}^{N} b_n|t|^n\right)$ for the determination of the slope by a fit to the cross section, see *e.g.* [40, 111].

### 2.2.2 *Spin Alignment and Spin-Density Matrix*

Gottfried and Jackson argued [79] that the spin alignment of a particle is linked to its production. In the case of a resonance decaying into two or more particles, the spin of the resonance is reflected in the angular distribution of the decay products. In the case of particle production by the exchange of an intermediate particle, the angular distributions of the products reflect the spin of the intermediate particle. The distributions are obtained from the angle between a spin analyser, which is sensitive to the spin of the particle, and the quantisation axis of the chosen reference

frame. The choice of a well-suited analyser and reference frame will be discussed later. If boosted to the rest frame of the studied particle, the angular distributions reveal the magnetic substate $m$. In the case of vector mesons, Gottfried and Jackson find that a substate $m = \pm 1$ exhibits a $\sin^2$ dependence, whereas a substate $m = 0$ exhibits a $\cos^2$ dependence. In the following, Gottfried's and Jackson's derivations are briefly revisited, concluding in the introduction of the spin density matrix.
In the last section, only spin-averaged processes have been considered, where an implicit sum over all spin states occurred. Writing the sums explicitly, one obtains

$$\frac{d\sigma}{d\Omega} = \frac{1}{(2s_1+1)(2s_1+1)} \frac{p_2}{s p_1} \sum_{\lambda} \left| \left\langle \lambda_4 \lambda_{\bar{2}} | \widetilde{T}(t,s) | \lambda_{\bar{3}} \lambda_1 \right\rangle \right|^2 \tag{29}$$

with $s_1, s_2$ being the spins of particles 1 and 2. The symbol $\lambda_i$ denotes the different spin projections on the momenta of the particles, which are known as *helicities*: $\lambda_i = (\vec{s}_i \cdot \vec{p}_i)/|\vec{s}_i \cdot \vec{p}_i|$. The transition matrix element $\widetilde{T}(t,s)$ is now spin-dependent which is denoted by the tilde.
As already mentioned before, a boost to the rest frame of particle 4 has to be performed. The direction of momentum transfer $\Delta P = \vec{p}_1 - \vec{p}_3$ is a natural choice for the quantisation axis. In this system, the helicity of particle 4 is the same as its magnetic substate $m$. Note, that the direction of $\Delta P$ in the new reference system corresponds to the negative of the direction of particle 2. The boost from any reference system to the new reference system can be expressed by a rotation by the three Euler angles $\alpha, \beta, \gamma$. This rotation is performed using the Wigner D-matrices and results in

$$\left\langle m; \lambda_{\bar{3}} | \widetilde{T}(t,s) | \lambda_2 \lambda_1 \right\rangle = \sum_{\lambda_{\bar{2}} \lambda_{\bar{3}} \lambda_1} \left\langle m \lambda_{\bar{2}} | T(t,s) | \lambda_{\bar{3}} \lambda_1 \right\rangle \cdot D^j_{\lambda_{\bar{3}} m}(\alpha, \beta, \gamma). \tag{30}$$

In the next step, the transition matrix $\rho_{mm'}$ from helicity $m$ to helicity $m'$ is introduced, which is commonly known as the *spin-density matrix*:

$$\left\langle m | \rho | m' \right\rangle = N \sum_{\lambda_{\bar{2}} \lambda_{\bar{3}} \lambda_1} \left\langle m \lambda_{\bar{2}} | \widetilde{T}(t,s) | \lambda_{\bar{3}} \lambda_1 \right\rangle \left\langle m' \lambda_{\bar{2}} | \widetilde{T}(t,s) | \lambda_{\bar{c}} \lambda_a \right\rangle^* \tag{31}$$

with N as the normalisation. The spin density matrix is hermetian ($\rho^\dagger \rho = \mathbb{1}$), symmetric ($\rho_{ij} = \rho_{ji}$), and positive semi-definite. The trace of the matrix corresponds to the total transition probability for all helicities, $\mathrm{Tr}\{\rho\} = 1$, while the trace of the squared matrix defines the grade of mixture of different helicities, $0 < \mathrm{Tr}\{\rho^2\} \leq 1$. A trace $\mathrm{Tr}\{\rho^2\} = 1$ corresponds to a pure state with only one helicity. The dimension of the spin-density matrix is given by $\dim(\rho) = 2J + 1$, thus resulting in a three by three matrix for the case of vector mesons.
The angular dependent part of the cross section now reads

$$W(\varphi, \cos\theta) \;=\; |A_0|^2 \sum_{mm'} D^1_{m',\lambda_1} \, \rho_{mm'} \, D^1_{m,\lambda_2} \tag{32}$$

with a normalisation factor $|A_0|^2$. The D-functions in the case of vector mesons simplify the last equation to

$$\begin{aligned} W(\varphi, \cos\theta) = |A_0|^2 \, (\rho_{11} \; \sin^2(\theta) + \rho_{00} \; \cos(\theta) - \sqrt{2}\rho_{10} \; \cos(\varphi) \; \sin(2\theta) \\ -\rho_{-11} \; \cos(2\varphi) \; \sin^2(\theta)) \end{aligned} \tag{33}$$

For the case of unpolarised initial state particles, one can integrate over $\varphi$. The normalised cross section then simplifies to

$$W(\cos\theta) = \frac{3}{4}(1 - \rho_{00} + (3\rho_{00} - 1)\cos^2\theta). \tag{34}$$

There is only one element of the spin-density matrix left which describes the full angular dependence of the cross section. This element corresponds to the spin alignment of a vector meson. For $\rho_{00} = 1/3$, angular distributions are isotropic. As already mentioned, there is a pure $\sin^2\theta$ dependence for $\rho_{00} = 0$ and the vector mesons are in the magnetic sub-state $m = \pm 1$ with respect to the quantisation axis. Finding $\rho_{00} = 1$ gives a pure $\cos^2\theta$ dependence and corresponds to $m = 0$.

## 2.3 PARTICLE PRODUCTION

In this section, more complex processes for particle production than shown in Figure 3 are included in the discussion (see Figure 7).

### 2.3.1 *Kinematics*

Up to now, mainly the final state was discussed without intermediate steps such as resonance production with a subsequent decay. In such more complex cases, the description of particle production requires the introduction of additional kinematical variables. If the process involves the excitation of an initial particle, a minimum momentum transfer $t_{\min}$ is necessary for the excitation. The reduced momentum transfer $t'$ for an excitation of particle 1 to the final state resonance 3 as shown in the left panel of Figure 7 is given as

$$|t'| = |t| - |t|_{\min} \tag{35}$$

with

$$\begin{aligned} |t| &= m_1^2 + m_3^2 - 2E_1E_3 + 2|p_1||p_3|\cos\theta_{13} \\ |t|_{\min} &= m_1^2 + m_3^2 - 2E_1E_3 + 2|p_1||p_3| \\ &\simeq \frac{(m_3^2 - m_1^2)^2}{4E_1^2} \end{aligned} \tag{36}$$

This approximation holds for the case of large values of $\sqrt{s} \gg |t|$. Furthermore, there is more than one momentum transfer in the case of processes with more than one exchange. For example in the central process depicted in the middle panel of Figure 7, there are momentum transfers between target and recoil proton ($t_1$) as well as between beam and scattered proton ($t_2$) with possibly different magnitudes. Feynman [67] introduced the variable $x_F$ to describe the longitudinal momentum sharing between the final state particles:

$$x_F = \frac{2p_l}{\sqrt{s}} \simeq \frac{p_l}{(p_l)_{\max}} \tag{37}$$

where $p_l$ is the longitudinal momentum in the centre-of-mass frame and $(p_l)_{max}$ its maximum value. The excess energy $\varepsilon$ for a reaction $AB \longrightarrow CD$ is given as $\varepsilon = \sqrt{s} - m_C - m_D$ where $m_C$ and $m_D$ are the masses of the particles $C$ and $D$, respectively.

### 2.3.2 *Exchange models*

Several models have been developed to explain the observed cross section behaviour. The one pion exchange model (*e.g.* [121]) is already able to describe low-energy cross sections well up to energies of 10 GeV. In this model, a single pion exchange graph is assumed for which the necessary parameters are taken from $\pi N$ scattering data. Several meson exchange models have been discussed [89], however they have never been able to describe the full shape of the cross section especially at higher energies.
After a partial wave expansion of the cross section in terms of Legendre polynomials, a very successful generalisation is found within Regge theory [114]. Several ideas for a categorisation of the known mesons (and baryons) were inspired by the observed increase of mass with higher orbital angular momentum. In particular, the squared mass shows a linear dependence on the angular momentum which suggests [48] the parameterisation $\ell = \alpha(m^2)$. Figure 6 (taken from [60]) shows the squared mass versus the quantum numbers $J^{PC}$ of mesons in the quark model for the so-called $\omega$ family (left panel, $I = 0$, $q\bar{q}$ states) and the $\phi$ family (right panel, $I = 0$, $s\bar{s}$ states). The calculated masses in the quark model (depicted by diamonds) fit well to the experimentally confirmed mesons (depicted by dots). The straight lines correspond to a $\chi^2$ fit to the calculated mass values and are called Regge trajectories. In the Regge model, the exchange process is extended to include the

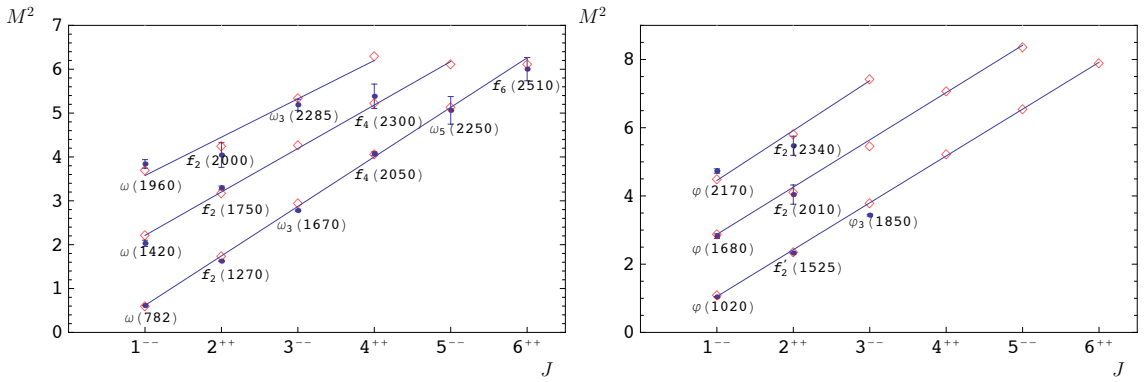


Figure 6: Regge trajectories for the $\omega$ (left) and $\phi$ family (right) taken from [60]. The calculated squared masses of the author's model are depicted by diamonds. The experimental data from [29] are given by dots with error bars and corresponding meson names. The straight lines correspond to a $\chi^2$ fit to the calculated mass values. The ordinate $M^2$ is given in units of $(\mathrm{GeV}/c^2)^2$.

exchange of more than one specific meson. The exchange is parameterised by a Regge trajectory and thus includes the possibility to exchange different quantum numbers at different mass/energy scales. The orbital angular momentum is no

longer considered as a discrete value, but can take arbitrary complex values. The cross section parameterisation follows [57, 111] as

$$\frac{\mathrm{d}\sigma}{\mathrm{d}t} = \frac{s_0^2}{16\pi}|h(t)|^2 \left(\frac{s}{s_0}\right)^{2\alpha(t)-2} \tag{38}$$

where $h$ is the amplitude for a specific production mechanism. The exponent is parameterised as $\alpha(t) = \alpha_0 + \alpha_1 t$ with an intercept $\alpha_0$ in the order of 0.5 for most of the parent (*i.e.* lowest lying) Regge trajectories. The mass scale is denoted by $s_0$, which is about $1\,\mathrm{GeV}/c^2$ for $pp$ collisions. Hence, Equation 38 in the case of $pp$ collisions takes the form

$$\frac{\mathrm{d}\sigma}{\mathrm{d}t} = \frac{s_0^2}{16\pi}|h(t)|^2 \left(\frac{s}{s_0}\right)^{2\alpha_0-2} e^{2\ln(s/s_0)\alpha_1 t} \tag{39}$$

Compared to the diffractive model, the exponential slope $b$ in the Regge model is given by $b = 2\ln(s/s_0)\alpha_1$. For low values of $t$, this results in a $1/s$ dependence of the cross section.
The Regge model predicts cross sections for low values of $\sqrt{s}$ with a precision of a few percent compared to measured values. However, at high values of $\sqrt{s}$, the cross section stays constant respectively rises slowly (see Section 2.2.1), which is in contrast to the Regge model prediction. Following an idea by Gribov [81], this behaviour is attributed to another Regge trajectory with $\alpha_0 \approx 1$, which does not correspond to any meson exchange. The pseudo-particle connected to this trajectory is called the *Pomeron*. In QCD, a Pomeron exchange is interpreted as a multi-gluon exchange much like a gluon ladder. The Pomeron has to be a colour singlet, has no electric charge, and carries vacuum quantum numbers. It has a positive/even parity.

### 2.3.3 *Production mechanisms*

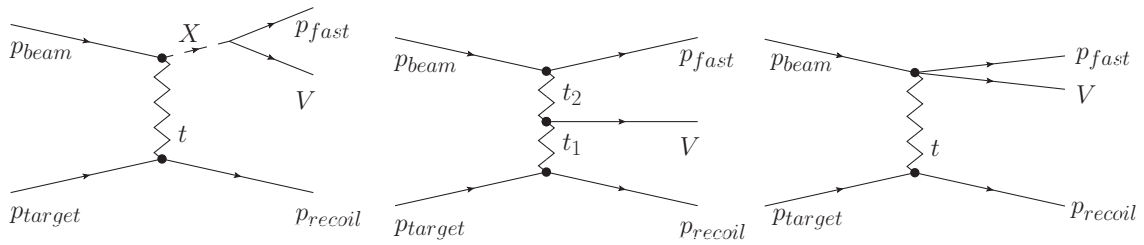


Figure 7: Mechanisms for exclusive vector meson production at high energies. Left: Resonant single diffractive excitation of the beam proton to a resonance X with subsequent decay. Middle: Central production. Right: Non-resonant single diffractive scattering of the beam proton.

The analogy of the cross section behaviour to observations in diffractive phenomena inspired the model of diffractive dissociation [65, 77]. In a $t$-channel Pomeron exchange, the beam particle is excited into a resonance conserving charge, isospin

and C-parity, but with potentially different spin and parity. In the present case of vector meson production, this means that the beam particle is excited into a $N^*$ resonance, which subsequently decays into a vector meson and a proton, see Figure 7, left panel. The target particle receives a small recoil but stays intact. The process has a strong forward peak in the angular distribution.

Central production for vector mesons is a non-resonant process, see Figure 7, middle panel. A Reggeon or Pomeron from the target and a Reggeon or Pomeron from the beam particle fuse in a central vertex. This means that there are two momentum transfers $t_1, t_2$ which are determined from the differences of the four momenta of incoming and outgoing proton at the lower vertex ($t_1$) and at the upper vertex ($t_2$). The production of $\omega$ and $\phi$ in Pomeron-Pomeron collisions is forbidden because of $G$-parity conservation. Central Production is characterised by large $x_\mathrm{F}$ gaps between all three final state particles. In the centre-of-mass system of the process, the forward proton peaks at $x_\mathrm{F} = 1$ and the recoil proton at $x_\mathrm{F} = -1$. The vector meson is produced around the central value of $x_\mathrm{F} = 0$, hence the name central production. In $pp$ collisions, central production was extensively studied by the WA102 collaboration at CERN, see *e.g.* [92] for an experimental summary and [97] for a phenomenological discussion.

A special case of non-resonant production is the shake-out of a $q\bar{q}$ pair from the nucleon sea [62, 63], which gets on-shell when interacting with a Pomeron from the other nucleon. In the case of shake-out, a larger $x_\mathrm{F}$ gap is expected between the recoil particle and the other two particles, but not necessarily between the fast proton and the vector meson. The shake-out process seems to be furthermore dependent on the momentum transfer $t$, which gives a scale to resolve structures in the nucleon such as possibly pre-formed, virtual vector mesons in the sea. Another related process is by bremsstrahlung, *i.e.* the radiation of a vector meson in the initial or final state. These processes are summarised in the right panel of Figure 7. Central production, shake-out and bremsstrahlung can be considered as similar processes in different regions of phase space.

Another theoretical possibility is a central Pomeron-Odderon fusion. An Odderon is similar to the Pomeron but with odd/negative parity, charge conjugation and G-parity. Since this process involves no quark lines, it has to reflect pure $\mathrm{SU}(3)_\mathrm{flavour}$ symmetry. Hence, the $\phi$ production rate should be of the same order as the $\omega$ rate with the only difference given due to the different $\omega$ and $\phi$ mass.

# THE COMPASS SPECTROMETER, DETECTORS AND TRIGGER SYSTEM

# 3

# EXPERIMENTAL SET-UP

The COmmon Muon Proton Apparatus for Structure and Spectroscopy (COMPASS) is located in the North Area of CERN, the European Organisation for Nuclear Research. CERN facilities include a wide range of particle accelerators as shown on Figure 8, ranging from anti-proton beams of a few MeV to the world's currently highest energy collider, the Large Hadron Collider (LHC). in 1996, the COMPASS collaboration proposed [28] a fixed-target experiment with a versatile two-stage magnetic spectrometer to commonly study both the spin structure of the nucleon and the hadronic spectrum, respectively. The spin structure is studied using high-intensity polarised muon beams at energies of about 100–200 GeV/$c^2$ impinging either on a polarised $^6$LiD target or a polarised $NH_3$ target. These inclusive or semi-inclusive measurements require a high luminosity, particle identification and a large angular acceptance. The setup for muon beams is detailed in [2]. For hadron spectroscopy, the measurements are performed using hadron beams impinging either on an unpolarised liquid hydrogen target or on unpolarised solid disks (Pb, Ni, W, C). Here, exclusive measurements are required, thus a hermitical experimental set-up is necessary which comprises a detector for the measurement of target recoils.The full setup which is used for data taking with hadron beams will be described in [10].
The collaboration was formed out of originally two separate proposals, HMC and CHEOPS: In 1987, physicists of the European Muon Collaboration (EMC) discovered that the spin of the nucleon is not completely given by its valence quarks which contribute only about half to the total spin of $1/2\hbar$. HMC [104] planned to continue the studies of EMC and the the successor experiment SMC on the nucleon spin structure with a stronger emphasis on the role of gluons. CHEOPS [15] proposed to study the hadron spectrum, with the aim to observe the first exotic charmed and doubly-charmed hadrons. Due to a strong overlap of the layout of both proposal, a common collaboration out of HMC and CHEOPS was founded finally, the COMPASS collaboration, with the aim to combine both physics programs in one multi-purpose experiment.

## 3.1 BEAM LINE

As depicted in Figure 8, the primary proton beam for COMPASS is accelerated first in LINAC2 followed by the PSB complex and the PS. From there, it is injected in the Super Proton Synchrotron. SPS began operation in 1976 and was capable of accelerating various types of particles up to 450 GeV prior to the necessary adjustments for LHC operation. Today, it is used to inject 400 GeV proton beams into the LHC and provides beams to so-called production targets in order to to produce secondary or tertiary beams for COMPASS and other experiments. The SPS proton beam is extracted into the North Area (NA) target area and split by magnets to

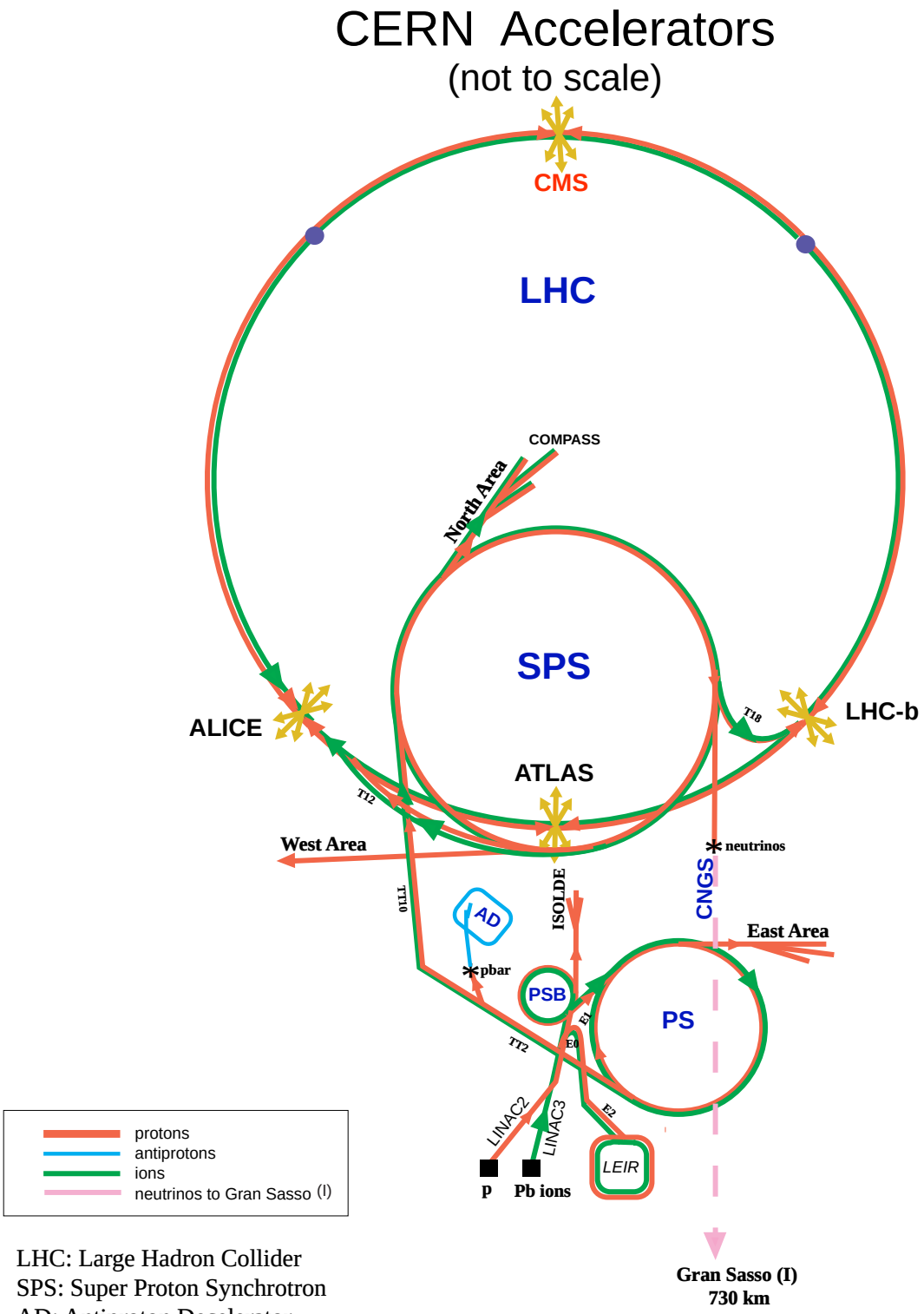


LHC: Large Hadron Collider
SPS: Super Proton Synchrotron
AD: Antiproton Decelerator
ISOLDE: Isotope Separator OnLine DEvice
PSB: Proton Synchrotron Booster
PS: Proton Synchrotron
LINAC: LINear ACcelerator
LEIR: Low Energy Ion Ring
CNGS: Cern Neutrinos to Gran Sasso

Rudolf LEY, PS Division, CERN, 02.09.96
Revised and adapted by Antonella Del Rosso, ETT Div.,
in collaboration with B. Desforges, SL Div., and
D. Manglunki, PS Div. CERN, 23.05.01

Figure 8: CERN accelerator complex. The COMPASS experiment is situated in the North Area as a part of the Super Proton Synchrotron complex. © CERN [45]

be able to be delivered simultaneously to the production targets. The SPS beam is delivered during time periods (so-called "spills") of 9.6 s once every about 45 s, the latter depending on LHC filling periods and beam usage of other experiments. The primary beam impinges on the different targets and is extracted under a fixed angle by which the maximum extractable momentum for the secondary beam is defined. Extraction angles vary for the different production targets, including 0 degree extraction which makes the use of primary beams possible, as well. For the COMPASS T6 target, the typical extraction angle is about −25 mrad in the horizontal plane and +10 mrad in the vertical plane for negatively charged beams [69]. The angle is given by both the positions of the extraction dipole magnets and their present current. There are multiple choices for production targets in terms of material and dimension: An empty target (air), in which the protons scatter in the residual gas and from which a very low intensity beam is extracted, a Silicon target, and one out of four Beryllium targets, which are 80 mm wide, 2 to 3 mm high and 40, 100 or 500 mm thick. The intensity of the extracted beam increases with the target thickness.

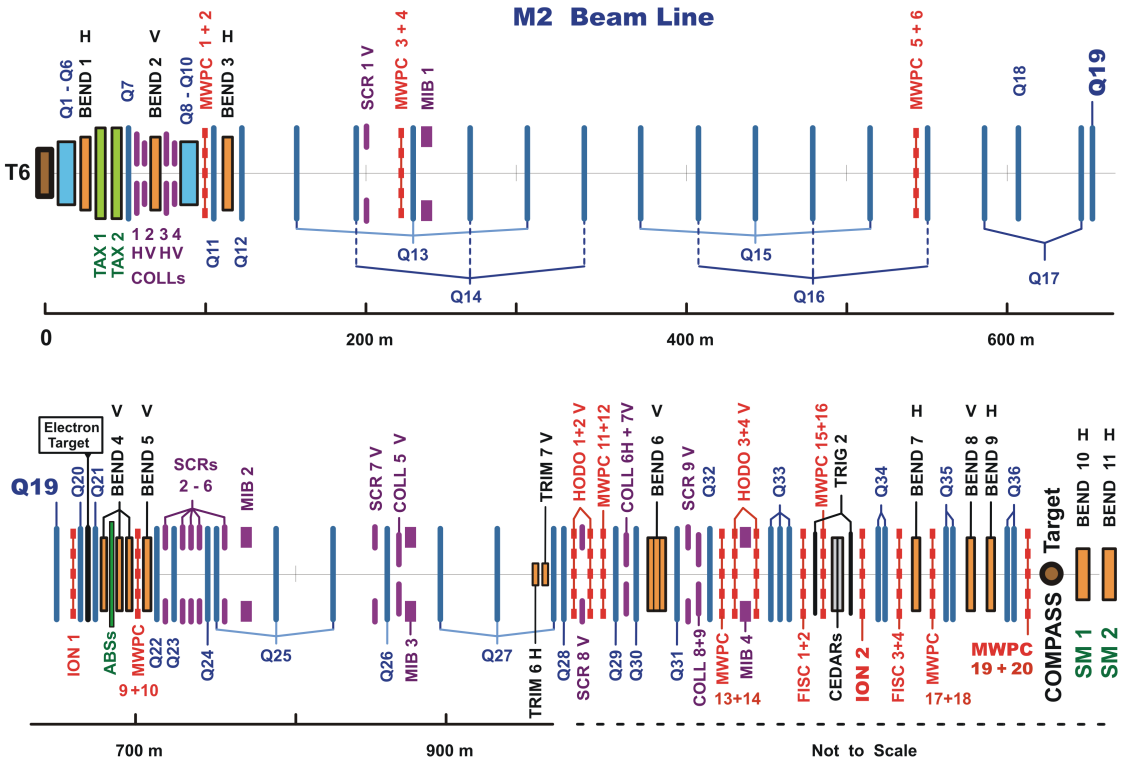


Figure 9: The M2 beam line in the North Area of CERN.

The secondary beam enters the M2 beam line, which is about 1.3 km long. The beam line is depicted in Figure 9. Initially, the beam momentum range is restricted with a set of magnetic bends and collimators with a spread of about 10 GeV. Then, the beam is transported through alternately focussing and defocussing quadrupole (FODO) sections over most of the distance. In the last stage, the beam momentum is set to 190 GeV/$c$ with BEND6. The beam momentum spread $\sigma_{\text{beam}}$ is 3 GeV/$c$.

In addition, the last stage of the beam line comprises CEDAR detectors for beam particle identification (see Section 3.1.1).
The very large pionic component of the secondary beam partly decays along the line into muons and muon neutrinos, providing therefore a naturally polarised muon beam. Beryllium absorbers with a total length of 9.9 m can be moved into the beam to filter out the remaining hadrons, therefore leaving a tertiary muon beam. For physics with hadron beams, the absorbers are moved out. The momentum spread of secondary particles is much lower (1%) than that of tertiaries (about 3-5%), which means that the leftover contamination of muons is cleaned up easily by changing the momentum acceptance of the FODO sections. The use of muon beams involves different additional techniques, which are explained in *e.g.* [2] and references therein. Both, negatively and positively charged hadron beams can be selected. The composition of particles in the beam depends strongly on the chosen energy as depicted in Figure 10 taken from [88]. The beam momentum of 190 GeV/$c$ beam momentum is chosen for a maximum kaon yield in the negative beam, which is used for most of the spectroscopy measurements at COMPASS. The same momentum is chosen for the positive beam for a better comparability of measurements. For a momentum of 190 GeV/$c$, the positive beam consists of 74.6% protons, 24% pions and 1.4% kaons whereas the negative beam consists of 96.8% pions, 2.4% kaons and 0.8% anti-protons [20] at the entrance of the experimental zone. Typical intensities for the hadron beams are $10^8$ particles per spill which is limited by the allowed radiation in the experimental zone.
The minimum reachable beam spot size (RMS) at the COMPASS target is 3 mm. Due to the special requirement of having a beam with minimum divergence within the CEDAR detectors (see Section 3.1.1) and to minimise the radiation exposition of the electromagnetic calorimeter ECAL2 close to the beam, the beam is focused 33 m downstream of the target. Thus, the spot size at the target increases horizontally to 8 mm RMS and vertically to 7 mm RMS with a local divergence of 80 $\mu$rad (horizontal) times 200 $\mu$rad (vertical).
For calibration purposes, also an electron beam can be provided. At 100 GeV/$c$ primary beam momentum, there is also an electron component of about 10% in the beam. The entergy of this component is spread due to the energy loss by Bremsstrahlung after moving a thin lead plate with a thickness corresponding to about one radiation length into the beam line. Different energies are selected by BEND6 which provides points of fixed energies for the calibration of the electromagnetic calorimeters, as described in Section 3.4.3.

### 3.1.1 *Beam Particle Identification*

Beam particles are identified through CEDAR detectors (ChErenkov Differential counter with Achromatic Ring focus). They are located in the beam line tunnel at about 30 m upstream of the COMPASS target. The particle identification is based on the Cherenkov effect: Particles travelling at a higher velocity than the speed of light in the traversed material emit light in a certain angle relative to their flight trajectory. The angle of emittance is anti-proportional to the velocity of that particle and to the refractive index of the medium, $\cos\theta = 1/(\beta n)$. Different beam particles

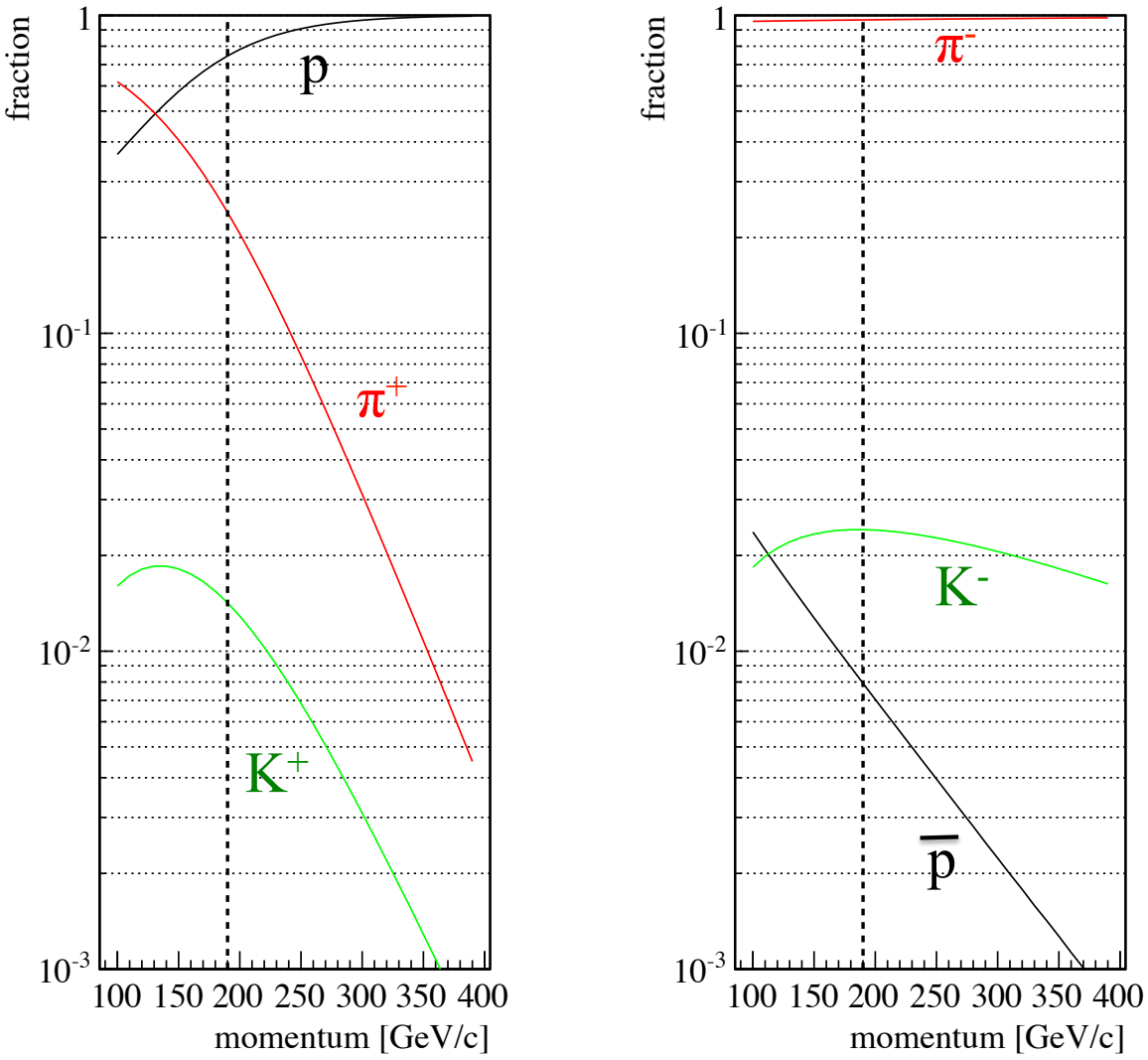


Figure 10: Hadronic beam composition as a function of the beam energy for positive (left) and negative (right) beams at the COMPASS target position. The black lines correspond to protons (left) and antiprotons (right), the red lines to pions and the green lines to kaons. The figure is taken from [88].

with the same momentum can therefore be discriminated by either measuring the angle - which is exploited by the RICH detector - or detecting light in a specific angle relative to the beam by adjusting the refractive index for the detection of specific particle types. The latter is done with the CEDAR detectors, as illustrated in Figure 11: Two types of beam particles with the same momentum enter from the left side into a gas medium, usually helium or hydrogen for momenta in the order of 100 GeV/$c$. Due to their different velocities, the particles emit Cherenkov light in different angles, indicated by red and green colour for the two types. The Cherenkov light is then focused onto a detector plane. For the correction of chromatic aberration, several lenses and a mirror are used. The result is a ring of light for each particle type at the detector plane. A diaphragm is installed in front of a set of eight photomultiplier tubes (PMTs) in order to select only one specific Cherenkov angle.

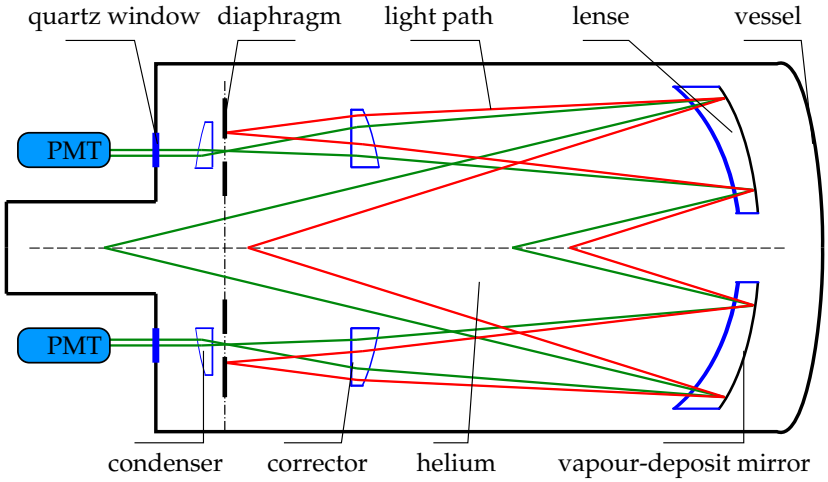


Figure 11: COMPASS CEDAR detectors: Two particles with the same momentum but different masses traverse a light gas-medium and emit light in different angles relative to their path. The light is focused and collected by photo multiplier tubes. By choosing a specific pressure of the helium gas, the opening of a diaphragm is selected to fit the ring radius of a specific particle type.

The PMTs are separated from the gas medium by a quartz window to prevent diffusion into the tubes which would degrade their lifetime considerably. The CEDARs at COMPASS are operated with helium at a pressure of 8-15 bar depending on the type of particle to be identified. The pressure together with the temperature fix the density of the gas which is directly connected with the refractive index. By changing the pressure in the vessel, the refractive index is therefore adapted to choose the Cherenkov angle such that only light from a certain type of particle passes the opening of the diaphragm. One CEDAR detector can only be used to identify one type of particle. Hence, two detectors are used to either identify protons and pions for the positively charged beam or kaons for the negatively charged beam.
Depending on the separation of the light rings, the beam particle is identified by the CEDARs when at least 4 PMTs per detector respond at the same time in the case of positive hadron beams and at least 6 PMTs at the same time for negative particle beams. The efficiency and purity of the CEDARs depends very much on the temperature and the pressure within the vessel. Both are monitored and the pressure can be adjusted remotely to correct for variations. The pressure and temperature values are stored and can be used to calculate instant purity and efficiency values which can be used in a later analysis. Further details and technical specifications can be found in [39] and [88]. The CEDARs are also used in the trigger system as described in Section 5.6.

## 3.2 SPECTROMETER

In this section, the spectrometer layout is described. Only a short summary over the most important features of the spectrometer set-up are given. The essential detectors for the particle identification used in this thesis are described in more detail.

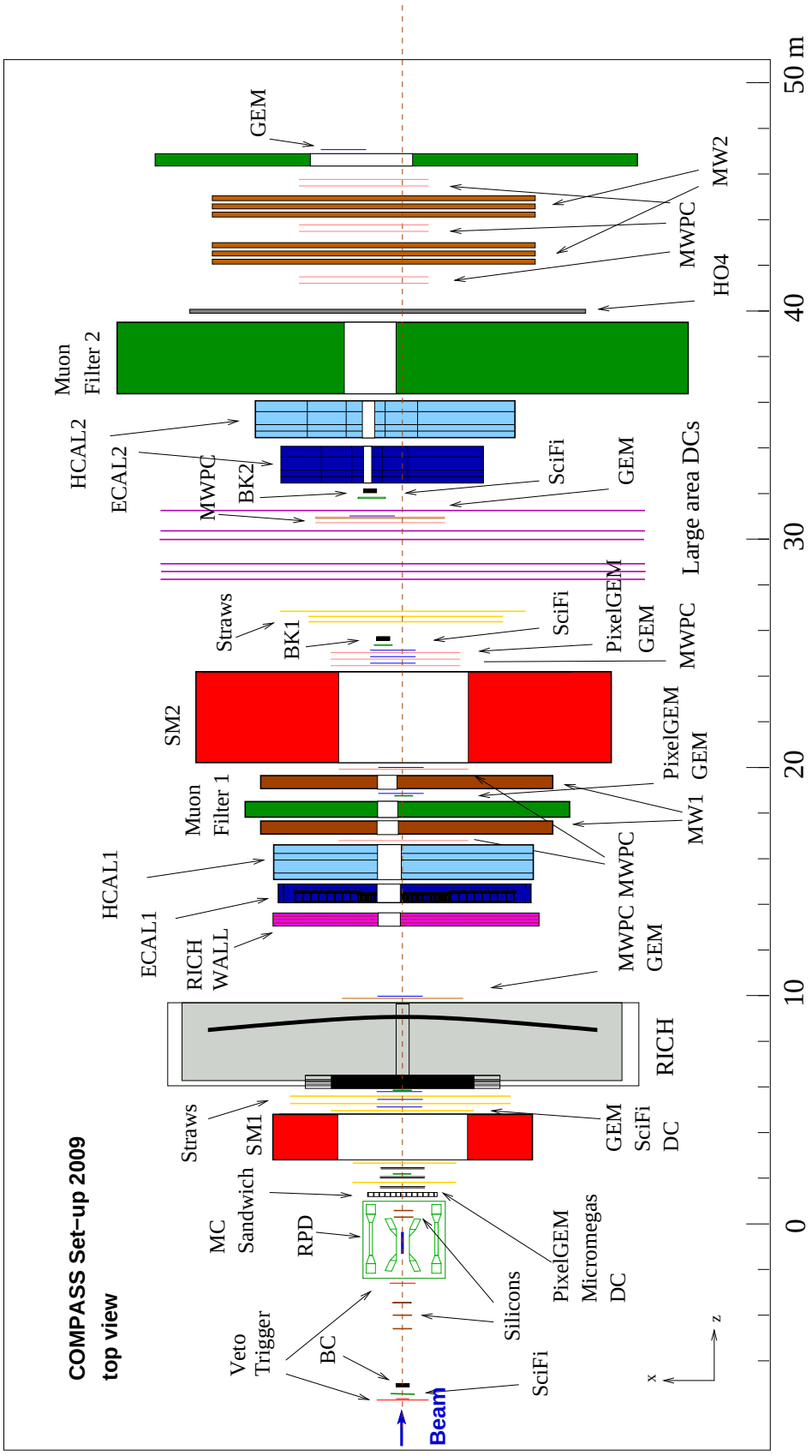


Figure 12: Top view of a sketch of the COMPASS setup as used for data taking during the hadron campaign. For details, see the text and [10].

### 3.2.1 *Target region for hadron spectroscopy*

The target region is specific to the physics programme as explained in the introduction of this chapter. For hadron spectroscopy, it contains the target itself, a beam telescope, a recoil detector, a vertex telescope and veto detectors (see Figure 13). The beam enters from the left through the silicon microstrip beam telescope (see *e.g.* [35, 80] and references therein). The detectors are placed within vacuum chambers and cooled to a temperature of 200 K in order to prevent damage as a result of radiation [110].
Three different configurations of the target are used for measurements. For diffractive data taking, a liquid hydrogen target is used. It has a diameter of 35 mm and is 400 mm long. The liquid hydrogen corresponds to 4.5% of a radiation length ($X_0$) and 5.5% of a nuclear interaction length ($\lambda_0$) along the beam direction. The diameter is chosen to be four times the 8 mm RMS of the beam spot plus margin for beam alignment inside the volume. After initial cooling, the hydrogen in the cell has a temperature slightly below the boiling temperature of about 20 K. The cell itself is a cylinder made of a thin Mylar foil with a thickness of only 0.125 mm to reduce any material in the path of recoiling particles from the target. The mylar cell is placed within an evacuated aluminium cryostat which has a wall thickness of 1.8 mm around the cell, which limits measurements of recoil particles to momenta above 100 MeV/$c$. The cryostat is connected to a refrigerator system which holds the equipment for cooling. Alternatively, the full target system can be removed from the central structure and can be replaced by a holding structure with solid target foils. This configuration has been used for Primakoff data taking with a 4.3 mm thick nickel disk and for a short diffractive data taking with both lead and tungsten foils of different thicknesses in the holder.
The target is surrounded by two concentric rings of scintillators which are part of the recoil proton detector (RPD). Its purpose is on the one hand to trigger on recoiling particles emerging from the target volume and on the other hand to identify those particles by measuring the time-of-flight between the inner ring and the outer ring. Chapter 4 is dedicated to a detailed description of the detector.
The target is followed by a silicon vertex telescope inside a conical cryostat. The detectors are similar to the silicon detectors used in the beam telescope.
Both upstream and downstream of the target, there is additionally a system of veto detectors installed. Details on these detectors are explained in Chapter 5.

### 3.2.2 *Large and Small Angle Spectrometer*

The COMPASS spectrometer is a large acceptance open dipole spectrometer. The set-up is depicted in Figure 12. It consists of two parts: the large angle spectrometer (LAS) with the dipole magnet SM1 between the target region and the muon identification system MW1, and the small angle spectrometer (SAS) around the dipole magnet SM2. Both spectrometer stages comprise similar setups which are optimised for the specific range of particle momenta and expected particle flux. The momentum acceptance ranges from about 1 GeV/$c$ to 60 GeV/$c$ in the LAS and 50 GeV/$c$ up to nearly the beam momentum of 190 GeV/$c$ in the SAS. The overall

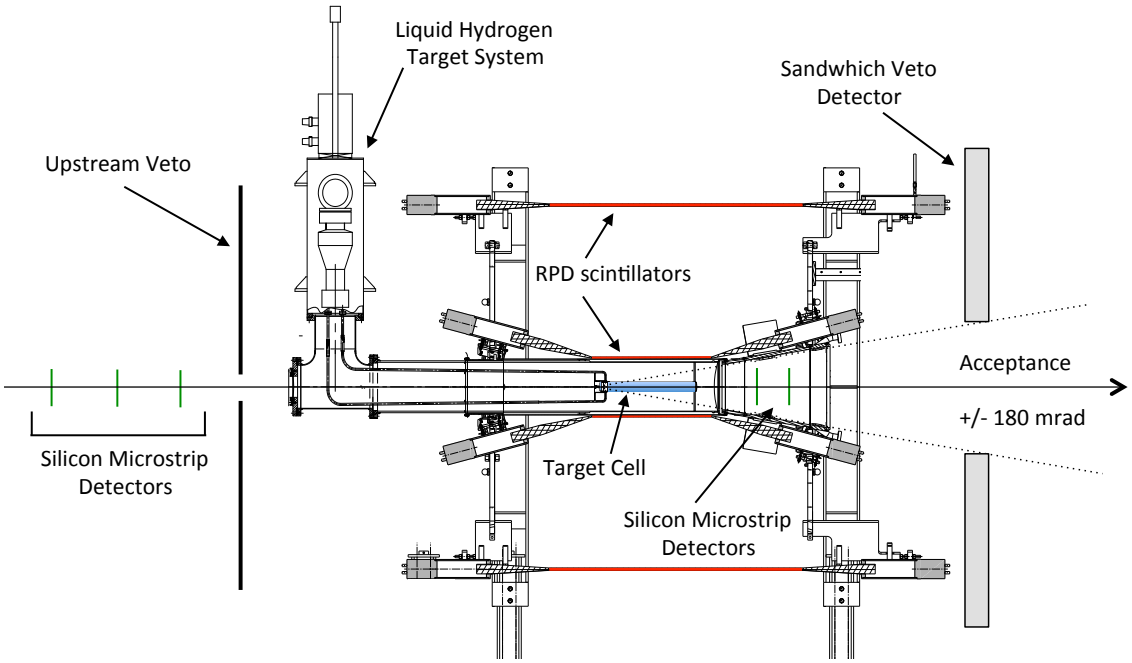


Figure 13: Schematic drawing of the target region. The beam enters from the left side through the silicon microstrip beam telescope. The liquid hydrogen target in the centre is surrounded by the recoil proton detector (RPD).

angular acceptance is $\pm 180$ mrad for charged particles. The detectors in the LAS comprise thin dead zones and central holes corresponding to the angular acceptance of the SAS.

*Charged Particle Tracking*

Both spectrometer stages include micro pattern gas detectors (GEMs [91, 116], PixelGEMs [21, 90], MicroMegas [96]) and scintillating fibre stations (SciFis [37, 84]) for small and very small angle tracking. For large angle tracking with rather low occupancies, *i.e.* the percentage of either time or area on which the detector is being hit by particles, the LAS is equipped with drift chambers (DCs [2]) and straw tube detectors (Straws [43]). The SAS has both multi-wire proportional chambers (MWPCs [2]) and Straws, as well as very large drift chambers. The large area DCs described in [41] were refurbished and upgraded with a digital read-out for the COMPASS data-taking.
The achieved momentum resolution is about 0.3% for tracks identified with SM1 and 0.1% for tracks identified with SM2 [2].

*Calorimetry*

The spectrometer comprises both hadron and electromagnetic calorimeters in each stage. Calorimeters measure the energy of particles by the detection of showers originating from particles passing through matter. In COMPASS, several types of

calorimeters are used. The hadron calorimeters are used for detecting pions, protons, and kaons and to distinguish between pions and muons. The hadron calorimeters are sampling calorimeters that consist of alternating layers of an absorber material and an active material for the detection of the shower particles, usually scintillators. For details on HCAL1, see [126]. HCAL2 is described in [2]. The electromagnetic calorimeters ECAL1 and ECAL2 are homogeneous calorimeters with lead-glass cells. They are presented in more detail in Section 3.4.

*Muon identification*

Muons do not interact strongly and therefore traverse large amounts of material without any interaction. Because external Bremsstrahlung is suppressed due to the high mass of the muon, energy is mostly lost by multiple scattering, which amounts to only small energy losses through the spectrometer set-up. Two thick absorbers are equipped with drift tube tracking detectors installed at the most downstream position of each spectrometer stage. Having passed through calorimeters and the absorber material, only muons can generate signals in the trackers downstream of the absorbers. The LAS features an iron absorber plus trackers (MW1 [1]) while the SAS has a concrete absorber plus trackers (MW2 [42]). Additionally, muon hodoscopes [32] are installed downstream of each absorber which are used in the muon trigger as well as for muon identification.

*Trigger*

A new trigger system has been build to accommodate the need of detecting complete events. Several triggers select events for specific processes. Both diffractive and central production feature a proton recoiling from the target. The system for this process triggers on recoil particles and the incoming beam and suppresses events with particles outside of the spectrometer acceptance.
A part of the new trigger system uses the same components as have been used in the muon programme, mainly the veto counters (indicated by "Veto trigger" in Figure 12). Several new detectors have been specifically build for triggering purposes: A beam counter (BC) with the same transverse size as the target cell gives the possibility to detect and trigger on beam particles impinging on the target. The RPD (see Chapter 4) is used to trigger on recoiling particles coming from the target. The Sandwich Veto detects both charged and neutral particles, which would be neither detected by the RPD nor the spectrometer. Another veto system made of the two beam killers (BK) is used to prevent recording of events for which the beam has not been scattered in the target. Several other detectors have been introduced to fit the needs for specialised data taking, such as measuring Primakoff events ($\pi N \rightarrow \pi N \gamma$) or events with higher multiplicities. Details on the trigger system and trigger concept are explained in Chapter 5.

## 3.3 PARTICLE IDENTIFICATION WITH THE RICH

The first stage of the spectrometer is equipped with a Ring Imaging CHerenkov detector (RICH) for identification of charged particles. The detector itself measures

the velocity of a passing particle which can be used to determine its mass when used in combination with its momentum measured by the deflection in SM1.

### 3.3.1 *Basic principle*

Particles travelling at a higher speed than the light speed in the traversed material emit light in a certain angle relative to their flight trajectory, which is given by the velocity $\beta$ of the particle and the refractive index $n$ of the material:

$$\cos\theta = \frac{1}{\beta n} \tag{40}$$

Combining Eq. 40 with the known energy–momentum relation $E = \sqrt{m^2 + p^2}$, with $m$ denoting the mass, $p$ denoting the momentum and $E$ being the energy of the particle, and combing this with $\beta = p/E$, the mass of the particle can be determined by

$$m = p\sqrt{n^2\cos^2\theta - 1} \tag{41}$$

The method works only for particles with $\beta > 1/n$, which means that there exists a lower boundary for slow particles. For very high momenta, the angular differences of different particles are very small, thus the particle identification is also limited in this case.
In the RICH detector, particles cross a large containment of a so-called "radiator" material and emit light along their trajectory. Similar to the CEDAR detectors, the light can be focused by a system of mirrors and lenses onto a plane. The only difference is that the particles do not necessarily have to follow the same path. As a result, the resulting ring image on the focal plane is located at arbitrary positions. Measuring the photons in the focal plane with the help of a large array of photo detectors, the ring image can be reconstructed. The radius of a ring directly corresponds to the velocity of the original particle. The ability to distinguish between different particle types is hence limited by the imaging resolution of the system.

### 3.3.2 *Layout*

Figure 14 shows the layout of the COMPASS RICH detector (RICH-1) (see [3, 5] and references therein). On the left panel of the figure, a charged particle enters the radiator volume from the left side and emits Cherenkov light. The detector vessel is 3.3 m long, has a height of 5.3 m and a width of 6.5 m. For the radiator gas, $C_4F_{10}$ is chosen with a refractive index of 1.0014 [125] and a high transparency for UV light yielding thresholds for particle identification of about 2.5, 9 and 17 GeV/$c$ for pions, kaons and protons respectively.
For the detection of Cherenkov photons, two different types of detectors are used. The central part with high occupancies is equipped with fast multi-anode PMTs [4]. The outer part is equipped with CsI-coated MWPCs behind quartz glass. The evaluation and analysis of the ring images is done *via* a log-likelihood method, as described in [5].

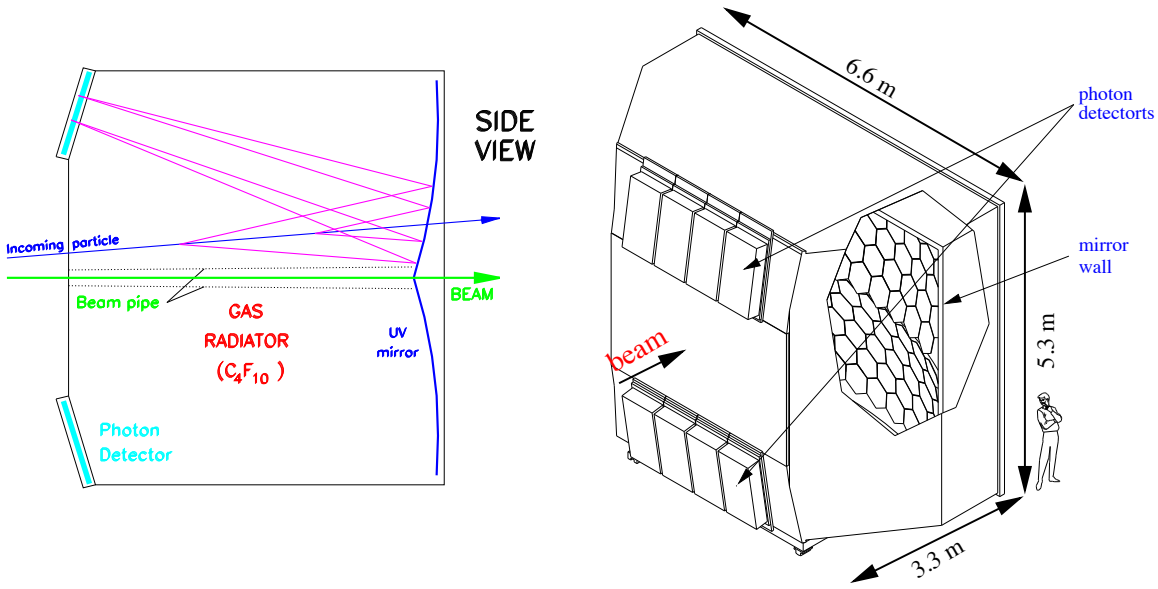


Figure 14: COMPASS RICH detector. Left: Schematic view of a particle passing the radiator vessel and emitting Cherenkov light. The light is focused and then detected by photo detectors. Right: Design concept.

The setup includes also a steel beam pipe in the central area of the detector which is filled with Helium to prevent an excess of light due to passing beam particles which have not interacted in the target volume.

## 3.4 ELECTROMAGNETIC CALORIMETERS

Both LAS and SAS, respectively, are equipped with electromagnetic calorimeters, abbreviated as ECALs.

### 3.4.1 *Measuring particle energies with ECALs*

Electromagnetically interacting particles at high energies experience energy losses when passing through matter mainly due to bremsstrahlung and pair production processes. In the former process, charged particles emit a photon when passing through the field of a nucleus. The latter process describes a photon turning into a pair of an electron and positron, also in the presence of a field. Both processes usually alternate until the energy of the involved particles is no longer high enough to create a pair. The multiplicity of charged particles increases with each turn, hence the term electromagnetic "shower". The shower properties are given by the radiation length $X_0$ and the critical energy $E_{crit}$, which are both given by the material. The radiation length is the thickness of material after which the energy of an electron has been reduced to $1/e$ of its original value. The critical energy is the energy at which the loss due to bremsstrahlung equals the collision losses. If the electron has lost so much energy that it falls under the critical energy, the shower stops. Another characteristic for describing a shower is its transverse dimension. Assuming the shower evolving like a conus through the material, the so-called Moliere radius

$R_M$ is the opening at which 90% of the total shower energy is deposited. Therefore, it is an important quantity to determine the size of an individual detector in order to be able to measure the full energy deposit. The Moliere radius is given by

$$R_M = 21\,\text{MeV}\,\frac{X_0\,[\text{cm}]}{E_{crit}} \tag{42}$$

In most electromagnetic calorimeters, the produced photons are measured with photo detectors. The amount of collected photons is proportional to total deposited energy in the calorimeter and is a good measurement of the particle energy if typically $10\,X_0$ are traversed in the calorimeter. A special type of detector material is lead glass, in which the conversion electrons emit Cherenkov light when passing through. Measuring the energy loss follows again the same principle with the difference that now the Cherenkov light needs to be detected.

### 3.4.2 *Layout*

*ECAL1*

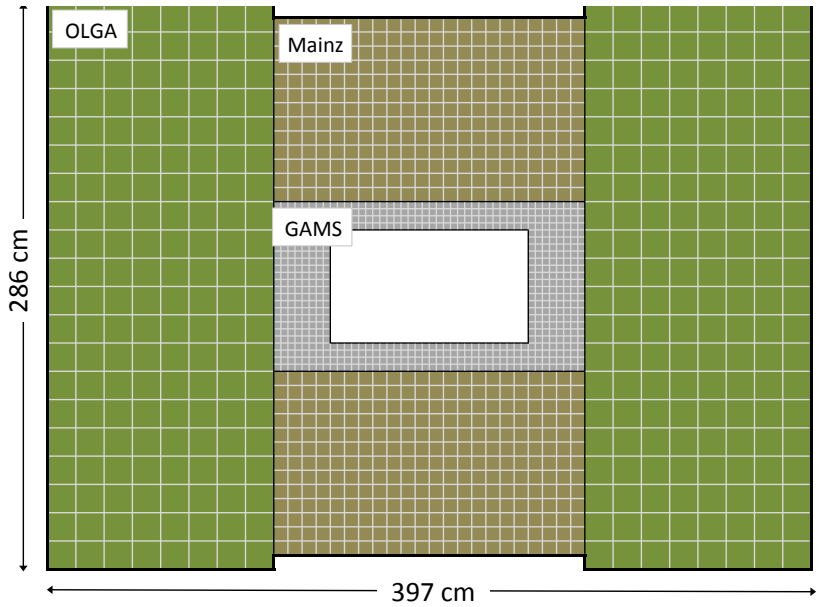


Figure 15: Layout of ECAL1. The central part features GAMS cells. The MAINZ cells are placed on both the top and the bottom of the central part. OLGA cells are used for the left and right sides.

The calorimeter ECAL1 is a homogenous calorimeter built of lead glass cells. It is located 15 m downstream of the target and has a width of 3.97 m and a height of 2.86 m with a central hole of 1.07 by 0.61 $\text{m}^2$. The angular acceptance is 37 to 136 mrad in the horizontal direction, and 21 to 98 mrad in the vertical direction, therefore smaller than the angular coverage of $\pm 180$ mrad of the tracking detectors. The detector consists of 1500 lead glass cells of three different types, arranged as depicted in Figure 15: The central part is equipped with GAMS [36] cells, the part

| Parameter | Units | GAMS rad.hard. | GAMS | MAINZ | OLGA |
|---|---|---|---|---|---|
| LG type | | TF101 | TF1 | SF57 | SF5 |
| Density | $g/cm^3$ | 3.86 | 3.86 | 5.51 | 4.08 |
| Rad. length | cm | 2.74 | 2.54 | 1.55 | 2.55 |
| Total thickness | $X_0$ | 15.2 | 16.4 | 23.3 | 18.5 |
| Moliere radius | cm | 3.7 | 4.7 | 2.61 | 4.3 |
| Refractive index | | 1.67 | 1.65 | 1.89 | 1.67 |
| Length | cm | 45 | 45 | 36 | 47 |
| Surface | $cm^2$ | $3.8 \times 3.8$ | $3.8 \times 3.8$ | $7.5 \times 7.5$ | $14.1 \times 14.1$ |
| PMT type | | FEU-84-3 | FEU-84-3 | EMI 9236KB | XP2050 |

Table 4: Overview of the different lead glass cells of ECAL1 and ECAL2.

on the top and bottom of GAMS is equipped with MAINZ [9] cells and the left and right side features OLGA [19] cells. As lead glass is a very expensive material, the cells were re-used from older experiments. Their origin is reflected by the name. Table 4 summarises the key features of the cells. The transverse size of the GAMS cells is much smaller than the Moliere radius which means a typical shower in this region will be spread over several cells. Showers in the OLGA part are mostly contained in one cell.
The Cherenkov light of the individual cells is detected by PMTs. The PMTs are read-out with sampling ADC [101] electronics which consist of shaping units and the ADCs themselves. The shaping unit stretches the PMT signal to length in the order of 100 ns while the ADC samples the signal amplitude every 12.5 ns. As described in Section 5.5, there exists also an algorithm to extract precise timing from the SADC information. The energy resolution $\sigma_E/E$ of the different lead glass types was measured to be $0.07/\sqrt{E} + 0.01$ for GAMS, $0.06/\sqrt{E} + 0.04$ for MAINZ and $0.06/\sqrt{E} + 0.01$ for OLGA [94].

*ECAL2*

The calorimeter ECAL2 is placed 33 m downstream of the target and covers an area of $2.44 \times 1.83\,m^2$, which is an angular acceptance of 1.3 to 39 mrad in the horizontal plane and between 1.3 and 29 mrad in the vertical plane. ECAL2 has a small hole of 2x2 cells at the position of the beam.
ECAL2 consists of 3068 calorimeter cells of three different types, but unlike ECAL1 they all have the same transverse dimensions of $38.3 \times 38.3\,mm^2$. They are arranged as shown in Figure 16 in a matrix of 64 by 48 cells. The outer part is made of the same GAMS cells as have been used for ECAL1. Closer to the centre, radiation-hard GAMS cells are used, see Tab. 4. In ECAL2, Shashlyk type cells are used in the very central, high-occupancy region, which are conceptually different from lead glass cells. Shashlyk cells are much more radiation-hard than lead glass cells and hence put in areas close to the beam, where the radiation is the highest. A photograph of a Shashlyk cell is shown in Figure 17. Shashlyk cells are made of alternating

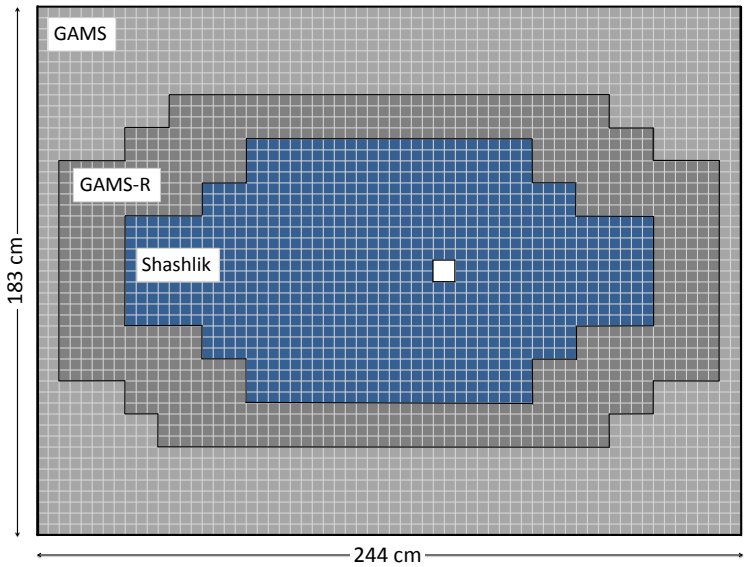


Figure 16: Layout of ECAL2. The inner part is equipped with Shashlyk type cells, the part surrounding with radiation-hard GAMS cells. The outer part consists of GAMS cells which are also used for ECAL1.

layers of lead and scintillator plates (Sandwich concept) where the lead acts as an converter due to its high density. The emerging shower particles pass through the scintillator layer and produce scintillating light throughout the material. The light is collected by wavelength shifting fibres and detected by PMTs like in the case of lead glass cells. The energy resolution $\sigma_E / E$ of the Shashlyk cells was measured to be $0.07/\sqrt{E} + 0.01$ [94].

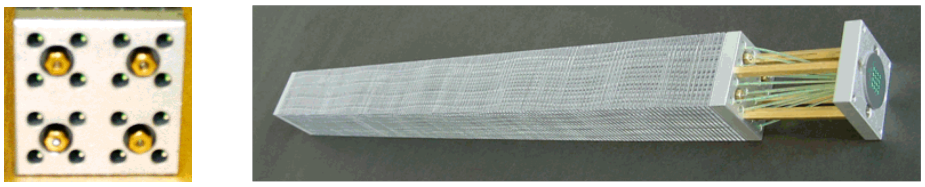

Figure 17: Shashlyk calorimeter cells. Left: upstream face of an cell, with four central holding rods and 16 wavelength shifting fibres. Right: Full cell with downstream face up front.

### 3.4.3 *Calibration*

Both ECALs are mounted on moveable platforms which allows for the possibility to reach each cell of each ECAL with the beam. Electron beams with different energies are used for initial calibration. At the beginning of each year of data taking and after important changes on the detectors themselves, the ECALs are newly calibrated. ECAL1 is calibrated with a beam energy of 15 GeV, ECAL2 with an energy of 40 GeV.

The calibration procedure involves two steps. First, the energy range of the calorimeter is set. This is done by choosing the high voltage (HV) of each PMT to create signals of up to a maximum of 2 V in the desired energy range due to the voltage limit of the SADC and shaper modules. The higher the HV setting, the lower is the accessible energy range, but the better is the energy resolution. An optimised setting needs to respect the expected maximum energies in a sector of the ECALs as well as the best achievable amplification for a good energy resolution. Naturally, HV settings should not exceed the maximum allowed amplification of the used PMT and allowed current on the voltage divider. During the procedure, the ECAL to be calibrated is automatically moved in the inter-spill break to allow the beam to hit one cell after the other. The signals in each cell are then checked for the correct energy range and the HV setting is adapted accordingly. For ECAL1, the dynamic range is set to detect energies of up tp 60 GeV in GAMS cells, 30 GeV in MAINZ cells and 20 GeV in OLGA cells. For ECAL2, the dynamic range of the central cells is set to a maximum energy of 150 GeV and to 60 GeV for the outermost two rows and lines for diffractive data taking. For Primakoff data taking, the maximum range for the innermost cells is then extended to 200 GeV. In a second step, the procedure is repeated after the new HV settings are applied to obtain the final calibration constants. Due to the fact that in particularly the GAMS and Shashlyk cells in general do not contain a full shower and hence not the full energy, the sum of all signal amplitudes coming from the surrounding cells is also considered and compared to the known beam energy. From this, calibration coefficients to translate signal amplitudes to energies are calculated and used in the physics analyses.

### 3.4.4 *Monitoring*

Both ECALs are equipped with monitoring systems which provide light of a certain wavelength and thus energy to each individual cell. In case of ECAL1, a laser system distributes light from a single laser source to each cell. For ECAL2, there are eight different LED light sources. Both systems are activated in the inter-spill break with a pulse frequency of about 1-10 Hz, which allows for a spill-based monitoring of the signal amplitudes and thus the gain of each PMT. The information is also provided online in the detector control system and enables fast reactions to possible problems in the calorimeters. Typical parameters which affect the stability are either temperature-related, such as day/night variations or instabilities in the HV supply. The information of the monitoring system is used during data processing to correct the above mentioned calibration coefficients for time variations. The monitoring system itself is also crosschecked for instabilities with the help of photo diodes which are supplied with light from the laser and each LED.

#### *Monitoring trigger*

The stability of the ECALs is essential for many measurements in the hadron spectroscopy programme, also within a spill period. The beam intensity is constant over the spill, which results in variations of PMT gains due to intensity related effects. Therefore a dedicated monitoring trigger was designed which automatically stops

the physics data taking, flashes the monitoring laser and LEDs, and resumes with data taking about 10 times per spill. The system is set-up with the help of a gate generator, which is gated itself by the begin of spill signal (BOS) and the end of spill signal (EOS). During a monitoring period, the gate signal inhibits all trigger signals at the level of the refresh discriminators, see Chapter 5 for details. After a break of about 250 ns, the laser and LED system is enabled. The gate signal is furthermore fed to the trigger controller in the same way as a physics trigger and timed in to trigger the data taking at the arrival time of the laser and LED pulses in the calorimeters.

# 4

# THE RECOIL PROTON DETECTOR

The Recoil Proton Detector (RPD) is used to detect and identify recoiling particles from the target volume by measuring their time-of-flight and energy loss. The detector is also a part of the trigger system, see Section 5.3. It consists of two concentric scintillator cylinders ("rings") surrounding the target. Charged particles emerging from the target at polar angles from about 50° to 90° with a minimum momentum of 270 MeV/$c$ are measured. The corresponding minimum velocity is $\beta = 0.28$. Possible recoils include protons, pions, kaons and electrons with momenta up to about 1 GeV/$c$. For the measurement of relevant physics processes, the separation of protons from other recoil particle types is required. This requirement is also demanded for the trigger system. Due to the limited time for a trigger decision, an online proton separation within 500 ns is necessary. The detector concept is based on the recoil detector of the GAMS NA12/2 experiment at CERN [13] and is adapted to the dimensions of the liquid hydrogen target.
In this chapter, a short overview over the basic principles of time-of-flight detection with scintillation counters is given. The detector set-up and read-out are described. Then, the commissioning and calibration is explained. The chapter concludes with the determination of the performance including efficiency and obtained resolutions.

## 4.1 TIME-OF-FLIGHT MEASUREMENTS

### 4.1.1 *Basic principles*

The time-of-flight (TOF) of a particle between a start counter and a stop counter in a certain distance from each other can be used to determine the particle velocity [83] . Adding another information makes it possible to identify the particle, *e.g.* with the particle momentum or it's energy loss in the traversed material. The velocity is determined by $\beta = L/(ct_2 - ct_1)$ where $L$ is the distance between the two detectors and $t_1$ and $t_2$ are the times measured by start counter (1) and stop counter (2). The velocity $\beta = v/c$ is given by the particle mass and momentum, $\beta = p/E = p/\sqrt{m^2c^4 + p^2c^2}$. Abbreviating $t = t_2 - t_1$, the mass of a particle is determined as

$$m = p\sqrt{\frac{c^2t^2}{L^2} - 1} \tag{43}$$

with a resolution of

$$\frac{\delta m}{m} = \frac{\delta p}{p} + \gamma^2\left(\frac{\delta t}{t} + \frac{\delta L}{L}\right) \tag{44}$$

with $\gamma = 1/\sqrt{1-\beta^2}$. With the safe assumption that the distance between start counter and stop counter is well measured, the time resolution is to be minimised

when constructing a time-of-flight detector. The mass determination is limited by the speed of the particle, which enters Equation 44. In practice, the mass is often not directly determined because the required time resolution cannot be achieved. In fact, it is only important to distinguish between different types of particles, *e.g.* to separate protons from pions. Two types of particles $a$ and $b$ with the same momentum differ in their time-of-flight by

$$\Delta t = \frac{L}{pc}\left(\sqrt{p^2c^2 + m_1^2c^4} - \sqrt{p^2c^2 + m_2^2c^4}\right) \tag{45}$$

Series expansion of Equation 45 for low momenta $p \ll m_{1,2}$ shows that $\Delta t$ is dominated by the mass difference $m_1 - m_2$:

$$\Delta t = \frac{L}{p}(m_1 - m_2). \tag{46}$$

The separation $\Delta t$ should be generally larger than the resolution $\delta t$, and commonly $3\delta t < \Delta t$ is demanded for safe separation.
In the COMPASS case, a typical separation of a recoil proton from a pion within a momentum range of about $0.3\,\mathrm{GeV}/c$ to $1\,\mathrm{GeV}/c$ is required. With a distance of 63 cm, this corresponds to a necessary separation of $\Delta t(0.3\,\mathrm{GeV}/c) = 5.6\,\mathrm{ns}$ to $\Delta t(1\,\mathrm{GeV}/c) = 1.7\,\mathrm{ns}$. Thus, a resolution of better than $\delta t = 560\,\mathrm{ps}$ is required for separating protons from pions.
Further details on time-of-flight techniques and modern applications can be found in [93] and [83].

### 4.1.2 *Time-of-flight measurements with scintillation detectors*

The ambitious requirements for the time resolution in a TOF measurement can only be met with a fast detector. Often, organic ("plastic") scintillators are used in combination with photomultiplier tubes (PMTs), which is also done for the COMPASS RPD.
The mean energy loss of a charged particle traversing a polyvinyltoluene scintillator with a momentum higher than about 100 MeV/$c$ is approximately 2 MeV/cm [29]. The energy is converted to photons due to admixed dye with a yield of about one photon per 100 eV energy loss. The fast response comes at the cost of photons in the UV range, which are either shifted to wavelengths suitable for standard PMT application or detected with UV-sensitive PMTs. Additional fluorescent dyes are admixed which absorb the photons and re-emit them at a different wavelength to decrease the absorption of light in the schintillator. This leads to a complex time structure of the detected light, usually rising fast to a maximum and decreasing slow afterwards. The time structure is affected by the scintillator geometry because of late arrival of the photons due to reflections on the surfaces. The time resolution is the better the steeper signal rises. The signal is also attenuated in the scintillator. The attenuation length determines the effective number of photons which are collected by the PMT read-out. Between scintillator and PMT, usually a matching element is used, called light-guide, which has a close to the same refractive index, *e.g.* polymethylmethacrylate.

PMTs are vacuum tubes with vapour-deposited photocathodes. Incident photons can knock out electrons from a powered photocathode (photoelectric effect), which in turn hit further powered electrodes ("dynodes") and hence are multiplied by secondary emission. The electrons are collected on an anode, giving an electrical signal. Its amplitude is proportional to the number of photons and hence the energy loss of the original particle in the scintillator. The time from the arrival of the incident photons to arrival of the electrons at the anode is called transit time. Its spread $\sigma_{PMT}$ depends on temperature and the quality of the PMT and enters the overall time resolution.
The time resolution of a scintillating detector is approximated [83] as

$$\delta_t = \sqrt{\frac{\sigma_{sc}^2 + \sigma_{geo}^2 + \sigma_{PMT}^2}{N} + \sigma_{r/o}^2} \tag{47}$$

where $\sigma_{sc}$ denotes the scintillator resolution due to its material properties and $N$ is the number of photoelectrons at the cathode. Here, the rise time is most important, which is the time between reaching 10% to 90% of the maximum light output. The resolution $\sigma_{geo}$ is given by scintillator and light-guide geometry and is optimised by ray-tracing simulations and prototype tests [33]. The resolution $\sigma_{r/o}$ is due to the read-out electronics. As the key criteria for the RPD design and construction, these resolutions were optimised, as will be discussed in the next section.

## 4.2 SET-UP

As depicted in Figure 18, the two scintillator rings are located at a radial distance of 12 cm (inner ring, "A") and 75 cm (outer ring, "B") from the target centre which is aligned at the zero beam line.
The inner ring [33] consists of 12 scintillator elements with dimensions of 50 cm × 6.6 cm × 0.5 cm, each element covering 30° of the azimuthal angle $\varphi$. The selected material is BC404 [123] from St.Gobain. As shown in Table 5, it features a fast rise time of 0.7 ns and a high light yield of 68 % compared to the one of anthracene on the expense of a short attenuation length. The light guides design is a result of ray-

| | |
|---|---|
| Density | 1.032 g/cm$^3$ |
| Refractive index | 1.58 |
| Light yield (in units of anthracene) | 68 % |
| Attenuation length | 140 cm |
| Rise time | 0.7 ns |
| Decay time | 1.8 ns |
| Wavelength of max. emission | 408 nm |

Table 5: Material characteristics of BC404 plastic scintillator (St.Gobain [123]).

tracing simulations and prototype tests. Several geometries were tested with the only constraint of having all PMTs outside of the forward spectrometer acceptance.

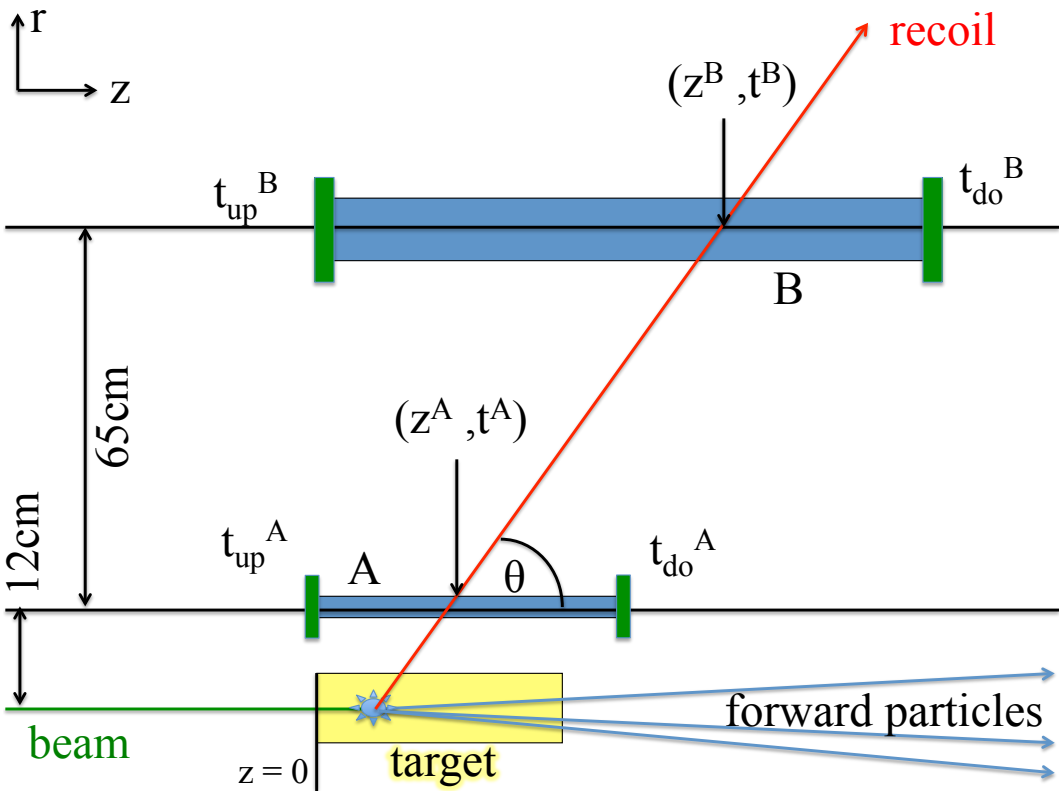


Figure 18: Schematic side-view of RPD and target.

Fish-tail geometry and adiabatic geometry yield similar results for time resolution, slightly favouring the fish-tail for a better light propagation speed. Hence, fish-tail light-guides have been chosen and were produced at KPH/Mainz. They are glued to the scintillators at a polar angle of 15°, bending away from the target. Thus, there is no material inside the 11° forward acceptance of the spectrometer. Both the scintillator elements and the light guides are enwrapped with a thin aluminised mylar foil and loosely enclosed in thin black PVC tape for light tightness. This is a result of attenuation length measurements with different wrapping foils with a $^{207}$Bi source.

The outer ring is segmented in 24 elements with dimensions of 173 cm × 20 cm ×1 cm produced at IHEP Protvino [16]. The end part of the scintillators are used as light-guides. They are twisted and melt to fit to a cylinder with 3.9 cm diameter. Each element is wrapped with aluminised mylar and black PVC tape and covers an azimuthal angle of 15°. Each inner ring counter faces 3 outer ring counters as viewed from the target.

All elements are read-out at both ends using EMI/Thorne 9813KB photomultiplier tubes. The PMTs are enclosed in both mu-metal and soft iron shieldings to protect against magnetic fields. For the expected high rates, special transistor-based voltage dividers were designed and built to allow for a stable operation in rate of up to 5-10 MHz with signal amplitudes of up to 5 V.

The read-out is designed to cope with the high dynamical ranges which are needed to cover signals from minimum ionising particles to stopping protons. Figure 19 shows the calculated energy losses in Ring A versus Ring B for pions and protons

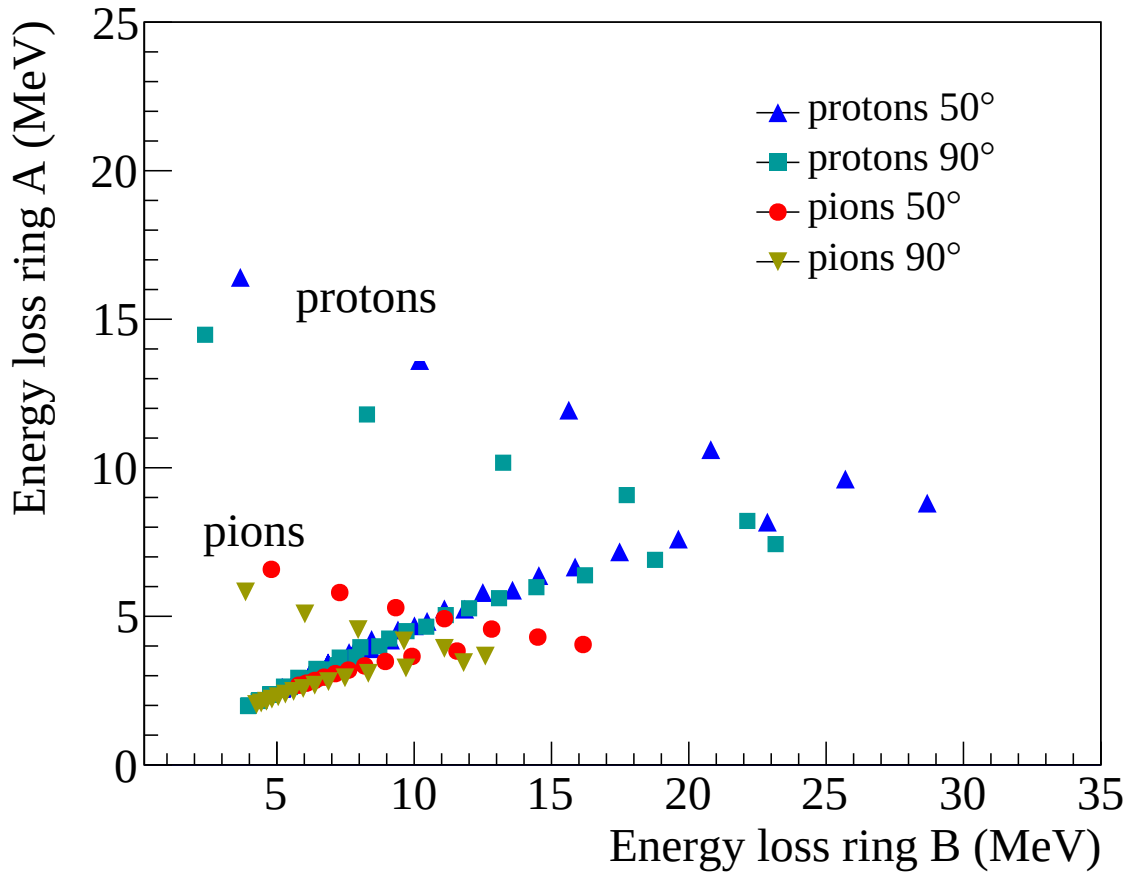


Figure 19: Calculated energy losses in Ring A and B for pions and protons emerging from the target at different polar angles (50° and 90°).

emerging from the target at different polar angles (50° and 90°) with a fixed momentum of 0.3 GeV/$c$. The energy loss in Ring A ranges from 2 MeV to 18 MeV while the energy loss in B ranges from 4 MeV to 30 MeV. The energy loss of a minimum ionising particle is 1 MeV in A and 2 MeV in B, see Section 4.1.2. In order to estimate the necessary dynamical range, the light attenuation in both scintillator and light-guide have to be taken into account as well. According to a simulation by the CEA Saclay group, the lowest signal to be detected in the inner ring has an energy of 0.28 MeV and 0.26 MeV for the outer ring. Tuning the PMT amplification for the maximum signal amplitude of 5 V, the lowest signal from the inner ring PMTs reaches about 75 mV. For the outer ring PMTs, the smallest signal is 35 mV.
Figure 21 depicts the electronic read-out scheme for the RPD. All 72 analogue signals are transported to the read-out area outside of the experimental zone, where they are connected to active 8-fold splitters [33]. The splitters were designed and build at the electronics workshop of KPH/Mainz. They have 5 outputs reproducing the original signal amplitude, plus one 70% output, one 20% output and one 10% output. The latter one is used for monitoring purposes. All splitter channels include a remotely controllable correction for DC voltages with a bias voltage. The channels are furthermore terminated by 50 Ohm resistors in both directions to prevent damage due to wrong connections. The input voltage respectively the amplitude is

limited with one Schottky diode per channel and can be varied from 0 to 5 V. During operation it was set to 4.2 V, which is the maximum amplitude expected after the signal attenuation in 50 m long cables. The signals are first inverted and then passively and symmetrically split to 6 channels. An amplification with a asymmetrically operated (-12 V,+3 V) operational amplifier follows, which allows for signal rise times of 1.8 ns. The signals are again inverted. One of the channels is afterwards passively split to 0.7:0.2:0.1, resulting in 8 outputs total. The output voltage is stable within 5 mV with no detectable noise ($< 1$ mV) at rates up to 55 MHz.
The 70% and 20% splitter outputs are put to analogue shapers, which stretch the signal in preparation for read-out with 12-bit sampling ADCs [101]. The two-fold ADC read-out allows for a better resolution for smaller signal amplitudes.
Two outputs of the splitters are connected to LeCroy 4413/4416 leading edge discriminators with two thresholds per PMT channel. The two thresholds are used for a time-walk correction. Time-walk is a feature of leading-edge discriminators, where the output/trigger time varies with the amplitude of the analogue signal. As illustrated in Figure 20, the thresholds sample the slope of the signals at the times $t_1$ and $t_2$. The slope then is used together with the ADC information to extrapolate to the signal start time $t_0$, which is determined with a better precision than $\delta t = t_2 - t_1$. The digital signal from the discriminators is converted from ECL to LVPECL and fed to F1 TDCs [68]. The TDCs have a resolution of 64 ps which dominates the read-out resolution.

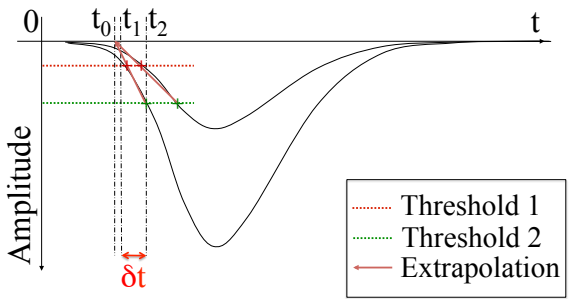


Figure 20: Determining signal slopes by sampling with two thresholds.

For the trigger system, two splitter outputs of each PMT channel are fed to leading edge discriminators (LeCroy 4413/4416) with two different thresholds, respectively, with the exception of the downstream signals of the inner ring. The latter are fed to constant fraction discriminators (CAEN V812), which are less affected to time-walk. The analogue signals of the outer ring are added by a summing unit built at KPH/-Mainz [33]. Operational amplifiers are used to add two input channels to one output signal. The symmetric supply voltage of $\pm 7.5$ V limits the input signal amplitude to 1.2 V for each channel. The output amplitude is then amplified by a factor of 5/3. For the maximum of two inputs of 1.2 V, the sum is 2.4 V, hence the maximum output amplitude after amplification is 4 V. Afterwards, the signal is actively split, keeping the same output amplitude on two output channels. The first output is used for the trigger logic, the second output is monitored with ADCs. Further details of the signal processing for the trigger are explained in Section 5.3.
The RPD is equipped with a laser pulser system which allows for online calibration. The system consists of a green semiconductor laser (Team Photonics NG 10120-110) with a wavelength of 532 nm [44]. The laser pulses have an energy of 2.2 $\mu$J with a duration of 0.53 ns and are repeated with a fixed frequency of 8.7 kHz. The laser beam impinges on a glass sphere working as a beam splitter to which 36 glass fibres are connected. They are directly coupled to the scintillator material at the

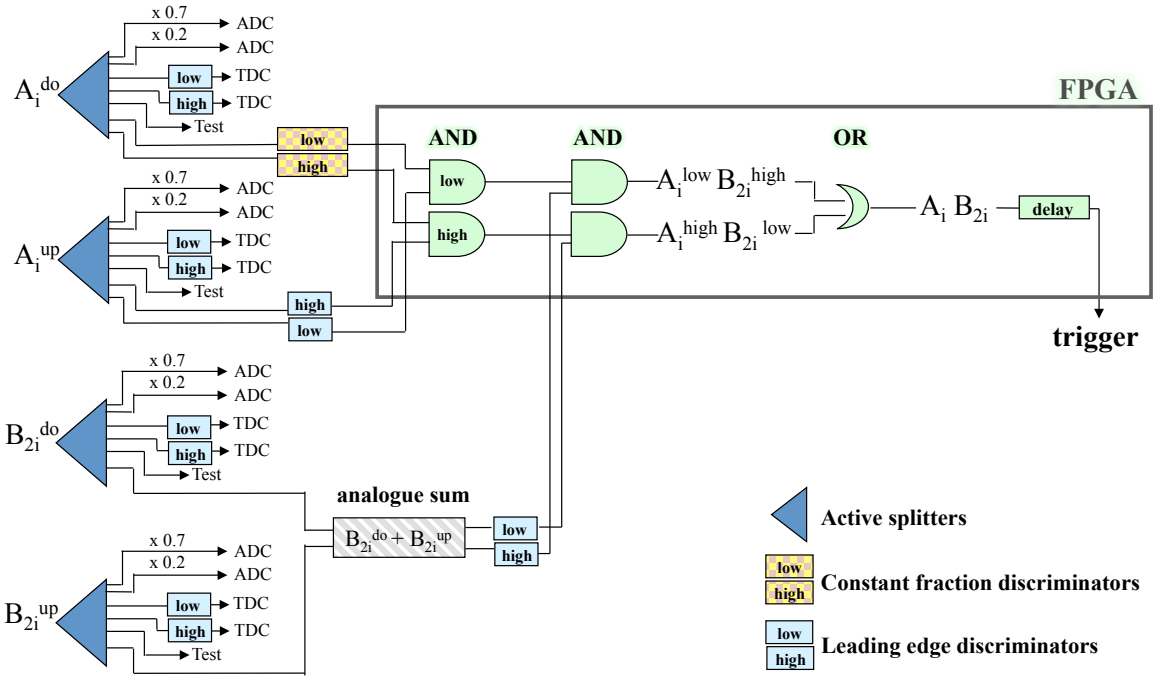


Figure 21: Electronic read-out scheme for the RPD. For details, see text.

middle of each inner and outer ring element. The laser can be remotely controlled from outside the experimental area and is only activated during checks outside of physics data taking.

## 4.3 COMMISIONING

The two RPD rings are mounted on a steel barrel, which can be rotated around the central axis. After assembly, the RPD with a fully equipped inner ring and a 25% equipped outer ring was tested in the muon beam halo. The barrel was positioned perpendicular to the beam. Five scintillation counters on each side were placed along the elements as external references. The measurement was used to check the basic properties, such as the achieved spatial resolution $\delta z$ and time resolution $\delta t$. The resolutions obtained were $\delta t = 200\,\text{ps} \pm 50\,\text{ps}$ and $\delta z = 2.7\,\text{cm} \pm 0.5\,\text{cm}$ for the inner ring elements and $\delta t = 400\,\text{ps} \pm 50\,\text{ps}$ and $\delta z = 5.0\,\text{cm} \pm 0.5\,\text{cm}$ for the outer ring elements, which is well within the specifications given in Section 4.1.1. The attenuation lengths of the elements of both rings were measured and found to be of the order of 60 cm.
Afterwards, the RPD was fully equipped and installed in the experimental area, but without the liquid hydrogen target placed inside, which was not yet available at the time. The RPD was aligned on the zero beam line. As a mimic for liquid hydrogen, a polyethylene cylinder was used for first calibrations. The cylinder matched

the 10% interaction length of the liquid hydrogen target. The amplifications of the PMTs were equalised by setting the high voltage on the voltage dividers such that the observed amplitudes of the calibration laser was the same for all channels. Afterwards, the signal amplitudes were checked with beam on the target. The PMT amplification was again adjusted for each channel in order to fully cover the allowed signal range. The smallest signals were found to be about 60 mV for the inner ring (75 mV expected) and 30 mV for the outer ring (35 mV expected). The discriminator thresholds were set accordingly with 30 mV as the low threshold and 60 mV as the high threshold.

## 4.4 RECONSTRUCTION AND CALIBRATION

The purpose of the offline reconstruction is the determination of the kinematical parameters of the recoil particle.

### 4.4.1 *Reference frame and alignment*

The reconstruction is performed in the RPD reference frame. The $z$ axis is the central axis of the target. The $y$ axis is the vertical axis in the upward direction and $x = z \times y$. The point of origin of the system is set at the upstream end of the target. The scintillator combination A0B0 corresponds to an azimuthal angle $\varphi = 0°$. The element numbering is done in the mathematical positive direction in the RPD reference frame.
The RPD was centred on the beam line during installation. Misalignments are within the precision of the installation survey and quoted to be below 1 mm in each direction. However, the RPD reference frame has an offset in $z$ with respect to the COMPASS frame and might be still slightly tilted. Therefore, the RPD reconstruction makes use the beam trajectory as a more precise $z$ axis, which is measured for each vertex with the beam telescope. As the beam enters the target with slightly different angles and positions, the $z$ axis is different in each event. The beam trajectory yields the $z$ axis for the analysis in this thesis, which in turn leads to better alignment of RPD and spectrometer.

### 4.4.2 *Preselection*

ADCs and TDCs provide information about the signal amplitudes and time hits from the discriminated PMT signals. The time-of-flight for a recoil particle from the inner to the outer ring is 2 ns for $\beta \approx 1$ particles at 90° and 10.5 ns for $\beta \approx 0.28$ particles at 50°. A time window for physical signals is selected to reduce the background from recoils which do not belong to the measured event. The window is determined by the maximum propagation time in the inner ring of 3 ns, the maximum propagation time in the outer ring of 7 ns, and the maximum difference between a hit at the entrance and at the exit of the target cell of 1.5 ns. Comparing the extreme cases, this results in a maximum difference of 20 ns which has to be taken as the minimum width for the time window. Compared to the trigger time,

the signals arrive about 970 ns later due to the signal propagation in the cables and electronics. This offset is subtracted. In addition, channel-by-channel timing variations occur due to different transit times in the PMTs and slightly different cable lengths. These variations are in the order of a few ns. For the preselection, the time window of 20 ns is hence doubled and all hits within 40 ns around the trigger time are selected.

### 4.4.3 *Track determination*

The schematic geometrical view of the RPD elements and the target is shown in Figure 18. The recoil particle hits a scintillator element $i$ at the time $t_i$ and the coordinate $z_i$ along the longitudinal direction. Each possible combination of an upstream and corresponding downstream PMT is used to determine $(z_i, t_i)$:

$$z_i = \frac{c^i_{eff}}{2}(t^i_{up} - t^i_{down} - t^i_{cor,up} - t^i_{cor,down}) + \frac{L_i}{2} + z^i_{offset,up} + z^i_{offset,down} \tag{48}$$

$$t_i = t^i_{up} + t^i_{down} - t^i_{cor,up} - t^i_{cor,down} + \frac{L_i/2 + z^i_{offset,up} + z^i_{offset,down}}{c^i_{eff}} \tag{49}$$

where $t^i_{up}$ is the hit time of the upstream PMT and $t^i_{down}$ is the hit time of the downstream PMT. The following offsets and constant have to be evaluated.

- $c^i_{eff}$: The effective propagation speed of light $c^i_{eff}$ in element $i$ is determined by the correlation of hit times and positions in the scintillator elements. The slope is determined by a linear fit to the $z - t$ relation. Due to the low resolution in $z$, the method is refined with an analysis of elastic $pp \to pp$ and $p\pi \to p\pi$ scattering. It is used to predict the $z$ position of the recoil hits in the RPD elements with the help of the scattered particle which is more precise than the measurement with the scintillator.

- $t^i_{cor}$: As described in Section 4.2, the measurement of the signal slope is used for the time-walk corrections $t^i_{cor,up}$ and $t^i_{cor,down}$.

- $z^i_{offset}$: The two offsets $z^i_{offset,up}$ and $z^i_{offset,down}$ are used to compensate offsets in $z$ for different elements in the RPD coordinate system. The obtained $z$ distributions are shifted such that they start at $z = 0$. This is done for both upstream and downstream signals and absorbs time differences due to different offsets because of different cable lengths and PMT transit times.

- $L_i/2$: The centres of the outer and inner ring elements are shifted with respect to each other for matching the geometrical acceptance of 50° to 90°, as seen in Figure 18. Thus, half the length $L_i$ of the read-out element is added to respect this geometry.

Hits with a reconstructed position outside of the scintillator fiducial dimensions with a generous safety margin of 20 cm are discarded, as well as pile-up hits for

which the outer ring was hit before the inner ring. If one PMT has more than 3 hits in one event, they are discarded as noise.
Reconstructed hits for the inner ring elements are associated to hits in the three corresponding outer ring elements. A straight line (track) for each hit combination is then extrapolated backwards to the target. The vertex reconstructed with the spectrometer and beam telescope which is closest to the track is used as the track origin. Figure 22 shows the difference $\Delta z = z_{\mathrm{RPD}} - z_{\mathrm{spectrometer}}$ versus $z_{\mathrm{spectrometer}}$ for the A0 B0 hit combination in elastic $pp$ scattering. The difference $\Delta z$ is calibrated in order to be centred around 0. The green bars depict the target volume. The width of the distribution along the ordinate is the spatial resolution. It is obtained with several Gauss fits to $\Delta z$ along the abscissa. The mean spatial resolution of an inner ring/outer ring combination is the average value of the determined widths, integrated over the abscissa. Values are typically between 3.5 cm and 4 cm.

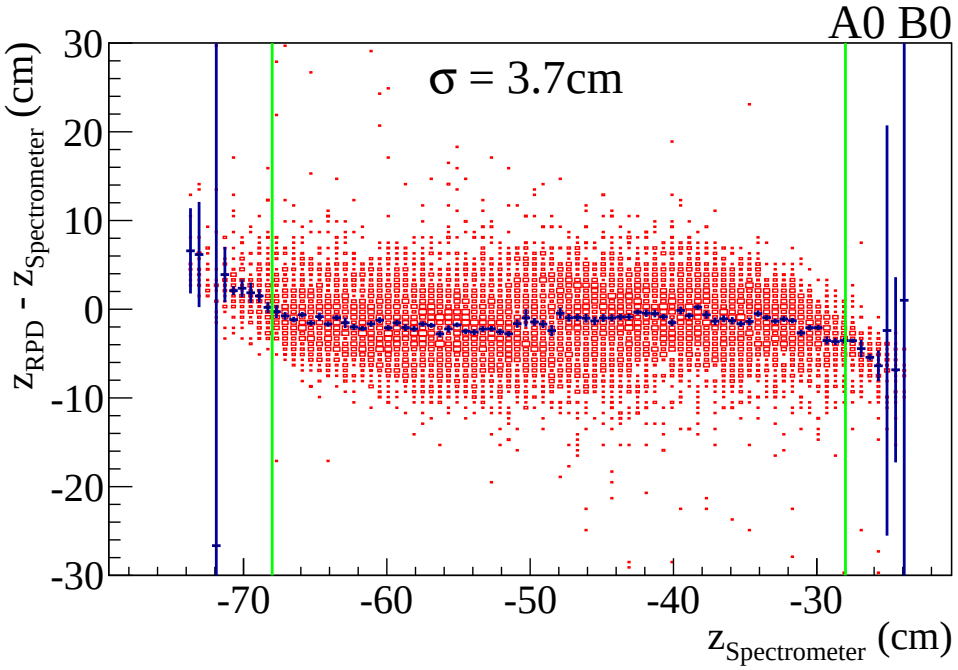


Figure 22: Difference of the reconstructed vertex $z$ position with the one obtained by the spectrometer versus the spectrometer $z$ position for the A0 B0 hit combination in elastic $pp$ scattering. The red boxed distribution is the original one, the blue crosses are the results of Gaussian fits along the ordinate.The green lines delimit the target volume. The mean spatial resolution $\sigma$ is the average value of the determined widths, integrated over the abscissa.

Combinations of all vertices with all hit combinations are stored as well for cases in which a physics analysis needs a dedicated vertex–track assignment.
In the next step, the track length between the inner and the outer ring is determined by $d = \sqrt{(z_i^B - z_i^A)^2 + \Delta_{AB}^2}$ with $\Delta_{AB} = 65\,\mathrm{cm}$ being the radial distance

between inner and outer ring. With the time-of-flight $t = t_i^B - t_i^A$, the recoil velocity $\beta$ consequently is

$$\beta = \frac{d}{ct} = \frac{\sqrt{(z_i^B - z_i^A)^2 + \Delta_{AB}^2}}{c(t_i^B - t_i^A)} \tag{50}$$

From Equation 43, the recoil momentum can be determined if some mass $m$ for the recoil particle is assumed

$$p = \frac{m}{\sqrt{1/\beta^2 - 1}} = \frac{m\beta}{1 - \beta^2} \tag{51}$$

Here, the recoil particle is assumed to be a proton due to the observations made in Section 4.4.4.

In order to determine the recoil momentum at the interaction vertex, the momentum has to be corrected for the rather large energy losses of slow recoil particles in the target volume and in the inner ring. The energy losses for protons with different momenta and the different crossed materials are tabulated and added to the reconstructed momentum respecting the proton path. For the lowest detectable momenta $p \approx 0.3\,\mathrm{GeV}/c$, the amount of target material crossed is crucial. Therefore, an extrapolation of the track to the interaction vertex has to take into account any transverse displacements $(x, y)$ from the beam line axis. The azimuthal resolution of the RPD is not enough to resolve $(x, y)$ of the vertex. Therefore, the coordinates of the nearest vertex that was reconstructed with the spectrometer are used.

The position measurement is also used to determine the polar angle $\theta$, with $\cos\theta = (z_B^i - z_A^i)/d$. The azimuthal angle $\varphi$ is determined from the azimuthal position of the hit element. Initially, $\varphi$ is determined with the outer ring element number $m$: $\varphi' = \frac{15}{180}\pi\, m$. Afterwards, $\varphi$ is corrected with the inner ring. An inner ring element hit $i$ directly facing the outer ring element $m = 2i$ yields no correction. A combination of the inner ring element $i$ with outer ring element $m = 2i \pm 1$ yields a correction of $\varphi_{cor} = \pm\frac{1}{4}\frac{15}{180}\pi$, so the azimuthal angle is determined with $\varphi = \frac{15}{180}\pi(m + \frac{1}{4}(m - 2i))$. This leads to two different $\varphi$ resolutions depending on the inner and outer ring combination, $\sigma_{\varphi 1} = \frac{15^\circ}{\sqrt{12}} = 4.3^\circ$ and of $\sigma_{\varphi 2} = \frac{15^\circ}{\sqrt{12}} = 2.2^\circ$. Due to the non point-like shape of the beam impinging on the target, the hit combinations are not uniformly distributed. Therefore, the individual contributions of $\sigma_{\varphi 1}$ and $\sigma_{\varphi 2}$ are not easily calculable and hence determined

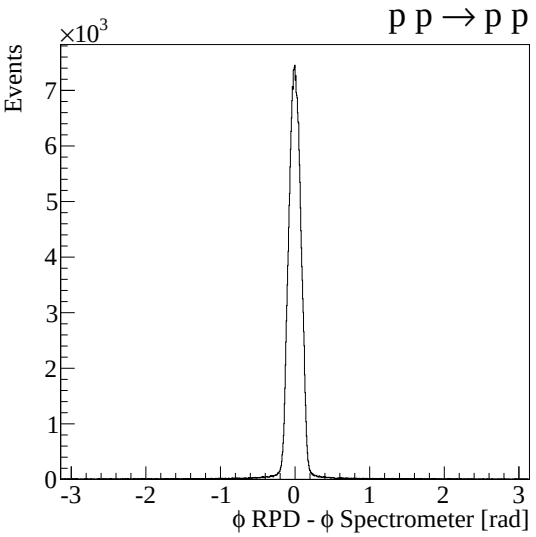


Figure 23: Difference of the azimuthal angle $\varphi$ measured with the RPD and the spectrometer for elastic $pp$ scattering.

by a measurement. Figure 23 shows the difference of $\varphi$ measured with the RPD to the one measured with the spectrometer for elastic $pp$ scattering. The measured angular resolution is $\sigma_\varphi = 5^\circ$ which is close to the expected resolutions.
The angular information is combined with the measured momentum and the full track information is available. After the above described reconstruction, a set of tracks matching to the found vertices is available for event selection and physics analysis.

### 4.4.4 *Energy loss*

The energy losses in the inner and outer ring are available from the SADC measurement. The calibration is done using the known kink seen in the $\Delta E_A$ versus $\Delta E_B$ distribution (see Fig, 19) which marks the transition region from a fully stopped proton loosing all energy to a proton barely passing an element. The measured values after calibration in Figure 24 show a good agreement to the estimated values in Figure 19. Without any assumptions for the energy loss measurement, only protons are seen in the measurement, so the pion background seems negligible.

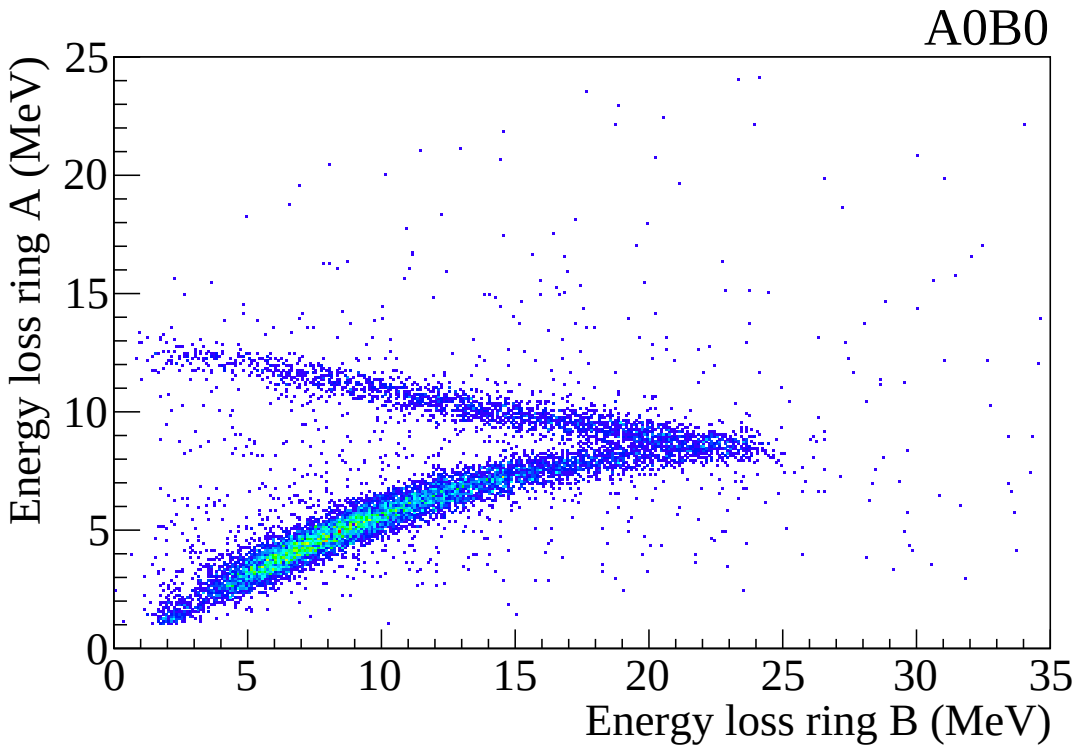


Figure 24: Energy loss in ring A versus energy loss in ring B for the A0B0 combination in elastic $pp$ scattering. Only protons are seen without a background from pions or minimum ionising particles.

## 4.5 PERFORMANCE

The efficiency is determined with elastic $pp$ scattering. Events recorded with the beam trigger (see Section 5.1) are selected, which have one incoming and one outgoing positively charged track and one reconstructed vertex to avoid ambiguities. The track momentum of the outgoing track must be within a window of 6.3 GeV/$c$ around the nominal beam momentum of 190 GeV/$c$. The window corresponds to $\pm 2$ times the beam momentum spread. Furthermore, the beam particle must be identified by the CEDARs. The recoil proton kinematics is calculated from the scattered forward proton. In order to use momentum conservation, the beam energy must be known. As there is no measurement of the beam energy but only of the beam direction, the energy is calculated with mass assumptions as outlined in Appendix C of [117] and Appendix B of [128], here for the special case of a proton beam:

$$E_{beam} = \left(1 - \frac{m_p}{E_{scattered}}\right) / \left(1 - \frac{E_{scattered}}{m_p} + \frac{|\vec{p}_{scattered}|cos\theta}{m_p}\right) + \left(\frac{m_p |\vec{p}_{scattered}|cos\theta}{2E^2_{scattered}}\right) / \left(1 - \frac{m_p}{E_{scattered}}\right) \tag{52}$$

where $m_p$ denotes the proton mass and $\theta$ denotes the scattering angle with respect to the beam trajectory. The scattered particle is assumed to be a proton. Predictions for recoil protons are selected, which are in the geometrical acceptance of the RPD ($50° < \theta < 90°$). Initially, there is no cut on the recoil momentum to be able to measure the momentum threshold of the RPD. The efficiency $\epsilon$ with respect to a kinematical variable is calculated by the ratio of found hits in an RPD element to the number of expected hits from elastic scattering. The efficiency is determined with respect to the transverse recoil momentum $p_T$ and the vertex $z$ position along the target.

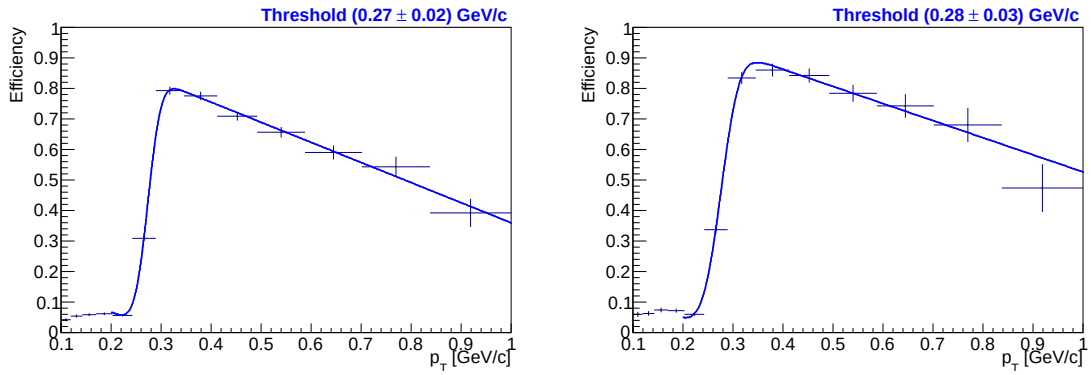


Figure 25: Efficiency with respect to the transverse recoil momentum $p_T$ determined with elastic $pp$ scattering. Left: Efficiency for A0. Right: Efficiency for B0.

Figure 25 shows the efficiency for the representative elements A0 and B0 with respect to the transverse momentum $p_T$. The distribution is flat and below 5% for

low $p_T$. This remaining efficiency originates from noise or pile-up protons, *i.e.* additional protons in the event coming from another interaction vertex. The efficiency starts to rise at the expected threshold at which protons start to reach the outer ring and reaches the maximum value of about 82% for A and 87% for B. The momentum threshold is determined by fitting an error function folded with a first degree polynomial to the efficiency distribution. The threshold $p_T = (0.27 \pm 0.01)\,\mathrm{GeV}/c$ is uniform for all elements and agrees with the expected value. Going to higher values of $p_T$, the time-of-flight gets smaller and thus the measurement is not always precise enough to reconstruct $\beta$ reliably. Due to the natural limitation $\beta < 1$, this results in a dropping efficiency.
The final distributions for $\epsilon(z)$ are determined with an additional cut on the transverse momentum $p_T > 0.27\,\mathrm{GeV}/c$ to assure that a potential recoil proton candidate has not lost too much energy in the traversed material and is able to reach the outer ring. Figure 26 shows the efficiency for the representative elements A0 and B0 with respect to the vertex position $z$. The overall efficiency is determined with a straight line fit to the distribution in the range of -68 cm $< z <$ -28 cm (target volume). The efficiencies vary from 85% to 90% for all elements. The determined efficiencies are tabulated and used as an input for the detector response in the Monte-Carlo simulation of the RPD.

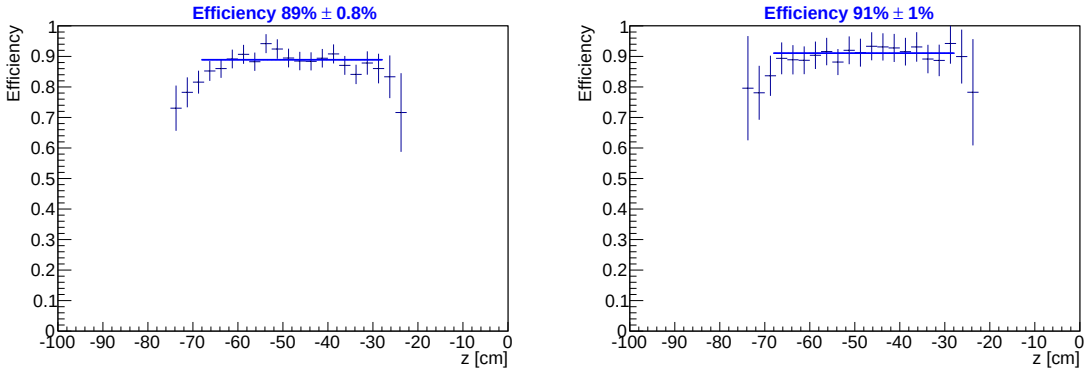


Figure 26: Efficiency with respect to the vertex $z$ position determined with elastic $pp$ scattering. Left: Efficiency for A0. Right: Efficiency for B0.

The correlation of the measured momentum transfer $|t|$ between forward tracks and the RPD for elastic events is presented in the upper panel of Figure 27. It shows a clean correlation up to momentum transfers of $|t| = 0.4\,(\mathrm{GeV}/c)^2$. The correlation for higher proton momenta is decreased due to the smaller momentum resolution, which is shown in the lower panel of Figure 27. The momentum resolution of the RPD is 5% for low momenta and becomes worse for higher momenta due to the small time-of-flights.

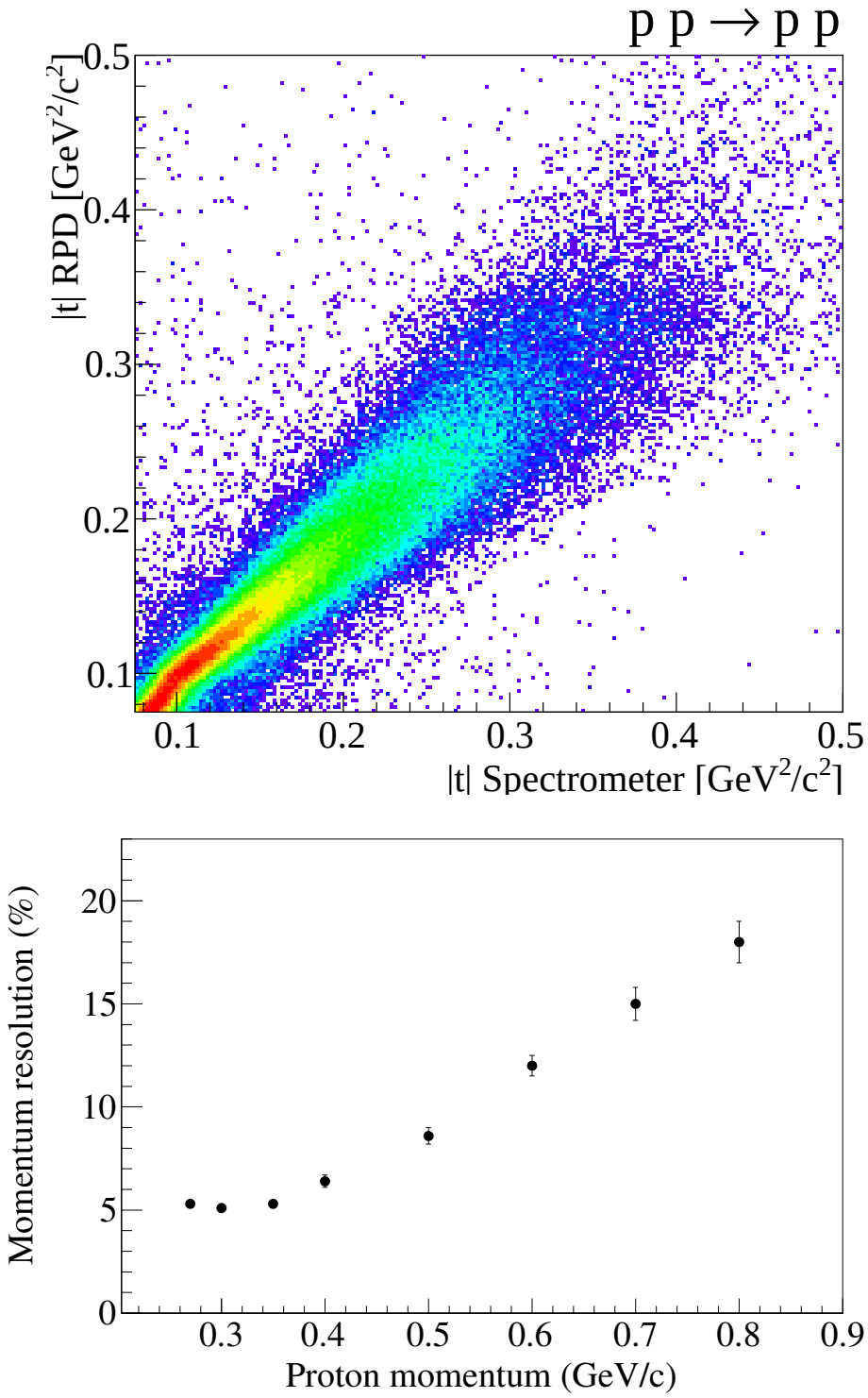


Figure 27: Upper panel: Correlation of the momentum transfer $|t|$ measured with the RPD and measured with the spectrometer. Lower panel: Momentum resolution of the RPD with respect to the recoil momentum.

# 5 TRIGGER

The trigger system for hadron beams is designed to select exclusive event candidates. A fast and precise response within 500 ns to 900 ns from the trigger detectors including signal processing is needed to provide the time reference for the readout of all detectors. A physics trigger consists of three sub-triggers: beam-defining elements to select beam particles crossing the target, veto detectors to reject events with tracks originating outside of the target or outside of the spectrometer acceptance, and specific detector systems to account for the different physics cases. The latter are the proton trigger (5.3) that is used for measurements of diffractive scattering and central production processes with momentum transfers $|t| > 0.07\,\mathrm{GeV}^2/c^2$, the multiplicity trigger that completes the coverage towards lower values of $|t|$ for reactions with higher charged tracks multiplicities (5.4) and the calorimeter trigger [85] that is used for Primakoff ($\pi N \to \pi N \gamma$) data taking. Figure 28 shows schematically the location of the main trigger elements in the spectrometer. In addition to the main physics triggers, a set of auxiliary triggers is available for alignment, monitoring and calibration tasks.
The trigger used for the analysis in the following chapters is the diffractive trigger DT0 which is based on the proton trigger.

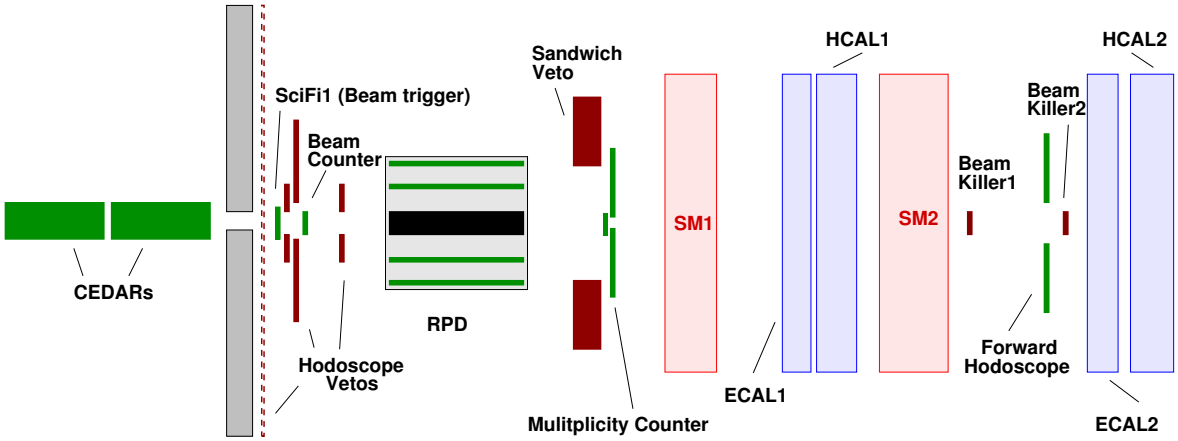


Figure 28: Arrangement of trigger elements in the spectrometer (schematic side view, not to scale).

## 5.1 BEAM TRIGGER

The beam trigger selects incoming beam particles and is used to define the time reference of an event. In addition, it reduces the geometric acceptance of the beam in the transverse plane to match the target geometry.

### 5.1.1 *Set-up*

The beam trigger uses a scintillating fibre station (SciFi1) and a beam counter as trigger detectors. SciFi1 is located 7 m upstream of the liquid hydrogen target. It consists of two planes with 6 x 16 readout channels in each projection. There are 6 multi-anode photomultiplier tubes per plane, which read out 16 fibres channels each. In addition, the multipliers are read out at the last dynode stage, thus giving 6 analogue sums for the X and Y plane of the detector, respectively.
The beam counter is located 50 cm downstream of SciFi1 and consists of a round scintillator disc as depicted in the right panel of Figure 30 that is centred at the beam. The disc has the same diameter as the target (3.2 cm) and 4 mm thickness. The scintillator material used is BC404 [123]. Light from the disc is transported with an air light guide to the photomultiplier tube read-out. The light guide is a thin, black PVC tube covered in the inside with aluminised Mylar foil with an internal reflection of better than 92 % [33]. The 35 cm long tube is connected to a single EMI 9813KB photomultiplier tube. It is equipped with a voltage divider for high rates which stands beam rates of up to 10 MHz. The beam trigger is given by the coincidence of the time-leading discriminated beam counter signal and the logical OR of the 6 analogue sums of the SciFi1 X plane.

### 5.1.2 *Performance*

The efficiency is determined by comparing hits in the beam counter with coinciding hits in the SciFi1X plane to coincidencing hits in both SciFi1X and Y planes. Ambiguous hits outside a time window of 1 ns for the coincidence are rejected from the analysis. The efficiency is uniformly distributed on the disc's surface at 99% and is depicted in the left panel of Figure 29. The distribution features some statistical fluctuations due to the limited data sample that was used for the analysis.
For monitoring purposes, the efficiency is checked every week during data taking. A welcome side-effect of this method is the check of alignment of the beam counter with respect to SciFi1 which can be monitored quasi-online. SciFi1 is aligned with the beam line and thus with the centre of the target. For the determination of the beam counter alignment, a circle with the beam counter diameter is fit to the distribution in order to retrieve the coordinates of the centre.
The time resolution of the beam trigger with respect to the SciFi1 Y plane is measured to be 450 ps $\pm$ 50 ps (see Figure 29). The SciFi1 time resolution is measured [2] to be 400 ns, hence the unfolded beam trigger resolution is in the order of 200 ns.
The beam trigger is always used as the time reference of a physics trigger system.

## 5.2 VETO DETECTORS

The veto system consists of two scintillation counters ("beam killers"), a sandwich veto detector and a hodoscope veto system. It inhibits false physics triggers.

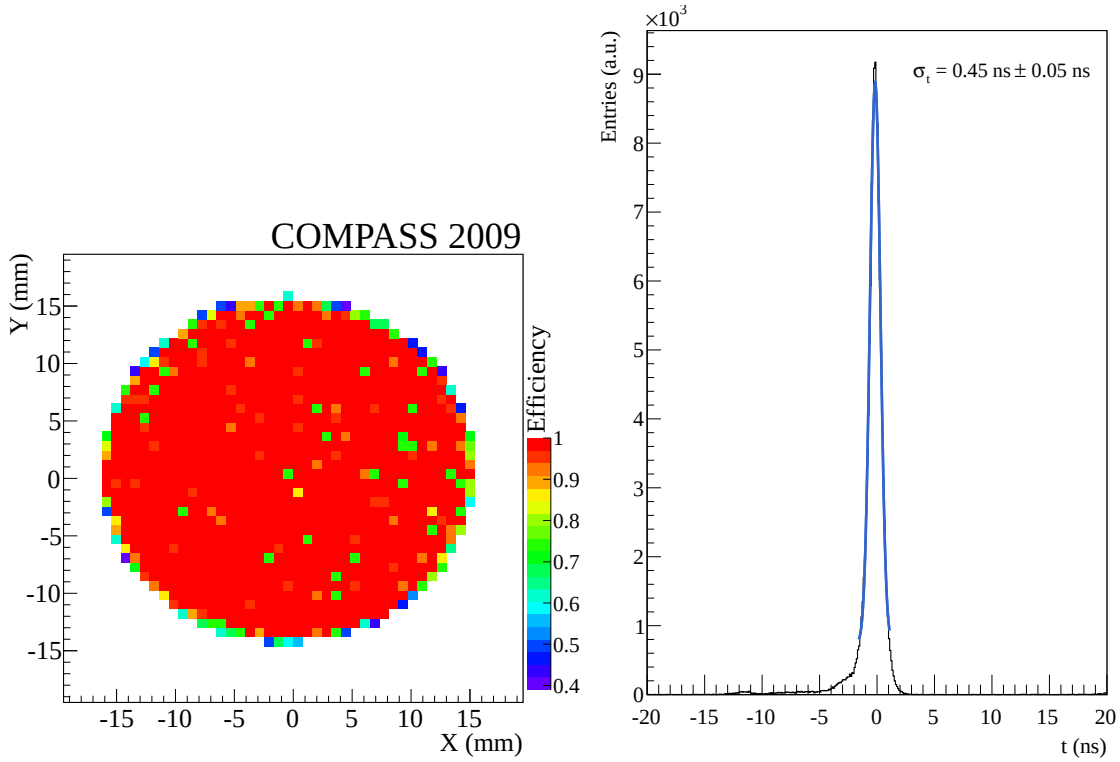


Figure 29: Left: Beam counter efficiency distribution in transverse coordinates in the COMPASS reference system. Right: Time resolution of the beam trigger, the blue line is the result of a Gaussian fit.

### 5.2.1 *Beam-killers*

Two scintillating counters with a similar design as the beam counter are positioned along the beam axis of the spectrometer at $z_1$ =+15 m and $z_2$ =+33 m. Photographs in Figure 30 show the two beam killer in the experimental area. The only difference of the beam killer set-up to the beam counter is the larger 35 mm diameter of the scintillator disks and the increased thickness of 5 mm. The purpose of the beam killers is to inhibit a trigger signal coming from non-interacting (*i.e.* non-scattered) beam. Using the beam-killers introduces an angular cut-off of $\theta = 0.97$ mrad with respect to the nominal beam axis. The diffractive trigger rate is reduced by a factor of 2.

### 5.2.2 *Sandwich Veto Detector*

A sandwich veto detector [118] is used to detect charged and neutral particles which are outside of the angular acceptance of the spectrometer. Reactions, where such particles are dominantly produced, are either inelastic, non-diffractive or reactions where target protons are diffractively exited.
The sandwich detector is segmented in 10 elements which form a central hole matching the acceptance of the spectrometer. Each element consists of a 2 m × 2 m stack of five layers of steel-covered lead plates and scintillators with a total thickness corresponding to 5.1 radiation lengths. The lead layers are 5 mm plates with

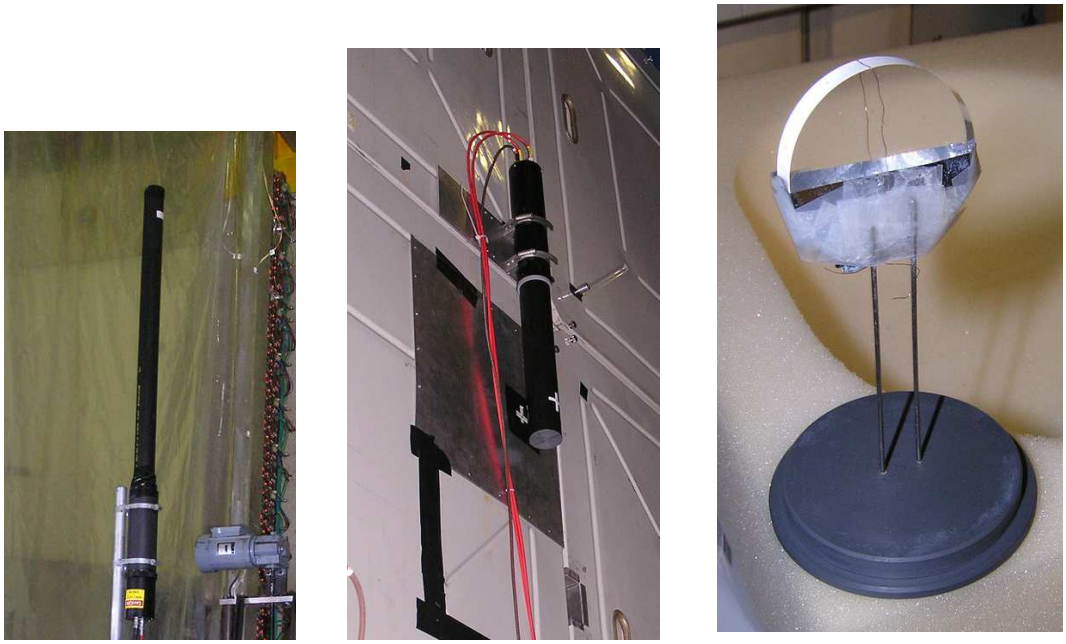

Figure 30: Beam killer detectors and beam counter. Left: BK1 at $z_1$ =+15 m. Middle: BK2 at $z_2$ =+33 m, attached to the electromagnetic calorimeter ECAL2. Right: Scintillator disc of the beam counter with holding structure. The disk is surrounded on one half with aluminised mylar to reflect the scintillator light in direction of the photomultiplier tube.

a 1 mm steel wrapping for stability reasons. Each scintillator layer is formed by a pair of 80 $\times$ 20cm$^2$ scintillators lying side-by-side. The first three layers of scintillators have a thickness of 10 mm while the other two layers are 5 mm thick. Light emitted from the scintillator is collected using wavelength shifting fibres connected to Phillips XP2020 PMTs with passive voltage dividers.
The efficiency for detecting minimum ionising particles is determined from the reconstruction of events without any veto condition in the trigger system and is found to be larger than $>$ 98%. The veto efficiency for different particle species is determined with the help of MC simulations. It is larger than 95 % for pions $>$ 50 MeV and larger than 90 % (80 %) for photons $>$ 100 MeV ($>$ 50 MeV). Exclusive events triggered by the diffractive trigger are enriched by a factor of 3.5.

### 5.2.3 *Hodoscope Veto System*

The hodoscope veto system is the same as the one used for the muon programme. It consists of three parts: The beam line veto hodoscope system is installed at $z = -20$ m, the Veto1 system is located at $z = -7.5$ m and the Veto2 counter at $z = -1.5$ m with respect to the target. A detailed description can be found in [2, 32]. The veto has the task to inhibit the trigger from beam particles which do not cross the

target. These particles are in particular harmful for the detection of recoil protons as they create large signals in the RPD's scintillator strips which are aligned parallel to the beam axis. Without the hodoscope veto system, large multiplicities in the proton trigger logic are introduced. The suppression factor on the proton trigger rate is 10, on the diffractive trigger it is 2.

### 5.2.4 *Veto Dead Time*

The veto system introduces a dead time for data taking due to fake coincidences. The overall dead time is measured by comparing the rate of the diffractive trigger with an off-time veto signal to the diffractive trigger rate without any veto condition. The off-time signal is the veto signal delayed by 64 ns, which corresponds to coincidental veto hits well outside the normal timing. The measurement is performed after all important changes in the trigger system and for the start of each physics programme, *e.g.* for data taking with negative and positive beams on liquid hydrogen, for solid targets, Primakoff data taking etc. For the typical beam intensity, the dead time is 13%-16% for both positive and negative beams. Higher veto rates because of back-scattering from solid targets are not observed. For Primakoff data taking, the dead time is reduced to 8%-10% due to the lower beam intensity.

## 5.3 PROTON TRIGGER

The proton trigger selects events with recoiling particles originating from the target material. It uses the RPD signals for two purposes: (1) target pointing and (2) discrimination of protons from pions and delta-electrons.

### 5.3.1 *Principle and Implementation*

Target pointing is ensured by allowing only combinations where hits in one scintillator of the inner ring are followed by a signal in one of the three corresponding outer ring scintillators, see Figure 31, left.
The discrimination of protons and pions is carried out by triggering on the energy loss in each ring of the RPD. The energy loss is linearly correlated to the signal amplitude of the PMTs. Therefore, two discriminator thresholds are used to constrain the correlation of energy losses between the inner and outer ring, as shown on the right panel of Figure 31 that shows the expected energy loss in both rings. The shaded area is a result of the combination of a low threshold for the inner ring and a high threshold for the outer ring and *vice versa*. This area includes pions and electrons and is excluded from triggering.

*Signal processing*

The trigger signal processing starts with the analogue signal of each RPD PMT. The signals are split as described in Section 4.2. Subsequently, two of the eight output signals of the splitter modules for each PMT channel are discriminated by LeCroy 4416 and 4413 leading edge discriminators, except the ones for the inner

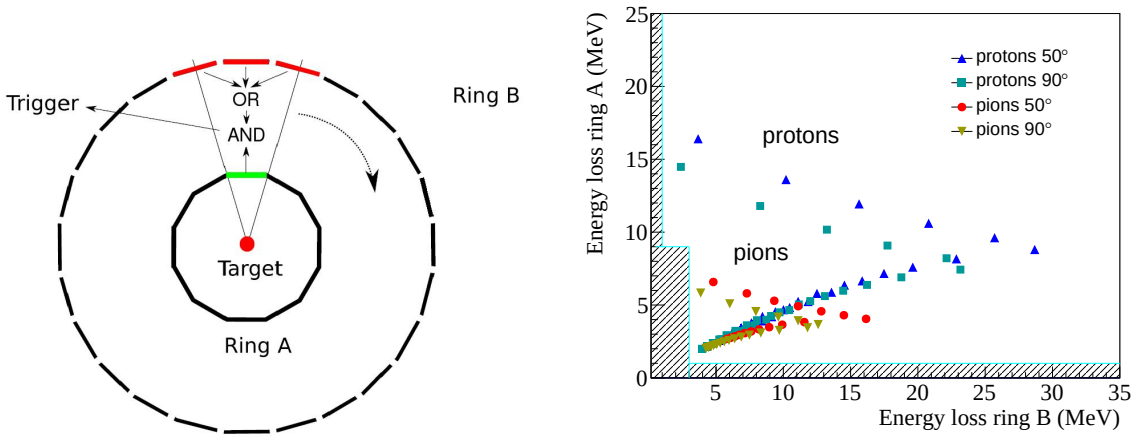


Figure 31: Left: Allowed combinations for target pointing in the RPD part of the proton trigger. Right: Calculated energy loss of the incident recoil proton in the two layers of the RPD. The region rejected by the trigger logic is shaded.

ring downstream PMTs. The latter require a better precision, independent of the signal amplitude. Consequently, constant fraction discriminators of the type CAEN V812 are used.
The coincidence of low thresholds signals for upstream and downstream PMTs of the inner (resp. outer) ring is written $A_i^{Low}$ (resp. $B_j^{Low}$). The coincidence of the two high thresholds signals receives the subscript "High". Hence, the trigger logic function for recoil protons has the expression:

$$RPD = \bigvee_{i=1}^{12} A_{i,Down}^{Low} \wedge \bigvee_{j=2i-1}^{2i+1} \left( A_i^{Low} B_j^{High} \vee A_i^{High} B_j^{Low} \right)$$

The function is implemented in a single CAEN V1495 FPGA module which is fed by the logic signals from the output of the aforementioned discriminator modules. At each 40 MHz clock signal, the system checks for the presence of a hit in any of the inner ring downstream PMTs and then opens a 50 ns coincidence window for the three allowed geometrical combinations. The resulting trigger signal is affected by a large variations due to the time-of-flight variations. Therefore, it is again put in coincidence with the corresponding downstream signal of the inner ring ("re-timing") to make use of the intrinsic time resolution of about 180 ps.

*Tuning*

The discriminator thresholds are chosen after performing online calibration runs for the RPD with the unbiased beam trigger. During the online calibration, the signal amplitudes of outer and inner ring PMTs are compared for a set of different discriminator thresholds. The results are checked against the theoretical expectations shown in Figure 31, right panel, and possible contributions due to detector noise. The latter is measured to be typically 1-2 mV and hence negligible. The final set of thresholds is found to be the same for all allowed combinations of inner and outer ring. It is 30 mV for the low and 60 mV for the high threshold.

*High Level Trigger Functions and Forward Hodoscope*

The proton trigger system features the possibility to suppress elastic scattering events. Elastic events feature a back to back correlation of the scattered particle with the recoiling one. Therefore, by requiring an azimuthal anti-correlation of the recoiling particle with the fast scattered particle, a condition for elastic events can be identified and a veto condition for such events can be applied. The recoil particle is identified by the proton trigger whereas the forward particle requires an additional detector, the so-called forward hodoscope which is explained in Appendix C. The anti-correlation for RPD and forward hodoscope is applied in the proton trigger FPGA board. Two trigger signal outputs are available: one with and one without the elastic veto condition. The overall proton trigger rate is reduced by 25 % when applying the elastic veto. In the final data taking, the diffractive trigger was set-up without the elastic veto due to the low reduction effect.

### 5.3.2 *Diffractive Trigger*

The diffractive trigger DT0 is introduced to enrich exclusive events from diffractive dissociation or central production. Both processes have a recoiling proton in the final state. Consequently, the proton trigger is used in the diffractive trigger.

*Set-up*

The diffractive trigger is the combination of beam trigger, veto system and proton trigger. The motivation for this set-up stems from the large number of background events accepted by the proton trigger due to secondary particles from the beam line or the material surrounding the target. Such particles traverse through large parts of the scintillator elements of both inner and outer rings, respectively. They are the origin of large energy losses, which can be mistaken for proton candidates. Due to the large rate of secondary particles, a fake coincidence of two uncorrelated secondary particles or a fake coincidence of a secondary with a low energy proton stopped in the inner ring may occur. The beam trigger confines beam particles effectively to the transverse target dimensions. The veto system covers the front surface of the RPD and thus inhibits events from particles crossing the RPD rings along the scintillator elements. Therefore, both systems reduce events from the proton trigger caused by secondary particles. The proton trigger rate is reduced by a factor of 10 if beam trigger and vetos are applied.

*Performance*

The efficiency for the diffractive trigger is studied with elastic pp scattering events, similar to the method described in Section 4.5. Elastic pp events are selected by requiring a single, positively charged track emerging from a single primary vertex within the target material. The selected events must have been triggered by either one of the beam triggers or a random trigger to ensure an unbiased sample. In addition, the CEDAR detectors identify the beam particle as a proton by requirement of multiplicities $> 3$ in both detectors. Another important condition is the

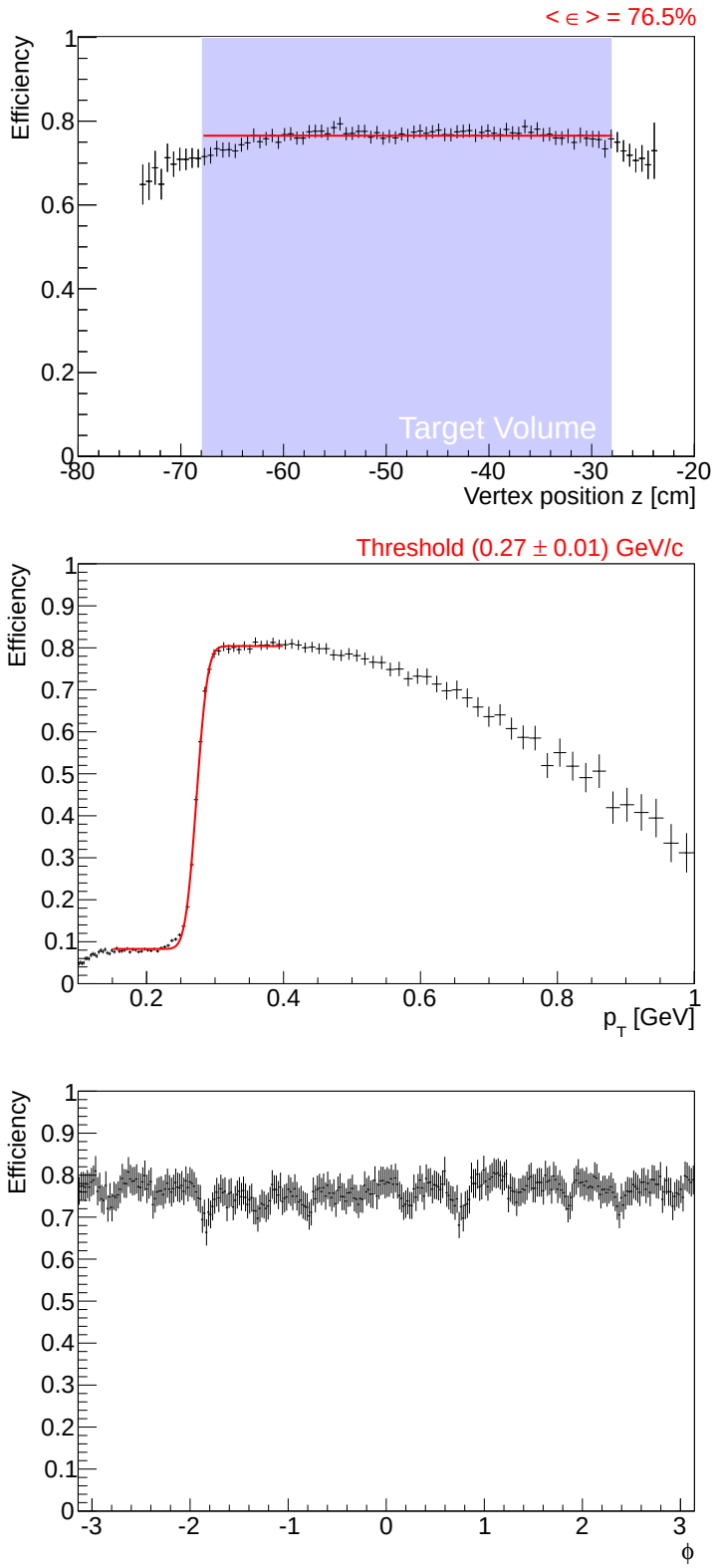


Figure 32: Upper left: DT0 efficiency as a function of the vertex location along the beam axis. Upper right: Efficiency as a function of the recoil particle's transverse momentum $p_T$. Lower panel: Efficiency as a function of the azimuthal angle $\phi$. Local variations of the efficiency are due to the gaps between the RPD scintillator elements.

energy of the scattered proton. Only tracks with energies of the beam (191 GeV) within a $\pm 2\sigma = 6.3$ GeV window are chosen to guarantee exclusive elastic events. The recoil proton track is predicted from the scattered proton kinematics, see Section 4.5 for details. The predicted track is required to be within the acceptance of the RPD, which means a polar angle $55^\circ < \theta < 90^\circ$ and a transverse momentum $p_T > 0.27\,\mathrm{GeV}/c$. Gaps between RPD scintillator elements are not treated and observed as local inefficiencies. The efficiency is determined as the ratio of events which have a diffractive trigger flag in addition to the aforementioned triggers fulfilling the criteria explained above and the expected triggers. The efficiency is presented as a function of the vertex position along the beam in Figure 32, upper left panel. It is uniformly 76.5 % ± 0.2 % in the target volume (shaded area in the figure) and drops slightly at the target borders. The trigger threshold is determined as a function of $p_T$ of the recoil particle with a fit of an error function to the data. For this study, the $p_T > 0.27\,\mathrm{GeV}/c$ cut is released. The results are shown in Figure 32, upper right panel. The measured threshold of $(0.27 \pm 0.1)\,\mathrm{GeV}/c$ reproduces the theoretical value for recoil particles which are able to reach the outer ring of the RPD. The trigger reaches full efficiency at $p_T = 0.3\,\mathrm{GeV}/c$. Above, the efficiency drops mainly due to the RPD efficiency behaviour explained in Section 4.5. It should be noted that most of the relevant events are in the low $p_T$ region with high trigger efficiency because of the steeply falling cross section with increasing $p_T$. The efficiency as a function of the azimuthal angle $\phi$ is relatively uniform (see Figure 32, lower panel), but shows local variations of the efficiency in the order of 5-10% due to the gaps between the RPD scintillator elements.
The trigger purity is a measure of the percentage of useful events in all triggered events. It is approximated by the percentage of interaction vertices with one or more outgoing tracks in the target material for DT0 events. The purity is 91 %, for the best alignment achieved so far and hence a lower limit.

## 5.4 MULTIPLICITY TRIGGER

A multiplicity trigger was built in order to complete the full range of momentum transfers $-t$ for final states with charged particles towards events with $|t| < 0.07\,(\mathrm{GeV}/c)^2$ which are outside the acceptance of the proton trigger. The multiplicity counter [133] as depicted in Fig. 33 consists of 12 trapezoidal-shaped scintillator slabs read out by EMI 9813KB photomultipliers with active voltage dividers, similarly to those of the RPD. The detector has a central hole of 3.2 cm diameter. It covers the 180 mrad charged-particle acceptance of the spectrometer at $z = +1.7$ m, which projects to a disk surface with a radius of 31 cm. It was upgraded in 2009 with a central scintillator disk covering the hole and read out by two photomultipliers. In order to minimise the material in the active area, the photomultipliers for the inner disk are connected through an 83 cm long air light guide made of a tube skeleton of 15 $\mu$m aluminised mylar inside a 150 $\mu$m thick plastic coating. All scintillators have a thickness of 3 mm, corresponding to 0.71 % radiation length.

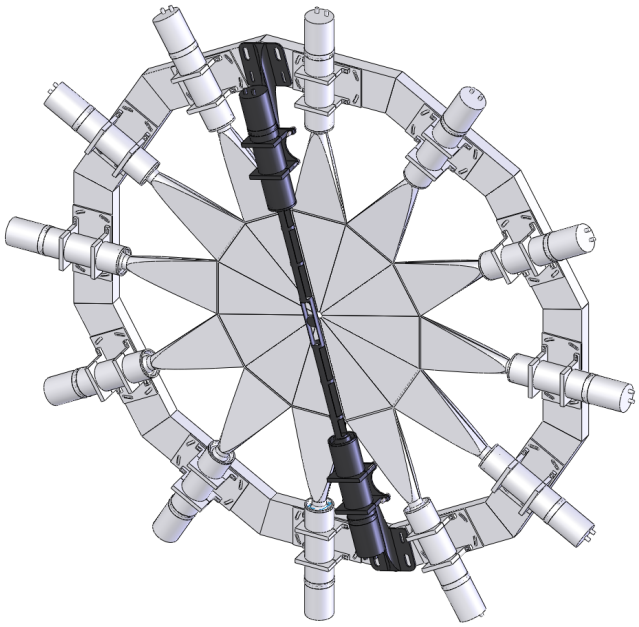

Figure 33: Schematic drawing of the multiplicity counter.

## 5.5 CALORIMETER TRIGGER

The calorimeter trigger selects high-energy photons detected by ECAL2 within 12x12 cells excluding 3x4 cells around the beam hole as depicted in Figure 34. The trigger is implemented in the existing FPGAs of the ADC readout, thus the trigger decision is slower compared to the other triggers. The sum of the time-correlated energies of a selected region of cells is compared with a programmable threshold. The typical accuracy is $\sigma = 4.35\,\text{GeV}$ for a 60 GeV threshold. The time resolution is in the order of 1 ns. Further details can be found in [85] .

## 5.6 CEDAR TRIGGER

Besides the usual data taking with these detectors, the CEDARs can also be used for trigger purposes. The analogue PMT signals are split for the standard read-out and trigger electronics. The analogue signal is fed into a discriminator for each individual PMT. The discriminator thresholds are chosen to suppress electronic noise. All eight digital signals from the discriminators are put in a multiplicity logic unit from which multiplicity signals of 6, 7 and 8 can be used as a trigger signal. Usually for negative beams, where the CEDARs are used for kaon identification, the multiplicity 6 signal of the CEDAR is used as the trigger signal. In this case, the CEDAR trigger is called kaon trigger (KT). For positive beams, the possibility to trigger on types of beam particles is not used.

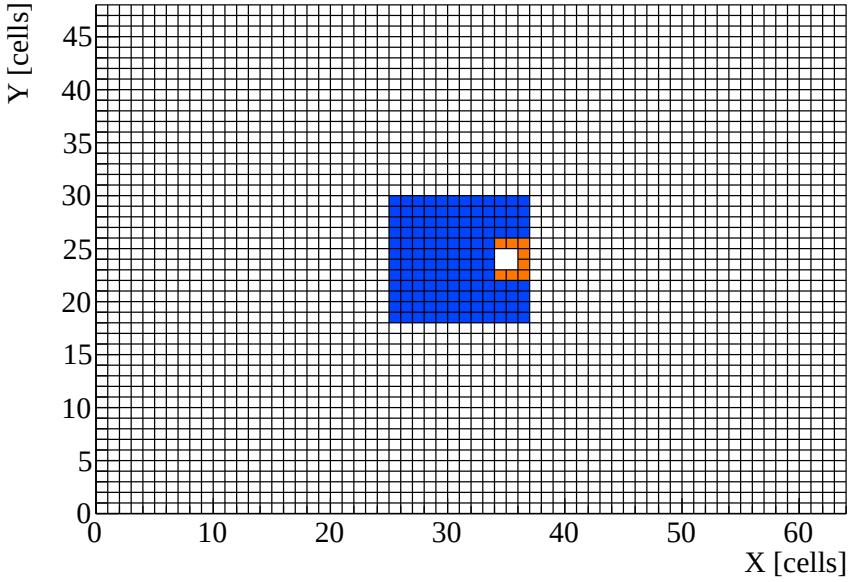


Figure 34: The active area of the ECAL2 trigger (shown in blue). The cells shown in orange are rejected due to high rates.

## 5.7 PHYSICS TRIGGERS

The final physics triggers are summarised in Table 6 alongside with typical trigger rates.
Physics triggers are combinations of the beam trigger, the veto system and one of the specialised trigger systems described before.
The diffractive trigger composition has been described before. The typical trigger rate for data taking with negative beams is 180 000 per 10 s spill at the typical beam intensity, for positive beams it is 240 000.
The two parts of the multiplicity trigger, the outer multiplicity counters and the inner counter, are applied as two independent triggers. The LT1 multiplicity trigger requires one or more hits in the outer multiplicity counter. The threshold per element is set to reject noise and selects charged particle multiplicities of one or larger. The trigger has typically 370 000 attempts per 10 s spill and is prescaled with a factor of 7 to allow data taking with other triggers, as well. LT1 is also used to take data with the condition of two hits in order to select final states with higher masses contributing with a trigger rate of 140 000 per 10 s spill. The LT2 trigger requires an energy deposit corresponding to 1.6 MIPs[1] or higher for a multiplicity of 2 or more in the inner counter which results in a trigger rate of 620 000 per 10 s spill. It is used with a prescaling factor of 8. The second configuration of LT2 requires an energy deposit equivalent to 2.5 MIPs for a multiplicity of 3, likewise in the interest of enriching final states with higher masses. It has a typical trigger rate of 260 000 per 10 s spill.
The main Primakoff trigger (Prim1) uses the calorimeter trigger with a 60 GeV threshold. It has a trigger rate of 260 000 per 10 s spill. The secondary Primakoff

1 minimum ionising particle

| **Sub-trigger** | **Logical composition** | |
|---|---|---|
| Beam trigger (BT) | SciFi1 $\wedge$ beam counter | |
| Beam killer veto | beam killer 1 $\wedge$ beam killer 2 | |
| Veto | Sandwich $\vee$ veto hodoscopes $\vee$ beam killer veto | |
| CEDAR trigger | CEDAR1 multiplicity $\wedge$ CEDAR2 multiplicity | |
| **Physics trigger** | **Logical composition** | **Rate / 10 s** |
| Diffractive trigger DT0 | BT $\wedge$ proton trigger $\bar{\wedge}$ veto | 180k |
| Multiplicity trigger LT1 | BT $\wedge$ 1 (later 2) el. of outer ring counter $\bar{\wedge}$ veto | 370k (140k) |
| Multiplicity trigger LT2 | BT $\wedge$ amp. inner disk $>$ 1.6 MIPs (later 2.5 MIPs) $\bar{\wedge}$ veto | 620K (260K) |
| Primakoff trigger Prim1 | BT $\wedge$ calorimeter trigger ($>$ 60 GeV) $\bar{\wedge}$ veto | 260k |
| Primakoff trigger Prim2 | BT $\wedge$ calorimeter trigger ($>$ 40 GeV) $\bar{\wedge}$ veto | 450k |
| Kaon trigger KT | BT $\wedge$ CEDAR $\bar{\wedge}$ veto | 30k |

Table 6: Overview of sub-triggers, vetos and physics triggers used for data taking.

trigger (Prim2) has a threshold of 40 GeV on the calorimeter trigger and runs with a prescaling factor of two. Its purpose is to monitor the Prim1 trigger threshold and allows for studies beyond pion polarisabilities. It has a trigger rate of 450 000 per 10 s spill before prescaling.
The kaon trigger (KT) is used as a kaon-enriched beam trigger for luminosity monitoring *via* $K \to 3\pi$ decays and for systematic studies. The typical trigger rate is 30 000 per 10 s spill for running with the negative hadron beam.
Further auxiliary triggers are set up for monitoring purposes, systematic studies and alignment purposes. They include two beam triggers of which one described in Section 5.1. The other beam trigger is the coincidence of both SciFi1 planes and thus has a quadratic transverse acceptance of $3.9 \times 3.9\,\text{cm}^2$. It is required for the alignment procedure. The Veto Inner trigger and Halo triggers make use of the hodoscope veto system to detect straight halo tracks for muon data taking, which is utilised in the alignment procedure. Finally, the detected decay products of a radioactive Na-22 source are exploited as a random trigger signal. Alternatively, the output of an electronic noise generator can be used for random triggers.
The trigger signal is fed into a prescaler module which (1) allows to apply prescaling factors in order to in-/decrease priorities within the available triggers and (2) performs an overall logical OR of all trigger signals. The latter is used as an input to the trigger control system (TCS, see [113]), which controls the read-out of all detectors. Each individual trigger signal is also monitored with scalers and TDCs. The TDCs are used to define the so-called trigger mask which contains information about the fired triggers. The prescaler and TCS are both clocked with 38.88 MHz. In addition, the signals of the individual sub-triggers and trigger detectors themselves are monitored with TDCs and scalers. The individual signals of the multiplicty counter are monitored by sampling ADCs.

# ANALYSIS

# 6

# DATA SELECTION AND SIGNAL EXTRACTION

The data analysed in this work were collected in the years 2008 and 2009. Only data with the liquid hydrogen target is considered that was recorded with the DT0 trigger (see Chapter 5). For the extraction of the $\omega$ and $\phi$ meson signal, the data selection is split two-fold: First, common criteria for both vector mesons are applied. Second, specific cuts are used to select the $p\pi^+\pi^-\pi^0 p$ channel, from which the $\omega$ signal is extracted later, and the $pK^+K^-p$ channel, from which the $\phi$ signal is singled out. The apparatus acceptance is determined with a Monte-Carlo simulation and used together with the determined detector efficiencies to correct the invariant mass distributions of the two channels. The $\omega$ and $\phi$ yields are determined with a fit and a sideband subtraction method. The chapter concludes with an overview of the systematic uncertainties.

## 6.1 EVENT SELECTION

The recorded raw data first undergo several calibration and correction procedures specific to each detector system. Then, tracks and interaction vertices are reconstructed with the software package CORAL[1]. The full procedure is internally referred to as "production". For the physics analysis, the processed data are analysed within the PHAST[2] framework which provides access to the relevant information about tracks, vertices, calorimetry and particle identification. The data sample is taken from the COMPASS data taking periods 2008W39 and 2009W29 to 2009W33 with a positive hadron beam.

### 6.1.1 *Event topology and common data selection*

Both channels which are investigated have the same topology with respect to unidentified, charged particles. For practical reasons, the data are preselected before further cuts for a specific channel are applied. Common selection criteria are the DT0 trigger flag, the target cut, the number of charged tracks in an event, and the identification of the beam particle and the target recoil.

*Target cut and select criteria for charged tracks*

Events with exactly one reconstructed interaction vertex within the target volume are selected. An interaction vertex within the Phast/Coral framework is given by the space point where an incoming (beam) track is scattered. Furthermore, events with three charged tracks emerging from this vertex are chosen, two positively

1 COmpass Reconstruction and AnaLysis, `http://coral.cern.ch`
2 PHysics Analysis Software Tools, `http://ges.home.cern.ch/ges/phast/`

charged and one negatively charged, resulting in an outgoing system with a total charge of $+1$. Figure 35 shows the primary vertex distribution along the beam direction ($z$, left panel) and in the transverse plane ($xy$, right panel) before cuts. The target material is clearly visible in both projections. Along the beam direction, most of the data in the event distribution stems already from the target due to the RPD part of the DT0 trigger logic, which ensures target pointing as described in Sec 5.3. In the transverse plane, the trigger acceptance matches the target cell diameter owing to the beam trigger (Section 5.1). In the outer radial region of Figure 35, right panel, a hint of a round structure is visible, which corresponds to the target cell. For the further selection, only data within $-68.4\,\text{cm} < z < -28.4\,\text{cm}$ and $r < 1.6\,\text{cm}$ is used.

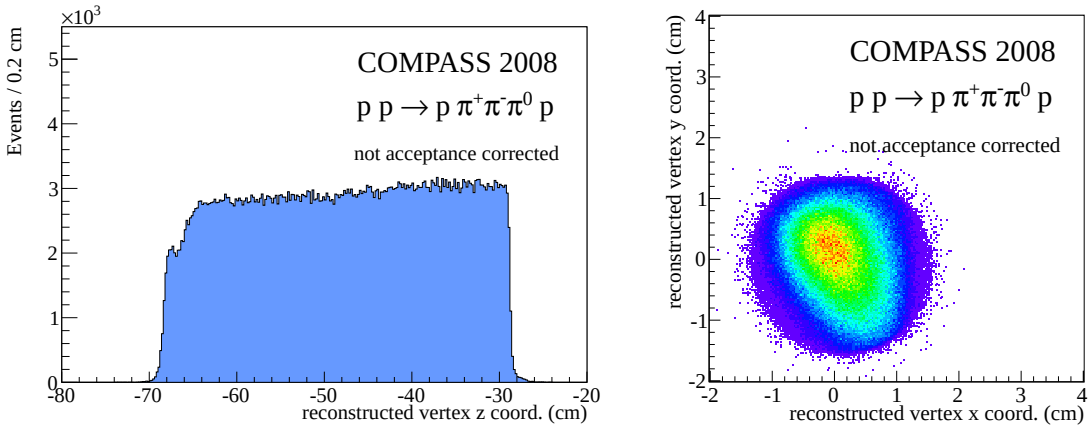


Figure 35: Measured distributions of the reconstructed primary vertex for the given event topology. Left: Projection in beam direction ($z$), right: Projection in the transverse plane ($xy$). The data is exemplary taken for the 2008 part of data taking.

*Beam particle identification*

The positive hadron beam at a momentum of 190 GeV/$c$ contains 71.5% protons, 25.5% $\pi^+$ and 3.0% $K^+$. In order to select protons, a positive proton identification is required in at least one of the two available CEDAR detectors. As described in Chapter 3, each CEDAR detector uses eight photomultiplier tubes centred on a ring surrounding the beam axis to collect light from the emission of Cherenkov photons from the beam particle. For positive identification, a signal from at least four of those photomultiplier tubes is required (multiplicity condition).

*Recoil proton identification*

The RPD is used to select events with exactly one recoiling particle. A further cut to identify the recoil particle as a proton is not necessary as can be seen in Figure 36: The energy loss $\Delta E_B$ of the recoiling particle in the outer scintillator ring B is plotted versus its velocity $\beta$. Only a band corresponding to the proton mass is seen, thus the background from other recoil particles is negligible.

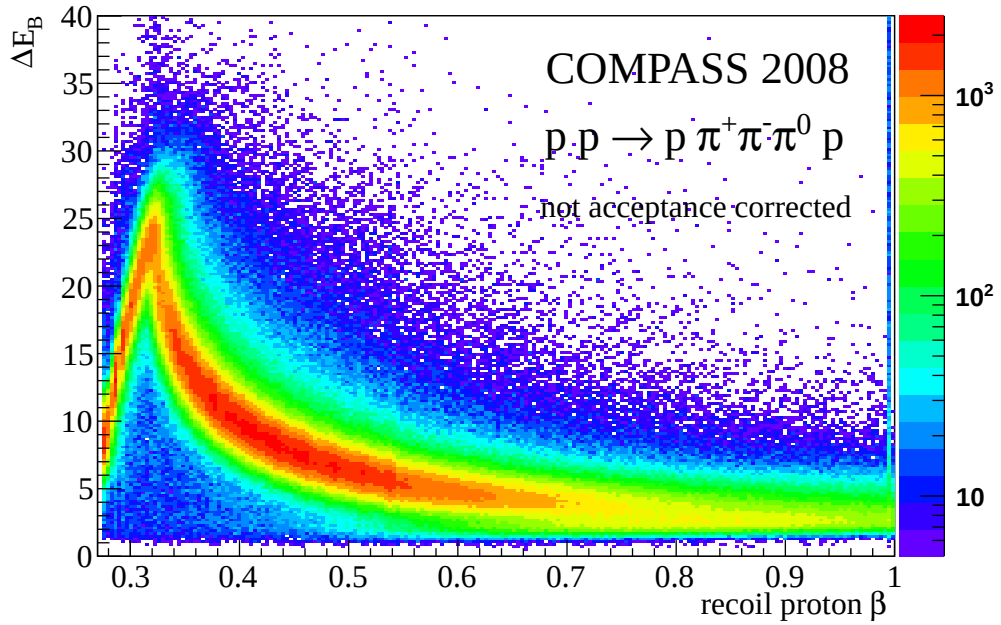


Figure 36: Energy loss $\Delta E_B$ of the recoiling particle in the outer scintillator ring B of the recoil proton detector versus the recoiling particle's velocity $\beta$. Only one band corresponding to the proton's mass can be seen.

### 6.1.2 *The $p\pi^+\pi^-\pi^0 p$ channel*

*Identification of the charged tracks*

The channel has two positively charged particles, a proton and a pion, which have to be discriminated. The RICH detector is used for particle identification. Figure 37 shows the distribution of the measured Cherenkov angles versus the track momentum. The bands correspond to different particle types as indicated in the figure, from which the different momentum ranges for particle separation are seen. Identification of $\pi^+$ candidates is chosen because the momentum range for pion identification (momenta of 3 GeV/$c$ up to 50 GeV/$c$) matches the $\pi^+$ phase space better than the momentum range for proton identification matches the phase space for protons. A likelihood ratio between pion hypothesis versus all other hypotheses including background of 1.0 is applied to identify pions. The other positive track in the event is assigned to be a proton. After the identification of a proton, the negative particle is assumed to be a pion due to strangeness conservation.

*Reconstruction of $\pi^0$ candidates*

Neutral pions decay into two photons after a very short distance of flight in the order of a few ten $\mu$m. The decay photons are measured with the help of the electromagnetic calorimeters ECAL1 and ECAL2 in the first and second stage of the spectrometer, respectively. Hits in nearby cells of the calorimeters are combined by the reconstruction software to a so-called cluster. A cluster is assigned to be

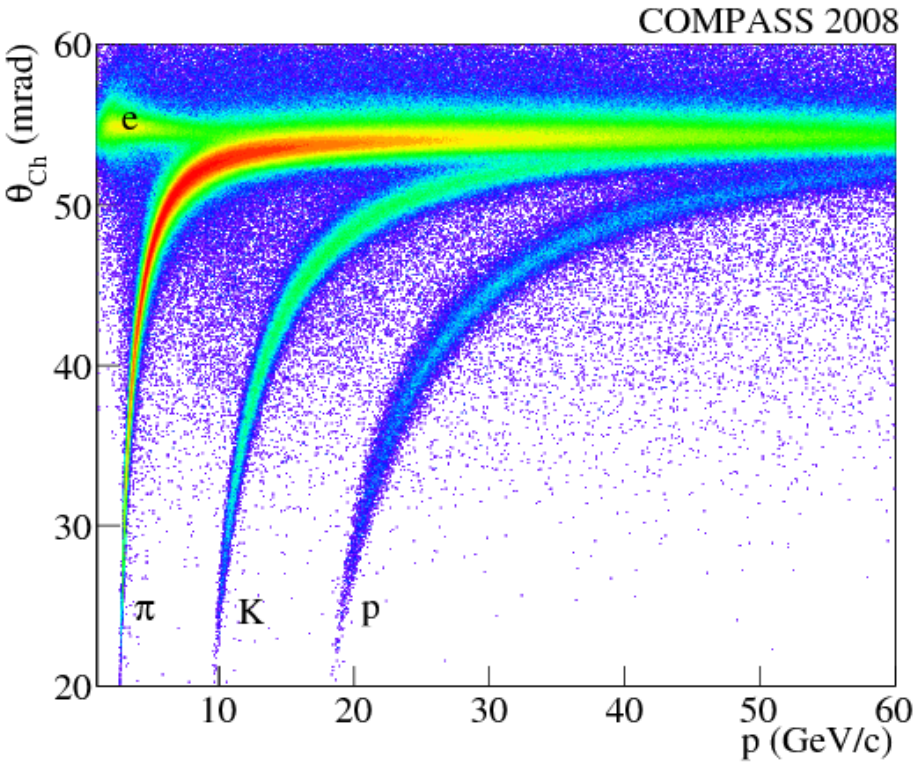


Figure 37: Cherenkov angle (RICH detector) vs. momentum of charged particles.

a photon if there is no corresponding charged track candidate pointing to it. The reconstruction of a $\pi^0$ is done in two steps. The first step involves calibration corrections and quality checks of the detector as will be explained in the following. The second step consists of several cuts in order to identify the measured photons as decay products of a $\pi^0$ where all possible combinations of two photons are probed for $\pi^0$ candidates.

*Step 1 - Calibration and quality checks*

Initially, malfunctioning ECAL cells are removed. There are three criteria for cell rejection: A cell can be either broken, display very high count rates due to noise or be located in a region where the photons traverse too much material to be reliably detected. Dead and noisy cells are identified by observing holes or hot spots in the cluster distribution as seen in Figure 38. These cells are also disabled in the Monte-Carlo simulation. In the most upper and lower rows of ECAL2, the occupancy is significantly lower compared to other regions as can be seen in the lower panel of Figure 38. Photons emerging from the target need to traverse the hadronic calorimeter HCAL1 to be detected in these cells, which is caused by an acceptance mismatch of the first and second spectrometer part. This mismatch is also seen with the help of Figure 38, upper panel, where the photon cluster distribution in the $x$ and $y$ projection of the polar angle for both calorimeters is shown. There is no

detector acceptance between the outer distribution, belonging to ECAL1, and the inner distribution, belonging to ECAL2.
The calibration of the electromagnetic calorimeters is done with a dedicated production of a small data sample before the full data sample is produced. It has to be refined to reach the necessary precision for this analysis. As a compensation for an overall offset in the calibration, the cluster energies are rescaled by a factor of 0.961 to centre the resulting $\pi^0$ peak at the PDG mass of 134.98 MeV/$c^2$. This correction is refined using the information of the LED and laser monitoring systems of the calorimeters. Due to a time-dependent drift effect in the gain of the photomultiplier tube readout, the stability is checked on a run-by-run basis. The resulting corrections are then applied on the analysis level. Figure 39 shows the variation of the $\pi^0$ mass peak (left panels) and width (right panels) for the 2009 data taking after laser and LED corrections for ECAL1 (top), ECAL2 (middle), and the ECAL1/ECAL2 combination. Still, instabilities are observed which call for a refined, additional correction method. The ratios of the observed peak positions with respect to the nominal PDG mass are used to rescale the $\gamma$ energies. This procedure is commonly known as $\pi^0$ calibration and usually done on a cell-by-cell basis. Due to the limited statistics, the calibration was performed on a run-by-run basis for the whole calorimeter due to the larger variations between runs than the lower variations which are observed between different cells. Runs are discarded for quality reasons if the width of the mass peak is off by more than 10 MeV/$c^2$ from the mean value or the width is more than 2 MeV/$c^2$ off the overall mean width. This is true for the runs 77590-77724, where there seems to be a general stability issue as seen in Figure 39.

*Step 2 - $\pi^0$ identification*

All possible combinations of two photons are probed for $\pi^0$ candidates. Thresholds on the reconstructed cluster energies of 1 GeV in ECAL1 and 2 GeV in ECAL2 are applied to reject noise. All cluster times in ECAL1 and ECAL2 are checked and required to coincide with the reconstructed beam track time within 3.2 ns of $\Delta t = t_{beam} - t_{cluster}$. The found photon energies are used to calculate the photon momentum by taking the ECAL resolution into account and assuming that the origin of the two photons is the interaction vertex. The three-momentum vector of a photon is expressed in the following way (see *e.g.* [117]):

$$\vec{p}_\gamma = E_\gamma \frac{\vec{x} - \vec{x}_0}{|\vec{x} - \vec{x}_0|} \tag{53}$$

where $E_\gamma$ is the measured energy of the cluster, $\vec{x}$ is the incident coordinate on the calorimeter and $\vec{x}_0$ is the coordinate of the interaction vertex. The invariant mass of each two photon combination is checked to be within a certain mass window, depending on the calorimeter, around the $\pi^0$ mass peak. The data are divided into three different cases, as shown in Figure 40: i) both photons are detected in ECAL1 (upper left panel) ii) both photons are detected in ECAL2 (upper right panel) and iii) the photons are detected in ECAL1 and ECAL2, respectively (lower panel). The different resolutions $\sigma$ are determined from fits of a gaussian to the data and are

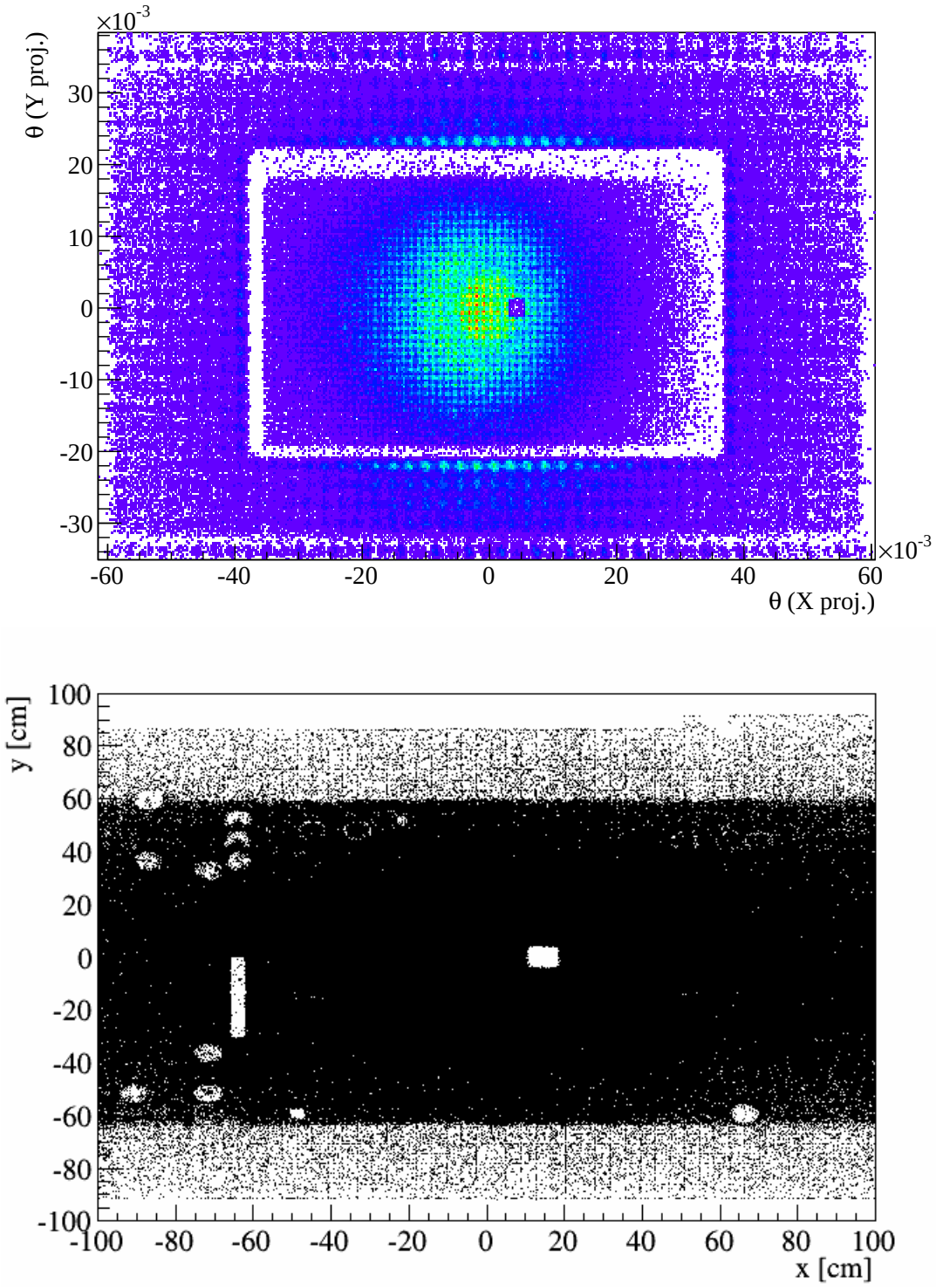


Figure 38: Distribution of $\gamma\gamma$ clusters. Top: Hit distribution in angular coordinates. The $x$ and $y$ projection of the polar angle for both calorimeters is shown. Bottom: Hit distribution of ECAL2.

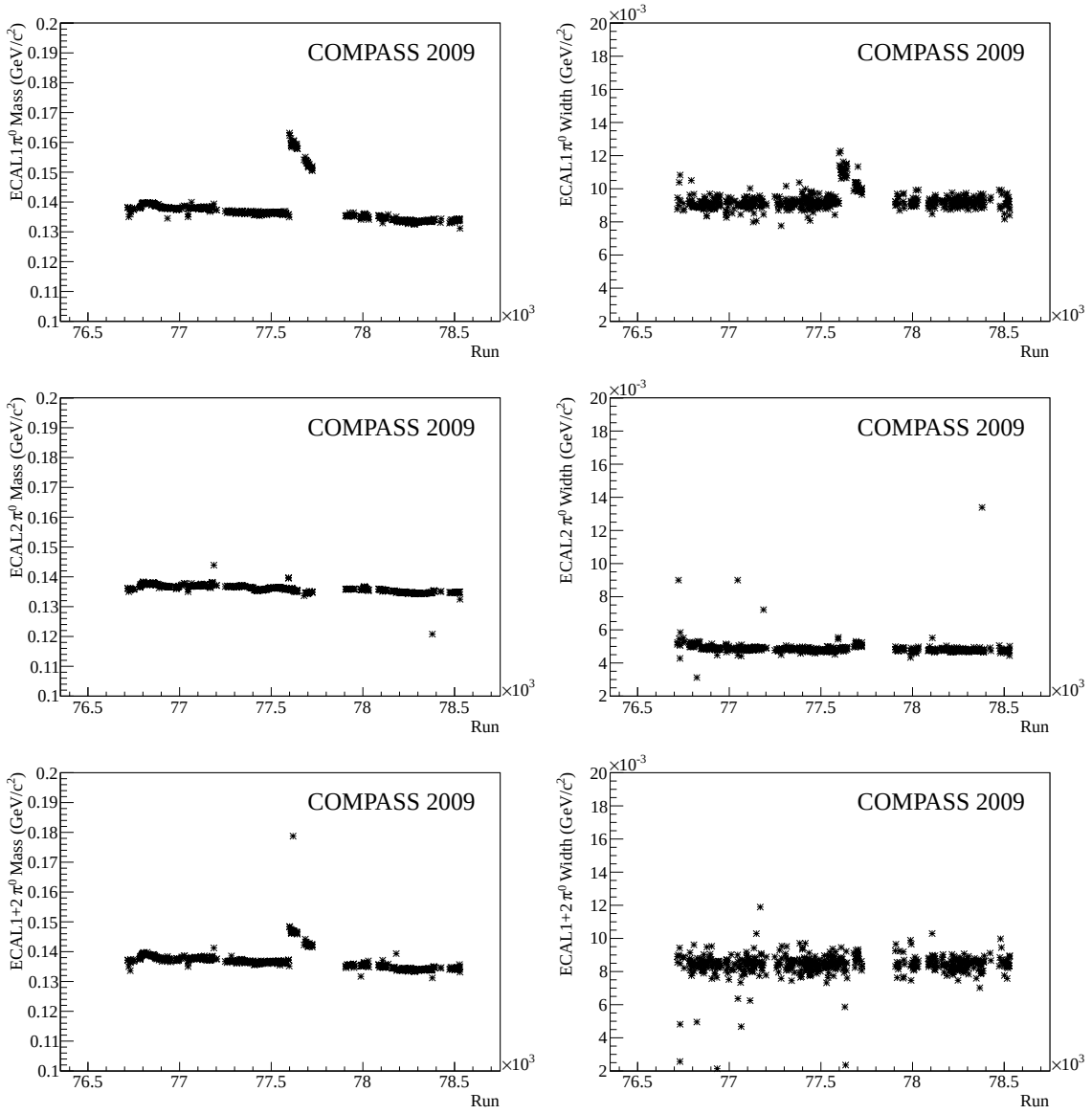


Figure 39: Stability of the electromagnetic calorimeters ECAL1 and ECAL2. Left panels: Position of the $\pi^0$ mass peak with respect to the run number. Right panels: Width of the $\pi^0$ mass peak with respect to the run number. From top to bottom: Both photons in ECAL1, both photons in ECAL2, one photon in each calorimeter.

10.9 MeV/$c^2$, 6.5 MeV/$c^2$ and 9.9 MeV/$c^2$ for the three cases. The full range of the photon-photon mass spectrum is depicted in Figure 41. The $\pi^0$ peak dominates the spectrum. The structures in the lower mass region are attributed to $\pi^0$ and $e^+e^-$ interactions in the spectrometer as outlined in [34]. These interactions are confirmed with Monte-Carlo studies which reproduce the structures. The peak at around 550 MeV/$c^2$ stems from two photon decays of $\eta$ mesons.

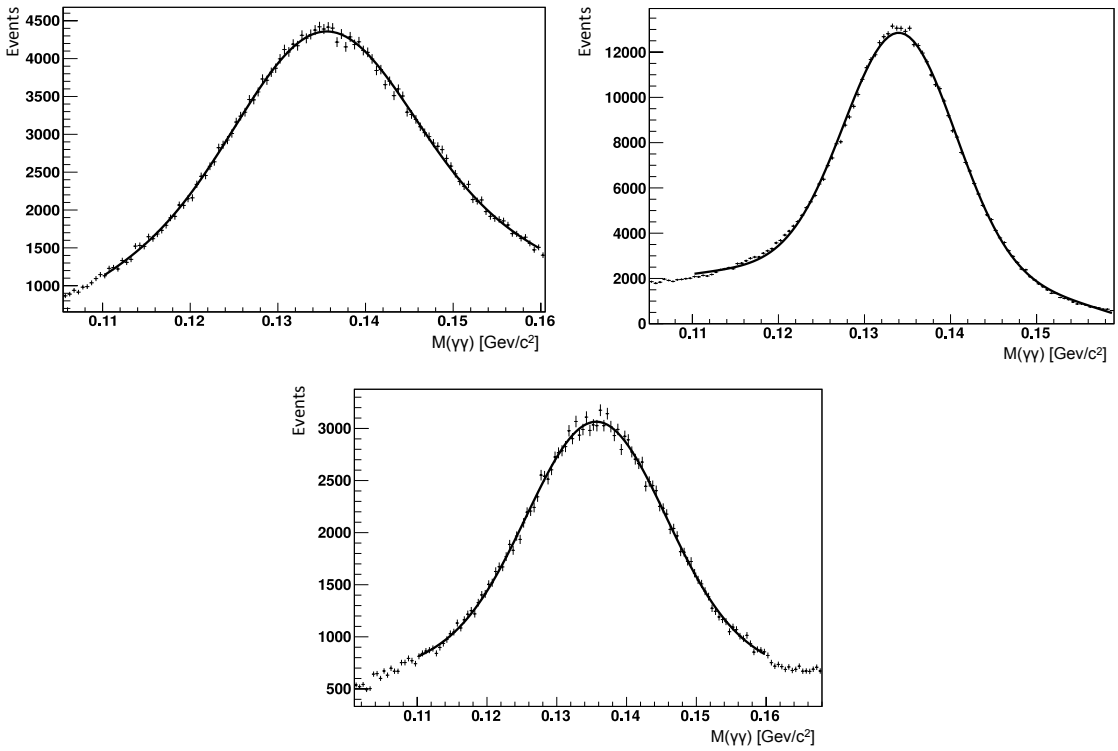


Figure 40: Invariant mass of the $\gamma\gamma$ system of different combinations of calorimeters in which they were detected in. Upper left: Both photons are detected in ECAL1, upper right: both photons are detected in ECAL2, lower panel: one photon is detected in ECAL1 and the other in ECAL2. The different resolutions $\sigma$ are determined from fits of a gaussian to the data and are 10.9 MeV/$c^2$, 6.5 MeV/$c^2$ and 9.9 MeV/$c^2$ for the three cases, respectively.

In the next step, the combination of the two photons is constrained to the PDG $\pi^0$ mass by scaling the photon energies. Figure 42 shows the $\pi^0\pi^+\pi^-$ invariant mass spectrum before (left panel) and after (right panel) the mass constraint. After constraining, the widths of both the $\eta$ peak at about 550 MeV/$c^2$ and the $\omega$ peak at about 780 MeV/$c^2$ are reduced considerably by a factor of about two coming close to PDG widths. The structure around 1300 MeV/$c^2$ is now also more pronounced and could be a contribution from $a_2(1320)$.

### 6.1.3 *The $pK^+K^-p$ channel*

This channel has the same topology for charged tracks, but in contrast to the $p\pi^+\pi^-\pi^0 p$ channel, the positive kaon has to be distinguished from a proton. Again, the RICH detector is used to perform the identification. The yield of the $pK^+K^-p$

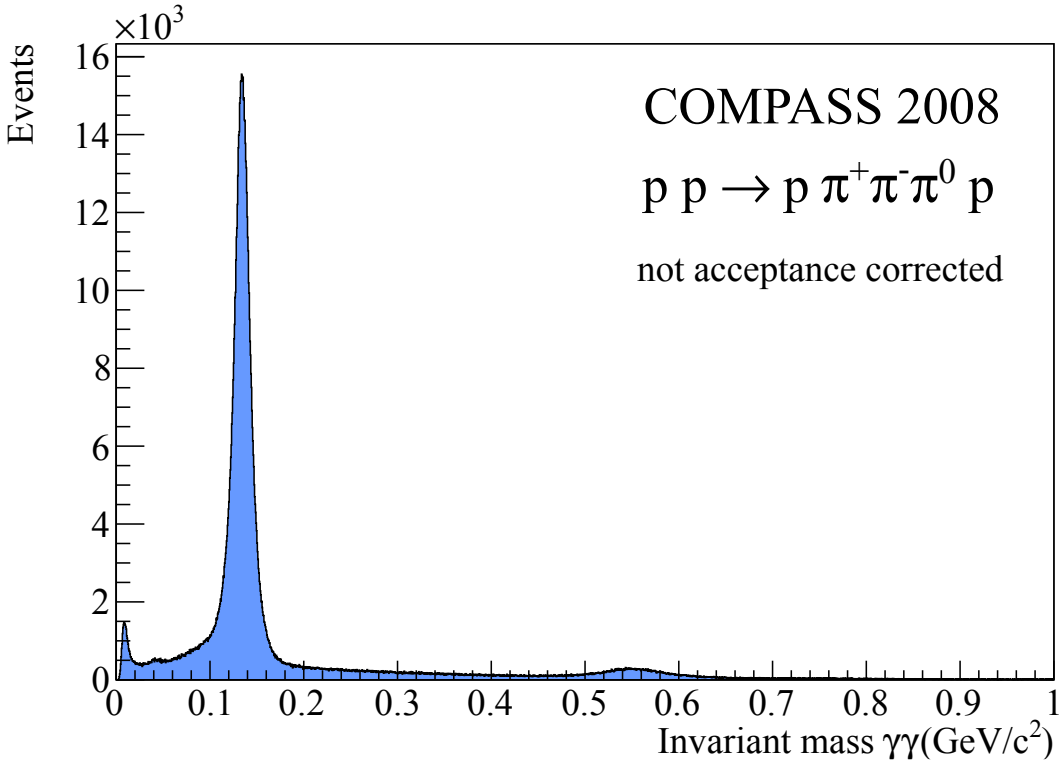


Figure 41: Invariant mass of the $\gamma\gamma$ system in a wide mass range for all possible calorimeter combinations.

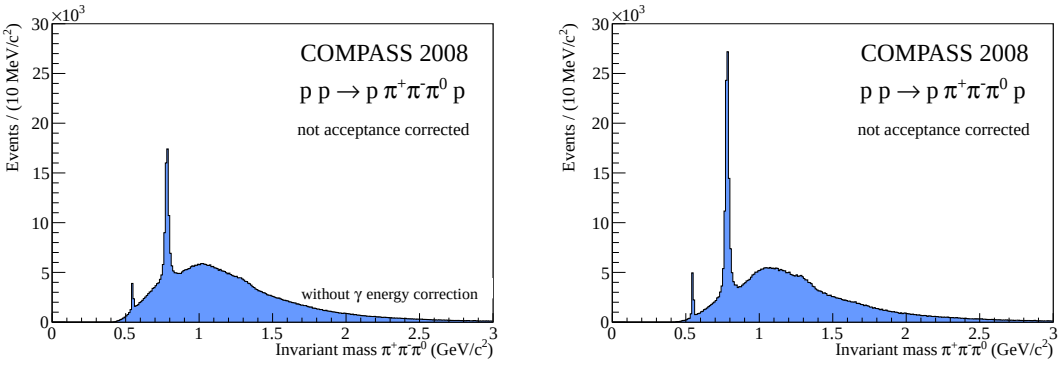


Figure 42: Invariant mass of the $\pi^0\pi^+\pi^-$ system. Left: Before energy correction, right: $\gamma$ energies corrected using the known $\pi^0$ mass as a constraint.

channel is about ten times smaller compared to that of $p\pi^+\pi^-p$, the former being OZI-suppressed. Thus, a relatively high likelihood ratio of 1.3 has to be chosen for a clean data sample with low backgrounds. In turn, this results in a lowered acceptance which is treated for purity. After identification of a $K^+$, the negative track is assumed to be a $K^-$ due to strangeness conservation.

### 6.1.4 *Exclusivity and coplanarity condition*

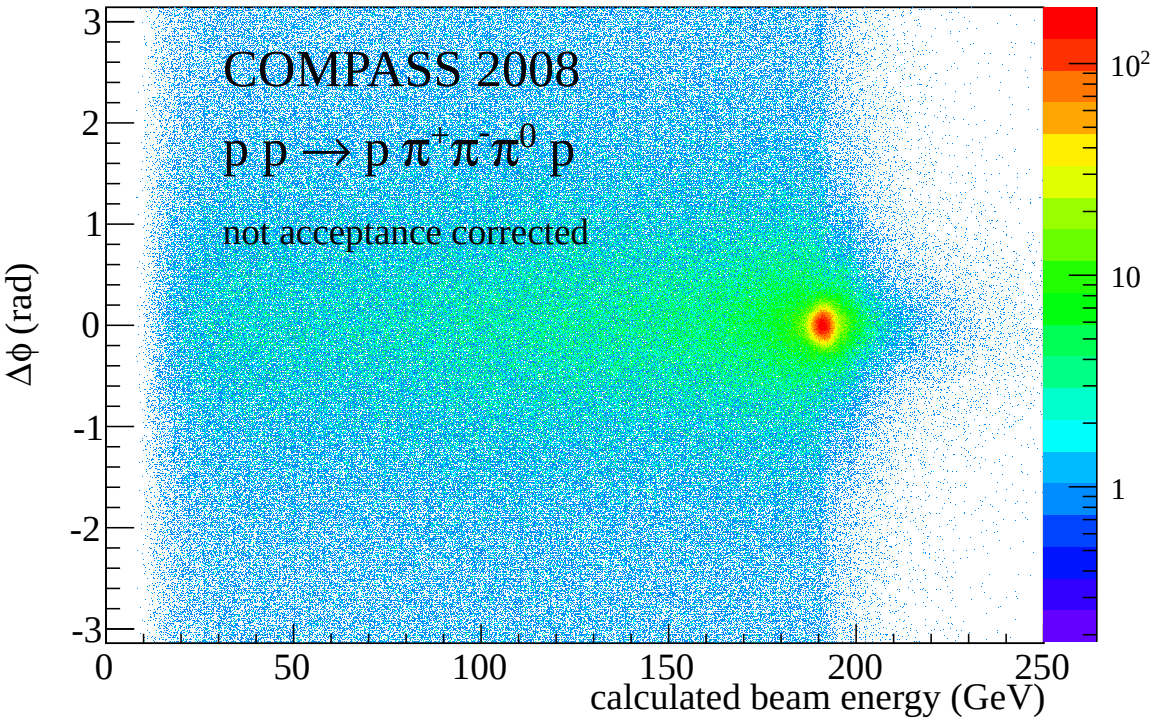


Figure 43: Total energy of the forward system versus angular correlation of the recoiling proton with the forward system.

The exclusive measurement of vector meson production means that all final state particles (vector meson, beam proton, recoil proton) have to be measured and the production of additional particles is rules out. This is ensured by both the energy balance of all outgoing tracks and the coplanarity between the outgoing forward system and the recoiling proton. In this section, the exclusivity criteria are discussed exemplary for $\omega$ mesons for shortness and apply for $\phi$ mesons in the same way. The energy balance and coplanarity for the data sample is depicted in Fig 43. Exclusive events are seen at the beam energy of 191 GeV and at $\Delta\varphi = 0$. The latter will be introduced in the following.
All energies of the forward particles are summed up to calculate the total energy. This energy is required to within a chosen window of $\pm 2\sigma_{\text{beam}} = \pm 6$ GeV around the beam energy. The total energy is shown in Figure 44 and peaks at the beam energy, as expected. The coplanarity reflects the transverse momentum conservation and is checked by requiring that the azimuthal angle $\varphi_{\text{forward}}$ of the outgoing fast system and the azimuthal angle $\varphi_{\text{recoil}}$ of the recoil proton are anti-correlated. The

difference $\Delta\varphi = \varphi_{\text{forward}} - \varphi_{\text{recoil}} - \pi$ is required to be smaller than 0.28, which corresponds to an angle of 16°. This is two times the width of the peak in the $\Delta\varphi$ distribution, which reflects mostly the overall azimuthal angular resolution of the recoil proton detector. The inclusive background appears to be small after both cuts, see Figure 44, where a restriction to the $\omega$ mass region for an illustration of the amount of useful signal compared to the data sample before exclusivity cleanup. For a better comparison of the exclusive signal and the inclusive background, Figure 45 depicts the invariant mass spectrum of the $\pi^0\pi^+\pi^-$ system for exclusive events and events outside exclusivity. Additionally, the exclusive events in the $\omega$ mass region are shown in order to get an impression of the reduction that is imposed by the cuts.

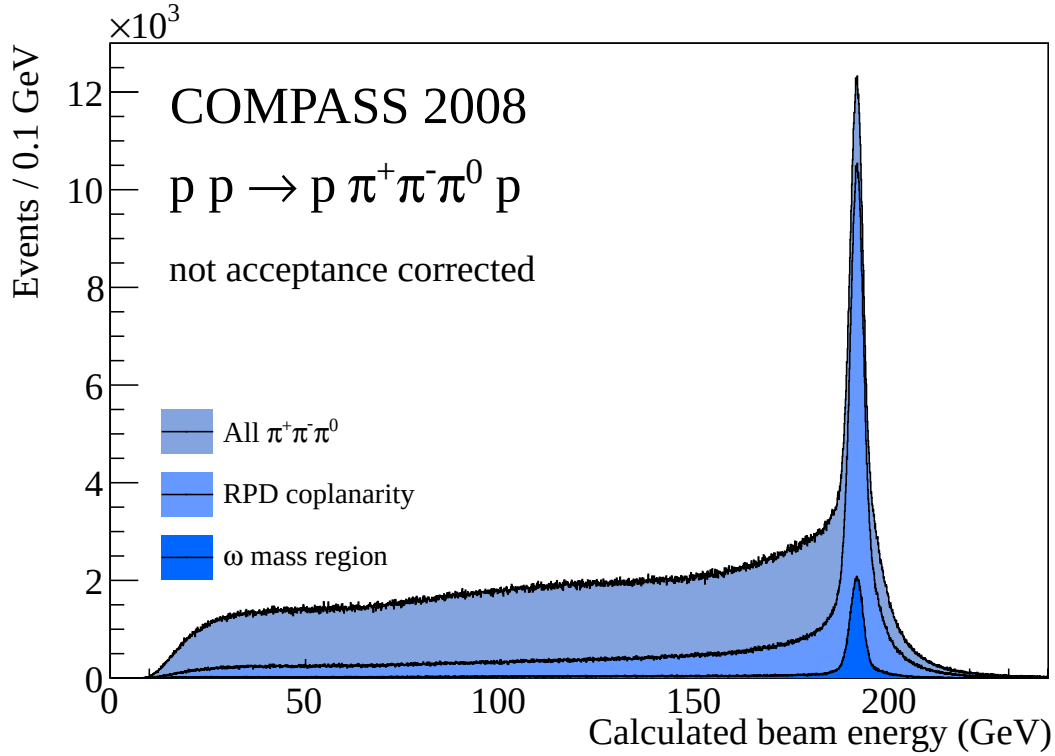


Figure 44: Total energy of the forward $p\pi^0\pi^+\pi^-$ system from the sum of all outgoing particles. The peak is centred at 191 GeV which is the initial beam energy for protons.

The final mass distribution of the $K^+K^-$ system after all cuts is shown in Figure 46. The distribution features the prominent $\phi$ peak at 1020 MeV/$c^2$ which will be selected later on. Several other structures are visible, such as a possible contribution from $a_2(1320)$ and some $f_0$ or $f_2$ mesons around 1500 MeV/$c^2$.
As one of the last steps before the signal extraction, the kinematic domain for both vector mesons has to be determined. In order to ensure that both vector mesons are compared within the same kinematic region, the influence of the spectrometer set-up on the measurable phase-space has to be determined with a Monte-Carlo simulation.

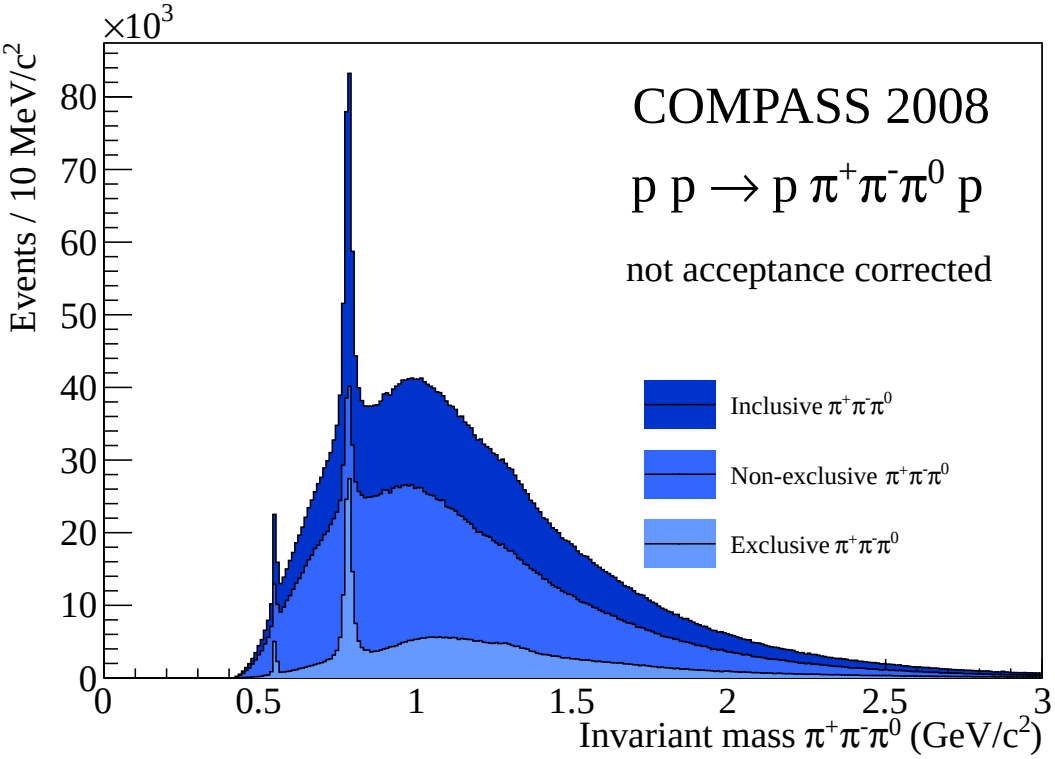


Figure 45: Invariant mass distribution of the $\pi^0\pi^+\pi^-$ system shown for a cut and an anticut on the exclusivity of the events: inclusive events (all $\pi^0\pi^+\pi^-$ candidates), non-exclusive events (anti-cut on exclusivity criteria as defined in the text) and exclusive events, which are selected by the total energy and coplanarity.

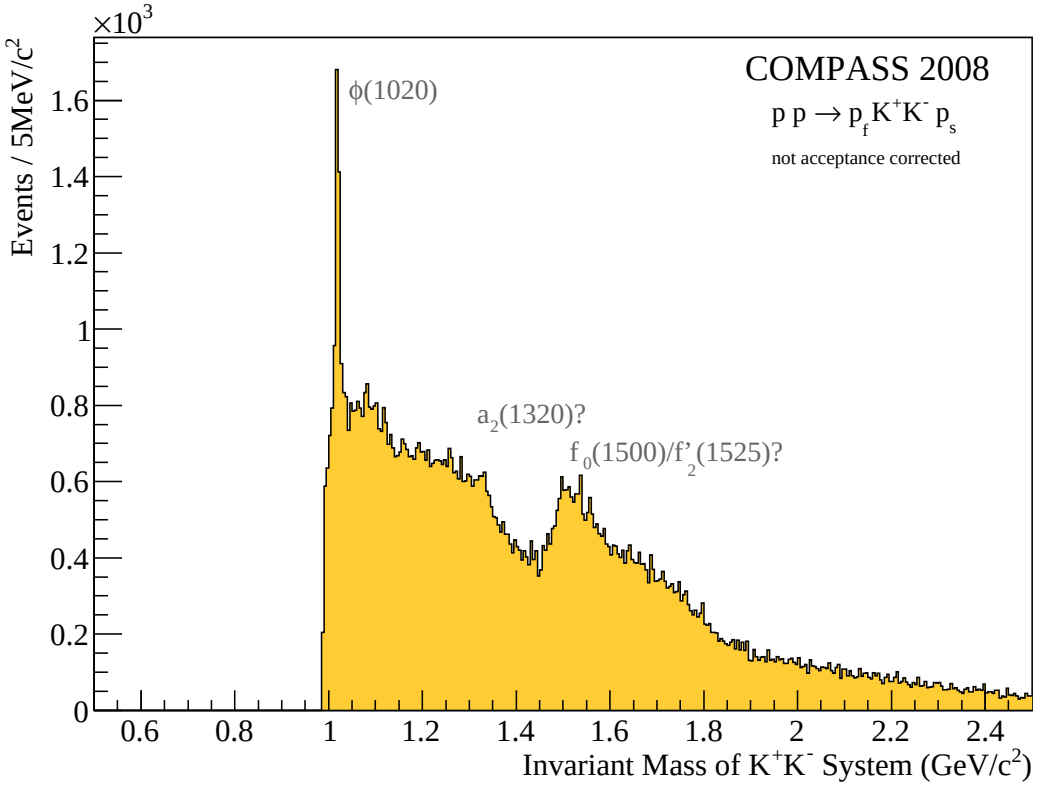


Figure 46: Invariant mass of the $K^+K^-$ system.

## 6.2 ACCEPTANCE DETERMINATION

For the correct estimation of the $\omega$ and $\phi$ meson yields, a Monte-Carlo (MC) simulation of the acceptance is mandatory. A comparison between generated physics events – referred to as MC truth – and the reconstructed events after the MC simulation reveals event losses. The result of this comparison is a differential acceptance with respect to either the kinematics of the process, such as momenta and their directions, or to characteristics of certain detectors, such as their dimensions or dead zones. The simulation is divided in several parts: First, the dynamics of the physical process is generated. Here, four-vectors of the initial and final state particles plus the interaction vertex are generated. In the next step, the particles are propagated through the spectrometer. In particular, this includes the application of magnetic fields, the calculation of energy losses due to passing through matter, smearing effects due to multiple scattering, and production of $\delta$ electrons, which are knocked-out of an atomic shell after being struck by a high energetic particle. For this, the generated data is handled by COMGeant[3], a COMPASS-specific implementation of GEANT3 [46] developed at CERN. The simulation includes the full geometry, response and material composition of each detector plus a description of all passive material, *e.g.* absorbers. In the next step, the MC data in a similar way as the real data during production by Coral. In addition, the detector response is also simulated at this stage.
In order to be as much independent as possible from any physics assumptions, a multidimensional acceptance determination is performed. The correction factors are parameterised through a three-dimensional matrix in the variables $t'$, $M_{pV}$ and $x_F$ of the fast proton. Each $K^+K^-$ or $\pi^+\pi^-\pi^0$ event from the collected data set is weighted by the corresponding entry in the three-dimensional cell ($t'$, $M_{pV}$ and $x_F$) of the acceptance matrix. In a different approach, the results are re-calculated using a different matrix where $x_F$ is replaced by the cosine of the helicity angle of the $pV$ system ($\cos\theta$), as introduced in Section 7.3.2. The results differ by less than 1%.

### 6.2.1 *Monte-Carlo generator*

The vector mesons are generated with the ROOTPWA [82] generator, assuming that the beam proton dissociates diffractively into a state X which then undergoes phase space decay into a fast proton and a vector meson. Due to the multi-dimensional approach for the acceptance determination, the full production mechanism and decay do not have to be simulated and the generator is merely used to provide an initial set of four-vectors.The $t'$ dependence of $\exp(-6.5t')$ and the minimum $t'$=0.07 GeV$^2/c^2$ is adjusted to match the real data in an iterative process. The events are generated in 100 MeV$/c^2$ mass bins, with 100 000 events in each bin. In the $\phi$ case, the bins are between 2000 MeV$/c^2$ and 6000 MeV$/c^2$ and in the $\omega$ case between 1700 MeV$/c^2$ and 6000 MeV$/c^2$. The $\phi$ and the $\omega$ mesons are generated with zero width, which is a simplification with respect to reality and justified by the small widths of the resonances. The three-body decay of $\omega$ mesons is not treated

3 http://wwwcompass.cern.ch/twiki/bin/view/DataReconstruction/MonteCarlo

by ROOTPWA, hence an additional step between ROOTPWA and COMGeant is introduced that handles the decay separately. A beam parameterisation obtained from real data is used as an input to the generator in order to achieve realistic beam conditions, including the horizontal and vertical divergence of the beam for any given position of the interaction vertex.

### 6.2.2 *Trigger acceptance*

The DT0 trigger acceptance is dominated by the RPD trigger geometry. The implementation of the MC simulation is done on the PHAST level in contrast to most other detectors or detector systems. This is necessary due to the special treatment of the RPD. Within the RPD software package, an MC event is searched for hits in the trigger detectors. Thresholds are applied and the detector efficiencies (see Section 5.3.2) are being accounted for by choosing a random number between 0 and 1 and accepting the MC event for the region below the value of the specific efficiency. All logic operations are performed and a single flag is returned, telling if the MC event was accepted or rejected. In the debug mode, also specific information on which detector rejected the event is also available.

### 6.2.3 *Statistical uncertainty of the MC acceptance determination*

The statistical error of an acceptance corrected invariant mass bin is $\sum_i w_i^2$. To be precise, the statistical uncertainty rising from the limited MC statistics needs to be propagated to the invariant mass distributions, as well.
The statistical error for the individual bins within the acceptance correction cannot be calculated by error propagation because the generated and accepted MC events are not independent. In Appendix B, the statistical error is derived similarly to [64]. The individual errors of the correction factors are afterwards calculated. the acceptance description is limited to the part of the phase space in which the statistical error of the correction factors has to be five times smaller compared to the statistical error in real data. Thereby, one can neglect the statistical MC uncertainty. As shown later, the phase space restrictions for real data eliminate almost every region of the MC phase space where larger errors are observed.

### 6.2.4 *Results*

The one-dimensional projections of the full acceptance as a function of $M_{pV}$, $t'$, $x_F$ and $\cos\theta$ are shown in Figure 47 and Figure 48. There is a slight dependence on $t'$ observed for both $\phi$ and $\omega$. The acceptance for $\cos\theta$ is flat for both mesons. The $\phi$ acceptance as a function of $x_F$ and $M_{p\phi}$ shows significant drops for the low mass region and the medium and very high $x_F$ domain. This is a direct result of the limited RICH momentum acceptance. A similar yet much less pronounced dependence is also observed for the $\omega$ acceptance. The range of available $x_\mathrm{F}$ is nearly twice as much, but the overall acceptance is smaller by a factor of about two compared to the $\phi$ acceptance. The $\omega$ and $\phi$ mesons share a reasonable acceptance

in the region $0.6 < x_F < 0.9$, which will be used in turn as a restriction for real data from now on.

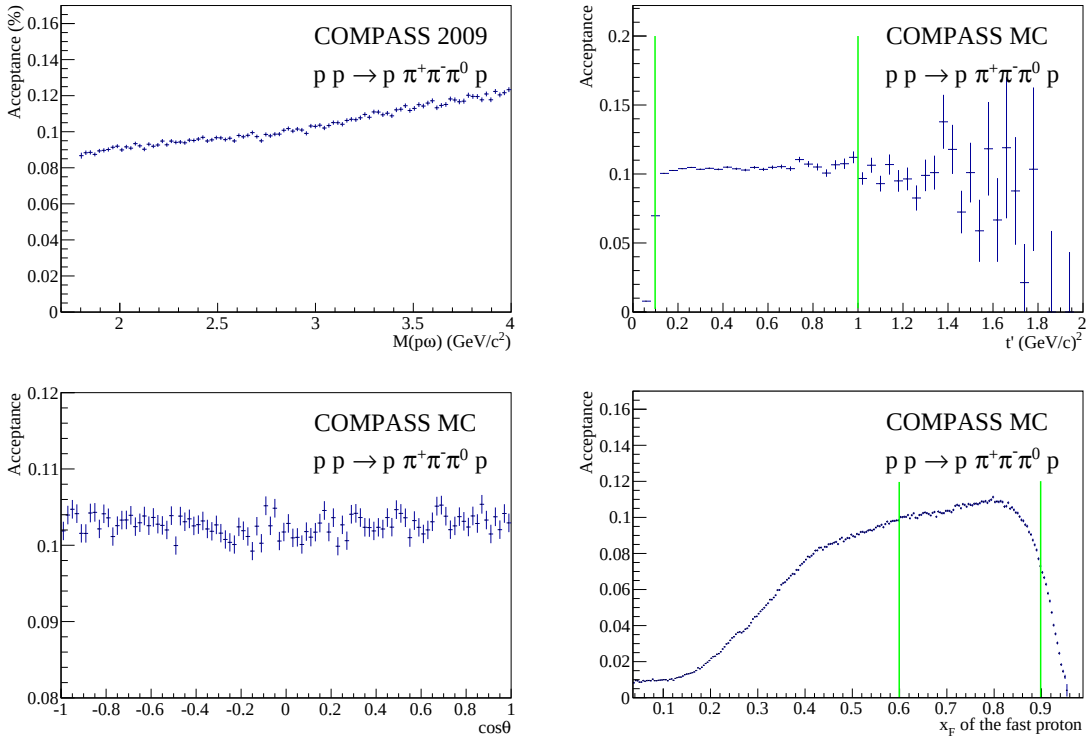


Figure 47: One-dimensional (integrated) acceptances for $pp \to pp\omega, \omega \to \pi^+\pi^-\pi^0$, as a function of $M_{p\omega}$, $t'$, $x_F$ of the fast proton and $\cos\theta$, respectively. Cuts used in the later analysis are marked in green.

## 6.3 DETECTOR EFFICIENCIES

The detector efficiencies are estimated in order to correct for the amount of undetected particles. The most important contributions stem from the RICH detector and the ECALs, which will be discussed in the following.

### 6.3.1 *RICH*

The RICH detector with its layout, material composition and read-out is fully described in the MC simulation, which is used to determine the geometrical acceptance. The detector efficiencies can be estimated by MC simulations as well as by real data. In Figure 49, the $K^+$ momentum distribution is shown for a small data sample with real data in black and MC data in blue. The real data histogram is sideband subtracted for a better comparison to the background-free MC data. The shapes of the curves are different but the momentum range in the data is reproduced in MC data. However, the match between MC description and real data is not precise enough to justify a use of MC-determined efficiencies. The determination with real data is more robust and is hence used. Decays of mesons and baryons

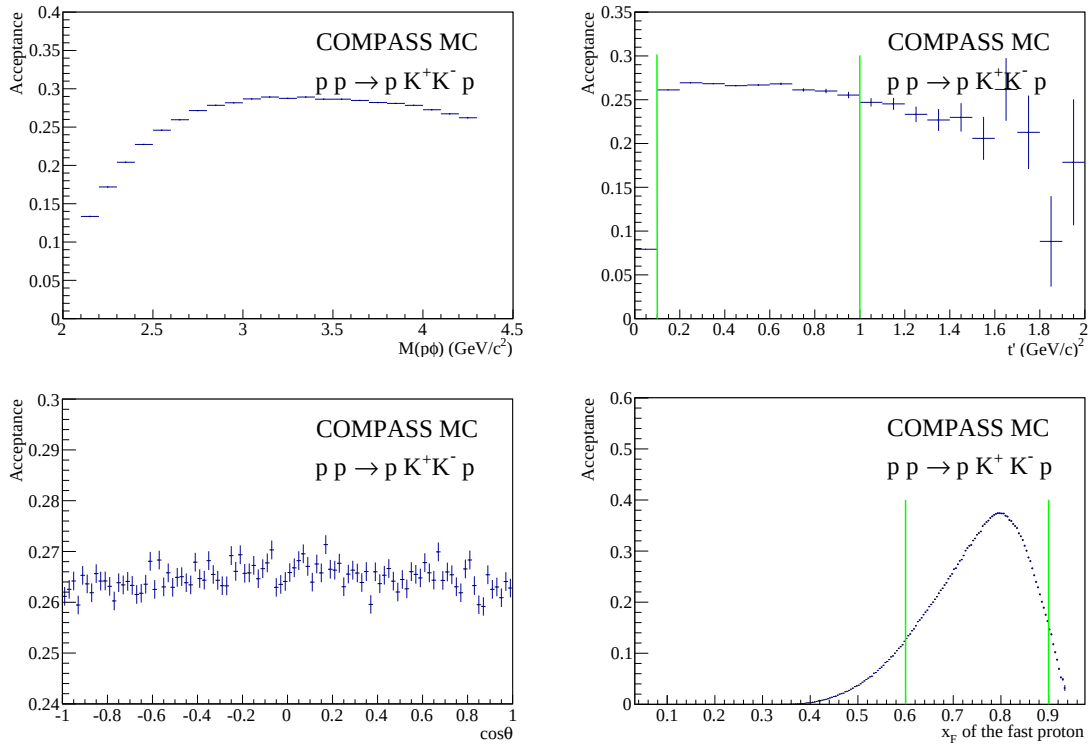


Figure 48: One-dimensional (integrated) acceptances for $pp \to pp\phi, \phi \to K^+K^-$, as a function of $M_{p\phi}$, $t'$, $x_F$ of the fast proton and $\cos\theta$, respectively. Cuts used in the later analysis are marked in green.

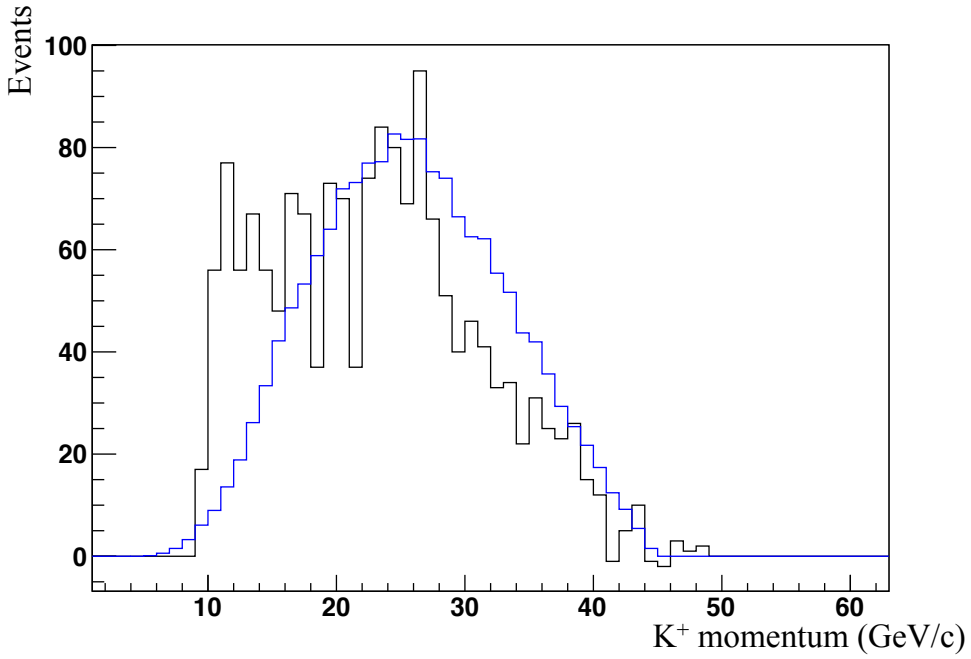


Figure 49: The momentum of the $K^+$ for real data (sideband subtracted but not acceptance corrected) in black and for MC data (scaled to have the same area as the histogram from real data). All cuts, including exclusivity, coplanarity and $\phi$ mass, have been applied.

provide a data sample. The $K^0$ decay provides a reliable source for pions, as does the $\phi$ meson for kaons. Protons can be identified using $\Lambda^0$ decays to $p\pi^-$.
The event selection for $\phi$ mesons includes all steps as described in Section 6.1.1 except the particle identification. The mass is determined from the negative particle and one of the positive particles in the data sample, which results in a high combinatorial background. The $\phi$ signal is then extracted fitting a Breit-Wigner/Gaussian convolution on top of a polynomial background to the data. This procedure is later refined for high precision $\phi$ extraction, see Section 6.4. The uncertainty due to the background subtraction on the extracted yields is about 5% in all fits. It is the main contribution to the systematic uncertainties of this method and hence used for an estimate of the systematic uncertainty for the RICH efficiencies.
Both $\Lambda^0$ and $K^0$ decays share the same topology: An interaction vertex with an incoming and an outgoing particle, and a displaced secondary vertex which has two outgoing, oppositely charged particles. The restriction to exactly one outgoing particle is made to avoid ambiguities in the association of the secondary vertex. Due to the mass-symmetric decay of the $K^0$ and the mass-anti-symmetric decay of the $\Lambda^0$, both particles can be identified via observed asymmetries in the transverse momentum of the two decay products. In addition, regions with very low transverse momenta are excluded because they most likely include positron-electron pairs. The mass of the decay products hence can be assigned. The RICH information is obtained separately with the given likelihoods as explained in Section 6.1. A comparison of this "true" information with the response of the RICH results in probabilities for identification and misidentification. Both are binned with respect to the track momenta and polar angles. In Figure 50, the lookup table for probabilities to identify positive pions with a likelihood ratio of 1.0 is depicted as two-dimensional histograms. On the upper left panel of the figure, the probability to identify a positive pion correctly is presented. The two structures reflect the internal structure of the RICH, which has two different read-out systems for the inner and outer region, see Chapter 3. The overall efficiency strongly depends on both track angle and momentum. For pions, the identification is possible for momenta up to 50 GeV/$c$. The upper right and lower panels of Figure 50 show the probabilities for a misidentification as a proton (upper right panel) and for no hypothesis/background (lower panel). These tables are used for the RICH identification of pions in the $\pi^+\pi^-\pi^0$ case. Figure 51 shows the same quantities for the case of kaon identification with a likelihood ratio of 1.3 which is used in the $K^+K^-$ case. The binning is coarse due to the small statistics available. The upper left panel shows again the probability for identification while the upper right panel shows the probability for a misidentification as a pion. The lower panel is again the probability for no identification/background.
The rather low acceptance in the $pK^+K^-p$ channel is caused by the requirement of RICH identification of $K^+$. In lack of a complementing RICH detector in the small angle spectrometer, the acceptance of particle identification with respect to the particle momentum is limited to 10-50 Gev/$c$ for kaons.
As explained in Section 6.1.3, the positive kaon has to be distinguished from the forward proton to avoid combinatorial background. Another important background

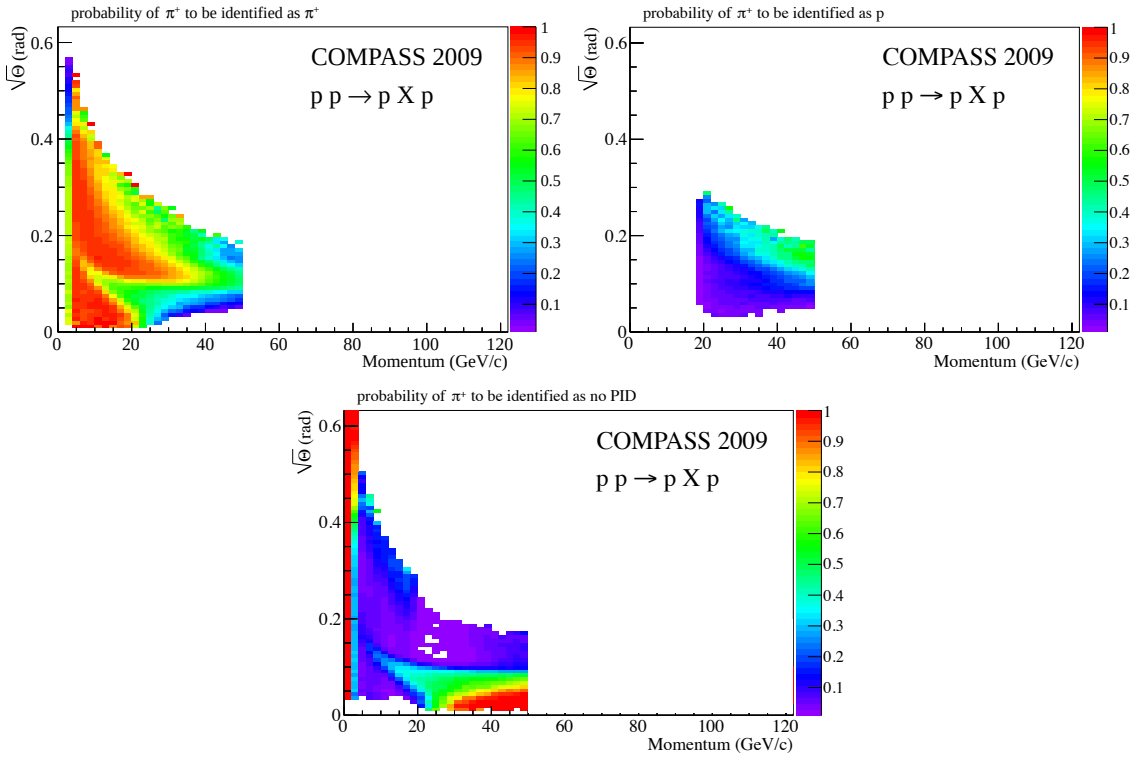


Figure 50: Identification probabilities of the RICH during the proton run 2009 as a function of track momentum and angle for a likelihood ratio of 1.0. Upper left: Probability of $\pi^+$ to be identified as $\pi^+$. Upper right: Probability of $\pi^+$ to be identified as proton. Lower panel: Probability of $\pi^+$ to be not identified.

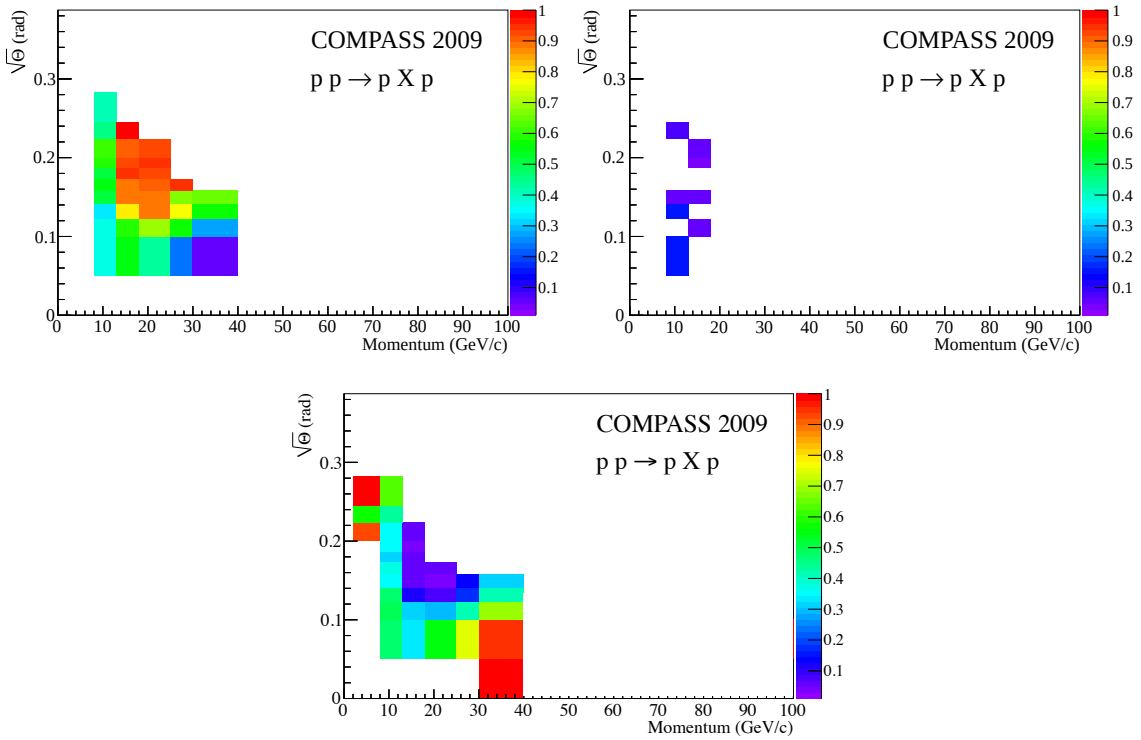


Figure 51: Identification probabilities of the RICH during the proton run 2009 as a function of track momentum and angle for a likelihood ratio of 1.3. Upper left: Probability of $K^+$ to be identified as $K^+$. Upper right: Probability of $K^+$ to be identified as $\pi^+$. Lower panel: Probability of $K^+$ to be not identified.

originates in the $p\pi^+\pi^-p$ channel. Misidentified pions assigned to the kaon mass contribute in particular to the low mass part of the invariant mass distribution.

### 6.3.2 *Photon reconstruction effiency*

The determination of the photon reconstruction effiency is an important part of the correct estimation of $\omega$ yields. In particular, the two photons from the $\pi^0$ decay traverse large parts of the spectrometer, which results in losses. In addition, the ECAL simulation in the Monte-Carlo does not include a full simulation of energy losses due to Cherenkov light emission in the cells. Hence, a crosscheck of the MC results with real data is mandatory.
The photon reconstruction efficiency is determined by a comparison of branches of a known resonance, involving neutral decay products. The $\omega$ meson decays with a 89.2% probability into $\pi^0\pi^+\pi^-$ and with 8.3% to $\pi^0\gamma$. Comparing the yields of the two branches and correcting for tracking efficiency for $\pi^+\pi^-$, the ratio corresponds to the single photon detection efficiency assuming a cancellation of the $\pi^0$ acceptances in the ratio. This estimate includes losses due to crossed material. It is important, that the comparison is done for the same $\pi^0$ phase-space.
The selection off the $p\omega p, \omega \to \pi^0\gamma$ channel is similar to the charged channel, see Section 6.1.1, but with one outgoing, unidentified charged track. The latter is assumed to be a proton. Only events with three photons in the final state are selected from which two have to be within the $\pi^0$ mass windows (Section 6.1.2). The resulting invariant mass distribution is depicted in Figure 52. The $\omega$ mass peak is visible on a much higher background as compared to the charged $\omega$ decay mode with a signal to background ratio of about 1:3.5. Due to the low branching and the consequent lack of statistics, a further differentiation with respect to the two calorimeters and/or different cell types is not possible.
Table 7 summarises the results of the photon reconstruction study. In the charged channel, 115 000 events are found, which result after acceptance correction and taking into account the branching ratio in a yield of 1 865 000 $\omega$ mesons. The neutral decay mode yields 5 600 events, which corrects to 1 824 000 $\omega$ mesons. The difference between the two channels amounts to 2% which could be used as an estimator for the systematic uncertainty due to the knowledge of photon reconstruction efficiency. The background subtraction error on the $\pi^0\gamma$ channel is little below 10% which in turn dominates the total systematic uncertainty. It is hence used as an upper limit.
For the determination of the overall photon reconstruction efficiency, both channels are separately compared in real data and MC data. For real data, the ratio of yields corrected for the branching ratio are

$$\frac{89.2\% \cdot (\omega \to \pi^0\gamma)}{8.3\% \cdot (\omega \to \pi^+\pi^-\pi^0)} = 44.5\%$$

which has to be corrected for the reconstruction efficiency of the two charged tracks, which is estimated to be 72%, see [117]. After correcting, the overall single photon detection efficiency is estimated to be 32%, which translates to a $\pi^0$ detection efficiency of roughly 10%. This number agrees well to previous estimates, such as

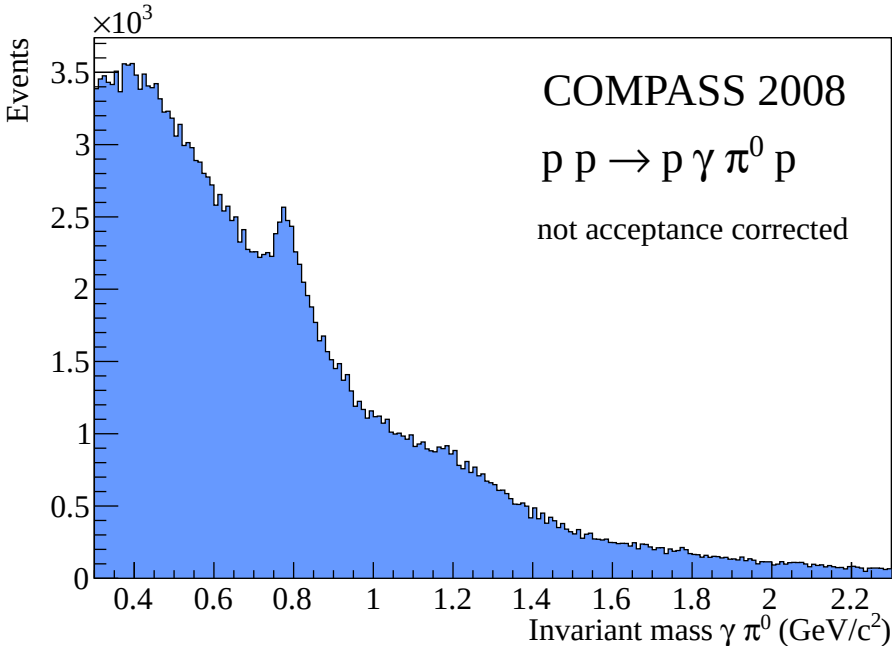


Figure 52: Mass distribution of $\pi^0\gamma$.

in the $\pi^-\pi^0\pi^0$ channel [105]. The same study was performed for MC generated and reconstructed events, where one finds 35% for the photon reconstruction efficiency and 12.5% for the $\pi^0$ detection efficiency. However, due to the described uncertainties of the background subtraction, the efficiencies are only an estimate.

| *Channel* | *Acc. (%)* | *BR (%)* | *Events in data* | *Corrected yield* |
|---|---|---|---|---|
| $\omega \to \pi^+\pi^-\pi^0$ | 6.9 | 89.2 | 115 000 | 1 865 000 |
| $\omega \to \pi^0\gamma$ | 3.7 | 8.3 | 5 600 | 1 824 000 |

Table 7: Yields of $\omega \to \pi^+\pi^-\pi^0$ and $\omega \to \pi^0\gamma$ after correcting for acceptance and branching ratio

## 6.4 SIGNAL EXTRACTION

The $\omega$ and $\phi$ signals are extracted from the acceptance corrected invariant mass distributions in bins of the studied kinematical variable such as $x_F$, $M_{pV}$, or $\cos\theta$. The signal of the $\omega$ mesons is extracted from the acceptance corrected $\pi^+\pi^-\pi^0$ mass distributions of the $p\pi^+\pi^-\pi^0 p$ final state. The number of $\omega$ candidates is determined by fitting a combination of two Gaussians folded with the same Breit-Wigner form (BW/G$_{1,2}$) on top of a second degree polynomial background [25], known as "Double-Voigt-Profile". The folding procedure is done numerical and for each iteration of the MINUIT minimiser. The fitting function has the form

$$a\,(\mathrm{BW}/\mathrm{G}_1) \;+\; (1-a)\,(\mathrm{BW}/\mathrm{G}_2)$$

where BW/G denotes the folded function. The two Gaussians take into account different resolutions, *e.g.* originating from the LAS and SAS, both in tracking and calorimetry.
For the $\phi$ meson, the signal is extracted from the acceptance corrected $K^+K^-$ invariant mass distribution of the $pK^+K^-p$ channel. The $\phi$ meson is located close to the $K\bar{K}$ threshold. A single Breit-Wigner function folded with a Gaussian on top of a background is used, where the background takes into account the phase-space opening [25]. The background distribution function is defined as

$$a\,(m(K\bar{K}) - m_1)^n\,(m(K\bar{K}) - m_2)^k$$

where $a, m_1, m_2, n$ and $k$ are the fit parameters.
In both cases, the Breit-Wigner width is fixed at the PDG value. The full BW-Gaussian peak is integrated and gives the final particle yield. Figure 53 shows the results of the fits in the $x_F$ regions 0.6-0.7, 0.7-0.8 and 0.8-0.9 for the extraction of both $\omega$ and $\phi$ yields, respectively. The signal part of the fit is marked in green, the background in red and the overall result in blue. The typical $\chi^2/NDF$ for these fits is 1.1 or better.
For illustration of the background and systematic checks, sideband subtraction is used in addition. For a corrected distribution of *e.g.* $M_{p\mathrm{V}}$, events within $\pm 3\sigma$ of the $M_{\pi^+\pi^-\pi^0}$ or $M_{K^+K^-}$ distributions are taken and events in the sidebands from $\pm 4\sigma$ to $\pm 7\sigma$ are subtracted.
A comparison of different fit models, including using a p-wave Breit-Wigner term or removing one Gaussian term, respectively, gives an estimate of the systematic uncertainties due to the fit model. The largest deviation between the different models observed is 5% which is used as the systematic uncertainty for the background subtraction.

## 6.5 SUMMARY OF SYSTEMATIC UNCERTAINTIES

Most efficiencies (CEDAR, RPD, track reconstruction) cancel in a direct comparison of $\phi$ and $\omega$ yields due to the same selection. Systematic effects introduced by the MC generator are generally small since a multidimensional acceptance correction is applied and since we restrict ourselves to a kinematic region which is well covered by the generator. The RICH detector has a much larger impact on the $\phi$ yield than on the $\omega$ yield since the accepted momentum range for kaon identification is smaller. The total uncertainty from the RICH is estimated to be 5%. The photon reconstruction efficiency is determined by comparing $\omega$ decays into $\pi^+\pi^-\pi^0$ and $\pi^0\gamma$ in both real data and MC with the assumption that the $\pi^0$ efficiency is the same in both channels. The deviation between measured efficiency and MC is found to be below 10% and used as an upper limit for the systematic uncertainty arising from the photon reconstruction. The uncertainty of the background subtraction was studied with several fit models and estimated to be 5%. The quadratic sum of these uncertainties results in a total systematic uncertainty of 12% for all results shown in the forthcoming chapters, unless otherwise denoted.The uncertainty of the RICH and photon reconstruction efficiencies are uniform with respect to variables such

as $M_{pV}$ and the angular distribution which will be later discussed and do not apply to results with extracted from distributions of these variables.

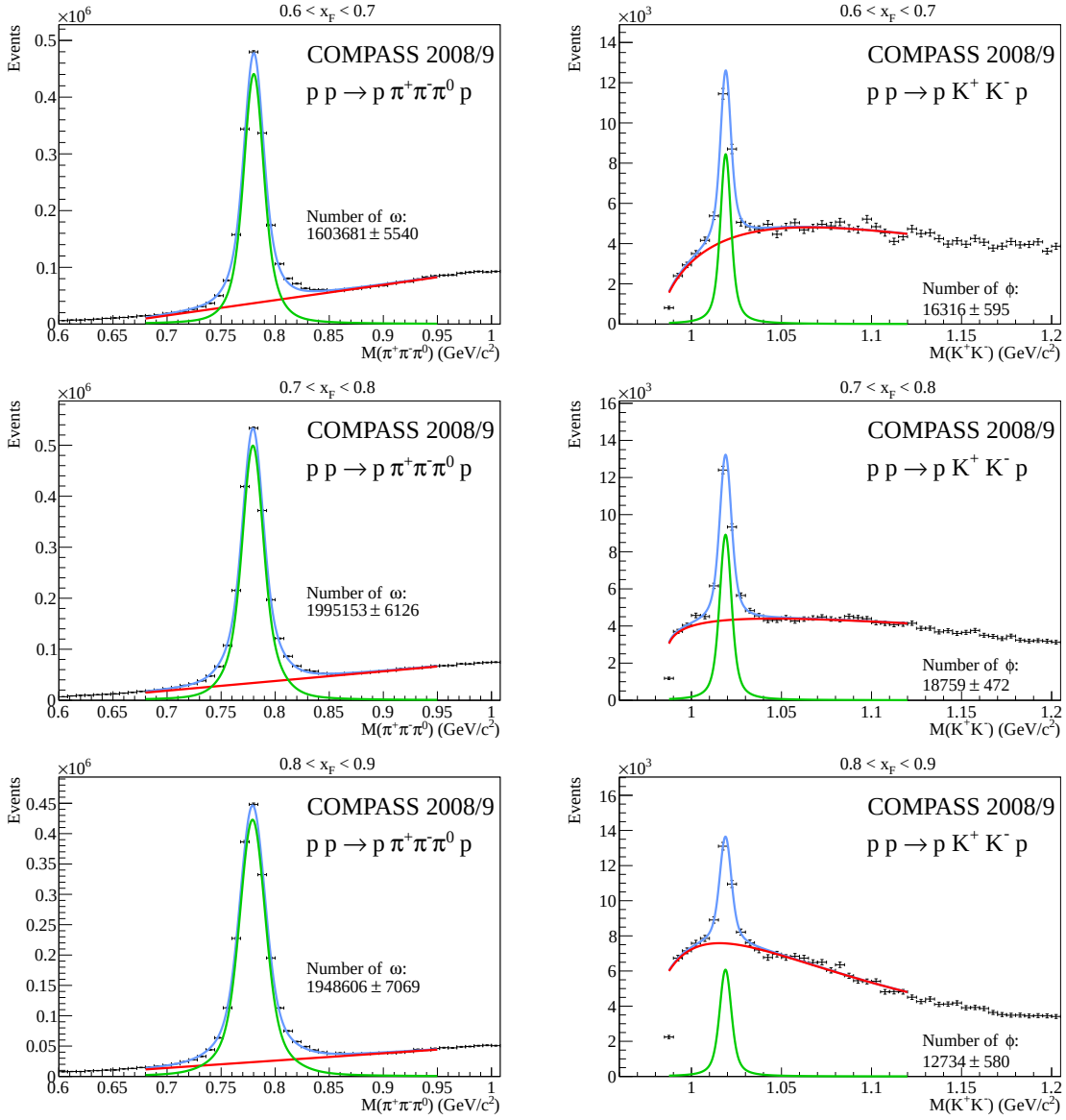


Figure 53: 2008 and 2009 combined analysis. Left column: Fit to the invariant mass distribution of the $\pi^+\pi^-\pi^0$ system. Right column: Fit invariant mass distribution of the $K^+K^-$ system. From top to bottom: Different $x_F$ regions of the fast proton with the intervals $0.6 < x_F < 0.7$, $0.7 < x_F < 0.8$ and $0.8 < x_F < 0.9$. The signal is marked in green, the background in red and the overall fit in blue.

# 7

# ANALYSIS OF PRODUCTION RATIOS AND SPIN ALIGNMENT

In this chapter, the measurements of production ratios and spin alignment are presented and discussed as tools for the investigation of production mechanisms. First, the kinematic distributions for $t'$, $x_F$, $M_{pV}$ and their properties are discussed. Later, the production ratio and spin alignments are surveyed in context of results of earlier experiments. The chapter concludes with the discussion of the combined results with regard to the production mechanisms.

## 7.1 KINEMATIC DISTRIBUTIONS

The acceptance-corrected $t'$ distributions are depicted in Figure 54 for $\omega$ mesons (upper panel) and $\phi$ mesons (lower panel). The $t'$ distributions are obtained as explained in Section 6.4.

The lines in Figure 54 represent a fit with different models which are motivated by the explanations given in Section 2.2 and in [72]. For $\omega$ mesons, the best fit[1] is reached with two exponentials of the form $A_1 \exp(t'/b_1) + A_2 \exp(t'/b_2)$. The achieved $\chi^2/\mathrm{NDF} = 1.6$ is about 20 times lower compared to a fit of a single exponential. The results for the two slopes are $b_1 = (-14.3 \pm 0.1 \pm 1.8)/(\mathrm{GeV}/c)^2$ and $b_2 = (-4.3 \pm 0.1 \pm 0.5)/(\mathrm{GeV}/c)^2$. Neither of them are compatible with the naïve expectation of $b_{\mathrm{diff}} \approx 10$ for the overall behaviour of diffractive scattering, but in general the slope is influenced by production of resonances. The exponential shape however points to diffractive production. A similar fit [92] with two slopes was performed by the WA102 collaboration that took data with $pp$ collisions at $\sqrt{s} = 29.1\,\mathrm{GeV}$ (450 GeV beam energy). WA102 extracted nearly the same slope $b_2^{\mathrm{WA102}} = (-3.8 \pm 0.2)/(\mathrm{GeV}/c)^2$, but a different slope $b_1^{\mathrm{WA102}} = (-24.5 \pm 0.1 \pm 0.5)/(\mathrm{GeV}/c)^2$.

For $\phi$ mesons, fits of a single exponential are compared to a model with an additional constant background term, $A_1 \exp(t'/b) + A_2$. The best fit results were obtained with the latter, with a $\chi^2/\mathrm{NDF}$ of 3.3 which is about 10 times better than the one for a single exponential. The resulting slope is $b = (-6.7 \pm 0.1 \pm 0.8)/(\mathrm{GeV}/c)^2$. The additional constant term hints to an admixture of another production process and is expected for central production. WA102 also measured the slope $b$ for $\phi$ mesons [92] with a comparable result of $b^{\mathrm{WA102}} = (-7.8 \pm 1.0)/(\mathrm{GeV}/c)^2$.

It should be noted again that the acceptance itself shows a $t$ dependence, which may influence the measurement. However, the determination of the slope is dominated by the points with small uncertainties in the low $t'$ region for which the acceptance shows only a small $t$ dependence and is close to being constant. Hence, the introduced systematic uncertainty is small compared to other systematic effects.

1 It should be noted that a fit of an exponential form with a linear background yields a slope of 7.9 at a comparable $\chi^2/\mathrm{NDF}$, however there is no preceeding application of such model.

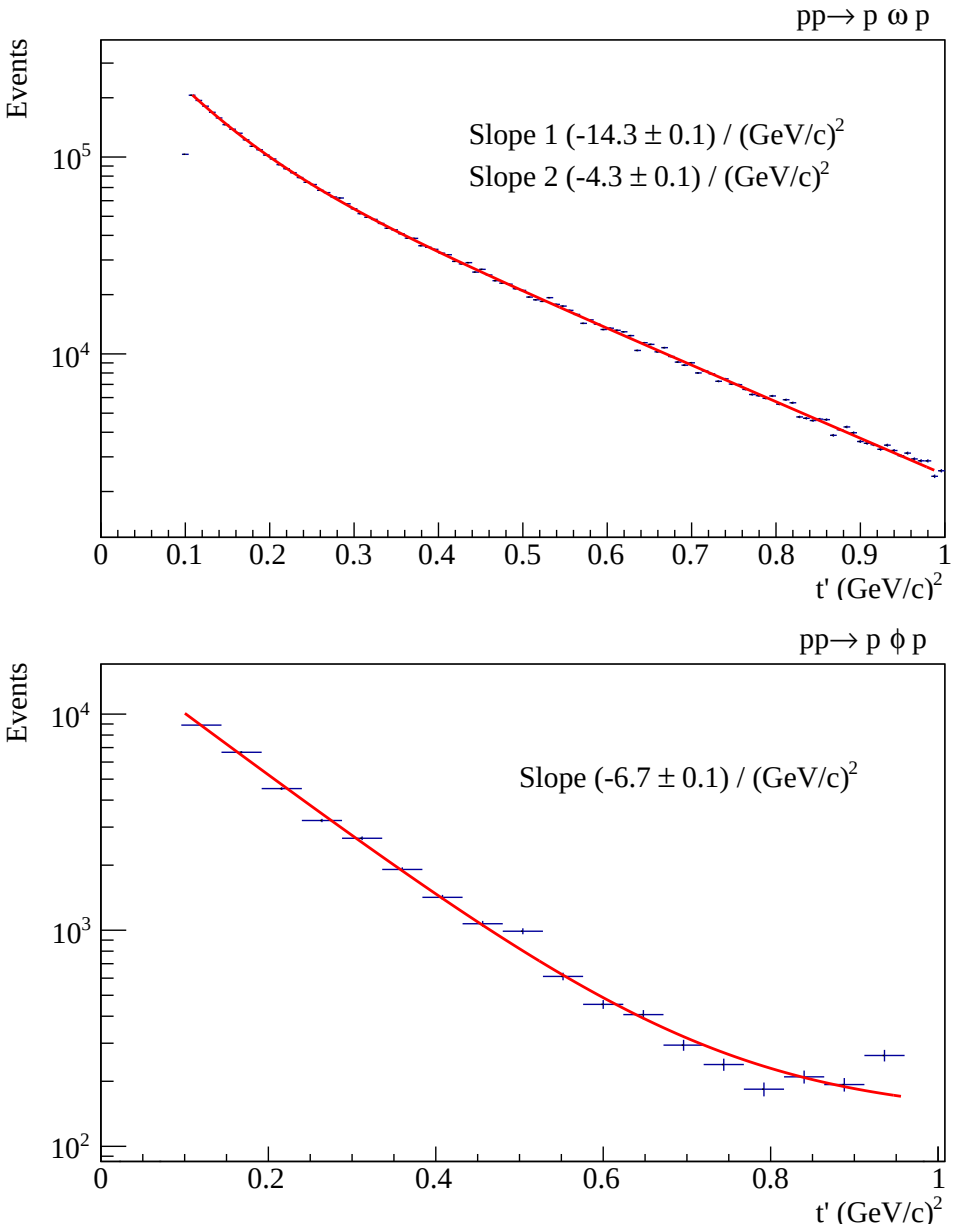


Figure 54: Acceptance corrected $t'$ distributions for $\omega$ mesons (upper panel) and $\phi$ mesons (lower panel). A fit of two exponentials, $A_1 \exp(t'/b_1) + A_2 \exp(t'/b_2)$, to the $t'_\omega$ distribution yields the two slopes $b_1 = (-14.3 \pm 0.1 \pm 1.8)/(\mathrm{GeV}/c)^2$ and $b_2 = (-4.3 \pm 0.1 \pm 0.5)/(\mathrm{GeV}/c)^2$. A fit of an exponential plus a constant term, $A_1 \exp(t'/b) + A_2$, to the $t'_\phi$ distribution yields the slope $b = (-6.7 \pm 0.1 \pm 0.8)/(\mathrm{GeV}/c)^2$.

Figure 55 illustrates the $x_\mathrm{F}$ distributions of the final state particles before (upper panels) and after (lower panels) applying acceptance corrections with $\omega$ mesons on the left side and $\phi$ mesons on the right side. In the upper panels for both $\omega$ and $\phi$ mesons, a gap between recoil particle and vector meson is seen, which is explained by the gap of coverage between RPD and spectrometer for polar angles from about 11° to 50° in the laboratory system. The distribution in the upper left panel for $\omega$ mesons and fast protons show a smooth overlap in the intermediate

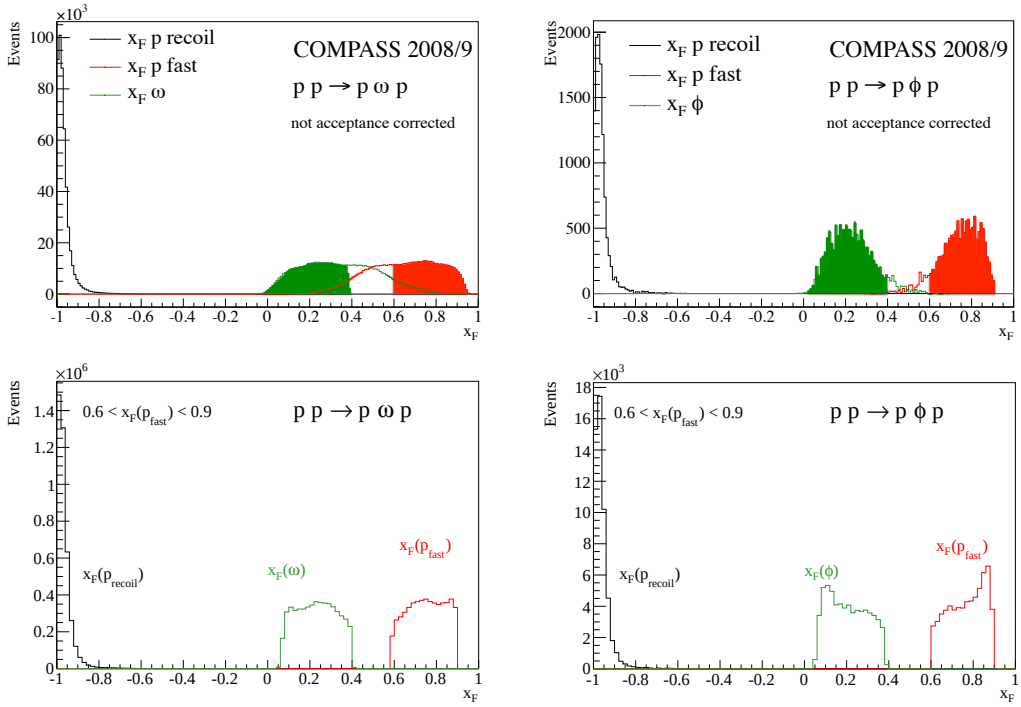


Figure 55: Upper panels: $x_F$ distributions for $pp \to pp\omega$, $\omega \to \pi^+\pi^-\pi^0$ (left) and $pp \to pp\phi$, $\phi \to K^+K^-$ without acceptance corrections. The filled areas correspond to data in the region $x_F > 0.6$. Lower panels: The same after acceptance corrections in case that the fast proton fulfils $0.6 < x_F < 0.9$.

$x_F$ range as it is expected for diffractive production. The distribution for the $\phi$ case (upper right panel) shows a $\phi$ accumulation in the more central region and, more separated from this, an accumulation of the fast proton at high $x_F$. This hints to central production of the $\phi$ in contrast to the $\omega$ case. The filled areas of the upper panels correspond to the data in the region $x_F > 0.6$. This restriction is necessary due to the limited acceptance as explained in Section 6.2.4 and leads to an artificial gap between the fast proton and the other final state particles. The lower panels show the distribution after acceptance corrections with the additional restriction to $x_F < 0.9$, which is introduced to study $\omega$ and $\phi$ mesons in comparable kinematic ranges.

The acceptance-corrected invariant mass distributions of the $pV$ system are shown in Figure 56. In the case of $\omega$, the distributions again are obtained using sideband subtraction. In the $M_{p\omega}$ spectrum, shown to the left in Figure 56, several structures – possibly resonances – on top of a smooth continuum are visible. Several structures appear if the data is divided into finer bins in $x_F$, shown in Figure 57. For higher $x_F$, the cut-off on the low mass side moves to higher mass values. The structures at higher masses are consistent with resonances listed in [29]. The leftmost structure is cut off on the low-mass side. In this mass region of about 1.8 to 1.9 GeV/$c^2$, there are mainly the $N^*(1875)$ with $J^P = 3/2^-$ and the $N^*(1900)$ with $J^P = 3/2^+$. At about 2.2 GeV/$c^2$, the PDG lists $N^*(2190)$ with $J^P = 7/2^-$, $N^*(2200)$ with $J^P = 9/2^+$ and $N^*(2250)$ with $J^P = 9/2^-$. The structure at about 2.6 GeV/$c^2$ could be $N^*(2600)$ with $J^P = 11/2^-$ and/or $N^*(2700)$ with $J^P = 13/2^+$. Notice-

ably, the resonances above $2\,\mathrm{GeV}/c^2$ all have high spin. A further investigation and clarification of these structures requires a partial wave analysis, which is beyond the scope of this thesis. However, it seems to be safe to assume that the low $p\omega$ mass region is dominated by resonances.
The $p\phi$ mass spectrum is depicted in the right panel of Figure 56. The background is subtracted using a fit (see Section 6.4) and the uncertainty from the fit is included in the error bars. Consistent with earlier findings [29], the spectrum appears without pronounced structures.

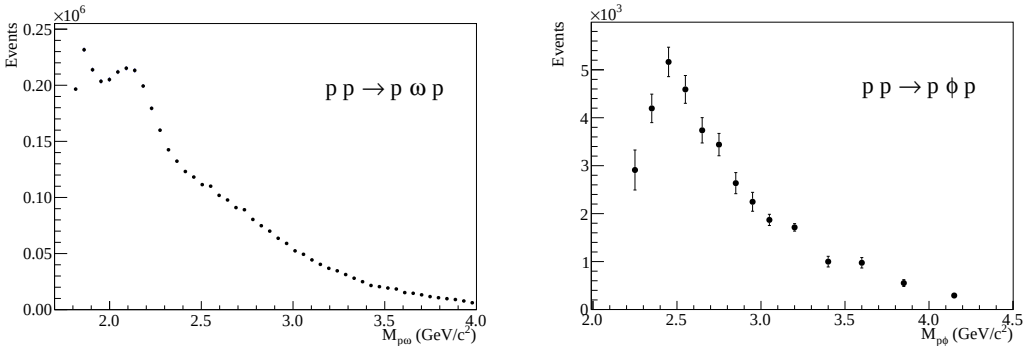


Figure 56: Distributions of the invariant mass of the proton – vector meson system for $0.6 < x_\mathrm{F} < 0.9$. Left: The $M_{p\omega}$ spectrum. The background is subtracted using the sideband method. Right: The $M_{p\phi}$ spectrum. The background is subtracted using a fit and the uncertainty from the fit is included in the error bars.

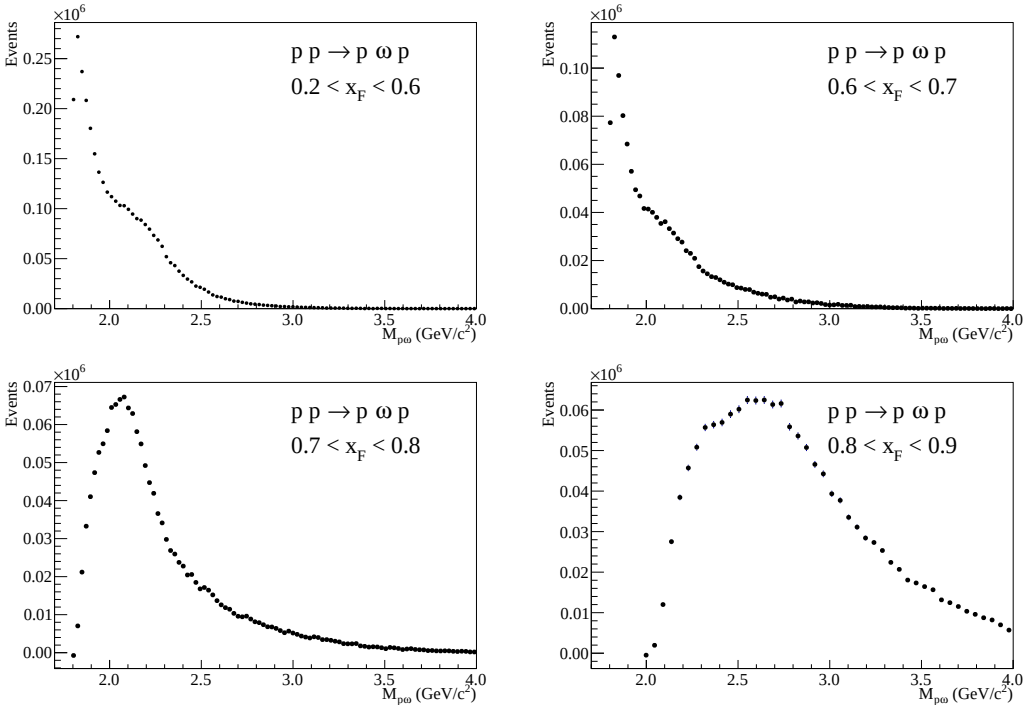


Figure 57: Distributions of the mass of the system of proton-$\omega$ for $0.2 < x_\mathrm{F} < 0.6$ (upper left), $0.6 < x_\mathrm{F} < 0.7$ (upper right), $0.7 < x_\mathrm{F} < 0.8$ (lower left) and $0.8 < x_\mathrm{F} < 0.9$ (lower right).

## 7.2 PRODUCTION RATIOS

The OZI rule is tested by the measurement of the production ratio $R_{\phi/\omega}$, which is the ratio of cross sections of $\phi$ to $\omega$ meson production. As described in Section 2.1.2, the OZI rule states that $R_{\phi/\omega}$ must only depend on the deviation from ideal mixing, $\Delta\theta = 3.7°$. Disregarding any phase space factors, the value of $R_{\phi/\omega}$ is predicted to be

$$R_{\phi/\omega} = \frac{\sigma(AB \to C + \phi)}{\sigma(AB \to C + \omega)} \stackrel{!}{=} \tan^2(\Delta\theta) = 4.2 \cdot 10^{-3} \equiv R_{\mathrm{OZI}} \tag{54}$$

if $A, B, C$ are hadrons without strangeness. In many experiments, the OZI prediction is found to be accurate up to the percent level. However, the prediction turns out to be violated quite drastically in some reactions, such as $p\bar{p}$ annihilation, $pd \to {}^3\mathrm{He}V$, $pp \to pVp$, and $\pi p \to \pi pV$, where $V$ denotes the vector mesons $\phi$ and $\omega$. For the further discussion of these findings, it is helpful to define the violation factor $F_{\mathrm{OZI}} = R_{\phi/\omega}/R_{\mathrm{OZI}}$.

There are several ideas to interpret OZI violations. Two categories of explanations emerged. The first considers "true" violation because there are simply no quark lines involved [98] in the reaction. The reaction would thus be $SU(3)_{\mathrm{flavour}}$ symmetric and the OZI rule would be maximally violated. The second category considers the OZI evaded by intermediate states [31, 100, 119] or because of a strangeness component in the nucleon [62, 63]. Another possibility for large OZI violations could also be cryptoexotic baryon resonances (*e.g.* "pentaquarks") decaying to $N\phi$ [122]. Up to now, there is no experimental support for this hypothesis.

### 7.2.1 *Analysis*

The $\pi^+\pi^-\pi^0$ and $K^+K^-$ data are divided into three intervals of $x_{\mathrm{F}}$: 0.6–0.7, 0.7–0.8 and 0.8–0.9. In each interval, the acceptance corrected $M(\pi^+\pi^-\pi^0)$ and $M(K^+K^-)$ yields are calculated using the method described in Section 6.4 and corrected for the branching ratios of the $\omega \to \pi^+\pi^-\pi^0$ (89.2%) and $\phi \to K^+K^-$ (48.9%) decays, respectively. The production ratio $R_{\phi/\omega}(x_{\mathrm{F}})$ is then calculated in each $x_{\mathrm{F}}$ interval:

$$R_{\phi/\omega}(x_{\mathrm{F}}) = \frac{d\sigma(p\,p \;\to\; p\,\phi\,p)/dx_{\mathrm{F}}}{d\sigma(p\,p \;\to\; p\,\omega\,p)/dx_{\mathrm{F}}}. \tag{55}$$

### 7.2.2 *Results*

The ratio $R_{\phi/\omega}(x_{\mathrm{F}})$ is measured to be 0.019, 0.017 and 0.012 in the three intervals of $x_{\mathrm{F}}$ (0.6–0.7, 0.7–0.8, 0.8–0.9). This corresponds to an OZI rule violation $F_{\mathrm{OZI}}$ of $4.5 \pm 0.6$, $4.0 \pm 0.5$, and $2.9 \pm 0.4$, see Table 8. The contributions to the uncertainty on $R_{\phi/\omega}(x_{\mathrm{F}})$ are listed separately, *i.e.* statistical uncertainty (stat.), uncertainty due to background subtraction (fit), and systematic uncertainties (syst.). The uncertainty of $F_{\mathrm{OZI}}$ is the quadratic sum of the afore-mentioned contributions. Notice that the violation seems to decrease with higher $x_{\mathrm{F}}$ values. The average value of $R_{\phi/\omega}$ =

| $x_F$ | $R_{\phi/\omega}(x_F)$ | Stat. | Fit | Syst. | $F_{OZI}$ |
|---|---|---|---|---|---|
| 0.6–0.7 | 0.019 | 0.0003 | 0.0006 | 0.0023 | $4.5 \pm 0.6$ |
| 0.7–0.8 | 0.017 | 0.0002 | 0.0004 | 0.002 | $4.0 \pm 0.5$ |
| 0.8–0.9 | 0.012 | 0.0002 | 0.0005 | 0.0014 | $2.9 \pm 0.4$ |

Table 8: Measured differential cross section ratios $R_{\phi/\omega}(x_F$ and corresponding OZI violation factors $F_{OZI}$. The contributions to the uncertainty on $R_{\phi/\omega}(x_F$ are listed separately, *i.e.* statistical uncertainty (stat.), uncertainty due to background subtraction (fit), and systematic uncertainties. The uncertainty on $F_{OZI}$ is the combined one.

$0.0160 \pm 0.0003 \pm 0.0020$ is consistent with the result from SPHINX [76], which is $0.0155 \pm 0.0005 \pm 0.0031$.

The $M_{p\omega}$ distributions (Figure 57) indicate that the production cross section is increased due to the resonances. Therefore, a measurement of $R_{\phi/\omega}$ will result in a decreased value by this effect. As no resonances are apparent above $M_{p\omega} = 3.3\,\mathrm{GeV}/c^2$, an approach to observe the undistorted ratio is a study of data in the region above this mass. Due to the different masses of $\phi$ and $\omega$, a different mass cut has to be applied in the two channels. Instead, the same phase space region for both mesons is selected by a cut on their momenta $p_V$, which are determined in the $pV$ rest system:

$$p_V = \frac{\sqrt{\left(M_{pV}^2 - (m_V + m_p)^2\right)\left(M_{pV}^2 - (m_V - m_p)^2\right)}}{2\,M_{pV}}. \tag{56}$$

The value of $M_{p\omega} = 3.3\,\mathrm{GeV}/c^2$ consequently corresponds to $p_V = 1.4\,\mathrm{GeV}/c$, which will be used as a cut for $\phi$, as well. Requiring $p_V > 1.4\,\mathrm{GeV}/c$ yields the ratios of 0.034 and 0.032 in the two bins $0.7 < x_F < 0.8$ and $0.8 < x_F < 0.9$, respectively, which corresponds to OZI violation factors of $7.9 \pm 1.1$ and $7.6 \pm 1.0$. In the $0.6 < x_F < 0.7$ bin, the $\phi$ yield is insufficient for a reliable $R_{\phi/\omega}$ estimate. The results together with the different contributions to the uncertainty are summarised in Table 9. Within experimental uncertainties, the OZI violation thus appears to be independent of $x_F$ in the observed range with $F_{OZI}$ about 8. In order to remove the resonant region, the SPHINX analysis used a cut of $1\,\mathrm{GeV}/c$ on the $p_V$ momentum, which is justified by the lower beam energy of 70 GeV. The cut corresponds to mass values of $M_{p\omega}$ of $2.6\,\mathrm{GeV}/c^2$ and $M_{p\phi}$ of $2.8\,\mathrm{GeV}/c^2$. The upper part of Table 9 shows $R_{\phi/\omega}$ for the SPHINX cut. The obtained value of $R_{\phi/\omega}$ of 0.032, 0.038 and 0.19 correspond to OZI violation factors $F_{OZI}$ of $7.6 \pm 1.0$, $9.0 \pm 1.1$, and $4.5 \pm 0.6$ respectively. For $x_F \leq 0.8$, the results are consistent with the SPHINX result $\frac{\sigma(p\,N \to p\,N\,\phi)}{\sigma(p\,N \to p\,N\,\omega)} = 0.040 \pm 0.0004 \pm 0.008$, but with the remark that the SPHINX $x_F$ range is not stated explicitly.

Figure 58 summarises the findings for $F_{OZI}$ with and without cuts on the vector mesons momentum. The violation indeed appears to be lowered due to resonant contributions, which are present if no cut is applied (green circles). The violation varies from about 3 to 4.5 with a tendency to be lower for high $x_F$. After removing

the low-mass region and hence apparent resonant contributions, no dependence on $x_F$ is observed and $F_{OZI}$ doubles to about 8 (red triangles).

| $p_V$ (GeV/$c$) | $x_F$ | $R_{\phi/\omega}(x_F)$ | Stat. | Fit | Syst. | $F_{OZI}$ |
|---|---|---|---|---|---|---|
| $> 1.0$ | 0.6–0.7 | 0.032 | 0.0007 | 0.0013 | 0.0038 | $7.6 \pm 1.0$ |
| $> 1.0$ | 0.7–0.8 | 0.038 | 0.0006 | 0.0010 | 0.0046 | $9.0 \pm 1.1$ |
| $> 1.0$ | 0.8–0.9 | 0.019 | 0.0003 | 0.0005 | 0.0023 | $4.5 \pm 0.6$ |
| $> 1.4$ | 0.7–0.8 | 0.033 | 0.0013 | 0.0025 | 0.0040 | $7.9 \pm 1.1$ |
| $> 1.4$ | 0.8–0.9 | 0.032 | 0.0011 | 0.0017 | 0.0038 | $7.6 \pm 1.0$ |

Table 9: Differential production ratios $R_{\phi/\omega}(x_F$ and corresponding OZI violation factors $F_{OZI}$ for different $p_V$ cuts.

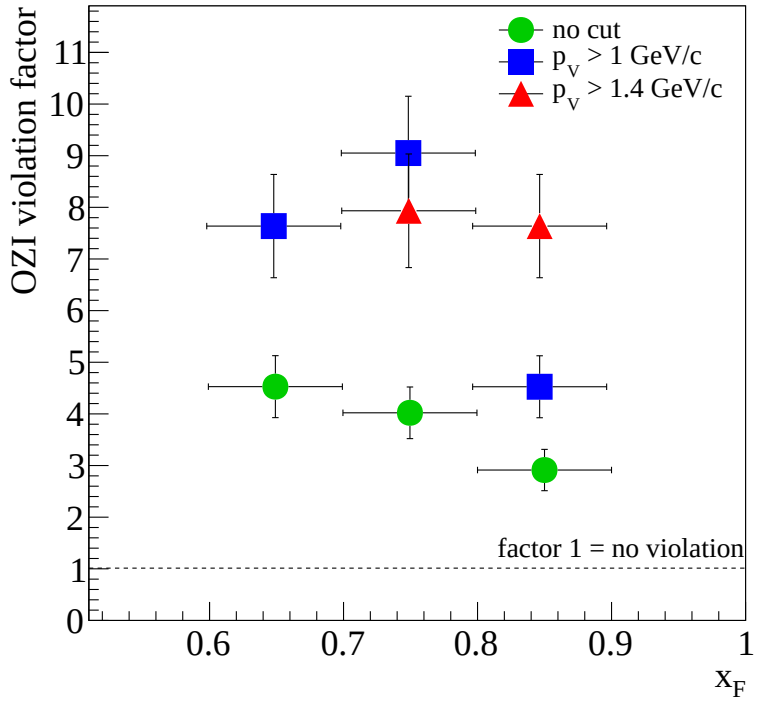


Figure 58: $F_{OZI}$ as a function of $x_F$ with several conditions on the vector meson momentum $p_V$.

### 7.2.3 *Previous findings*

There is a long list of earlier measurements of $R_{\phi/\omega}$, which were done over a wide energy range starting from threshold to beam energies up to 70 GeV. Table 10 gives an overview of experimental results for $R_{\phi/\omega}$ in different reactions including results from inclusive measurements, as well.
In general, proton–proton collisions exhibit large OZI violations, which seems to favour explanations by the hidden strangeness component of the nucleon. Figure 59

| Reaction | $p_{\text{beam}}$ [GeV/$c$] | $R_{\text{OZI}}$ [$10^{-3}$] | Reference |
|---|---|---|---|
| $pp \to pVp$ | 2.85 | $3.8 \pm 0.2^{+1.2}_{-0.9}$ | [24] |
| $pp \to pVp$ | 10 | $20 \pm 5$ | [23] |
| $pp \to pVp$ | 24 | $26.5 \pm 18.8$ | [38] |
| $pp \to \pi^+\pi^- pVp$ | 24 | $1.2 \pm 0.8$ | [38] |
| $pp \to pVp(\pi^+\pi^-)_{\times 0,1,2}$ | 24 | $19 \pm 7$ | [38] |
| $pp \to XVp$ | 70 | $16.4 \pm 0.4$ | [74] |
| $pp \to pVp$ | 70 | $15.5 \pm 0.5 \pm 3.0$ | [76] |
| $pp \to XV$ | 360 | $4^{+5}_{-4}$ | [12] |
| $\bar{p}p \to \pi^+\pi^- V$ | 0.7 | $19 \pm 5$ | [51] |
| $\bar{p}p \to \rho^0 V$ | 0.7 | $13 \pm 4$ | [51] |
| $\bar{p}p \to \pi^+\pi^- V$ | 1.2 | $11^{+3}_{-4}$ | [56] |
| $\bar{p}p \to \pi^+\pi^- V$ | 2.3 | $17.5 \pm 3.4$ | [47] |
| $\bar{p}p \to \pi^+\pi^- V$ | 3.6 | $9^{+4}_{-7}$ | [56] |
| $\bar{p}d \to nV$ | 0.1-0.2 | $156 \pm 29$ | [18, 78, 106] |
| $pd \to {}^3\text{He}V$ | 1.28–1.86 | $63 \pm 5^{+27}_{-8}$ | [131, 132] |
| $\pi^+ n \to pV$ | 1.54–2.6 | $21 \pm 11$ | [53, 55] |
| $\pi^+ p \to \pi^+ pV$ | 3.54 | $19 \pm 11$ | [8] |
| $\pi^- p \to nV$ | 5–6 | $3.5 \pm 1$ | [22] |
| $\pi^- p \to nV$ | 6 | $3.2 \pm 0.4$ | [50] |
| $\pi^- p \to \pi^- Vp$ | 10 | $6 \pm 3$ | [23] |
| $\pi^- p \to \pi^-\pi^+\pi^- Vp$ | 19 | $5^{+5}_{-2}$ | [130] |
| $\pi^- p \to nV$ | 32.5 | $2.9 \pm 0.9$ | [58] |
| $\pi^- p \to XV$ | 360 | $14 \pm 0.9$ | [11] |

Table 10: Overview of $R_{\phi/\omega}$ measurements in different reactions. The beam momentum $p_{\text{beam}}$ always refers to the first particle in the reaction. For further details, see text.

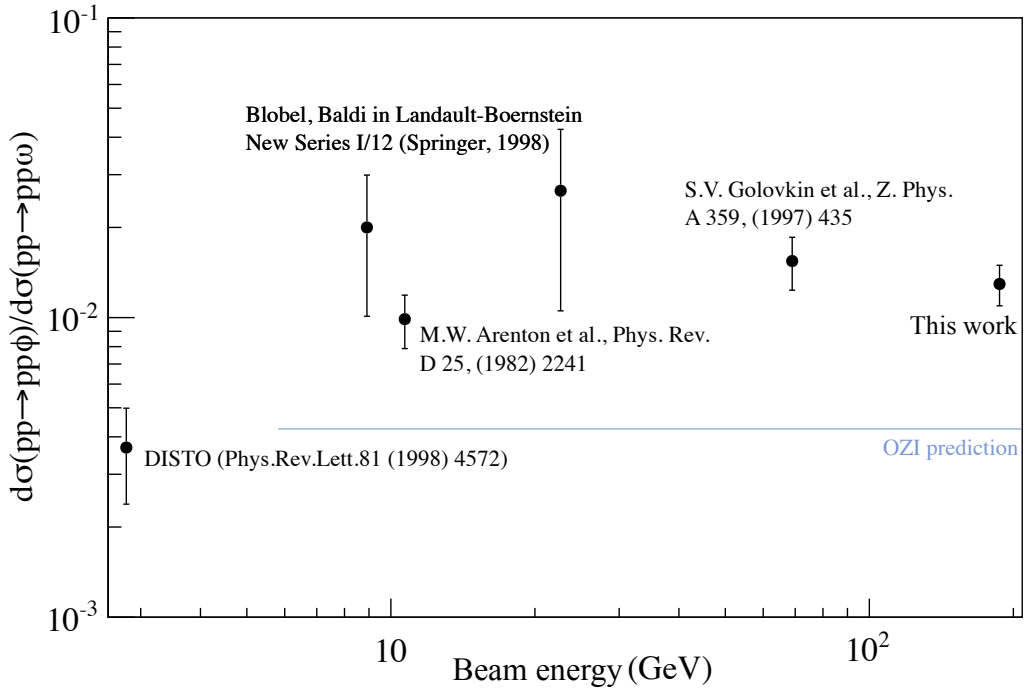


Figure 59: Overview of $R_{\phi/\omega}$ measurements in $pp$ collisions. The line represents the OZI rule prediction of 0.0042 which is obtained without phase space corrections.

summarises the available data as a function of beam momentum. The DISTO [24] collaboration measured $R_{\phi/\omega} = 3.8 \cdot 10^{-3}$ very close to the threshold, which at the first look seems to show no violation at all. However, so close to the threshold the ratio has to be corrected for the available phase space, which leads to a large corrected value of about $53 \cdot 10^{-3}$. The measurement closest to COMPASS energies is the one from SPHINX [76] at 70 GeV beam momentum, with $R_{\phi/\omega} = 15.5 \cdot 10^{-3}$. As can be seen from the first panel of Table 10, the violation seems to be more or less independent of the measured final state as long as it still has at least one intact proton and the measurement is exclusive. The violation also seems to be weakly dependent on the beam energy. With the exception of the DISTO point, all measurements are in the range of about $15 \cdot 10^{-3} - 25 \cdot 10^{-3}$. In Figure 59, the COMPASS result (right-most point) is compatible with other findings for $pp$ collisions at lower beam energy. There seems to be no obvious dependence of $R_{\phi/\omega}$ on the beam energy.

The available data for annihilation experiments, mostly for $\bar{p}p$, exhibits also large OZI violations. The violation ranges from $9 \cdot 10^{-3} - 19 \cdot 10^{-3}$, again independent of final state and energy. One more time, a possible explanation is found by a hidden strangeness component in the nucleon. With this argument, the violation in pion–induced reactions should be smaller, which is indeed observed. The lowest panel of Table 10 summarises the results for such reactions. Interestingly, the results vary a lot between similar final states, but also for different energies, so no clear conclusion can be drawn. More details and an overview of further explanations can be found in the review [106].

## 7.3 SPIN ALIGNMENT

The spin alignment of vector mesons is highly sensitive to the production mechanism, as discussed in Section 2.2.2. With the help of the spin-density matrix formalism, the spin alignment is determined from angular distributions of the angle between an analyser and the quantisation axis of a chosen reference system. The choice of a reference is specific to the investigated production process. For a better illustration of the following discussion, Figure 7 of Section 2.3.3 is repeated by Figure 60.

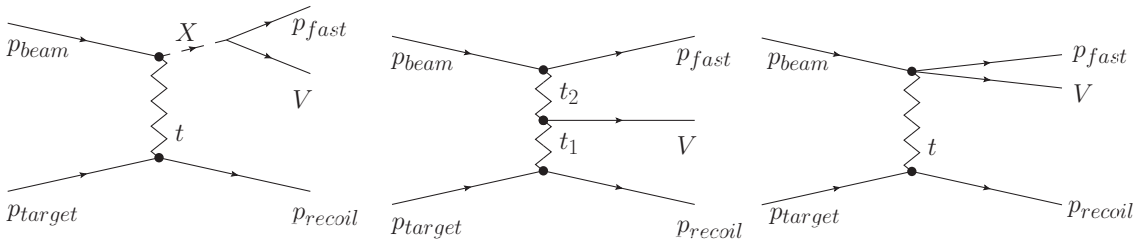


Figure 60: Left: Resonant single diffractive excitation of the beam proton to a resonance X with subsequent decay. Middle: Central production. Right: Non-resonant single diffractive scattering of the beam proton.

For diffractive production (Figure 60, left panel), the quantisation axis along the direction of the $pV$ system in the rest system of the vector meson $V$ is well-suited, especially if $pV$ is the result of a resonance decay. The $pV$ system with such a definition of the quantisation axis is referred to as the helicity frame, originally introduced by Gottfried and Jackson [79]. As discussed in the previous section, it is observed that resonances play an important role in the $pp \to p\omega p$ cross section. It was already noted in Section 7.1 that all possible resonance candidates possess high spin, which means they have to transfer significant angular momentum in their decay. This should be evident in measured angular distributions of the vector mesons. A high anisotropy is expected if considerable angular momentum has to be transferred. If $p$ and $V$ do not originate from the same vertex as would be the case for central production, then isotropy is expected.
For central production (Figure 60, middle panel), the quantisation axis is chosen in the direction of the momentum transfer from the beam proton to the fast proton. If the fast proton and the vector meson stem from the same vertex (Figure 60, left and right panel), *e.g.* from resonance decay, there will be no given direction and isotropy is expected. If the production vertex of the vector meson is separated from the vertex from incoming beam to fast proton, anisotropy is expected.

### 7.3.1 *Analysis*

The angular distributions are obtained as explained in Section 6.4. The data are divided in 10 equidistant bins of $|\cos\theta|$, where $\theta$ denotes the angle between the chosen analyser and the selected quantisation axis. The analyser for $\phi$ is one of the momentum vectors of the decay kaons. The $\omega$ decays into three particles. As shown

in *e.g.* [49, 79] or by explicit calculation of the $D$-functions, the corresponding angle of three-body decays compared to two-body decays is the normal vector to the decay plane.
Due to the quadratic $\cos\theta$ dependence of the spin alignment $\rho_{00}$, the data is represented as a function of $\cos^2\theta$. The spin alignment $\rho_{00}$ is extracted by fitting a linear function of the form $a + bx, x = \cos^2\theta$ to the data points (full circles in the figures) and then solving for Equation 34. In the figures of this part of the analysis, the error bars represent the statistical uncertainty and the point-to-point uncertainty of the background subtraction. Systematic effects such as efficiencies are flat with respect to $\cos\theta$. They would show up as a constant, global shift of the distribution which is absorbed in the fit as a normalisation constant. Thus, these types of uncertainties do not contribute. In addition to the signal points, the background distribution in the sidebands of the signal is shown by open circles in the figures.

### 7.3.2 *Spin alignment with respect to the direction of the pV system*

The angular distributions are determined in three equidistant $x_F$ intervals between 0.6 and 0.9. The interval $0.2 < x_F < 0.6$ is added for the $\omega$ meson because the acceptance is still substantial in this region in contrast to the $\phi$ case. The distributions are shown in Figures 61 for $\omega$ and 62 for $\phi$. In both cases, the background distribution is isotropic. It is noteworthy that the slope of the angular distributions is varying with $x_F$ in the case of the $\omega$ meson (see Figure 61), going from a negative slope in the interval $0.2 < x_F < 0.6$ passing through isotropy in the interval $0.7 < x_F < 0.8$ to a positive slope in the interval $0.8 < x_F < 0.9$. No such behaviour is observed in the case of the $\phi$ meson in Figure 62. Here, the distributions are isotropic within uncertainties in all three $x_F$ intervals. The statistical uncertainty for the $\phi$ case is significantly larger compared to the $\omega$ case. Fitting a constant function to the angular distributions of the $\phi$ meson yields a similar $\chi^2$ compared to a linear function.
The fit results for $\rho_{00}$ are shown in Table 11 and summarised in Figure 63. The SPHINX collaboration measured $\rho_{00}$ in $pN \to pN\omega$, $\omega \to \pi^0\gamma$ in the $\omega$ helicity frame. They studied the two regions of $x_F(\omega) > 0.79$ and $x_F(\omega) > 0.86$, which corresponds to about $x_F < 0.2$ and $x_F < 0.12$ and obtained $\rho_{00} = 1.0 \pm 0.16$ and $\rho_{00} = 1.0 \pm 0.22$, respectively [75]. Due to the very different kinematic regime, the SPHINX and COMPASS measurements are not comparable and the SPHINX results are only listed for the sake of completeness.
The same $p_\omega > 1\,\mathrm{GeV}/c$ cut as for the production ratio determination was applied in order to reject the low-mass region with visible resonances. Figure 66 in Appendix A.1 shows the obtained angular distributions. The $\omega$ meson alignment with respect to the $p\omega$ direction almost vanishes for $p_\omega > 1\,\mathrm{GeV}/c$ and $x_F < 0.8$ as it is expected for non-resonant production. However, the production ratio result indicates that still resonances contribute at large $x_F$ which cannot be seen from the angular distributions within the given uncertainties.
For the tighter cut $p_\omega > 1.4\,\mathrm{GeV}/c$ , the angular distribution of the $\omega$ meson decay is isotropic for the high $x_F$ bin. The distributions are shown in Figure 67 in Appendix A.1. This is in line with the observation of the production ratio, where the

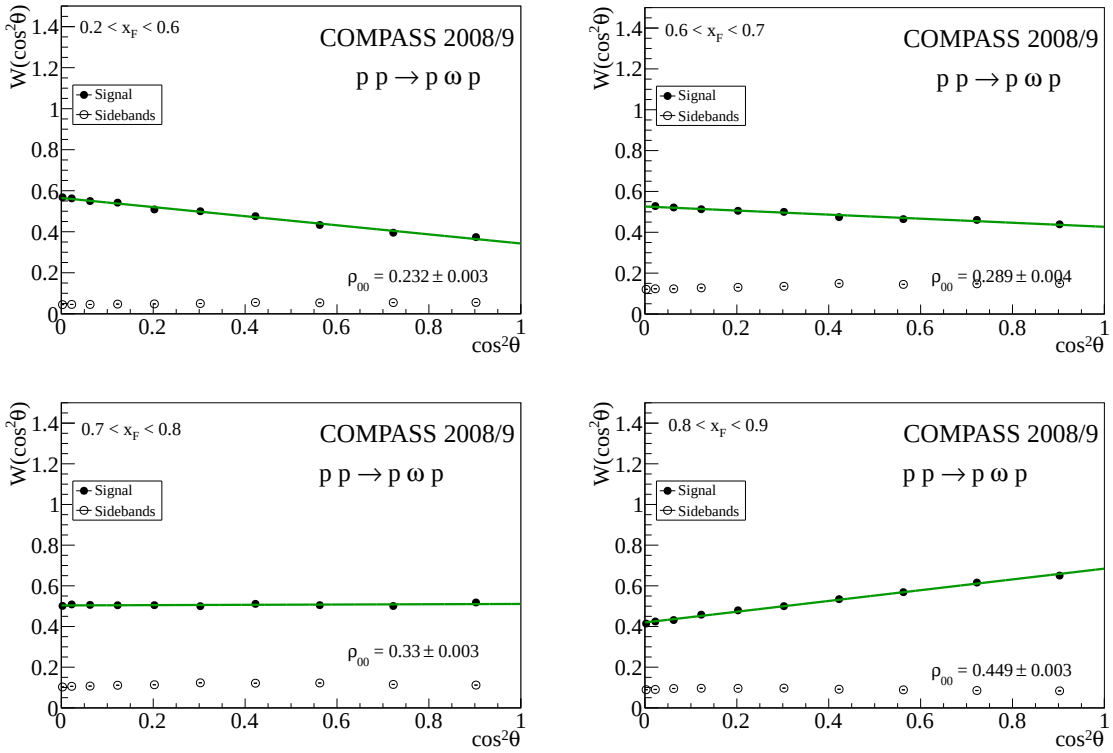


Figure 61: Helicity angle distributions for the $\omega$ meson. The full circles represent the angular distributions of $\cos^2\theta$. The distributions are obtained in different $x_F$ regions as described in the text. The open circles show the background distribution in the sidebands.

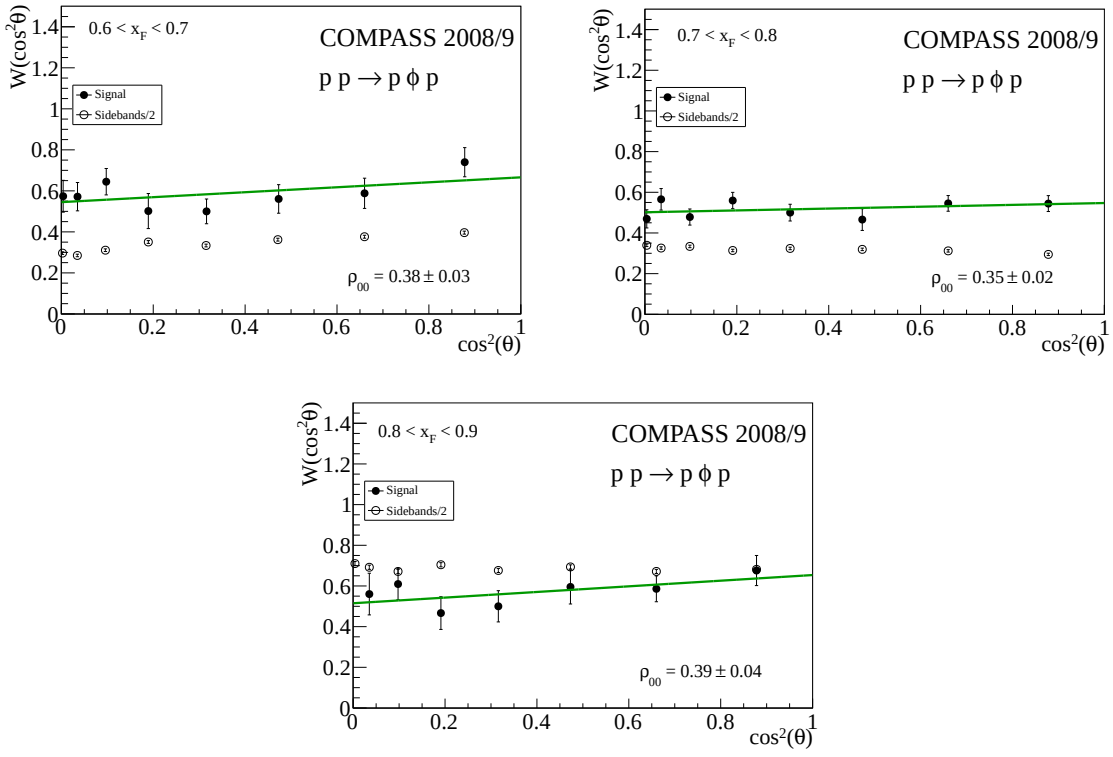


Figure 62: Helicity angle distributions for the $\phi$ meson. The full circles represent the angular distributions of $\cos^2\theta$. The distributions are obtained in different $x_F$ regions as described in the text. The open circles show the background distribution in the sidebands.

ratio becomes independent of $x_F$ for the tighter cut. There is no SPHINX analysis with $p_\omega$ cut available for comparison.

| Reaction | $x_F$ | $\rho_{00}$ |
|---|---|---|
| $pp \to pp\phi, \phi \to K^+K^-$ | 0.6–0.7 | $0.38 \pm 0.03$ |
| $pp \to pp\phi, \phi \to K^+K^-$ | 0.7–0.8 | $0.35 \pm 0.02$ |
| $pp \to pp\phi, \phi \to K^+K^-$ | 0.8–0.9 | $0.39 \pm 0.04$ |
| $pp \to pp\omega, \omega \to \pi^+\pi^-\pi^0$ | 0.2–0.6 | $0.232 \pm 0.003$ |
| $pp \to pp\omega, \omega \to \pi^+\pi^-\pi^0$ | 0.6–0.7 | $0.289 \pm 0.004$ |
| $pp \to pp\omega, \omega \to \pi^+\pi^-\pi^0$ | 0.7–0.8 | $0.330 \pm 0.003$ |
| $pp \to pp\omega, \omega \to \pi^+\pi^-\pi^0$ | 0.8–0.9 | $0.449 \pm 0.003$ |
| $pp \to pp\omega, \omega \to \pi^+\pi^-\pi^0, p_V > 1.0$ GeV/$c$ | 0.2–0.6 | $0.30 \pm 0.01$ |
| $pp \to pp\omega, \omega \to \pi^+\pi^-\pi^0, p_V > 1.0$ GeV/$c$ | 0.6–0.7 | $0.34 \pm 0.01$ |
| $pp \to pp\omega, \omega \to \pi^+\pi^-\pi^0, p_V > 1.0$ GeV/$c$ | 0.7–0.8 | $0.306 \pm 0.006$ |
| $pp \to pp\omega, \omega \to \pi^+\pi^-\pi^0, p_V > 1.0$ GeV/$c$ | 0.8–0.9 | $0.463 \pm 0.003$ |
| $pp \to pp\omega, \omega \to \pi^+\pi^-\pi^0, p_V > 1.4$ GeV/$c$ | 0.8–0.9 | $0.37 \pm 0.03$ |

Table 11: Spin alignments $\rho_{00}$ extracted from the helicity angle distributions for $\phi$ and $\omega$ production, the latter case with various cuts on $p_\omega$.

In order to study closer the role of resonances, a "scan" over the $M_{p\omega}$ spectrum is performed. Figure 68 in Appendix A.2 shows the angular distributions and Table 12 and Figure 64 the results for $\rho_{00}$. A clear dependence of $\rho_{00}$ on $M_{p\omega}$ is seen, which is consistent with the previous findings and can be explained by the existence of intermediate states or resonances. The dependence of $\rho_{00}$ on $x_F$ seems to be connected to the $\rho_{00}$ dependence on $M_{p\omega}$ *via* the observed intermediate states. Different structures dominate the $\omega$ production in the different $x_F$ regions, which seem to dominate the spin alignment.

Due to the limited statistics, the $\phi$ data is divided into two mass bins for 2.1 GeV/$c^2$ $< M_{p\phi} <$ 2.6 GeV/$c^2$ and 2.6 GeV/$c^2$ $< M_{p\phi} <$ 3.3 GeV/$c^2$. The corresponding angular distributions are shown in Figure 69 in Appendix A.2 and turn out to be isotropic. This is in line with the $p\phi$ spectrum in Figure 56, which does not exhibit apparent structures. Production of $\phi$ mesons *via* a resonance including possible cryptoexotic states [122] is therefore excluded in the studied kinematic region. Since the acceptance is small close to $M_{p\phi}$=2.1 GeV/$c^2$, no conclusions can be drawn concerning resonances close to the production threshold. In general, no baryon resonances are known to decay into $p\phi$ [29]. This together with the close-to-isotropic angular distributions indicates that the $\phi$ mesons are not produced *via* diffractive excitation. A central/non-resonant production seems to be more likely within the studied kinematical range.

In order to better compare $\rho_{00}$ for $\phi$ and $\omega$ within corresponding $M_{pV}$ ranges, the $\omega$ mesons are selected within the same $p_V$ ranges as for the $\phi$ case. The last panel of Table 12 shows the results for a high mass and a low mass bin. The angular distribu-

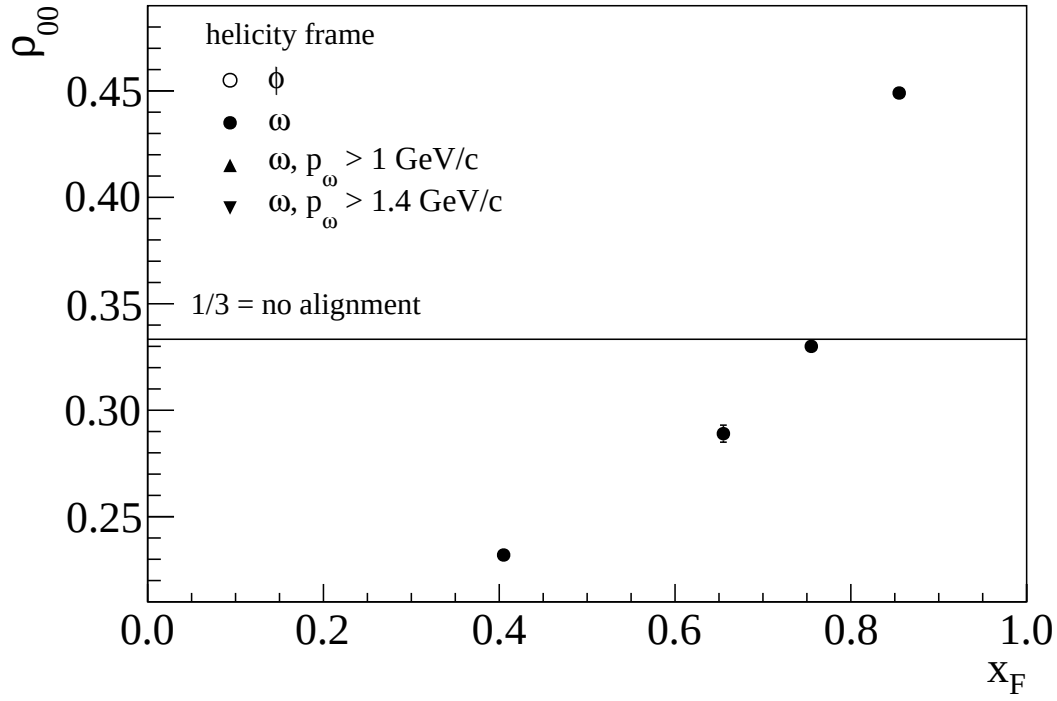


Figure 63: Overview of results for $\rho_{00}$ as a function of $x_F$ in the helicity frame with and without cuts on the momentum $p_\omega$.

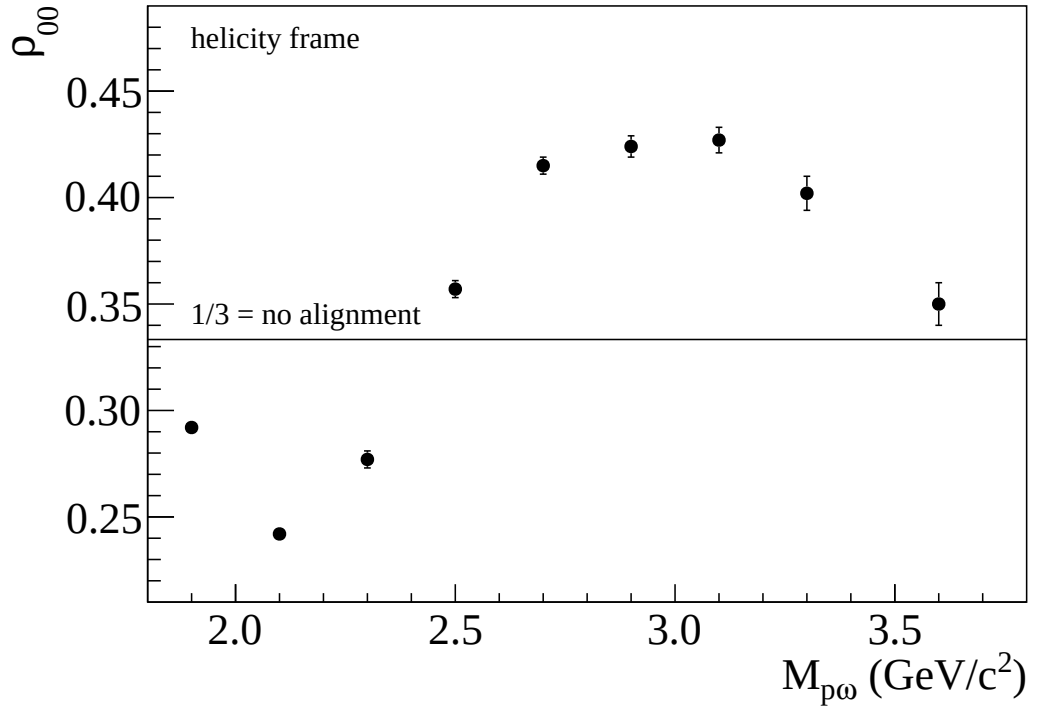


Figure 64: Overview of results for $\rho_{00}$ as a function of the mass of the $p\omega$ system in the helicity frame.

| Reaction | $M_{p\mathrm{V}}$ in GeV/$c^2$ | $\rho_{00}$ |
|---|---|---|
| $0.2 < x_\mathrm{F} < 0.9$ | | |
| $pp \to pp\omega, \omega \to \pi^+\pi^-\pi^0$ | 1.8–2.0 | $0.292 \pm 0.002$ |
| $pp \to pp\omega, \omega \to \pi^+\pi^-\pi^0$ | 2.0–2.2 | $0.242 \pm 0.003$ |
| $pp \to pp\omega, \omega \to \pi^+\pi^-\pi^0$ | 2.2–2.4 | $0.277 \pm 0.004$ |
| $pp \to pp\omega, \omega \to \pi^+\pi^-\pi^0$ | 2.4–2.6 | $0.357 \pm 0.004$ |
| $pp \to pp\omega, \omega \to \pi^+\pi^-\pi^0$ | 2.6–2.8 | $0.415 \pm 0.004$ |
| $pp \to pp\omega, \omega \to \pi^+\pi^-\pi^0$ | 2.8–3.0 | $0.424 \pm 0.005$ |
| $pp \to pp\omega, \omega \to \pi^+\pi^-\pi^0$ | 3.0–3.2 | $0.427 \pm 0.006$ |
| $pp \to pp\omega, \omega \to \pi^+\pi^-\pi^0$ | 3.2–3.4 | $0.402 \pm 0.008$ |
| $pp \to pp\omega, \omega \to \pi^+\pi^-\pi^0$ | 3.4–3.8 | $0.35 \pm 0.01$ |
| $0.6 < x_\mathrm{F} < 0.9$ | | |
| $pp \to pp\phi, \phi \to K^+K^-$ | 2.1–2.6 | $0.39 \pm 0.06$ |
| $pp \to pp\phi, \phi \to K^+K^-$ | 2.6–3.3 | $0.35 \pm 0.02$ |
| $pp \to pp\omega, \omega \to \pi^+\pi^-\pi^0$ | 1.88–2.42 | $0.321 \pm 0.002$ |
| $pp \to pp\omega, \omega \to \pi^+\pi^-\pi^0$ | 2.42–3.17 | $0.423 \pm 0.002$ |

Table 12: Upper section: $\rho_{00}$ extracted from the helicity angle distributions for $\omega$ production in the region $0.2 < x_\mathrm{F} < 0.9$ for different $M_{p\omega}$ regions. Middle section: The same but for $\phi$ production in the range $0.6 < x_\mathrm{F} < 0.9$. Lower section: The $\rho_{00}$ values extracted for $\omega$ within $0.6 < x_\mathrm{F} < 0.9$ and in the corresponding mass range as in the case of $\phi$ as explained in the text.

tions for the low mass bins for $\phi$ and $\omega$ are fairly isotropic and the spin alignments agree within uncertainty. However, the agreement seems to be coincidental because the different slopes for the $\omega$ case seem to average out in the studied mass region. With the limited statistics of $\phi$ mesons, such an averaging effect cannot be ruled out for the $\phi$ case, as well. The results for the high mass bin differ. While no alignment of the $\phi$ is observed, the $\omega$ alignment seems to be dominated by resonances in this mass region.

### 7.3.3 *Spin alignment with respect to the transferred momentum*

The isotropic spin alignment for $\phi$ and the absence of resonances in the $p\phi$ system hint to a different production mechanism where the $\phi$ does not originate from the scattering vertex between incoming beam and fast proton, *e.g.* central production. As discussed in the introduction to this section, a well-suited choice is the reference system with a quantisation axis along the direction of the transferred momentum in order to study central production. This quantisation axis is opposite to the momentum transfer from the target to the recoil in the rest system of the vector meson. The angle $\theta$ is calculated in the rest system of the vector meson with the same analyser as before.

The angular distributions for $\omega$ are shown in Figure 70 and the distributions for $\phi$ in Figure 71, both in Appendix A.3. The extracted values of $\rho_{00}$ are presented in Table 13 and Figure 65. The angular distribution of the background (open circles) is isotropic in all cases. Both $\phi$ and $\omega$ mesons are aligned transverse to the direction of the exchange Reggeon/Pomeron. The alignment is stronger when $x_F$ increases. In production processes without an intermediate state or resonance, the vector meson will "remember" the direction of momentum transfer of the incoming Pomeron which in turn should affect the spin orientation of the vector meson. This is the case in central production and when the vector meson is produced by a shake-out of a $q\bar{q}$ object in the proton. The alignment of the $\omega$ meson reaches a maximum in the $0.7 < x_F < 0.8$ region while it is slightly smaller in $0.8 < x_F < 0.9$.
As discussed in the previous section, the low mass region dominated by $p\omega$ resonances are excluded by a $p_V$ cut. The results with $p_V > 1\,\mathrm{GeV}/c$ and $p_V > 1.4\,\mathrm{GeV}/c$ show the same trend (increasing anisotropy with increasing $x_F$) and are consistent within uncertainties, see Figure 72 in Appendix A.3 and for a summary, Figure 65. This is a cross-check that this reference axis is indeed only weakly sensitive to diffractive (resonant and non-resonant) production and strongly sensitive to central production, as expected. Non-resonant diffractive production may contribute at low and intermediate $x_F$ while central production should dominate at high $x_F$.

| Reaction | $x_F$ | $\rho_{00}$ |
|---|---|---|
| $pp \to pp\phi, \phi \to K^+K^-$ | 0.6–0.7 | $0.51 \pm 0.03$ |
| $pp \to pp\phi, \phi \to K^+K^-$ | 0.7–0.8 | $0.58 \pm 0.02$ |
| $pp \to pp\phi, \phi \to K^+K^-$ | 0.8–0.9 | $0.67 \pm 0.04$ |
| $pp \to pp\omega, \omega \to \pi^+\pi^-\pi^0$ | 0.2–0.6 | $0.408 \pm 0.002$ |
| $pp \to pp\omega, \omega \to \pi^+\pi^-\pi^0$ | 0.6–0.7 | $0.492 \pm 0.003$ |
| $pp \to pp\omega, \omega \to \pi^+\pi^-\pi^0$ | 0.7–0.8 | $0.582 \pm 0.002$ |
| $pp \to pp\omega, \omega \to \pi^+\pi^-\pi^0$ | 0.8–0.9 | $0.572 \pm 0.002$ |
| $pp \to pp\omega, \omega \to \pi^+\pi^-\pi^0$, $p_V > 1.0\,\mathrm{GeV}/c$ | 0-.6-0.7 | $0.39 \pm 0.01$ |
| $pp \to pp\omega, \omega \to \pi^+\pi^-\pi^0$, $p_V > 1.0\,\mathrm{GeV}/c$ | 0.7–0.8 | $0.527 \pm 0.005$ |
| $pp \to pp\omega, \omega \to \pi^+\pi^-\pi^0$, $p_V > 1.0\,\mathrm{GeV}/c$ | 0.8–0.9 | $0.577 \pm 0.002$ |
| $pp \to pp\omega, \omega \to \pi^+\pi^-\pi^0$, $p_V > 1.4\,\mathrm{GeV}/c$ | 0.8–0.9 | $0.601 \pm 0.005$ |

Table 13: Spin alignment $\rho_{00}$ for $\phi$ and $\omega$ production with respect to the direction of the transferred momentum. In addition, results for different $p_V$ cuts are given for $\omega$.

### 7.3.4 *Previous findings*

The MOMO collaboration measured $\rho_{00}$ of the $\phi$ meson in $p\,d \to {}^3\mathrm{He}\,\phi$ near the kinematic threshold and the result was consistent with a complete alignment of the $\phi$ meson with respect to the incoming beam [30]. This is in sharp contrast to the

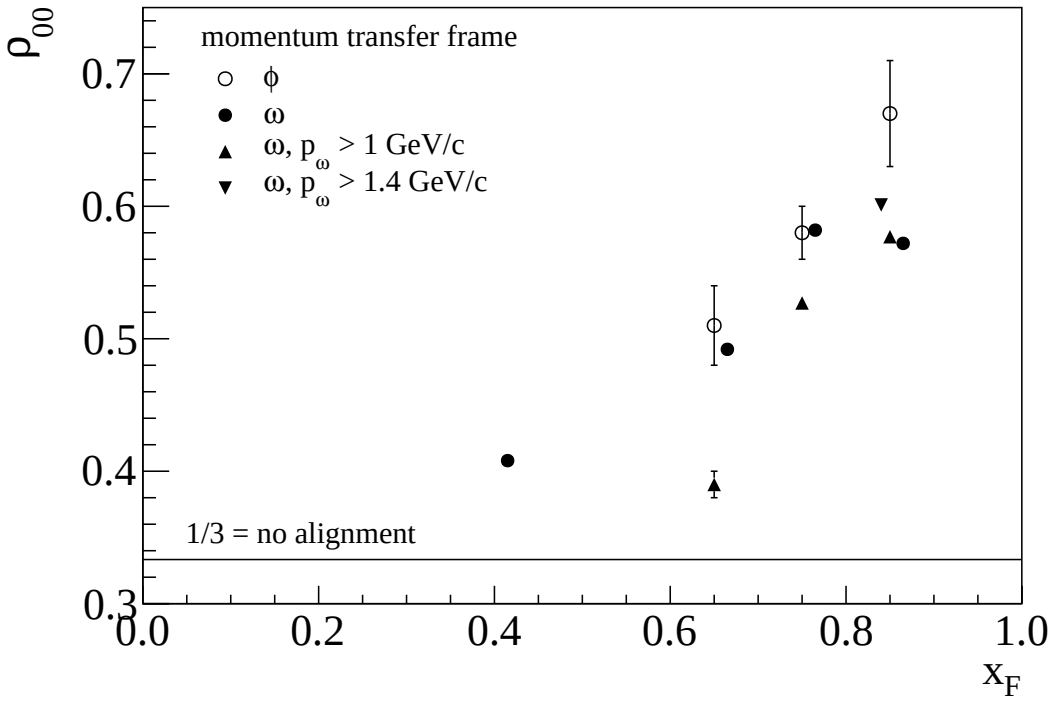


Figure 65: Overview of results for $\rho_{00}$ in the reference system with respect to the direction of the transferred momentum with and without cuts on $p_\omega$.

case of the $\omega$ meson, which is produced unaligned at the same excess energy and the same initial state, as found by the WASA collaboration [120]. The alignment of the $\omega$ meson in $pp$ collisions was measured close to threshold by the COSY-TOF collaboration [6]. An increasing value of $\rho_{00}$ was found for increasing excess energies, ranging from $\rho_{00} = 0.17$ to $\rho_{00} = 0.24$. It should be noted that the definition of the $\omega$ analyser for COSY-TOF differs by a rotation to the definition used in this thesis. With the latter, the COSY-TOF results are all above $\rho_{00} = 0.33$ and decreasing with increasing excess energy. The spin alignment was also measured in $pN$ collisions at a beam momentum of 70 GeV/$c$ by SPHINX [75]. In the region of $x_\mathrm{F}(\omega) < 0.2$, the $\omega$ mesons were found to be aligned with results close to $\rho_{00} = 1$. The $\phi$ alignment was measured at high energies by ACCMOR [54] and by STAR at RHIC [7]. In both measurements, the spin alignment was found to be consistent with $\rho_{00} = 0.33$, *i.e.* unaligned. Prior to the measurement presented in this thesis, the only known simultaneous measurement of $\phi$ and $\omega$ alignment using the same experimental set-up was performed by the SAPHIR collaboration [26, 27] in photoproduction. The spin alignment for $\omega$ mesons in the helicity frame ranges from $\rho_{00} = 0.31$ to $\rho_{00} = 0.16$ with a trend to lower $\rho_{00}$ values for higher excess energies. The spin alignment for $\phi$ mesons in the helicity frame was measured in one bin over the full range of excess energies and found to be $\rho_{00} = 0.25$.

## 7.4 DISCUSSION

The results of production ratio, spin alignments and their kinematic dependencies are discussed in order to draw conclusions about the involved production processes. The general observation is that $\omega$ mesons appear to be produced in two different processes while $\phi$ mesons are produced in one process. The process of exclusive $\omega$ meson production appears to be dominantly diffractive excitation of the beam proton with the excitation into nucleon resonances followed by a two-body decay $N^* \to p\omega$. In addition, $\omega$ mesons are also produced in central/non-resonant processes. Diffractive excitation is supported by the structures in the $M_{p\omega}$ spectra in Figs. 56 and 57, which are consistent with known high-spin resonances [29], and the significant alignment of the $\omega$ meson with respect to the direction of the $p\omega$ system. The alignment is strongly dependent on $M_{p\omega}$ and changes its slope when scanning over the $M_{p\omega}$ spectrum. Furthermore, the $x_\mathcal{F}$ dependence of the alignment is correlated to $M_{p\omega}$ and allows to enhance structures through cuts on $x_\mathcal{F}$. If the vector meson is aligned with the path of flight of the $p\omega$ system, it is safe to assume that the spin alignment of a possible $p\omega$ resonance was also in the same direction. In a two body decay, resonances have to emit the vector meson with an orbital angular momentum, $\vec{J} = \vec{L} + \vec{J}_p + \vec{J}_\mathrm{V}$. If the the vector meson is preferentially aligned with the direction of the orbital angular momentum, then we expect an increasing anisotropy of the vector meson decay in the helicity frame of the $N^*$ with increasing spin of the resonance. In other words, high spin resonances lead to spin alignments which are far off the central value of $\rho_{00} = 1/3$. The observed alignment is however close to this value, in the order of $\rho_{00} \approx 0.4$, so the production of very high spin resonances can be excluded. The observation is still compatible with the possible resonance candidates outlined in Section 7.1.

The fact that no structures are visible in the $p\phi$ spectrum and the observation that the $\phi$ meson is unaligned with the $p\phi$ system indicates that $N^*$ decays into $p\phi$ are suppressed and the OZI rule works. The observed small violation of the OZI rule by a factor of 3–4 (see Table 1) indicates that diffractive excitation of resonances blow up the $pp \to p\omega p$ cross section and therefore lower the observed violations. This is in line with observations from SPHINX[76] where also $N^*$ production is evident. An alternative, though more speculative explanation would be an admixture of other, OZI-violating reaction processes, or a genuine violation as discussed in the introduction of this chapter.

Removing the low-mass region with visible resonances by a cut in the vector meson momentum in the $pV$ rest system, $p_\mathrm{V} > 1.4\,\mathrm{GeV}/c$, *i.e.* $M_{p\omega} > 3.3\,\mathrm{GeV}/c^2$, the picture changes significantly. The $\omega$ spin is found to be no longer aligned with respect to the $p\omega$ system, consistent with the absence of resonances. Furthermore, the OZI violation increases and reaches a value of about 8, independently of $x_\mathrm{F}$. This is again in agreement not only with the SPHINX analysis [76] after removal of the low-$M_{p\omega}$ region, but interestingly also with data close to threshold as can be seen in Table 10.

The high mass part of the $M_{p\mathrm{V}}$ spectrum shows no structures, but may still contain $N^*$ resonances which probably are broad and largely overlap. The angular

distributions are isotropic, which means that either low-spin resonances contribute, however unlikely in this mass region, or the contribution of resonances is small.
In the high-mass continuum, the decays of $\omega$ and $\phi$ mesons are both strongly aligned with the direction of the momentum transfer. The similar behaviour of the alignment together with increasing $\rho_{00}$ values with increasing $x_F$ indicates that the production mechanism is the same for $\omega$ and $\phi$ in this region. This may point to a central Pomeron–Reggeon fusion which produces a vector meson. The OZI violation then reflects a hidden flavour-flow with the emitted Reggeon. The observed $x_F$ dependence of $\rho_{00}$ with respect to the direction of the transferred momentum ($\rho_{00}$ increases with increasing $x_F$) hints to this process since central production favours large $x_F$ of the fast proton. Another, more speculative viewpoint of this reaction is obtained assuming an alignment of the spin of the vector meson with the angular momentum of its emission with respect to the direction of the transferred momentum. Then, the transferred angular momentum has to be perpendicular to this direction. We can regard these events as scattering of a Pomeron radiated from the target proton and absorbed by a colourless object in the beam proton wave function, carrying some momentum fraction. This kind of mechanism may be associated with non-resonant diffractive dissociation. In a very simple picture, the proton dissociates into a proton plus a virtual (off-shell) vector meson $V^*$ (in [62, 63], this process is referred to as a shake-out). If the Pomeron emitted from the target recoil proton is absorbed by $V^*$ we would observe a free vector meson recoiling along the direction of momentum transfer of the Pomeron. In other words, we expect that at some resolution scale, the Pomeron should resolve structures in the extended proton. The high OZI violation indicates a higher effective resolution scale in this process and reflects the probability of finding a preformed $\phi$ meson relative to the preformed $\omega$ meson at a resolution scale near $m_\phi \approx 1\,\mathrm{GeV}/c^2$. The natural angular momentum quantisation axis for such a process is the direction of the momentum transfer mediated by the Pomeron as explained in Section 2.2.2. Both $\omega$ and $\phi$ have substantial alignment of their spins perpendicular to this axis, indicating a transferred orbital angular momentum. The latter is naturally oriented perpendicular to the direction of momentum transfer if spin-orbit couplings occur.
It has been already noted that Pomeron-Pomeron fusion into a $J^{PC}(I^G) = 1^{--}(0^-)$ meson is forbidden due to G-parity conservation. Another theoretical possibility is a central Pomeron-Odderon process. Since this process involves no quark lines and the only difference between $\omega$ and $\phi$ is the mass, the $\phi$ production rate should be of the same order as the $\omega$ rate reflecting perfect $\mathrm{SU}(3)_{\mathrm{flavour}}$ symmetry. This is in sharp contrast to our data, in which the $\omega$ cross section is thirty times larger than that of the $\phi$.The data therefore show no evidence for Pomeron-Odderon fusion in the studied kinematic domain.
As a summary of the discussion, in the $p\,p \to p\omega\,p$ case, there is strong evidence for at least two competing production mechanisms: Diffractive excitation of the beam proton into an $N^*$ resonance which subsequently decays into $p\,\omega$ and central production/non-resonant production that can also be viewed as a Pomeron scattering off a virtual vector meson-like object in the proton. In the case of $\phi$ production, Pomeron-virtual vector meson scattering and Reggeon-Pomeron fusion should be more important due to OZI suppression of the $N^* \to p\,\phi$ decays.

# 8

# CONCLUSIONS AND OUTLOOK

A study on production mechanism by investigating vector meson production has been carried out. The reaction $p_{\text{beam}}\, p_{\text{target}} \rightarrow p_{\text{fast}}\, V\, p_{\text{recoil}},\ V = \omega, \phi$ is studied with the COMPASS spectrometer at the M2 beam line at the CERN SPS accelerator. The measurement was performed in the years 2008 and 2009 with a 190 GeV/$c$ proton beam impinging on a liquid hydrogen target surrounded by a recoil proton detector (RPD), which is a central detector for the analysis.

A method for reconstruction of recoil protons as well as a method for calibration is introduced. The performance analysis shows that the detector works well within design specifications. The measured time resolution of $\delta t_A = 200$ ps for the inner ring and $\delta t_B = 400$ ps for the outer ring results in a combined resolution of $\sigma = 450$ ps which is well below the necessary resolution of 560 ps for pion–proton separation. A spatial resolution along the beam axis of $\delta z_A = 2.7$ cm for the inner ring and $\delta z_B = 5$ cm for the outer ring has been achieved. After data reconstruction and offline corrections, the combined spatial resolution ranges from $\delta z = 3.5$ cm to $\delta z = 3.9$ cm depending on the inner and outer ring combination. The azimuthal angular resolution of $\delta\varphi = 5^\circ$ is in the order of the expected resolution of $4.3^\circ$. The RPD efficiency including hardware performance and software reconstruction is found to be between 85% and 90% depending on the inner and outer ring combination and is uniformly distributed along the beam axis coordinate. The momentum resolution $\delta p/p$ stays constant at 5% for proton momenta up to 370 MeV/$c$ and then rises by 3% per 100 MeV/$c$ for higher proton momenta. The recoil detector and several newly build trigger detectors have been integrated in the new hadron trigger system. This system comprises triggers for different physics objectives. The main physics trigger selects events with recoil protons with an estimated efficiency of about 75% and a purity of larger than 90%. Additionally, multiplicity triggers extend the trigger acceptance towards lower momentum transfers, several monitoring triggers have been employed and an electromagnetic calorimeter trigger for data taking for Primakoff physics has been implemented in the trigger system.

The analysis searches for $\omega$ mesons *via* the decay $\omega \rightarrow \pi^+\pi^-\pi^0$ and the $\phi$ mesons *via* the decay $\phi \rightarrow K^+K^-$ originating from proton–proton collisions. The mass distributions are selected within the same kinematical conditions and are corrected for the spectrometer acceptance. The latter is determined with a multi-dimensional Monte-Carlo simulation of the apparatus with respect to the kinematical variables $t'$, $x_{\text{F}}$ of the fast proton and the mass $M_{p\text{V}}$ of the fast proton and the vector meson. The production ratio $R_{\phi/\omega}$ of $\phi$ to $\omega$ mesons shows violations of the OZI rule prediction of 0.0042 ranging from a factor $F_{\text{OZI}} = 3$ to a factor $F_{\text{OZI}} = 9$ depending on the kinematic region. For the $p\omega$ system, the invariant mass of vector meson and scattered proton, $M_{p\text{V}}$, exhibits resonant structures. In addition, a significant spin alignment of the $\omega$ meson with respect to the direction of the $p\omega$ system is found. Both observations together suggest resonant diffractive excitation of the beam pro-

ton as the main production mechanism for $\omega$ mesons. No structures in the $M_{p\phi}$ spectrum are observed in combination with isotropic spin alignment of the $\phi$ meson with respect to the direction of the $p\phi$ system. This indicates that the decay of resonances into $p\phi$ is OZI suppressed and a diffractive excitation is disfavoured for $\phi$ production. The small observed violation of the OZI rule prediction by a factor 3-4 in this region is found to be low due to the higher $\omega$ production cross section which is inflated by $p\omega$ resonances. The violation is found to be dependent on the Feynman variable $x_{\mathrm{F}}$. Removing the region with visible structures by requiring high masses $M_{p\omega} > 3.3\,\mathrm{GeV}/c^2$ and corresponding $M_{p\phi}$ masses leads to a significantly higher OZI rule violation of the order $8 \pm 1$ independent on $x_{\mathrm{F}}$. Moreover, the spin of both $\omega$ and $\phi$ is found to be unaligned with respect to the $pV$ system. The behaviour of both vector mesons is similar in the system defined by the direction of transferred momentum. This indicates that the production mechanism in this region for both $\omega$ and $\phi$ is central Reggeon–Pomeron fusion with the observed OZI violation reflecting a hidden flavour flow. A more speculative explanation of the behaviour in this reference system is that the process is regarded as a Pomeron resolving preformed colourless objects in the proton wave function. These off-shell objects would be consequently ejected in a shake-out. In this case, the observed OZI violation reflects the probability of resolving a $s\bar{s}$ state in the nucleon.
Further studies on the production ratio $R_{\phi/\omega}$ with respect to the magnitude of the transferred momentum squared $|t'|$ could yield more information on the scale dependence of the studied production mechanisms. A first look at the $|t'|$ dependence reveals that a much more refined analysis of the detector acceptance is necessary in order to correctly describe the resolution and the time dependence of the scattering angle which enters $|t'|$. More information on diffractive excitations can be obtained with a partial wave analysis to extract spin, parity, and resonance parameters of the observed structures in the $M_{p\omega}$ spectrum which is beyond the scope of this thesis.

# APPENDIX

# A

# RESULTS FOR SPIN ALIGNMENTS $\rho_{00}$

## A.1 HELICITY ANGLE DISTRIBUTIONS IN DIFFERENT $x_F$ REGIONS FOR $\omega$ MESONS WITH $p_\omega$ CUTS

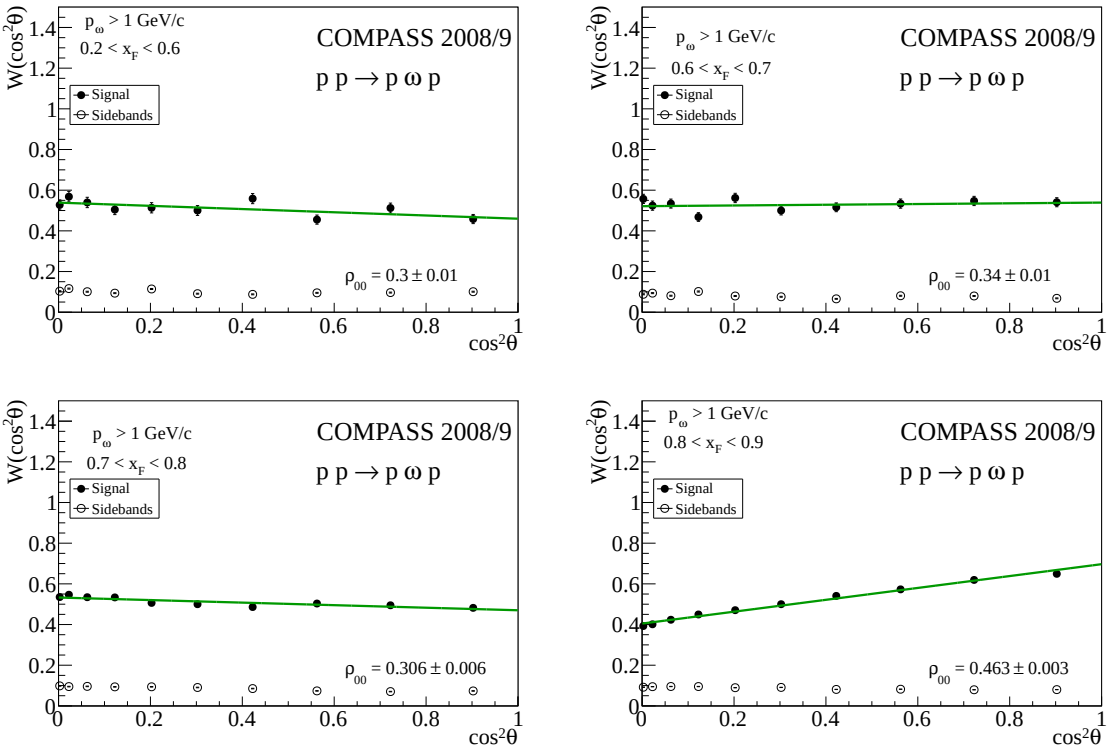


Figure 66: Helicity angle distributions for the $\omega$ meson for $p_\omega < 1\,\mathrm{GeV}/c$. The full circles represent the angular distributions of $\cos^2\theta$. The distributions are obtained in different $x_F$ regions as indicated in the figures. The open circles show the background distribution in the sidebands.

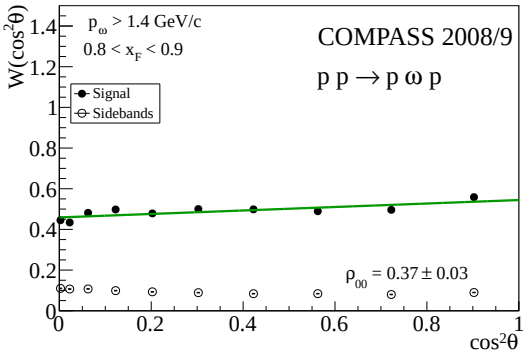


Figure 67: Helicity angle distributions for the $\omega$ meson for $p_\omega < 1.4\,\mathrm{GeV}/c$ in the $0.8 < x_F < 0.9$ region.

## A.2 HELICITY ANGLE DISTRIBUTIONS IN DIFFERENT MASS REGIONS

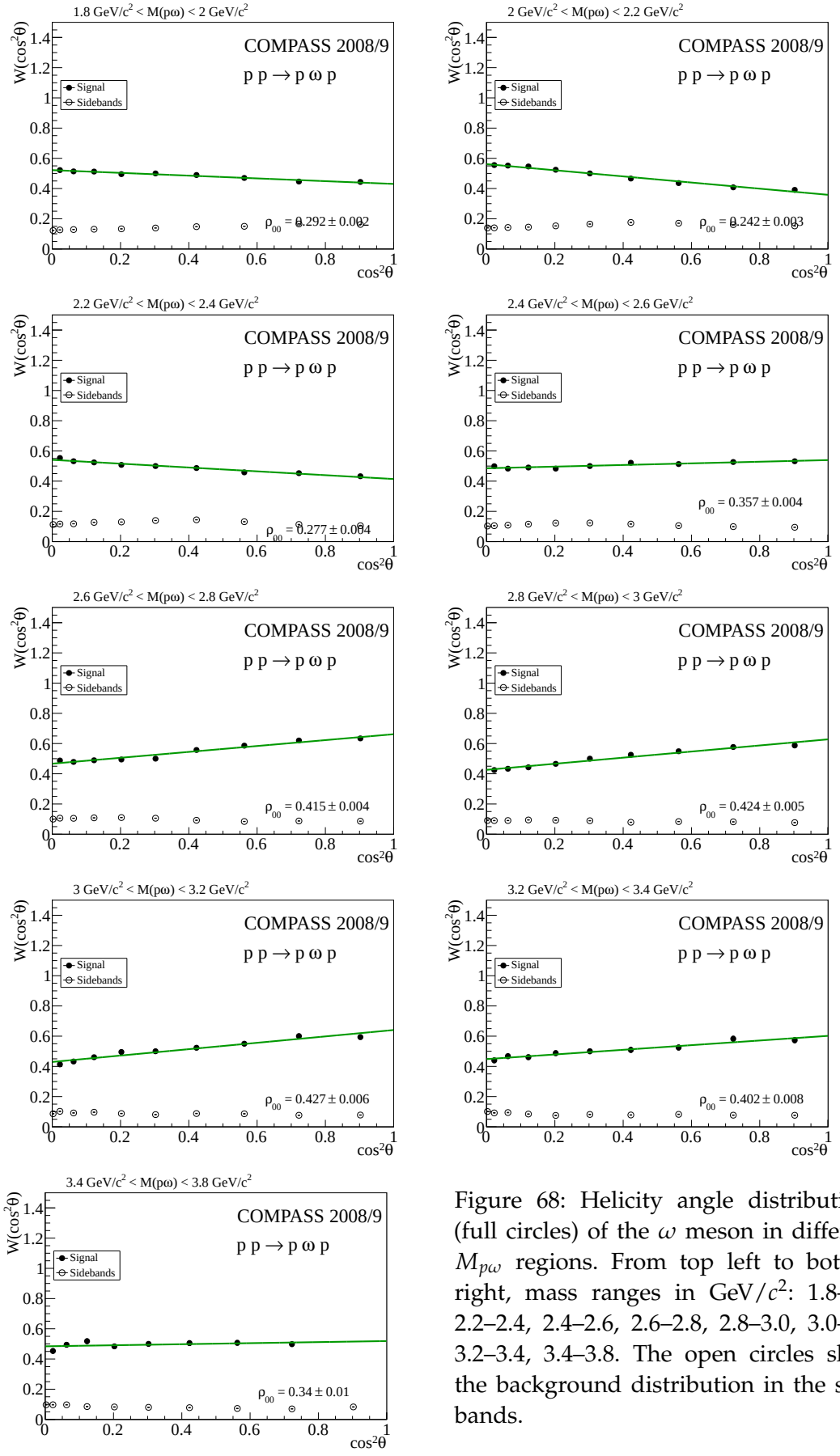


Figure 68: Helicity angle distributions (full circles) of the $\omega$ meson in different $M_{p\omega}$ regions. From top left to bottom right, mass ranges in GeV/$c^2$: 1.8–2.0, 2.2–2.4, 2.4–2.6, 2.6–2.8, 2.8–3.0, 3.0–3.2, 3.2–3.4, 3.4–3.8. The open circles show the background distribution in the sidebands.

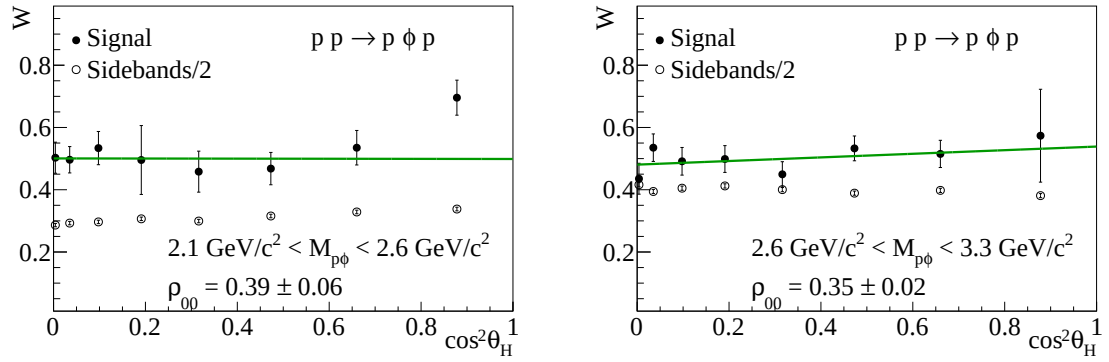


Figure 69: Helicity angle distributions (full circles) of the $\phi$ meson in different $M_{p\omega}$ regions. Distributions for $2.1\,\mathrm{GeV}/c^2 < M_{p\phi} < 2.6\,\mathrm{GeV}/c^2$ (left) and for $2.6\,\mathrm{GeV}/c^2 < M_{p\phi} < 3.3\,\mathrm{GeV}/c^2$ (right). The open circles show the background distribution in the sidebands.

## A.3 ANGULAR DISTRIBUTIONS WITH RESPECT TO THE DIRECTION OF MOMENTUM TRANSFER

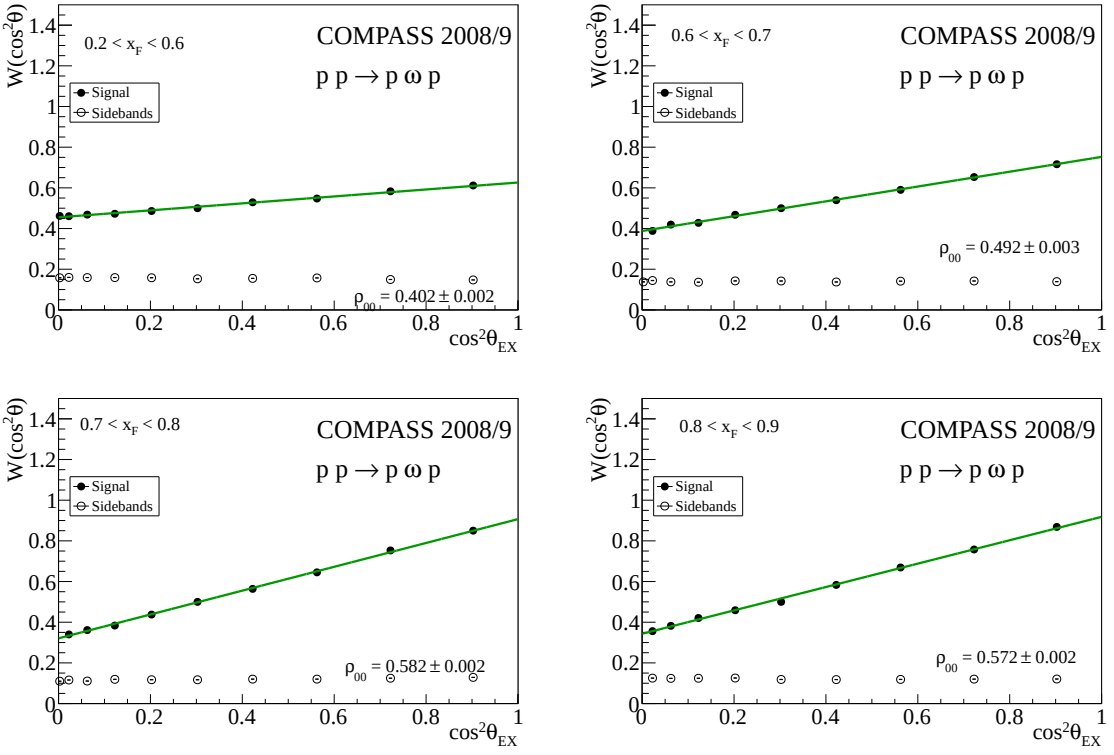


Figure 70: Angular distributions (full circles) with respect to the direction of momentum transfer for $\omega$. The panels show different $x_\mathrm{F}$ regions (upper left: $0.2 < x_\mathrm{F} < 0.6$, upper right $0.6 < x_\mathrm{F} < 0.7$, lower left $0.7 < x_\mathrm{F} < 0.8$ and lower right $0.8 < x_\mathrm{F} < 0.9$. The open circles show the background distribution in the sidebands.

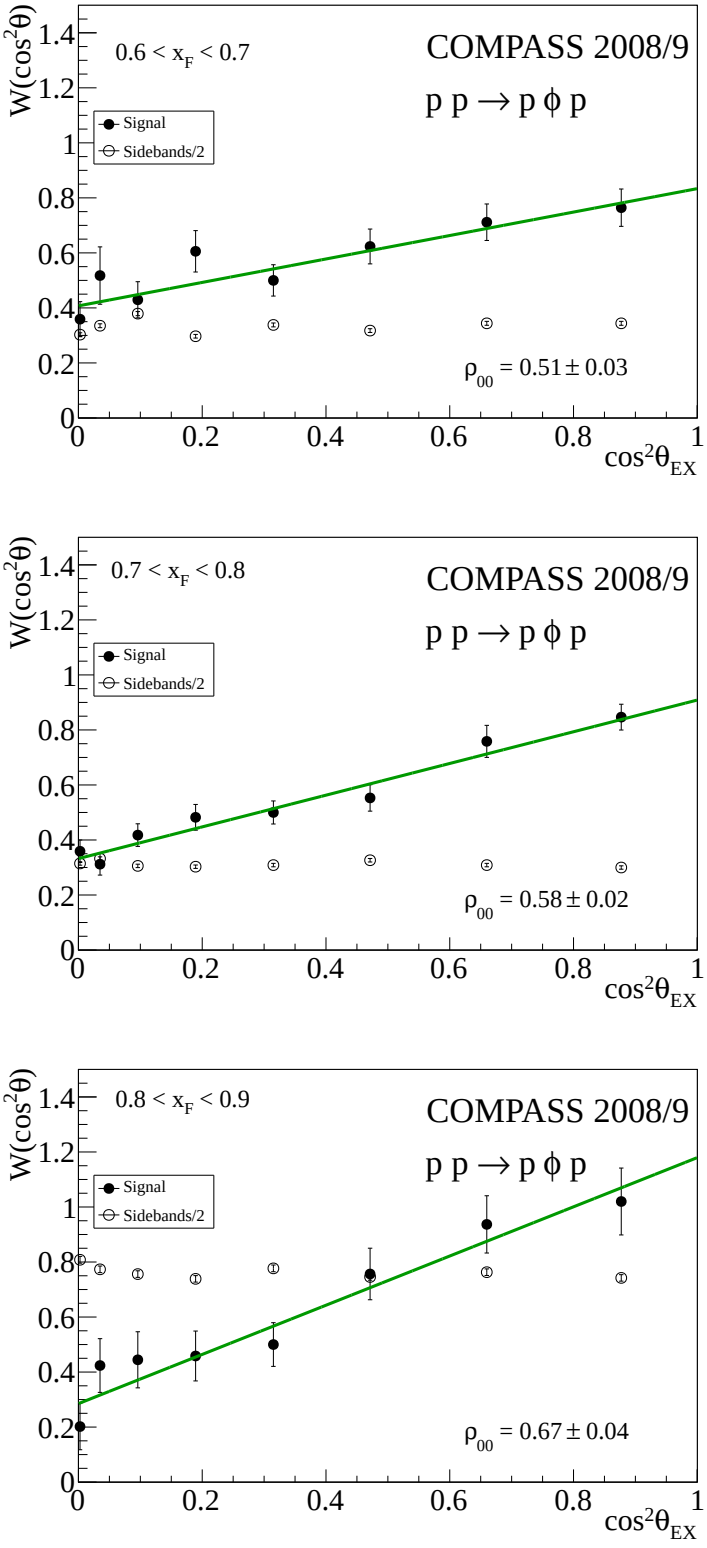


Figure 71: Angular distributions (full circles) with respect to the direction of momentum transfer for $\phi$. The panels show different $x_F$ regions: 0.6–0.7 (upper panel), 0.7–0.8 (middle panel) and 0.8–0.9 (lower panel). The open circles show the background distribution in the sidebands.

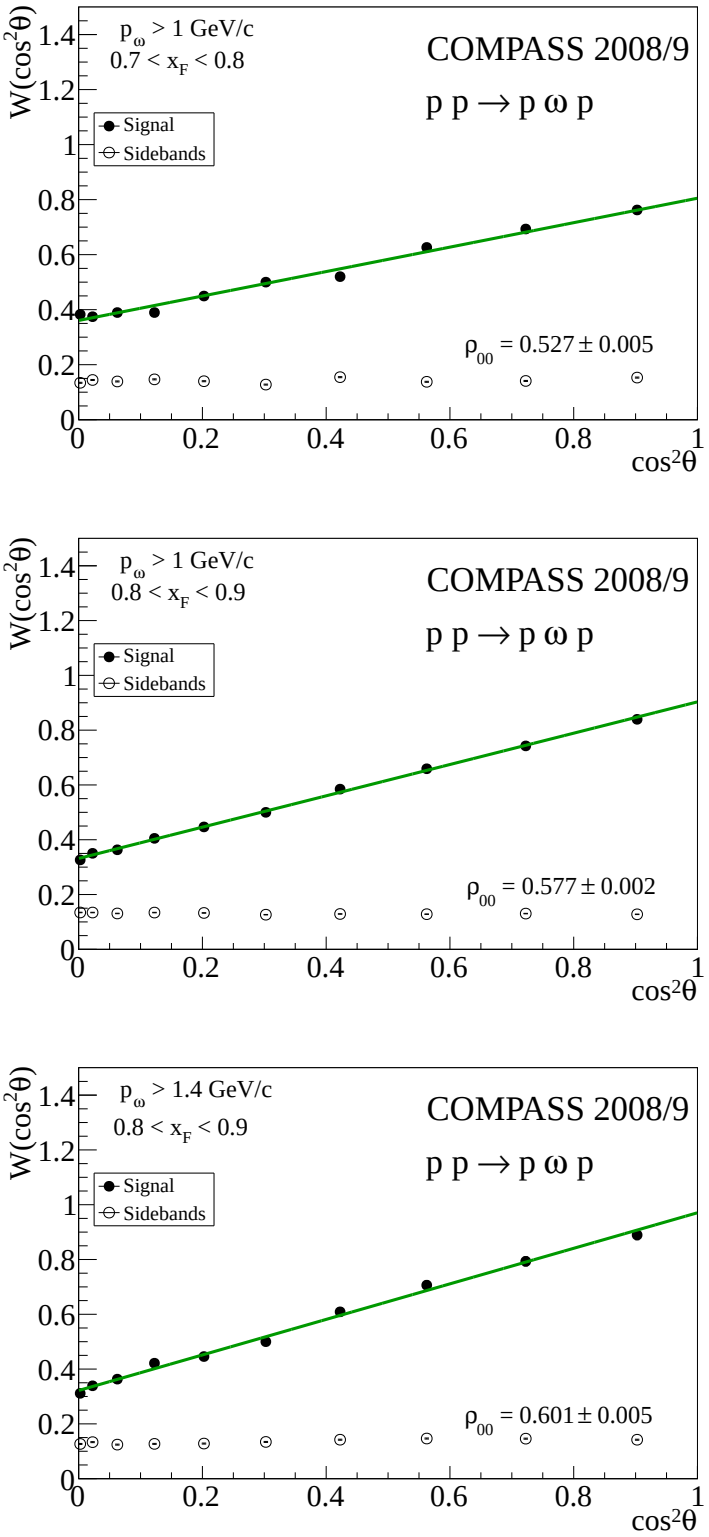


Figure 72: Angular distributions (full circles) with respect to the direction of momentum transfer for $\omega$ with different vector meson momentum cuts. Upper panel: $0.7 < x_F < 0.8$ region for $p_V > 1\,\mathrm{GeV}/c$. Middle panel: $0.8 < x_F < 0.9$ region for $p_V > 1\,\mathrm{GeV}/c$. Lower panel: $0.8 < x_F < 0.9$ region for $p_V > 1.4\,\mathrm{GeV}/c$.The open circles show the background distribution in the sidebands.

# B

# DETERMINATION OF THE STATISTICAL MONTE-CARLO UNCERTAINTY

The acceptance in a certain phase space region is defined as $w = \frac{A}{G}$, where $A$ is the number of accepted and $G$ the number of generated Monte-Carlo events. Using error propagation, one finds for the statistical uncertainty $\sigma_w^2 = \frac{A^2(A+G)}{G^3}$, which is obviously wrong. Consider the case of 0 accepted events, independently of the number of generated events. The statistical uncertainty from error propagation is 0 in this case, which means there is a full certainty on having no acceptance, even if only 1 MC event was generated. Error propagation fails completely in a case $A = G$, as well, resulting in allowed efficiencies of above 100% within uncertainty.
The probability of an acceptance $p$ can be derived from a binomial distribution, following [64]:

$$W(p)_{G,A} = C \frac{G!}{A!(G-A)!} p^A (1-p)^{G-A} \tag{57}$$

where $C$ is the normalisation. All $p$-independent terms can be absorbed in $C$, thus: $\frac{1}{C} = \int_0^1 p^A (1-p)^{G-A} \, \mathrm{d}p$. We use as a short-hand notation for the integral $I(a,b) = \int_0^1 p^a (1-p)^b \, \mathrm{d}p$, where $a = A$ and $b = G - A$.
The statistical uncertainty is

$$\begin{aligned}\sigma_w^2 &= \langle p^2 \rangle - \langle p \rangle^2 \\ &= \frac{I(a+2,b)}{I(a,b)} - \left( \frac{I(a+1,b)}{I(a,b)} \right)^2\end{aligned}$$

Partial integration of $I(a+1,b)$:

$$\begin{aligned}I(a+1,b) &= \frac{a+1}{b+1} I(a,b+1) \\ &= \frac{a+1}{b+1} \left( I(a,b) - I(a+1,b) \right) \\ &= \frac{a+1}{a+b+2} I(a,b)\end{aligned}$$

which results in

$$\begin{aligned}\sigma_w^2 &= \frac{(a+2)(a+1)}{(a+b+3)(a+b+2)} - \left( \frac{a+1}{a+b+2} \right)^2 \\ &= \frac{(A+1)(G-A+1)}{(G+2)^2(G+3)}\end{aligned} \tag{58}$$

In the later steps of the analysis, the data is weighted event-by-event with $w^{-1} = \frac{G}{A}$. The uncertainty on this value, $\sigma_{w^{-1}}$, can be calculated directly from $\sigma_w^2$. In general, $\sigma(y(x)) = \left| \frac{\partial y}{\partial x} \right| \sigma(x)$, which means with $y = x^{-1}$: $\frac{\sigma(y)}{|y|} = |-1| \, \frac{\sigma(x)}{|x|}$. The relative uncertainties on $w$ and $w^{-1}$ are thus the same.

# C

## FORWARD HODOSCOPE

The forward hodoscope depicted in Figure 73 was build by the Bonn university team and is installed at $z = +33\,\text{m}$. It consists of 12 trapezoidal-shaped BC408 scintillators (Figure 74, upper panel) connected to plexiglas light-guides (Figure 74, lower panel). The dimensions of the scintillators are matched to cover 95 % of the area at $z = +33\,\text{m}$, in which scattered protons from elastic scattering events are expected. The RPD detects recoiling particles for polar angles $\theta > 55°$. Therefore, to correlate a forward particle with the recoil, a minimum polar angle of 1.7 mrad for the forward particle is required. The radial dimension of the inner hole of 55 mm reflects this minimum polar angle. The light is detected by Phillips XP2900 PMTs with active voltage dividers. The analogue signals are discriminated with a CAEN V812 constant fraction discriminator at a threshold of 30 mV per channel.

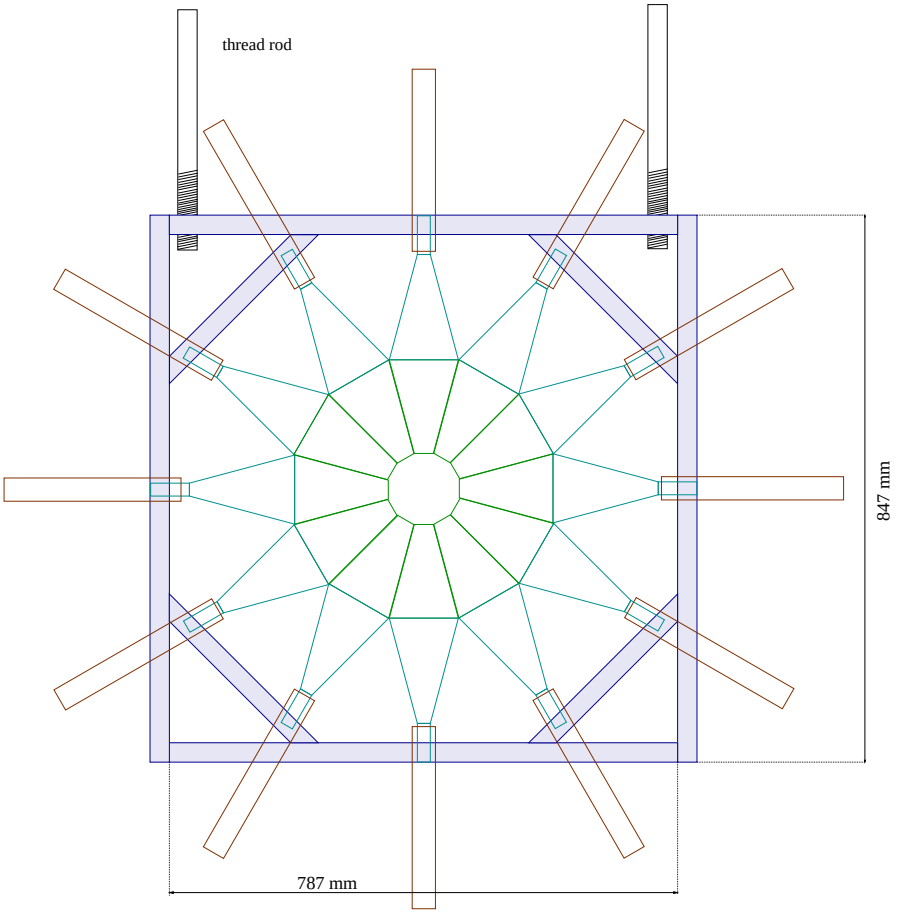


Figure 73: Forward hodoscope design.

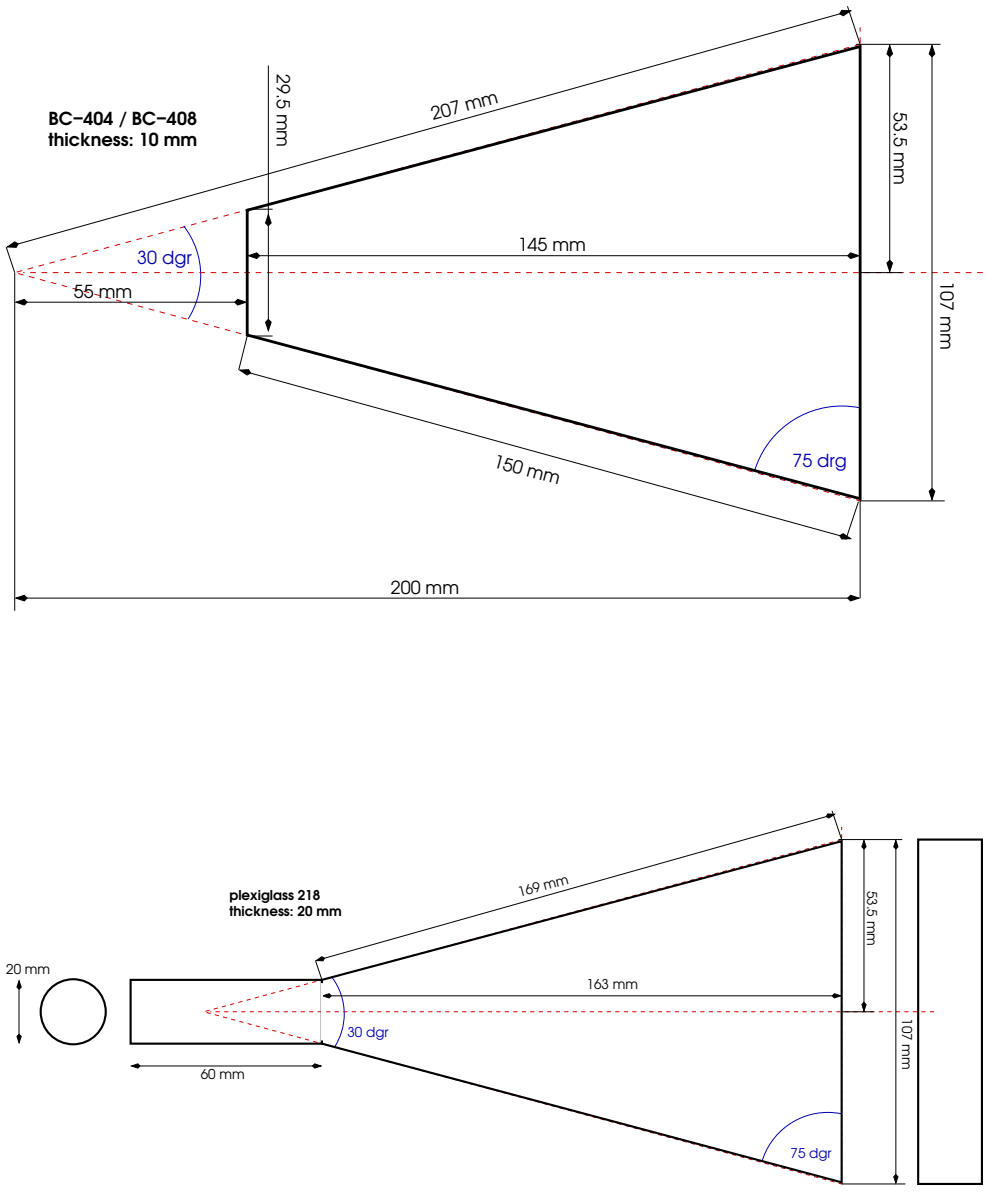


Figure 74: Upper panel: Design of one scintillator element for the forward hodoscope. Lower panel: Design for the corresponding light-guide.

# BIBLIOGRAPHY


[1] V. Abazov, et al., The Muon system of the run II D0 detector, Nucl.Instrum.Meth. A552 (2005) 372–398. (Cited on page 34.)

[2] P. Abbon, et al., The COMPASS experiment at CERN, Nucl. Instr. and Meth. A 577 (2007) 455–518. (Cited on pages 25, 28, 33, 34, 60, and 62.)

[3] P. Abbon, et al., Nucl. Instr. and Meth. A 587 (2008) 371–387. (Cited on page 35.)

[4] P. Abbon, et al., Nucl. Instr. and Meth. A 616 (2010) 21–37. (Cited on page 35.)

[5] P. Abbon, et al., Nucl. Instr. and Meth. A 631 (2011) 26–39. (Cited on page 35.)

[6] M. Abdel-Bary, et al., Systematic study of the $pp \to pp\omega$ reaction, The European Physical Journal A 44 (1) (2010) 7–22.
URL http://dx.doi.org/10.1140/epja/i2010-10924-0 (Cited on page 111.)

[7] B. I. Abelev, et al., Spin alignment measurements of the $K^{*0}(892)$ and $\phi(1020)$ vector mesons in heavy ion collisions at $\sqrt{s_{NN}} = 200$ GeV, Phys. Rev. C 77 (2008) 061902.
URL http://link.aps.org/doi/10.1103/PhysRevC.77.061902 (Cited on page 111.)

[8] M. Abolins, et al., Production of Multimeson Resonances by $\pi^+ p$ Interaction and Evidence for a $\pi\omega$ Resonance, Phys. Rev. Lett. 11 (1963) 381–385.
URL http://link.aps.org/doi/10.1103/PhysRevLett.11.381 (Cited on page 102.)

[9] M. Adamovich, et al., WA92: A fixed target experiment to trigger on and identify beauty particle decays, Nucl. Instrum. Meth. A379 (1996) 252–270. (Cited on page 38.)

[10] C. Adolph, et al., The COMPASS Setup for Physics with Hadron Beams, in preparation for Nucl. Instr. and Meth. A. (Cited on pages 25 and 31.)

[11] M. Aguilar-Benitez, et al., Vector meson production in $\pi^-$ p interactions at 360 GeV/$c$, Z. Phys. C 44 (4) (1989) 531–539.
URL http://dx.doi.org/10.1007/BF01549075 (Cited on page 102.)

[12] M. Aguilar-Benitez, et al., Inclusive particle production in 400 GeV/$c$ pp-interactions, Z. Phys. C 50 (3) (1991) 405–426.
URL http://dx.doi.org/10.1007/BF01551452 (Cited on page 102.)

[13] D. Alde, et al., The slow proton position sensitive time-of-flight detector of the GAMS NA-12/2 experiment at CERN, Nucl.Instrum.Meth. A342 (1994) 389–397. (Cited on page 43.)

[14] M. Alekseev, et al., Observation of a $J^{PC} = 1^{-+}$ exotic resonance in diffractive dissociation of 190 GeV/$c$ $\pi^-$ into $\pi^-\pi^-\pi^+$, Phys.Rev.Lett. 104 (2010) 241803. (Cited on page 7.)

[15] Y. Alexandrov, et al., CHarm Experiment with Omni-Purpose Setup, CERN/SPSLC 95-22, SPSC/I 202 (March 1995). (Cited on page 25.)

[16] T. Alimova, A. Gorin, T. Ershova, V. Lapshin, P. Mekshun, et al., Characteristics of extruded scintillation strips, plates and rods for particle counters, IFVE-86-35. (Cited on page 46.)

[17] C. Amsler, N. A. Törnqvist, Mesons beyond the naive quark model, Physics Reports 389 (2) (2004) 61 – 117.
URL http://www.sciencedirect.com/science/article/pii/S0370157303003351 (Cited on page 6.)

[18] C. Amsler, et al., First observations of Pontecorvo reactions with a recoiling neutron, Z. Phys. A 351 (3) (1995) 325–331.
URL http://dx.doi.org/10.1007/BF01290916 (Cited on page 102.)

[19] P. Astbury, et al., Measurement of deep inelastic Compton scattering of high energy photons, Phys. Lett. B152 (1985) 419. (Cited on page 38.)

[20] H. Atherton, et al., Precise measurements of particle production by 400 GeV/$c$ protons on beryllium targets, CERN Yellow Report, CERN 80-07 (1980). (Cited on page 28.)

[21] A. Austregesilo, et al., First results of the PixelGEM central tracking system for COMPASS, Nucl. Phys. B (Proc. Suppl.) 197 (2009) 113–116, 11th Topical Seminar on Innovative Particle and Radiation Detectors (IPRD08). (Cited on page 33.)

[22] D. S. Ayres, et al., $\phi$ Meson Production in $\pi^- p$ and $K^- p$ Interactions from 3 to 6 GeV/$c$, Phys. Rev. Lett. 32 (1974) 1463–1467.
URL http://link.aps.org/doi/10.1103/PhysRevLett.32.1463 (Cited on page 102.)

[23] R. Baldi, et al., Comparison of $\phi$ production by $\pi, K$ and $p$ incident on protons at 10 GeV, Physics Letters B 68 (4) (1977) 381 – 384.
URL http://www.sciencedirect.com/science/article/pii/0370269377904993 (Cited on page 102.)

[24] F. Balestra, et al., $\phi$ and $\omega$ meson production in pp reactions at $p_{\text{lab}} = 3.67$GeV/$c$, Phys. Rev. C 63 (2001) 024004.
URL http://link.aps.org/doi/10.1103/PhysRevC.63.024004 (Cited on pages 102 and 103.)

[25] J. Barth, Photoproduktion der Vektormesonen omega(782) und phi(1020) am Proton von der Erzeugungsschwelle bis zu einer Photon-Energie von 2.6 GeV, Ph.D. thesis, Universität Bonn (2002). (Cited on pages 92 and 93.)

[26] J. Barth, et al., Low-energy photoproduction of $\omega$-mesons, The European Physical Journal A 18 (1) (2003) 117–127.
URL http://dx.doi.org/10.1140/epja/i2003-10061-y (Cited on page 111.)

[27] J. Barth, et al., Low-energy photoproduction of $\phi$-mesons, The European Physical Journal A 17 (2) (2003) 269–274.
URL http://dx.doi.org/10.1140/epja/i2002-10154-1 (Cited on page 111.)

[28] G. Baum, et al., COMPASS: A proposal for a COmmon Muon and Proton Apparatus for Structure and Spectroscopy, CERN/SPSLC 96-14, SPSC/P 297 (March 1996). (Cited on page 25.)

[29] J. Behringer, et al., Review of Particle Physics, Phys. Rev. D 86 (2012) 010001. (Cited on pages 2, 9, 10, 14, 19, 44, 97, 98, 107, and 112.)

[30] F. Bellemann, et al., Experimental study of the $pd \to {}^3\mathrm{he}\, K^+K^-$ and $pd \to {}^3\mathrm{he}\, \phi$ reactions close to threshold, Phys. Rev. C 75 (2007) 015204.
URL http://link.aps.org/doi/10.1103/PhysRevC.75.015204 (Cited on page 110.)

[31] E. Berger, C. Sorensen, Dynamical violation of the zweig rule and the energy dependence of $\pi^- p \to \phi n$, Physics Letters B 62 (3) (1976) 303 – 307.
URL http://www.sciencedirect.com/science/article/pii/0370269376900812 (Cited on page 99.)

[32] C. Bernet, et al., The COMPASS trigger system for muon scattering, Nucl. Instr. and Meth. A 550 (2005) 217–240. (Cited on pages 34 and 62.)

[33] J. Bernhard, Aufbau des inneren Rings eines Recoildetektors am COMPASS-Experiment, Diploma thesis, Johannes-Gutenberg-Universität Mainz (2007). (Cited on pages 45, 47, 48, and 60.)

[34] J. Bernhard, et al., Comment on 'Material Evidence of a 38 MeV Boson', arXiv[hep-ex/1204.2349]. (Cited on page 80.)

[35] K. Bicker, Construction and Commissioning of a Cooling and Support Structure for the Silicon Detectors for the COMPASS Experiment, Diploma thesis, Technische Universität München (2011). (Cited on page 32.)

[36] F. Binon, et al., Nucl. Instr. and Meth. A 248 (1986) 86. (Cited on page 37.)

[37] J. Bisplinghoff, et al., Nucl. Instr. and Meth. A 490 (2002) 101. (Cited on page 33.)

[38] V. Blobel, et al., Test of the Zweig selection rule in $\phi$ production by pp collisions, Physics Letters B 59 (1) (1975) 88 – 92.
URL http://www.sciencedirect.com/science/article/pii/0370269375901641 (Cited on page 102.)

[39] C. Bovet, et al., The CEDAR counters for particle identification in the SPS secondary beams: a description and operation manual (1982). (Cited on page 30.)

[40] J. Bowcock, P. Cotterill, N. Queen, Slope of forward diffraction peaks, Il Nuovo Cimento A 49 (4) (1979) 561–574. (Cited on page 16.)

[41] F. W. Brasse, G. Falley, K. Thiele, P. Warnecke, Construction of a Large Drift Chamber and Test Measurements, Internal Report, DESY F21-76/02 (August 1976). (Cited on page 33.)

[42] C. Brown, et al., Nucl. Instr. and Meth. A 279 (1989) 331. (Cited on page 34.)

[43] V. N. Bychkov, et al., The large size straw drift chambers of the COMPASS experiment, Nucl. Instr. and Meth. A 556 (2006) 66–79. (Cited on page 33.)

[44] CERN, Initial Safety Info Laser (2007).
URL https://edms.cern.ch/document/816962/ (Cited on page 48.)

[45] CERN, Cern accelerators overview (2014).
URL http://ps-div.web.cern.ch/ps-div/PSComplex/accelerators.pdf (Cited on page 26.)

[46] CERN-IT, GEANT - detector description and simulation tool, CERN Program Library Long Writeup W5013 (1993).
URL http://wwwasdoc.web.cern.ch/wwwasdoc/geant_html3/geantall.html (Cited on page 85.)

[47] C. Chen, et al., Properties of the reaction $pp \to K^+K^-\pi^+\pi^-$ at 2.32 GeV/$c$, Nuclear Physics B 130 (2) (1977) 269 – 294.
URL http://www.sciencedirect.com/science/article/pii/0550321377901079 (Cited on page 102.)

[48] G. Chew, S. C. Frautschi, Regge Trajectories and the Principle of Maximum Strength for Strong Interactions, Phys.Rev.Lett. 8 (1962) 41–44. (Cited on page 19.)

[49] S. Chung, Spin Formalisms, in: Yellow Report CERN-71-8, 1971. (Cited on page 105.)

[50] D. Cohen, et al., $\phi$-Meson Production in the Reactions $\pi^\pm N \to K^-K^+N$ at 6 GeV/$c$, Phys. Rev. Lett. 38 (1977) 269–272.
URL http://link.aps.org/doi/10.1103/PhysRevLett.38.269 (Cited on page 102.)

[51] A. Cooper, et al., $\phi$ and $\omega$ meson production in pp annihilations at 0.70-0.76 GeV/$c$ and the OZI rule, Nuclear Physics B 146 (1) (1978) 1 – 10.
URL http://www.sciencedirect.com/science/article/pii/0550321378904273 (Cited on page 102.)

[52] V. Crede, C. Meyer, The experimental status of glueballs, Progress in Particle and Nuclear Physics 63 (1) (2009) 74 – 116.
URL http://www.sciencedirect.com/science/article/pii/S0146641009000052 (Cited on page 7.)

[53] J. S. Danburg, et al., Production and Decay of $\eta$ and $\omega$ Mesons in the Reaction $\pi^+ d \to (p)p\pi^+\pi^-\pi^0$ between 1.1 and 2.4 GeV/$c$, Phys. Rev. D 2 (1970) 2564–2588.
URL http://link.aps.org/doi/10.1103/PhysRevD.2.2564 (Cited on page 102.)

[54] C. Daum, et al., Inclusive $\phi$-meson production in 93 and 63 GeV hadron interactions, Nuclear Physics B 186 (2) (1981) 205 – 218.
URL http://www.sciencedirect.com/science/article/pii/0550321381900675 (Cited on page 111.)

[55] D. W. Davies, et al., Strange-Particle Production in $\pi^+ d$ Interactions from 1.1 to 2.4 GeV/$c$, Phys. Rev. D 2 (1970) 506–517.
URL http://link.aps.org/doi/10.1103/PhysRevD.2.506 (Cited on page 102.)

[56] R. Donald, et al., The applicability of Zweig's rule to $\bar{p}p$ annihilations at 3.6 GeV/$c$, Physics Letters B 61 (2) (1976) 210 – 212.
URL http://www.sciencedirect.com/science/article/pii/0370269376906286 (Cited on page 102.)

[57] S. Donnachie, H. Dosch, P. Landshoff, O. Nachtmann, Pomeron physics and QCD, Cambridge monographs on particle physics, nuclear physics and cosmology, 2002. (Cited on pages 13 and 20.)

[58] V. Dorofeev, et al., (Lepton-F collaboration), in: Proc. NAN95, 1995. (Cited on page 102.)

[59] E2m (2013).
URL http://en.wikipedia.org/wiki/File:Meson_nonet_-_spin_0.svg, http://en.wikipedia.org/wiki/File:Meson_nonet_-_spin_1.svg (Cited on page 8.)

[60] D. Ebert, R. N. Faustov, V. O. Galkin, Mass spectra and regge trajectories of light mesons in the relativistic quark model, Phys. Rev. D 79 (2009) 114029.
URL http://link.aps.org/doi/10.1103/PhysRevD.79.114029 (Cited on page 19.)

[61] R. Eden, P. Landshoff, D. Olive, J. Polkinghorne, The Analytic S-Matrix, Cambridge University Press, 2002. (Cited on page 13.)

[62] J. Ellis, M. Karliner, D. Kharzeev, M. Sapozhnikov, Abundant $\phi$-meson production in pp annihilation at rest and strangeness in the nucleon, Physics Letters B 353 (2-3) (1995) 319 – 328.
URL http://www.sciencedirect.com/science/article/pii/0370269395005734 (Cited on pages 21, 99, and 113.)

[63] J. Ellis, M. Karliner, D. Kharzeev, M. Sapozhnikov, Hadronic probes of the polarized intrinsic strangeness of the nucleon, Nuclear Physics A 673 (1-4) (2000) 256 – 278.

URL http://www.sciencedirect.com/science/article/pii/S0375947400001287 (Cited on pages 21, 99, and 113.)

[64] T. Ernst, Diploma thesis, ALU Freiburg (1985). (Cited on pages 86 and 125.)

[65] E. Feinberg, I. Pomerancuk, High energy inelastic diffraction phenomena, Il Nuovo Cimento Series 10 3 (4) (1956) 652–671. (Cited on page 20.)

[66] E. Fermi, J. Orear, Nuclear Physics: A Course Given by Enrico Fermi at the University of Chicago, Midway reprint, University of Chicago Press, 1950. (Cited on page 11.)

[67] R. P. Feynman, Very high-energy collisions of hadrons, Phys. Rev. Lett. 23 (1969) 1415–1417.
URL http://link.aps.org/doi/10.1103/PhysRevLett.23.1415 (Cited on page 18.)

[68] H. Fischer, et al., Implementation of the dead-time free F1 TDC in the COMPASS detector readout, Nucl. Instr. and Meth. A 461 (2001) 507–510. (Cited on page 48.)

[69] L. Gatignon, The M2 beam for COMPASS, Presented as part of the SPS shutdown lectures, 2006.
URL http://jwenning.home.cern.ch/jwenning/documents/TrainingOP/ShutdownLectures06-NorthArea.ppt (Cited on page 27.)

[70] M. Gell-Mann, The eightfold way: A theory of strong interaction symmetry, 1961, cTSL-20, Caltech.
URL http://www.osti.gov/scitech/servlets/purl/4008239 (Cited on pages 7 and 9.)

[71] H. Georgi, Lie Algebras in Particle Physics: From Isospin to Unified Theories, Frontiers in physics, Westview Press, 1999. (Cited on page 10.)

[72] G. Giacomelli, Strong interactions at high energies, eConf C720906V3 (1972) 219–320. (Cited on pages 15, 16, and 95.)

[73] S. Glashow, Partial Symmetries of Weak Interactions, Nucl.Phys. 22 (1961) 579–588. (Cited on page 1.)

[74] S. Golovkin, et al., (SPHINX collaboration), in: Proc. NAN95, 1995. (Cited on page 102.)

[75] S. Golovkin, et al., Study of quasiexclusive neutral meson production in pN interactions at Ep = 70 GeV in the deep fragmentation region, Z. Phys. A 327 (3) (1997) 327–335. (Cited on pages 105 and 111.)

[76] S. Golovkin, et al., Study of the OZI selection rule in hadronic processes, Z. Phys. A 359 (4) (1997) 435–444. (Cited on pages 100, 102, 103, and 112.)

[77] M. L. Good, W. D. Walker, Diffraction dissociation of beam particles, Phys. Rev. 120 (1960) 1857–1860.
URL http://link.aps.org/doi/10.1103/PhysRev.120.1857 (Cited on page 20.)

[78] O. Gorchakov, et al., Measurement of the $\bar{p}d \to \phi n$ Pontecorvo reaction for antiproton annihilation at rest, Physics Letters B 528 (1-2) (2002) 34 – 42.
URL http://www.sciencedirect.com/science/article/pii/S0370269302011759 (Cited on page 102.)

[79] K. Gottfried, J. Jackson, On the connection between production mechanism and decay of resonances at high energies, Il Nuovo Cimento Series 10 33 (2) (1964) 309–330.
URL http://dx.doi.org/10.1007/BF02750195 (Cited on pages 16, 104, and 105.)

[80] S. Grabmüller, Cryogenic Silicon Detectors and Analysis of Primakoff Contributions to the Reaction $\pi^-$ Pb $\to \pi^-\pi^-\pi^+$ Pb at COMPASS, Ph.D. thesis, Technische Universität München (2012). (Cited on page 32.)

[81] V. Gribov, A reggeon diagram technique, Sov.Phys.JETP 26 (1968) 414–422. (Cited on page 20.)

[82] B. Grube, et al., Rootpwa generator (2012).
URL http://sourceforge.net/projects/rootpwa/ (Cited on page 85.)

[83] C. Grupen, Teilchendetektoren, BI-Wiss.-Verlag, 1993. (Cited on pages 43, 44, and 45.)

[84] S. Horikawa, et al., Development of a scintillating-fibre detector with position-sensitive photomultipliers for high-rate experiments, Nucl. Instr. and Meth. A 516 (2004) 34–49. (Cited on page 33.)

[85] S. Huber, Development of a Digital Trigger of Electromagnetic Calorimeter, Diploma thesis, Technische Universität München (2010). (Cited on pages 59 and 68.)

[86] J. Iizuka, Systematics and phenomenology of meson family, Prog.Theor.Phys.Suppl. 37 (1966) 21–34. (Cited on page 10.)

[87] C. Itzykson, J. Zuber, Quantum Field Theory, Mcgraw-Hill, 1980. (Cited on page 1.)

[88] P. Jasinski, Analysis of diffractive dissociation of $K^-$ into $K^+\,\pi^-\pi^+$ on a liquid hydrogen target at the COMPASS spectrometer, Ph.D. thesis, Universität Mainz (2012). (Cited on pages 28, 29, and 30.)

[89] N. Kaiser, pp $\to$ pp$\omega$ reaction near threshold, Phys. Rev. C 60 (1999) 057001.
URL http://link.aps.org/doi/10.1103/PhysRevC.60.057001 (Cited on page 19.)

[90] B. Ketzer, A. Austregesilo, F. Haas, I. Konorov, M. Krämer, A. Mann, T. Nagel, S. Paul, A triple GEM detector with pixel readout for high-rate beam tracking in COMPASS, in: Nuclear Science Symposium Conference Record, 2007. NSS '07. IEEE, vol. 1, IEEE, Piscataway, NJ, 2007, pp. 242–244. (Cited on page 33.)

[91] B. Ketzer, et al., Triple GEM tracking detectors for COMPASS, IEEE Trans. Nucl. Sci. 49 (2002) 2403–2410, CERN-OPEN-2002-004. (Cited on page 33.)

[92] A. Kirk, Resonance production in central pp collisions at the CERN Omega Spectrometer, Physics Letters B 489 (1-2) (2000) 29 – 37.
URL http://www.sciencedirect.com/science/article/pii/S0370269300009448 (Cited on pages 21 and 95.)

[93] W. Klempt, Review of particle identification by time of flight techniques, Nuclear Instruments and Methods in Physics Research Section A: Accelerators, Spectrometers, Detectors and Associated Equipment 433 (1999) 542 – 553.
URL http://www.sciencedirect.com/science/article/pii/S016890029900323X (Cited on page 44.)

[94] V. Kolosov, et al., Present performances of COMPASS electromagnetic calorimetry from data analysis, COMPASS-Note 2008-05. (Cited on pages 38 and 39.)

[95] A. S. Kronfeld, C. Quigg, Resource Letter QCD-1: Quantum chromodynamics, American Journal of Physics 78 (11) (2010) 1081–1116.
URL http://scitation.aip.org/content/aapt/journal/ajp/78/11/10.1119/1.3454865 (Cited on page 2.)

[96] F. Kunne, et al., The gaseous microstrip detector micromegas for the COMPASS experiment at CERN, Nuclear Physics A 721 (0) (2003) C1087 – C1090.
URL http://www.sciencedirect.com/science/article/pii/S0375947403012910 (Cited on page 33.)

[97] P. Lebiedowicz, O. Nachtmann, A. Szczurek, Exclusive central diffractive production of scalar and pseudoscalar mesons; tensorial vs. vectorial pomeron, arXiv[hep-ph/1309.3913]. (Cited on page 21.)

[98] S. Lindenbaum, The OZI rule and glueballs, Il Nuovo Cimento A 65 (2) (1981) 222–238.
URL http://dx.doi.org/10.1007/BF02902136 (Cited on page 99.)

[99] H. Lipkin, Experimental tests and implications of the Zweig-Iizuka rule, Physics Letters B 60 (4) (1976) 371 – 374.
URL http://www.sciencedirect.com/science/article/pii/037026937690753X (Cited on page 11.)

[100] H. J. Lipkin, Exchange degeneracy, flat total cross sections and the absence of exotic resonances, Nuclear Physics B 9 (3) (1969) 349 – 363.
URL http://www.sciencedirect.com/science/article/pii/0550321369901345 (Cited on page 99.)

[101] A. Mann, I. Konorov, S. Paul, A Versatile Sampling ADC System for On-Detector Applications and the AdvancedTCA Crate Standard, 15th IEEE-NPSS Real-Time Conference (2007) 1–5. (Cited on pages 38 and 48.)

[102] V. Mathieu, N. Kochelev, V. Vento, The physics of glueballs, International Journal of Modern Physics E 18 (01) (2009) 1–49.
URL http://www.worldscientific.com/doi/abs/10.1142/S0218301309012124 (Cited on page 7.)

[103] C. A. Meyer, Y. Van Haarlem, Status of exotic-quantum-number mesons, Phys. Rev. C 82 (2010) 025208.
URL http://link.aps.org/doi/10.1103/PhysRevC.82.025208 (Cited on page 7.)

[104] E. Nappi, et al., Semi-inclusive Muon Scattering from a Polarised Target, CERN/SPSLC 95-27, SPSC/I 204 (March 1995). (Cited on page 25.)

[105] F. Nerling, D. Ryabchikov, Observation of a $J^{PC} = 1^{-+}$ exotic resonance in $\pi^-\pi^0\pi^0$ final states diffractively produced on proton, COMPASS-Note 2013-01. (Cited on page 92.)

[106] V. Nomokonov, M. Sapozhnikov, Experimental tests of the Okubo-Zweig-Iizuka rule in hadron interactions, Phys.Part.Nucl. 34 (2003) 94–123. (Cited on pages 102 and 103.)

[107] S. Okubo, Note on Unitary Symmetry in Strong Interaction. II: Excited States of Baryons, Progress of Theoretical Physics 28 (1) (1962) 24–32.
URL http://ptp.oxfordjournals.org/content/28/1/24.abstract (Cited on page 9.)

[108] S. Okubo, Note on Unitary Symmetry in Strong Interactions, Progress of Theoretical Physics 27 (5) (1962) 949–966.
URL http://ptp.oxfordjournals.org/content/27/5/949.abstract (Cited on page 9.)

[109] S. Okubo, $\phi$-meson and unitary symmetry model, Physics Letters 5 (2) (1963) 165 – 168.
URL http://www.sciencedirect.com/science/article/pii/S0375960163925489 (Cited on page 10.)

[110] V. Palmieri, et al., Evidence for charge collection efficiency recovery in heavily irradiated silicon detectors operated at cryogenic temperatures, Nucl. Instr. and Meth. A 413 (1998) 475–478. (Cited on page 32.)

[111] M. Perl, High energy hadron physics, Wiley-Interscience publication, Wiley, 1974. (Cited on pages 12, 13, 16, and 20.)

[112] M. E. Peskin, D. V. Schroeder, An introduction to quantum field theory, Westview Press, 1995. (Cited on page 1.)

[113] RD12 Collaboration, 1997 status report on the RD12 project, CERN/LHCC 97-29 (April 1997). (Cited on page 70.)

[114] T. Regge, Introduction to complex orbital momenta, Nuovo Cim. 14 (1959) 951. (Cited on page 19.)

[115] A. Salam, Weak and Electromagnetic Interactions, Conf.Proc. C680519 (1968) 367–377. (Cited on page 1.)

[116] F. Sauli, GEM: A new concept for electron amplification in gas detectors, Nucl. Instr. and Meth. A 386 (1997) 531–534. (Cited on page 33.)

[117] T. Schlüter, The $\pi^-$ $\eta$ and $\pi^-$ $\eta'$ systems in exclusive 190 GeV reactions at COMPASS(CERN), Ph.D. thesis, LMU München (2012). (Cited on pages 55, 77, and 91.)

[118] T. Schlüter, et al., Large-Area Sandwich Veto Detector with WLS Fibre Read-out for Hadron Spectroscopy at COMPASS, Nucl. Instr. and Meth. A 654 (2011) 219–224. (Cited on page 61.)

[119] C. Schmid, D. Webber, C. Sorensen, The iizuka-okubo-zweig rule and exotic exchanges: A connection through unitarity, Nuclear Physics B 111 (2) (1976) 317 – 340.
URL http://www.sciencedirect.com/science/article/pii/0550321376905459 (Cited on page 99.)

[120] K. Schönning, et al., Polarisation of the $\omega$ meson in the $pd \to {}^3\mathrm{He}\,\omega$ reaction at 1360 and 1450 MeV, Physics Letters B 668 (4) (2008) 258 – 262.
URL http://www.sciencedirect.com/science/article/pii/S0370269308010563 (Cited on page 111.)

[121] A. Sibirtsev, Heavy-meson production cross sections from proton-proton collisions, Nuclear Physics A 604 (4) (1996) 455 – 465.
URL http://www.sciencedirect.com/science/article/pii/0375947496001029 (Cited on page 19.)

[122] A. Sibirtsev, J. Haidenbauer, U.-G. Meißner, Aspects of $\phi$-meson production in proton-proton collisions, The European Physical Journal A 27 (3) (2006) 263–268.
URL http://dx.doi.org/10.1140/epja/i2005-10269-9 (Cited on pages 99 and 107.)

[123] St.Gobain, BC-404 data sheet, http://www.crystals.saint-gobain.com/document.aspx?docId=274290 (2013). (Cited on pages 45 and 60.)

[124] J. Swart, The crossing matrix in the octet model, Il Nuovo Cimento Series 10 31 (2) (1964) 420–426.
URL http://dx.doi.org/10.1007/BF02733646 (Cited on page 13.)

[125] P. Ullaland, et al., Fluid systems for RICH detectors, Nucl. Instr. and Meth. A 553 (2005) 107–113. (Cited on page 35.)

[126] N. V. Vlasov, et al., Hadronic calorimeter HCAL1 in COMPASS, Instruments and Experimental Techniques 49 (2006) 41–55. (Cited on page 34.)

[127] S. Weinberg, A Model of Leptons, Phys.Rev.Lett. 19 (1967) 1264–1266. (Cited on page 1.)

[128] Q. Weitzel, Precision Meson Spectroscopy: Diffractive Production at COMPASS and Development of a GEM-based TPC for PANDA, Ph.D. thesis, TU München (2008). (Cited on page 55.)

[129] K. G. Wilson, Confinement of quarks, Phys. Rev. D 10 (1974) 2445–2459. URL http://link.aps.org/doi/10.1103/PhysRevD.10.2445 (Cited on page 2.)

[130] P. Woodwarth, et al., Test of the Zweig rule in $\pi^- p$ interactions at 19 GeV/$c$, Physics Letters B 65 (1) (1976) 89 – 91. URL http://www.sciencedirect.com/science/article/pii/0370269376905414 (Cited on page 102.)

[131] R. Wurzinger, others., Near-threshold production of $\omega$ mesons in the $pd \to {}^3\mathrm{He}\omega$ reaction, Phys. Rev. C 51 (1995) R443–R446. URL http://link.aps.org/doi/10.1103/PhysRevC.51.R443 (Cited on page 102.)

[132] R. Wurzinger, et al., Observation of $\eta'$ and $\phi$ meson production very close to threshold in the $pd \to {}^3\mathrm{He}X$ reaction , Physics Letters B 374 (4) (1996) 283 – 288. URL http://www.sciencedirect.com/science/article/pii/0370269396002213 (Cited on page 102.)

[133] C. Wuttke, Konzeption eines Multiplizitätszählers für das COMPASS Experiment, Diploma thesis, Johannes-Gutenberg-Universität Mainz (2007). (Cited on page 67.)

[134] G. Zweig, An SU(3) model for strong interaction symmetry and its breaking. Version 1, CERN-TH-401. (Cited on page 10.)

[135] G. Zweig, An SU(3) model for strong interaction symmetry and its breaking. Version 2, CERN-TH-412. (Cited on page 10.)

# PUBLICATIONS

The following publications of the author have been issued previously during the work of this thesis and may include ideas and figures presented here.

## PUBLICATIONS

1. *Measurement of OZI rule violation and spin alignment in $\phi$ and $\omega$ production at COMPASS*, J. Bernhard on behalf of the COMPASS collaboration, EPJ Web Conf. **37** (2012) 09008

2. *Test of the OZI rule in vector meson production with the COMPASS experiment*, J. Bernhard on behalf of the COMPASS collaboration, J.Phys.Conf.Ser. **381** (2012) 012028

3. *Comment on 'Material Evidence of a 38 MeV Boson'*, J. Bernhard, J.M. Friedrich, T. Schlüter, K. Schönning, for the COMPASS Collaboration, arXiv:1204.2349 [hep-ex]

4. *Test of OZI violation in vector meson production with COMPASS*, J. Bernhard on behalf of the COMPASS collaboration, Hadron 2011 Proceedings, arXiv:1109.0272 [hep-ex]

5. *Diffractive dissociation into $K_s K^{\pm}\pi^{\mp}\pi^{-}$ final states*, J. Bernhard on behalf of the COMPASS collaboration, Hadron 2011 Proceedings, arXiv:1109.0219 [hep-ex]

6. *Hadron spectroscopy with COMPASS*, J. Bernhard on behalf of the COMPASS collaboration, Nucl.Phys.Proc.Suppl. **207-208** (2010) 200-203

7. *Study of central production of charged pionic modes at COMPASS*, J. Bernhard on behalf of the COMPASS collaboration, AIP Conf.Proc. **1257** (2010) 482-486

## TALKS & PRESENTATIONS

1. *Test of the OZI rule and spin alignment measurements with the COMPASS experiment at CERN* (Talk)
   MENU2013, Rome, Italy

2. *OZI violation and spin alignments at COMPASS* (Poster)
   INCP2013, Florence, Italy

3. *Spin alignment and OZI rule violation in exclusive $\omega$ and $\phi$ production in pp collisions at COMPASS* (Talk)
   DPG Spring Meeting 2013, Dresden, Germany

4. *Measurement of OZI rule violation and spin alignments in $\omega$ and $\phi$ production at COMPASS* (Poster)
   MESON2012, Cracow, Poland

5. *OZI rule violation in vector meson production at COMPASS* (Talk)
   DPG Spring Meeting 2012, Mainz, Germany

6. *Test of the OZI rule in vector meson production with the COMPASS experiment* (Talk)
   Rutherford Centennial Conference on Nuclear Physics 2011, Manchester, United Kingdom

7. *Test of OZI violation in vector meson production with COMPASS* (Poster)
   HADRON2011, Munich, Germany

8. *Diffractive dissociation into $K_s K^{\pm}\pi^{\mp}\pi^{-}$ final states* (Poster)
   HADRON2011, Munich, Germany

9. *Vector meson production and OZI violation at COMPASS* (Talk)
   DPG Spring Meeting 2011, Münster, Germany

10. *Hadron spectroscopy at COMPASS* (Talk)
    QCD10, Montpellier, France

11. *Central Production in the four charged pion channel at the COMPASS experiment* (Talk)
    DPG Spring Meeting 2010, Bonn, Germany

12. *Hadron spectroscopy at COMPASS* (Talk)
    Sèminaire – Service de Physique Nuclèaire, 22.01.2010, CEA Saclay, France

13. *Study of central production of charged pionic modes at COMPASS* (Talk)
    HADRON2009, Tallahassee, United States

14. *Identification of Central Production in the $4\pi^{\pm}$ Channel at COMPASS* (Talk)
    SPIN-Praha2009, Prague, Czech Republic

15. *The COMPASS Recoil Proton Detector - calibration* (Talk)
    DPG Spring Meeting 2009, Bochum, Germany

16. *The COMPASS Recoil Proton Detector - commissioning* (Talk)
    DPG Spring Meeting 2008, Darmstadt, Germany

# LIST OF FIGURES

# LIST OF TABLES